

**SYNTHESIS AND CHARACTERIZATION OF BRANCHED
IONOMERS FOR PERFORMANCE IN IONIC LIQUID –
SWOLLEN IONIC POLYMER TRANSDUCERS**

by

Andrew J. Duncan

Dissertation submitted to the faculty of the
Virginia Polytechnic Institute and State University
in partial fulfillment of the requirements for the degree of

Doctor of Philosophy

in

Macromolecular Science and Engineering

Donald J. Leo, Co-Chair
Timothy E. Long, Co-Chair
Barbar J. Aklé
Nakhiah C. Goulbourne
S. Richard Turner
Garth L. Wilkes

October 29, 2009
Blacksburg, VA

Keywords: polysulfone, branching, ionomer, ionic liquid, ionic polymer transducer, actuator.

© 2009 by Andrew J. Duncan

SYNTHESIS AND CHARACTERIZATION OF BRANCHED IONOMERS FOR PERFORMANCE IN IONIC LIQUID – SWOLLEN IONIC POLYMER TRANSDUCERS

by

Andrew J. Duncan, Ph.D.

Virginia Tech, October 2009

Advisors: Donald J. Leo and Timothy E. Long

Abstract

Ionic polymer transducers (IPT) are a class of electroactive polymer devices that exhibit electromechanical coupling through charge transport in ionomeric membranes that contain a charge mobilizing diluent and are interfaced with conducting electrodes. Applications of these active materials have been broadly developed in the field of actuators and sensors. Advances in fundamental understanding of IPT performance mechanisms and tuning of the device components has primarily focused on transducers constructed with the commercial ionomer Nafion[®] due to its overall stability, high ionic conductivity, and availability. The much smaller number of studies conducted with non-perfluorosulfonated ionomers concentrated on changes in chemical composition to address processability, price, ionic conductivity, and hydrated modulus of the final IPT. Also, nearly all ionic polymer transducers operated with water as the diluent until the recent successful development of IPTs with ionic liquids.

The objective of this research is to increase the understanding of electromechanical transduction in ionic polymer transducers through the synthesis and characterization of novel branched ionomers. Controlled branching is achieved in sulfonated polysulfones (sBPS) through employment of an oligomeric $A_2 + B_3$ step-growth polymerization. Structure – property relationships are established for a series of linear and branched sulfonated polysulfones to

resolve the effects of polymer topology and charge content on ionomer properties such as hydrated modulus and ionic conductivity. Furthermore, the variation of these parameters is investigated in the presence of ionic liquids as a function of ionic liquid uptake using two methods for introduction of the diluent. One of those methods, based on casting of IPT components in the presence of the ionic liquid, was applied to the Direct Application Process to produce a controlled set of IPT electrodes and transducers to investigate percolation effects of RuO₂ on the device's electrical properties and actuation characteristics. Equivalent circuit modeling of the component and transducer electrical impedance accurately modeled variations in contributing processes and material interfaces to estimate the evolution of effective capacitance based on the electrode composition.

Combination of optimized electrode composition, ionic liquid uptake, and the series of linear and branched sulfonated polysulfones allowed for fabrication of a tailored set of novel ionic polymer transducers. Effects of the fabrication process on the ionic conductivity of the membranes and transducers are evaluated using electrical impedance spectroscopy, which also allowed for equivalent circuit modeling to calculate effective capacitance for the series of IPTs that varied in composition, topology, and uptake for both types of fabrication processes. The transducers described in this dissertation are the first IPTs to be designed and actuated with novel ionomers, specifically linear and branched sulfonated polysulfones, in the presence of ionic liquids. Use of sulfonated polysulfones allowed for realization of transducers with high uptakes of the ionic liquid diluent that retained significant hydrated modulus on the order of 2 GPa. Characterization of electromechanical transduction for the series of sBPS – IPTs was demonstrated in cantilever bending through frequency response analysis and step responses in the time domain to low input voltages. Both the ion content and polymer topology of the sBPS ionomeric matrix demonstrated a significant effect on the final actuation performance in relation to variations in charge transport. Also, IPTs constructed with a co-diluent swelling method which emphasized the formation and stability of the ionomer's charge transport pathway demonstrated the greatest actuation responses, up to a peak-to-peak strain of ~0.45 % and strain rates on the order of 0.1 % / s while producing significant blocked force (180 N/V·m). Combination of these actuation performance metrics resulted in maximum energy densities of 1150 mJ/kg and 2.23 mJ/mm³ for the corresponding IPT.

*To my wife,
Catherine*

ACKNOWLEDGEMENTS

I would like to express my sincerest gratitude to my academic advisors, Dr. Donald J. Leo and Dr. Timothy E. Long. Within the balancing act that is a co-advising relationship you both contributed greatly to my growth as an engineer and a scientist during my time at Virginia Tech. Thank you for your encouragement, advice, direction, motivation and the many opportunities you both provided to help me see and reach for the bigger picture. I would also like to thank Dr. Barbar Aklé, Dr. Nakhiah Goulbourne, Dr. S. Richard Turner, and Dr. Garth Wilkes for serving on the committee and for the many interactions, discussions, and challenges that encouraged my scientific curiosity. Similar thanks go out to all participants of the MAP MURI and the ILEAD MURI with whom I've had the privilege of collaborating with on numerous occasions, especially Dr. Ralph Colby, Dr. Rick Beyer, Dr. Jim Snyder, and Dr. Joshua Orlicki. I also want to sincerely thank Dr. Robert Moore and Jong Keun Park for their collaboration, discussions, and for running the synchrotron SAXS experiments.

Working with two advisors also comes with the benefit of interacting with and participating in two research groups. I would like to thank all of the Long Group members, Fall 2004 to present, with whom I spent much of my first couple of years at VT and beyond learning polymer synthesis and characterization. Special thanks go out to the Davidson crew and Fall '04 1st years: Matthew Cashion, Rebecca Huyck Brown, Matthew Hunley, John Layman, Sharlene Williams, Gozde Ozturk, Min Mao, Shauntrece Hardrict, Yi Li, Matt Green, Bill Heath, Takeo Suga, Sean Ramirez, and Tianyu Wu. I also cannot thank enough all the members of CIMSS (faculty, students, and staff) for helping make 310 Durham Hall such a great place to work. I would like to thank Leo Group members, Fall 2004 to present, with whom I spent the last few years learning active materials and smart structures. Special thanks go out to Andy Sarles, Austin Creasy, Barbar Aklé, Matt Bennett, Vishnu Baba Sundaresan, David Griffiths, Kevin Farinholt, and Thomas Wallmersperger. Thank you to all of you for your help, collaboration, time, discussions, encouragement, laughs, patience and most of all friendship.

For all the details that go on seemingly in the background yet are so important to a graduate student's success I want to thank all of the administrative staff with CIMSS and MII: Beth Howell, Tammy Jo Hiner, Mary Jane Smith, Angie Flynn, Laurie Good, and Millie Ryan.

I also greatly appreciate the financial support of: the National Science Foundation Macromolecular Science and Infrastructure Engineering Integrative Graduate Education and Research Traineeship (MS & IE IGERT), the U.S. Army Research Laboratory and the U.S. Army Research Office under contract/grant number DAAD19-02-1-0275 Macromolecular Architecture for Performance (MAP) MURI and contract number W911NF-07-1-0452 Ionic Liquids in Electro-Active Devices (ILEAD) MURI.

I cannot express in such a small space my thanks for all the support of my friends and family. I owe my parents, Jay and Candace Duncan, my brother Nathan, and my sister Megan more than I could ever give in thanks for their support and love that I always know are there with me. I also want to thank my wife's family, affectionately "the Wallace crew" for all their support, interest, and love for us during these last five years. I want to specifically thank my dear friend and aunt, Cheryl Hargrove, for always presenting the challenge to look beyond what was set out for me and to do it ever with an open mind. Thank you also to my great friends Jake Kirby, Brent Stover, and Hunter Wright for their love, support, and for remembering me outside the lab.

Saving the best for last, I want to express my never ending, day-in-day-out, never expressed enough love and thanks to my wonderful wife, Catherine. You have been there with me since before this process ever started and have understood, sacrificed, persevered, encouraged, motivated, helped, and loved me more than I ever could have asked. This work, the labors of my hands and mind, is dedicated to you.

Andrew J. Duncan

October 2009

TABLE OF CONTENTS

Abstract	ii
Acknowledgements	v
Table of Contents	vii
List of Figures	xi
List of Tables	xviii
Chapter 1 Introduction and Literature Review	1
1.1 Introduction.....	1
1.2 Charged macromolecules applied in ionic polymer transducers	2
1.2.1 Ionic polymer transducer fundamentals.....	3
1.2.2 The benchmark: Nafion [®]	9
1.2.3 Step-growth ionomers.....	15
1.2.4 Chain-growth ionomers	19
1.2.5 Summary	27
1.3 Motivation.....	29
1.4 Research objectives.....	31
1.5 Contributions.....	31
1.6 Document organization.....	32
Chapter 2 Oligomeric A₂ +B₃ Synthesis of Branched Polysulfone Ionomers	34
2.1 Motivation.....	35
2.2 Experimental methods	37
2.2.1 Materials	37
2.2.2 A ₂ oligomer synthesis	39
2.2.3 A ₂ + B ₃ polymerization of sulfonated polysulfones	39
2.2.4 Characterization techniques	40
2.3 Results and Discussion	41
2.3.1 A ₂ sulfonated polysulfone oligomers.....	41
2.3.2 A ₂ + B ₃ sulfonated polysulfones	45
2.3.2.1 Composition, structure, and molecular weight characterization	46
2.3.2.2 Characterization of mechanical and thermal properties	53

2.3.2.3	Small-angle X-ray scattering for morphological investigation	60
2.4	Summary	64
Chapter 3	Investigation of the Ionomer – Conductor Interface in sBPS Electrodes and Transducers	66
3.1	Motivation.....	66
3.2	Experimental materials and methods	68
3.2.1	Materials	68
3.2.2	Electrode and transducer fabrication	69
3.2.3	Electrical impedance spectroscopy	71
3.2.4	Electromechanical transducer characterization.....	71
3.3	Results and discussion	72
3.3.1	Stand-alone IPT components	72
3.3.1.1	Electrical impedance spectroscopy	73
3.3.1.2	Equivalent electrical circuit modeling.....	77
3.3.2	Fully constructed IPTs	80
3.3.2.1	Electrical impedance spectroscopy	81
3.3.2.2	Equivalent electrical circuit modeling.....	83
3.3.2.3	Estimation of an effective capacitance from IPT impedance	88
3.3.2.4	Electromechanical actuator performance	91
3.4	Summary	96
Chapter 4	Methods for Augmentation of Charge Transport at the Ionomer – Ionic Liquid Interface	97
4.1	Motivation.....	97
4.2	Experimental	99
4.2.1	Materials	99
4.2.2	Methods.....	100
4.3	Results and discussion	102
4.3.1	IPT membranes cast in the presence of ionic liquids.....	103
4.3.1.1	Small-angle X-ray scattering.....	106
4.3.1.2	Dynamic mechanical analysis	109
4.3.1.3	Electrical impedance spectroscopy	114

4.3.2	IPT membranes swollen with ionic liquids.....	120
4.3.2.1	Swelling methods applied to sBPS.....	121
4.3.2.2	Impedance characterization of swollen membranes.....	124
4.3.3	Comparison of the casting and co-diluent swelling methods	128
4.4	Summary.....	131
Chapter 5	Design, Fabrication, and Characterization of Optimized sBPS Ionic Polymer Transducers	133
5.1	Motivation.....	133
5.2	Experimental materials and methods	134
5.2.1	Transducer fabrication	134
5.2.2	Electrical impedance spectroscopy	136
5.2.3	Electromechanical transducer characterization.....	136
5.3	Results and discussion	139
5.3.1	sBPS – IPT fabrication.....	139
5.3.2	Electrical impedance spectroscopy	143
5.3.2.1	Central membrane	143
5.3.2.2	IPT processing stages	145
5.3.3	Equivalent circuit modeling for IPT capacitance.....	149
5.3.4	Evaluation of electromechanical transduction for sBPS – IPTs	155
5.3.4.1	Frequency response functions for IPT actuation	156
5.3.4.2	Actuation responses to step inputs	160
5.3.4.3	Estimation of blocked force and energy densities.....	171
5.4	Summary.....	175
Chapter 6	Conclusions.....	178
6.1	Summary and conclusions	178
6.2	Significant contributions.....	182
6.3	Recommendations for future work	183
Bibliography	187	
Appendix A: Synthesis of long-chain branched polysulfones for multifunctional transport membranes.....	204	
Motivation.....	204	

Experimental materials and methods	205
Results and discussion	207
Summary	214
Appendix B: Initial investigations of sBPS membranes with SAXS performed at the U.S. Army Research Laboratory	216
Appendix C: Dielectric relaxation spectroscopy of sBPS membranes performed at the Pennsylvania State University	221
Appendix D: Copyright Permissions.....	223

LIST OF FIGURES

Figure 1.1: Schematic of typical IPT under (A) short circuit conditions (B) applied voltage [actuator] or imposed deformation [sensor].....4

Figure 1.2: Schematic of the actuation process in an ionic polymer transducer, also showing a typical electrode with the particles surrounded by a charged sphere of ionomer.[39] "Adapted from Akle, B. J. and Leo, D. J.: Characterization and modeling of extensional and bending actuation in ionomeric polymer transducers. *Smart Mater. Struct.* 2007. 16. p.1348–1360. Copyright IOP Publishing Limited. Reproduced with permission."6

Figure 1.3: IPT publications (peer reviewed) employing commercial or synthetic ionomers.....10

Figure 1.4: The chemical structure of Nafion[®] in the sulfonate salt form11

Figure 1.5: Deflected shapes for an ionic liquid–swollen Nafion[®]–IPT as a function of voltage amplitude for a square wave potential input.[20] "Reprinted from *Sens. Actuators, A: Phys.*, 126, Akle, B. J., Bennett, M. D., and Leo, D. J., High strain ionomeric–ionic liquid electroactive actuators, p.173–181, Copyright (2006), with permission from Elsevier."12

Figure 1.6: Actuation of Nafion[®]–IPTs (a) unoriented, (b) 3 V square-wave at 0.1 Hz, oriented and cut (c) parallel to draw, (d) perpendicular to draw. Membrane orientation fixture with indicator of IPTs cut (e) parallel to draw and (f) perpendicular to draw.[100] "Reprinted with permission from Park, J. K. and Moore, R. B., 2009, Influence of Ordered Morphology on the Anisotropic Actuation in Uniaxially Oriented Electroactive Polymer Systems, *ACS Appl. Mater. Interfaces*, 1, 697-702. Copyright 2009 American Chemical Society."14

Figure 1.7: Chemical structures for (a) SPAES (b) SPATS17

Figure 1.8: (a) Microstrain per volt (b) normalized force (c) capacitance and (d) modulus versus frequency for BPS 35 (red), PATS 30 (black), and Nafion[®] 117 (blue) to construct IPTs using impregnation–reduction and RuO₂–based direct assembly electrodes[108] "Reprinted from *J. Electrochem. Soc.*, 154, Wiles, K. B., Akle, B. J., Hickner, M. A., Bennett, M. D., Leo, D. J., McGrath, J. E., Directly Copolymerized Poly(arylene sulfide sulfone) and Poly(arylene ether sulfone) Disulfonated Copolymers for Use in Ionic Polymer Transducers, p. P77-P85. Copyright (2007), with permission from the Electrochemical Society."18

Figure 1.9: Synthetic scheme for crosslinking EVOH with sulfosuccinic acid.....21

Figure 1.10: Solid-state ²³Na NMR spectra of (a) as received Nafion[®] 117 and (b) 15 wt % sulfosuccinic acid modified PE-co-VA.[142] "Reprinted from *Polymer*, 46, Phillips, A. K. and Moore, R. B., Ionic actuators based on novel sulfonated ethylene vinyl alcohol copolymer membranes, p.7788–7802, Copyright (2005), with permission from Elsevier."22

Figure 1.11: Schematic representation and chemical structures of the ionic networking membrane composed of cross-linked PS- <i>alt</i> -MI and PVDF [152] Lu, J., Kim, S.-G., Lee, S., Oh, I.-K.: A Biomimetic Actuator Based on an Ionic Networking Membrane of Poly(styrene- <i>alt</i> -maleimide)-Incorporated Poly(vinylidene fluoride). <i>Adv. Funct. Mater.</i> 2008. 18. p.1290–1298. Copyright Wiley-VCH Verlag GmbH & Co. KGaA. Reproduced with permission.....	24
Figure 1.12: Displacement of PVDF-co-HFP (VH), PE-co-TFE (ET), PTFE-co-HFP (TH), and Nafion [®] (NM) IPMCs recorded for 100 s with an applied DC voltage of 2 V [154] Han, M. J., Park, J. H., Lee, J. Y., Jho, J. Y.: Ionic Polymer-Metal Composite Actuators Employing Radiation-Grafted Fluoropolymers as Ion-Exchange Membranes. <i>Macromol. Rapid Commun.</i> 2006. 27. p.219-222. Copyright Wiley-VCH Verlag GmbH & Co. KGaA. Reproduced with permission.....	27
Figure 2.1: Synthesis of the disulfonated DCDPS monomer	38
Figure 2.2: Synthesis of the TFPPO branching agent (B ₃)	38
Figure 2.3: Synthesis of controlled molecular weight hydroxyl terminated A ₂ oligomers	42
Figure 2.4: ¹ H NMR spectra and assignments for polysulfone A ₂ oligomers with a target M_n of 3 000 g/mol and target degrees of sulfonation of (a) 0 % (b) 20 % (c) 40 %....	44
Figure 2.5: Synthesis of highly branched poly(arylene ether sulfone) ionomers through an oligomeric A ₂ + B ₃ method.....	46
Figure 2.6: ³¹ P NMR spectrum of a highly branched 20 mol % disulfonated polysulfone synthesized with a 10 000 g/mol oligomeric spacer between dendritic (D), linear (L), and terminal (T) branch points [M indicates shift for TFPPO monomer].....	48
Figure 2.7: DLS size distributions by intensity for linear and branched sulfonated polysulfones in NMP, (a) 0 M LiBr (b) 0.01 M LiBr (c) 0.2 M LiBr.	50
Figure 2.8: SEC chromatogram showing the RI traces for the series of linear and branched ionomers (NMP, 0.2 M LiBr, 50 °C)	52
Figure 2.9: Comparison of stress–strain behavior for linear and highly branched polysulfones (A ₂ M_n = 3 000 g/mol) with varied degrees of sulfonation as indicated.....	54
Figure 2.10: TGA for thermal stability of highly branched polysulfones (A ₂ M_n = 3 000 g/mol) with various degrees of sulfonation as indicated (N ₂ , 10 °C/min)	57
Figure 2.11: (a) E' (b) E'' (c) $\tan \delta$ versus temperature for highly branched polysulfones (A ₂ M_n = 3000 g/mol) of varied degrees of sulfonation as indicated (5 °C/min, 1 Hz).....	58
Figure 2.12: 2-D SAXS profiles for comparison of linear versus branched sBPS membranes containing 20 % disulfonation	62
Figure 2.13: 2-D SAXS profiles for comparison of linear versus branched sBPS membranes containing 20 % or 40 % disulfonation.....	63

Figure 3.1: Chemical structures for (a) HB-3kBPS-20 and (b) EMI-Tf.....	69
Figure 3.2: Bending actuation setup for a novel IPT fabricated from HB-3kBPS-20, EMI-Tf, and RuO ₂	72
Figure 3.3: Through-thickness ionic conductivity versus molar uptake of EMI-Tf in cast HB-3kBPS-20 membranes.....	74
Figure 3.4: Bode plot for the impedance of stand-alone electrodes constructed with varied volumetric loading of RuO ₂ (<u>LEGEND</u> : 7.5%, pink circle; 15%, grey square; 22.5%, red X; 30%, green triangle; 37.5%, blue star, 45%, black cross).....	75
Figure 3.5: Bulk resistance and ionic conductivity versus RuO ₂ loading in stand-alone electrodes as characterized with both the Autolab and HP Impedance Analyzers	76
Figure 3.6: EC-1: equivalent circuit model for stand-alone electrodes	77
Figure 3.7: Representative fits of EC-1 to experimental EIS data for stand-alone electrodes with RuO ₂ volumetric loading of (a) 15 % (b) 22.5 % (c) 30 % (d) 37.5 %	78
Figure 3.8: Equivalent circuit parameters for (a) resistor and (b) capacitive elements of EC-1 as determined from fits and calculations based on impedance data for stand-alone electrodes.....	79
Figure 3.9: Bode plot for the impedance of built IPTs constructed with varied volumetric loadings of RuO ₂ in the electrodes (<u>LEGEND</u> : 7.5%, pink circle; 15%, grey square; 22.5%, red X; 30%, green triangle; 37.5%, blue star, 45%, black cross).....	82
Figure 3.10: Bulk resistance and ionic conductivity versus RuO ₂ electrode loading in novel HB-3kBPS-20 / EMI-Tf – IPTs	83
Figure 3.11: EC-2: extended equivalent circuit model for built IPTs.....	84
Figure 3.12: (a) Bode plot and (b) Nyquist plot from EIS characterization and modeling with EC-2 of an IPT with 37.5 vol % RuO ₂ electrodes	85
Figure 3.13: Equivalent circuit parameters for (a) resistors and (b) CPEs in EC-2 as determined from fits and calculations based on impedance data for IPTs	86
Figure 3.14: Ionic conductivity of R ₁ and R ₂ components as calculated from experimental results and EIS modeling with EC-2.....	87
Figure 3.15: Frequency dependence for the normalized effective capacitance when calculated with various components of EC-2 for an IPT with 37.5 vol % RuO ₂ electrodes ..	90
Figure 3.16: Calculated effective capacitance associated with each CPE in EC-2 from fits of impedance data for built IPTs.....	91
Figure 3.17: Displacement response curves to step input voltages of varied magnitude and direction for an EMI-Tf swollen HB-3kBPS-20–IPT with 45 vol % RuO ₂ DAP electrodes	92

Figure 3.18: (a) peak strain achieved within 300 s and (b) normalized strain rate resulting from step input voltages of varied magnitude and direction for IPTs with varied vol % RuO ₂ electrodes	93
Figure 3.19: SEM micrographs of HB-3kBPS-20 – IPTs designed with electrodes containing (a) 7.5 (b) 15 (c) 22.5 (d) 30 (e) 37.5 (f) 45 vol % RuO ₂	94
Figure 4.1: Chemical structures for (a) Lin-BPS-YY, (b) HB-XkBPS-YY and (c) EMI-Tf.....	99
Figure 4.2: SEM micrographs of (a) the cross-section of an sBPS–IPT and (b) its central membrane cast from HB-3kBPS-20 solution and 75 wt % EMI-Tf uptake	104
Figure 4.3: 2-D SAXS profile for HB-3kBPS-20 cast in the presence of 0% EMI-Tf (filled triangles) and 25 % EMI-Tf (open triangles).....	107
Figure 4.4: DMA (a) E' , (b) E'' , and (c) $\tan \delta$ versus temperature for Lin-BPS-20 cast in the presence of 0 – 100 wt % uptake of EMI-Tf	111
Figure 4.5: Matrix $T_{g,m}$ and cluster $T_{g,cl}$ versus wt % uptake for sBPS cast in the presence of EMI-Tf	112
Figure 4.6: Storage modulus (hydrated) versus wt % uptake for sBPS cast in the presence of EMI-Tf	113
Figure 4.7: (a) Semi-log and (b) linear plots of in-plane ionic conductivity versus molar uptake for sBPS membranes cast in the presence of EMI-Tf. “prev” indicates data for comparison from a previous study. A and B represent the faces of the ionomer membranes tested.	115
Figure 4.8: Semi-log and linear plots of in-plane ionic conductivity versus (a & b) normalized molar uptake (c & d) wt % uptake for sBPS membranes cast in the presence of EMI-Tf. “Prev” indicates comparison data from a previous study. .	118
Figure 4.9: Confirmation experiments for ionic conductivity versus molar uptake of sBPS cast in the presence of EMI-Tf.....	119
Figure 4.10: Uptake versus time for the sBPS series swollen in 100 % EMI-Tf at (a) RT + 55 °C (b) 110 °C	122
Figure 4.11: EMI-Tf uptake versus time for sBPS immersed in (a) 20/80 (b) 40/60 (c) 60/40 (d) 80/20 w/w MeOH/EMI-Tf	123
Figure 4.12: In-plane conductivity (left, solid line) and swelling uptake of EMI-Tf (right, dotted line) versus co-diluent ratio of MeOH / EMI-Tf for the (a) A face and (b) B face of sBPS membranes	124
Figure 4.13: Dependence of in-plane ionic conductivity on uptake of EMI-Tf when swollen with varied co-diluent ratios of MeOH to EMI-Tf for the series of sBPS ionomers.....	125
Figure 4.14: 3-D plot (lines) of ionic conductivity vs. uptake of EMI-Tf and co-diluent ratio of MeOH to EMI-Tf for the sBPS series. Open symbols are 2-D projections on each plane.....	127

Figure 4.15: Ionic conductivity versus molar uptake for (a) Lin-BPS-20 (b) Lin-BPS-40 (c) HB-3kBPS-20 (d) HB-3kBPS-40 cast in the presence of EMI-Tf or swollen in varied ratios of MeOH / EMI-Tf.....	129
Figure 4.16: IPT design space based on ionic conductivity versus (a) molar uptake (b) wt % uptake for sBPS membranes swollen in co-diluents or cast in the presence of EMI-Tf	130
Figure 5.1: Schematic of the experimental setup[88] employed to measure free displacement and current for sBPS – IPTs subjected to voltage inputs. "Reprinted from Akle, B. J. and Leo, D. J.: Single-Walled Carbon Nanotubes – Ionic Polymer Electroactive Hybrid Transducers. <i>J. Intell. Mater. Syst. Struct.</i> 2008. 19. p.905–915. Copyright SAGE Publications. Reproduced with permission."	139
Figure 5.2: Target and experimental ionic conductivity versus molar uptake for central membranes cast in the presence of EMI-Tf or swollen in varied ratios of MeOH / EMI-Tf.....	144
Figure 5.3: Schematic representation of the fabrication stages for IPT construction and EIS characterization points	146
Figure 5.4: Ionic conductivity measured at each stage of IPT fabrication for (a) Lin-BPS-20 (b) Lin-BPS-40 (c) HB-3kBPS-20 and (d) HB-3kBPS-40.....	147
Figure 5.5: Ionic conductivity versus molar uptake for the full series of sBPS – IPTs after fabrication	148
Figure 5.6: Representative fits of EC-2 to experimental EIS data for IPTs fabricated with (a) cast Lin-BPS-20 and (b) co-diluent swollen HB-3kBPS-40.....	150
Figure 5.7: (a) Resistive and (b) capacitive equivalent circuit parameters from EC-2 as determined from fits and calculations based on impedance data for sBPS – IPTs.....	151
Figure 5.8: Ionic conductivity of R_1 and R_2 components for sBPS – IPTs as calculated from experimental results and EIS modeling with EC-2.....	153
Figure 5.9: Calculated effective capacitance associated with each CPE in EC-2 from fits of impedance data for built sBPS – IPTs	153
Figure 5.10: Comparison of effective capacitance (C_1) for sBPS – IPT impedance modeled as a series of RC circuits (x-axis, Equation 3.7) or with EC-2 (y-axis, Equation 3.10)	155
Figure 5.11: Representative frequency response functions for the series of sBPS – IPTs expressed as (a) microstrain per volt (b) impedance (voltage per current) and (c) microstrain per areal charge	157
Figure 5.12: (a) Damping ratios and (b) effective bending modulus for the full series of sBPS – IPTs as determined from the frequency response to a random input at 0.5 V_{rms}	159
Figure 5.13: Bending actuation response of representative sBPS – IPTs subjected to a +2 V step input for 300 s.....	161

Figure 5.14: Peak strain measured for sBPS – IPT responses to step voltages for 300 s	162
Figure 5.15: Back relaxation as a percentage of peak strain for sBPS – IPT step responses to various voltage magnitudes and directions	163
Figure 5.16: Bending actuation response of representative sBPS – IPTs subjected to a ± 2 V square wave input at 10 mHz.....	164
Figure 5.17: Initial strain rates for sBPS – IPTs versus the applied step voltage	165
Figure 5.18: Initial strain rates (normalized to step voltage) versus the corresponding through thickness conductivity of the sBPS – IPT determined with EIS, plotted on a (a) linear scale (b) log-log scale.....	166
Figure 5.19: Initial 10 s of bending actuation response for sBPS – IPTs subjected to a +2 V step input (10 IPTs from full fit in Figure 5.18b)	168
Figure 5.20: Initial strain rates (normalized to step voltage) versus experimental uptake in (a) mol EMI-Tf / mol SO_3^- (b) weight percent, of ionic liquid in the central membrane and electrodes.....	170
Figure 5.21: Estimated blocked force vs. experimentally measured free deflection at 0.5, 1, and 2 V for sBPS – IPTs constructed with (a) Lin-BPS-20 cast, (b) HB-3kBPS-20 cast, (c) Lin-BPS-40 cast, (d) Lin-BPS-40 co-diluent, (e) HB-3kBPS-40 cast, (f) HB-3kBPS-40 co-diluent	173
Figure A.1: $\text{A}_2 + \text{B}_2 + \text{B}_3$ synthesis of long-chain branched PSF-PO	208
Figure A.2: [i.] LIN-PSF-PO and [ii.] LCB-0.4-PSF-PO analyzed with 2-D FTIR in (a) DMAc solution with (b) K_2CO_3 and (c) DHDPs for disappearance of the aromatic C-F bond [664 cm^{-1}] from the monomers (d) BFP3O and (e) TFPPO reacting to form the polymers (f) LIN-PSF-PO and (g) LCB-0.4-PSF-PO (alphanumeric characters indicate each individual curve).....	209
Figure A.3: ^1H NMR spectra overlaid for the series of linear and branched PSF-PO.....	210
Figure A.4: SEC traces and molecular weight results for LIN-PSF-PO (maroon) and LCB PSF-PO (mol % TFPPO: 0.2 = green, 0.4 = light blue, 0.6 = dark blue)	211
Figure A.5: DSC heat capacity traces and T_g for LIN-PSF-PO (blue) and LCB PSF-PO (mol % TFPPO: 0.2 = black, 0.4 = red, 0.6 = green)	212
Figure A.6: DMA storage modulus and tan delta signals versus temperature showing T_g and sub- T_g transitions for LIN PSF-PO	213
Figure A.7: Combined Bode plot ($ Z $, phase) for LIN PSF-PO cast (blue: diamond, X) in the presence of $\text{Li}^+ \text{Tf}^-$ (red: square, asterisk) or $\text{Li}^+ \text{Bim}^-$ (green, up triangle, down triangle) against an empty background (black: circle, cross).....	214
Figure B.1: SAXS spectrum of highly branched sulfonated polysulfones synthesized with a 3 000 g/mol oligomeric spacer between branch points (Na^+ form).....	217
Figure B.2: SAXS spectrum of highly branched sulfonated polysulfones synthesized with a 3 000 g/mol oligomeric spacer between branch points (H^+ form).....	218

Figure B.3: SAXS spectrum of highly branched sulfonated polysulfones synthesized with a 5 000 g/mol oligomeric spacer between branch points (H ⁺ form).....	218
Figure B.4: SAXS spectrum of linear polysulfones with varied degrees of sulfonation (Na ⁺ form)	219
Figure B.5: SAXS spectrum of linear polysulfones with varied degrees of sulfonation (H ⁺ form)	219
Figure B.6: SAXS spectrum of highly branched sulfonated polysulfones synthesized with a 10 000 g/mol oligomeric spacer between branch points (Na ⁺ form).....	220
Figure B.7: SAXS spectrum of highly branched sulfonated polysulfones synthesized with a 10 000 g/mol oligomeric spacer between branch points (Na ⁺ form).....	220
Figure C.1: DRS spectrum of dielectric constant (black) and dielectric loss (blue) for highly branched polysulfones with varied ionic content from 120 – 180 °C.....	222

LIST OF TABLES

Table 1.1: Physical properties of commercial and synthetic IPT membranes (H ₂ O hydrated)	20
Table 2.1: Results of ¹ H NMR analysis for A ₂ oligomer M_n and degree of sulfonation	45
Table 2.2: Polymer topology characterization for A ₂ + B ₃ polysulfones with varied oligomeric spacer lengths and ionic content.....	49
Table 2.3: Molecular weight characterization for polysulfones with varied oligomeric spacer lengths and ionic content	53
Table 2.4: Stress – strain properties for polysulfones as a function of topology and degree of sulfonation.....	55
Table 2.5: Thermal transition temperatures for the series of linear and branched polysulfones measured with DSC, DMA, and TGA	56
Table 2.6: Storage and loss moduli for the series of linear and branched polysulfones.....	60
Table 2.7: Scattering vector positions and corresponding Bragg spacings for the ionomer peak present in SAXS analysis of linear and branched polysulfones.....	64
Table 3.1: Average HB-3kBPS-20–IPT layer thickness \pm one standard deviation	95
Table 4.1: Chemical and physical properties for sBPS employed in the EMI-Tf uptake study ..	100
Table 4.2: Scattering features from peak fits of 2-D SAXS experiments with uptake	108
Table 4.3: Thermal transitions from DMA of sBPS ionomers cast with EMI-Tf	109
Table 5.1: sBPS – IPT compositions for ionic liquid uptake and electrode RuO ₂ loading	141
Table 5.2: Representative sBPS – IPT dimensions and densities.....	156
Table 5.3: Experimental free deflection and estimated blocked force and energy densities for sBPS – IPTs subjected to a positive step voltage	175

Chapter 1 INTRODUCTION AND LITERATURE REVIEW

1.1 Introduction

Electromechanical transducers are composite devices that are able to transform an electrical energy input, normally an applied voltage or current, into an output in the form of a mechanical response. The response may also be an electric signal induced by a mechanical deformation of the transducer. One of the most common materials used in this field are piezoelectrics, which may be in the form of ceramics or polymers. Electromechanical transducers from the class of electroactive polymer devices (EAPs) operate in either a wet or dry state depending on the system and desired application. The focus of this dissertation is on so-called wet EAPs that specifically operate through charge transport in devices using ionomeric membranes swollen with a charge mobilizing diluent. Those composite devices are referred to herein as ionic polymer transducers (IPTs). IPTs are most commonly referred to as ionic polymer-metal composites (IPMCs). However, the IPT classification broadens the definition to include electrodes with non-metallic conductor materials and varied configurations.

Ionic polymer transducers are composed of ion-conducting polymer membranes saturated with an ion-conducting diluent, a high surface area electrode layer, and an electrically conductive surface layer. These composite devices are presently under broad development for applications as sensors and actuators based on various configurations that emphasize their electromechanical properties. The projected fields of interest for application are the biomedical arena, biomimetics, robotics, animatronics, aerospace, and consumer products.[1, 2] Application of a DC voltage to an IPT clamped in a cantilever configuration causes a resultant strain in the form of bending. This form of transduction is referred to as actuation and may also be used to measure force production capabilities of the transducer. Conversely, deformation of the IPT under an applied force will generate a voltage which can be detected as an electrical signal, displaying sensitivity quasistatically and/or dynamically. The physics of transduction from electrical input to mechanical response and vice versa remains as an active area of research. However, generally

accepted models agree that applied DC voltage causes a redistribution of charge within the composite that is directly linked with the mechanical response. In sensing mode, the charge redistribution is believed to be instigated by the reorientation of dipoles induced by mechanical deflection.[3, 4] Real-time investigation of this redistribution of charge during actuation has been recently performed with both small-angle neutron scattering (SANS) [5] as well as nuclear magnetic resonance imaging (MRI).[6]

As reviewed in the following sections, the research area of ionic polymer transducers is mostly composed of technology based on Nafion[®]. This ionomer is commercially available in membrane form from Dupont and set the benchmark in ion conducting membranes after its introduction in the early 1960s. Before its extensive use in the development of IPT technology, Nafion[®] was originally applied in permselective membranes for chlor-alkali separations. The bulk of recent research concerning Nafion[®] and its more minor counterparts concerns the development of better fuel-cell proton-exchange membranes.[7] Nafion[®]'s use as a model IPT ionomer has to this point allowed for extensive development and understanding of IPT construction techniques, transduction models, diluent interaction effects, electrode composition and morphological contributions, and potential applications. After the development of these areas the main component of the device least explored is ionomer design specifically for application in ionic polymer transducers.

1.2 Charged macromolecules applied in ionic polymer transducers

*This section is primarily derived from and expanded upon: [8] Duncan A J, Leo D J and Long T E 2008 Beyond Nafion: Charged Macromolecules Tailored for Performance as Ionic Polymer Transducers *Macromolecules* **41** 7765-7775

Ionic polymer transducers (IPT) based on electroactive polymer (EAP) compositions display electromechanical coupling that may enable breakthroughs in the design of high performance actuators and sensors. The ion-exchange membrane Nafion[®] remains as the benchmark for a majority of research and development in IPT technology. Advances in IPT performance, elemental understanding of transduction mechanisms, and the development of future technologies (e.g., artificial muscles) are due to significant efforts to tailor complementary transducer compositions relative to commercially available Nafion[®]. Current fundamental

advances in the synthesis, characterization, and application of tailored ion-containing polymers for increased performance, decreased cost, and improved processing of IPTs are reviewed here. Recent attention to the correlation of morphological structure to ion conduction mechanisms has led to new paradigms for performance. Tailoring of ionomeric membranes to isolate material interactions within the composite IPT that contribute to performance is also highlighted. Novel compositions such as ion-containing polysulfones, poly(ethylene-*co*-vinyl alcohol), polystyrene, and fluorinated acrylic copolymers have broadened the range of electromechanical performance for IPTs. This section discusses recent research efforts and rapidly emerging fundamental understanding of the tailored synthesis and application of ionomers in IPTs.

1.2.1 Ionic polymer transducer fundamentals

Many functional macromolecules offer promise in electromechanical transducers that exhibit coupling between stimuli in the electrical and mechanical domains. For example, it is well-established that several natural and synthetic materials exhibit the piezoelectric effect, which is a phenomenon that provides coupling between electrical and mechanical stimuli.[9-11] Application of a voltage to a piezoelectric material will produce strain, and likewise, the application of a mechanical strain will produce an electrical signal. The existence of the piezoelectric effect in inorganic and polymeric materials such as lead-zirconate-titanate (PZT) and poly(vinylidene fluoride) (PVDF) respectively has enabled the development of numerous devices in sensing and motion control.[12]

Recently, significant attention has been directed to the field of *electroactive polymer (EAP)* transducers.[2, 13-15] Electroactive polymer composites exhibit behavior that is functionally similar to piezoelectric materials, however, EAPs potentially enable larger strains ($> 1\%$) at lower applied voltages ($< 10\text{ V}$). The inherent mechanism in piezoelectric ceramics is also present in piezoelectric/electrostrictive polymers, a specific class of EAP, where coupling occurs due to the rotation of electronic dipoles that exist in the crystalline lattice or polymer backbone. Other classes of EAPs include dielectric elastomers, liquid crystal elastomers, ionic polymer transducers, conducting polymers, carbon nanotube actuators, and molecular actuators.[16, 17] EAP operation involves necessary physical processes such as electrostatic attraction between charged electrodes, Maxwell stress that is generated upon the application of an electric field, and ion transport to facilitate electromechanical coupling.[18, 19] An emerging class of EAP

materials, which is the focus of the present research efforts, involves structures that are fabricated from ion-containing polymeric membranes. We term this class of devices *ionic polymer transducers*. The field of ionic polymer transducers (IPT) evolved from the discovery that many electroactive polymer composites exhibit coupling properties that enable a variety of engineering devices. Despite relatively high cost, tailored ionic polymer transducers offer numerous advantages over other classes of EAP transducers. IPTs are easily fabricated, flexible, lightweight, and the final structures are considered as low-voltage, low-power devices that are silent to operate. A primary engineering application for IPTs is the replacement of motion-control devices where small electrical stepper motors or piezoelectric ceramics were previously the predominant option. In applications that do not require large actuation force or high frequency operation, imposing a constant current or constant voltage allows for precision positioning without the need for multiple moving parts such as gears, pistons, or shafts. The device functions both as a motion-control device and simultaneously as a motion sensor.

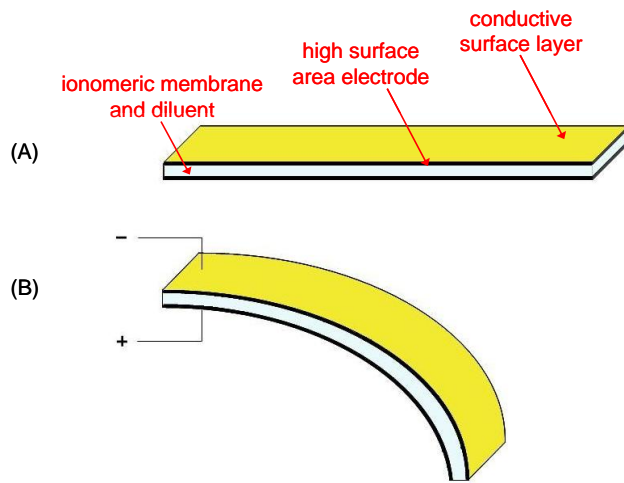


Figure 1.1: Schematic of typical IPT under (A) short circuit conditions (B) applied voltage [actuator] or imposed deformation [sensor]

The majority of commercial IPT development has employed the most directly accessible aspect of electromechanical coupling, i.e. actuation, where an applied voltage results in movement of the device. Quantification of displacement in bending is relative to the radius of curvature of the actuated IPT, which experimentally is nearly constant [20] and is depicted in Figure 1.1. If the device's displacement is restricted to zero, the result of actuation is development of force under the applied voltage. The overall concept of electromechanical

coupling is reversible such that an imposed deflection of the IPT device produces a detectable output current. This active conversion typically allows for sensing or power harvesting. Several representative applications under development include a fluid–flow wall shear sensor,[21] an active surgical catheter,[22, 23] robotic prosthetic grippers, a cell–phone camera aperture,[24] a multifunctional tactile sensor,[25] energy harvesters,[26, 27] propulsion for underwater vehicles,[28, 29], and micropumps/mixers.[30, 31]

IPTs are designed as composite devices that display electromechanical transduction within a hydrated ion–exchange membrane that has an electrically conducting electrode on both faces. The ionomeric membrane contains a certain molar percentage of negatively or positively charged sites covalently bound to the polymer backbone. Macromolecular composition determines both polarity and the concentration of charged versus non-charged monomeric segments, and a microphase separated morphology, referred to as a cluster network, often results.[32] The network of hydrophilic clusters and/or channels[33] facilitates charge transport when swollen in the presence of an added diluent. Typically, free cationic counterions move toward the cathode under the application of an actuation voltage (< 10 V) while the bound anionic species remain immobile. Earlier studies suggest that the accumulation of excess counterions in a boundary layer at the cathode increases electro–osmotic pressure in the clusters. Flow of the diluent into the clusters causes internal strain in the polymer matrix that manifests as swelling.[34–38] Simultaneous depletion of solvated counterions at the anode boundary layer results in contraction that pushes the diluent out of the clusters. In a cantilever configuration, the IPT experiences bending actuation toward the anode. Recent results also demonstrated that when one face of the IPT is fixed to a surface that electromechanical coupling produces extensional actuation in the thickness direction.[39] Figure 1.2 represents the process of electromechanical transduction in an IPT for the purpose of bending or extensional actuation.

Actuator performance is typically quantified by measuring blocked force and free displacement under an applied voltage. These tests allow for the maximum actuation response under the limits of zero displacement or zero load respectively. Measures of blocked force and free displacement are also used to calculate the gravimetric and volumetric energy density of the transducer.[40] Initial actuation is normally rapid and is correlated with the size of the free cation associated with the polymer-bound charged sites.[41] Water-swollen IPTs often suffer from back relaxation of the transducer after the initial voltage–induced displacement. Back relaxation

occurs when the actuator motion decays back toward its original position after reaching a maximum forward displacement.

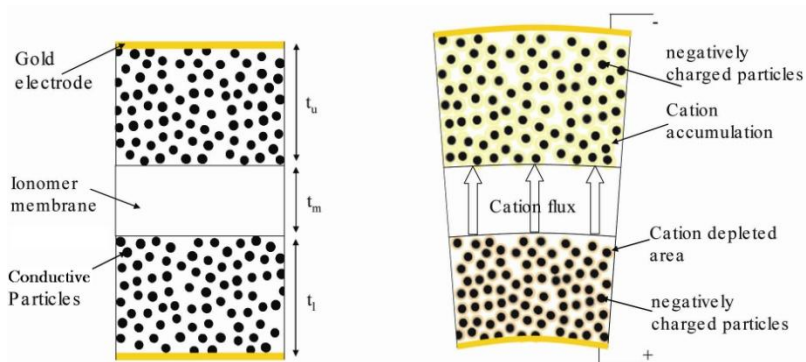


Figure 1.2: Schematic of the actuation process in an ionic polymer transducer, also showing a typical electrode with the particles surrounded by a charged sphere of ionomer.[39]
"Adapted from Akle, B. J. and Leo, D. J.: Characterization and modeling of extensional and bending actuation in ionomeric polymer transducers. *Smart Mater. Struct.* 2007. 16. p.1348–1360. Copyright IOP Publishing Limited. Reproduced with permission."

The endpoint, which is reached under continued application of dc potential, is not typically located at the origin. Several mechanisms were proposed earlier to explain this behavior beyond the elastic nature of the polymer matrix surrounding the clusters. Due to the continued detection of current and accumulating charge at the cathode during observed back relaxation, Nemat-Nasser *et al.* proposed that hydraulic pumping of diluent out of the clusters was responsible.[41] However, these hydraulic effects were thought to originate from realignment of the sulfonate salt dipoles in the presence of an excess of free cations, causing a cation redistribution that changes the osmotic and electrostatic pressures in the cluster. Other researchers employed cyclic voltammetry and observed electrochemical reactions in platinum IPT electrodes with variation of applied potential.[36, 42] Deposition of platinum oxide compounds was linked in *real-time* to observation of back relaxation. This occurrence suggested that stresses at the ionomer – electrode interface counteracted the bending motion during both cathodic and anodic scans. Overall, back relaxation limits the frequency range and accuracy of the actuator's motion control while decreasing the ability to deliver a constant peak force to a target. The proposed mechanisms suggest back relaxation results from the interface of all three IPT components and optimization is required to limit its occurrence.

The main components of the IPT include an ionomeric membrane, a high surface area electrically conducting electrode, and an ion-conducting diluent. The selection and properties of all three components target ease of device construction, performance, and the specific application.[43] Ideal IPT membranes are characterized by a range of elastic modulus and ionic conductivity that combine to enhance their electromechanical coupling once integrated into the device. These properties are crucial because the ionomeric membrane's main roles during actuation are to provide structure and ion transport while encapsulating the electrolyte diluent. Dependent upon the range of desired displacement and force actuation, the ionomeric membrane should display a hydrated modulus of at least 50 MPa. This specific modulus was chosen based on the benchmark performance of Nafion[®] as an actuator for both force and displacement.[40, 41] As expected, the intended application for actuation leads to variation in this value, especially in terms of durability. In order to allow for practical and useful lifetimes in a variety of environments, film stability is critical in all forms, preferably under actuation conditions for several million cycles. Operating environments presently include open air, varied relative humidity, submersion in liquids, temperature changes, and applied potentials. Stability is not defined solely for the neat membrane, but must also apply during manufacture and performance when the membrane is in intimate contact with the diluent and electrodes.[44] Design and preservation of the well-defined microphase-separated morphology should provide a sufficiently polar interface with the diluent to resist dissolution or loss of definition.[45, 46] The cluster-type morphological structure associated with ionomers typically produces a high ionic conductivity on the order of 100 mS/cm when swollen with a diluent (e.g. H₂O). The final ionic conductivity of the IPT is also directly dependent on the magnitude of the diluent uptake during processing. Uniaxial stiffness typically scales to the -4/3 power with increased diluent uptake that leads to increased ionic conductivity.[47] However, high ionic conductivity is necessary to produce both high free deflection and blocked force. Solution and/or melt processability are also essential to ease of manufacture, customization of IPT geometry, and production of high surface area electrodes with certain methods and materials. Overall, the ionomeric membrane should balance thermal, electrical, electrolytic, oxidative, morphological, and mechanical stability[48, 49] to maximize actuation.

The high surface area electrode is either composed of conducting particles dispersed in a matrix of the ionomer [50, 51] or metal particles that are impregnated into the film as salts and

reduced on or near its surface.[52, 53] The former case also requires attachment of a thin metal surface layer with low electrical resistance, usually gold leaf. The latter case is specifically referred to as an ionic polymer–metal composite (IPMC) due to the electroless deposition of metals (e.g. Ag, Au, Cu, Pd, Pt) on the ionomeric membrane surface. The high interfacial surface area between the electrode and the ionomeric membrane is important for the development of charge accumulation since capacitance is directly related to the total strain performance of the resulting IPT.[54] IPT design uses metal surface layers with low electrical resistance to permit the assumption that a constant potential difference is applied through the thickness of the device along its entire length. Several studies demonstrated that fatigue and cracking in this layer causes significant performance losses in IPTs, regardless of the electroding technique.[44, 55] Ionomer design to compositionally increase compatibility and adhesion with the electrodes is one possible future strategy to address this limitation.

A range of diluents have been investigated for submerged and/or open–air IPT operation including water, ethylene glycol, glycerol, formamide, and various ionic liquids.[47, 56-59] Important factors in the choice of an IPT diluent are viscosity, vapor pressure, electrolytic stability, dielectric constant, and hydrophilicity. The diluent viscosity was directly related to IPT strain rate due to an influence on both the mobility of free ions as well as resistance to flow in and out of the ionic aggregates in the boundary layer. Thus, within certain time scales of applied ac and dc potential, higher diluent viscosity can minimize back relaxation but often with decreased initial strain rates.[60] In applications that required submersion the IPT is typically open to equilibration with the surrounding liquid as its internal diluent and a source of external forces. Diluent vapor pressure is extremely important to open air operation where evaporation during actuation significantly decreases performance. Enhanced electrolytic stability of the diluent prevents degradation during actuation and allows larger ranges of voltage that typically lead to increased performance. Increases in the dielectric constant of the diluent regularly lead to higher ionic conductivity of the final device. In the case of ionic liquids, the diluent also acts as an electrolyte where its fully ionic composition contributes both free cations and free anions to the mechanism of charge transport. The wide range of diluent properties contribute to the performance magnitude, limits, and lifetime of IPTs, especially due to the influence of the diluent’s solvation power within the ionomeric morphology.[61] Optimization of charge transport and charge accumulation within the IPT are critical to performance. Tailored IPT

membranes expand the Nafion[®]-based understanding of IPTs to improve processing, morphological structure, and electrical and mechanical properties for augmented charge transport, increased modulus, larger strains, larger applied force, and increased energy density. The remainder of this review focuses on recent efforts in ionomer design specific to step-growth and chain growth polymers that attempt to improve IPT performance with novel ionomers and hybrid compositions.

1.2.2 The benchmark: Nafion[®]

Since IPMCs were first proposed fifteen years ago,[62-64] the area of ionic polymer transducers experienced the enormous growth shown in Figure 1.3 (as measured by peer-reviewed publications). Despite the large increase in recent publications, the number of studies involving non-commercial synthetic ionomeric membranes remains relatively small. Bar-Cohen's recent review highlighted the performance of commercial ionomer-based IPTs in various actuator applications from robotic fish to miniature grippers.[65] Cumulative modeling efforts combined with empirical data from experiments also provided a design loop for better understanding of the electromechanical transduction mechanism in actuator and sensor applications.[4, 35, 38, 39, 66-75] The interactions between the ionomeric membrane, diluent, and electrodes are better understood on the basis of Nafion[®] and its analogs; however, many opportunities for tailoring new ionomers exist to enhance IPT performance.

Prior to a discussion of next generations of ionomers beyond Nafion[®], it is important to note the synthetic design and structure-property relationships that make Nafion[®] desirable for constructing IPTs. DuPont reportedly synthesizes Nafion[®] through the radical copolymerization of a sulfonyl fluoride-terminated perfluoroether monomer and tetrafluoroethylene. The final polymer is semicrystalline with a polytetrafluoroethylene (PTFE) backbone and short perfluoroether branches that are terminated with sulfonyl fluoride groups. The precursor form is processable using both solvent and melt fabrication techniques. Reaction of the precursor membranes with potassium hydroxide in dimethyl sulfoxide and water converts the sulfonyl fluoride functionalities to potassium sulfonate salts that are freely converted to other cations through soaking in specific salt solutions or strong acids. Similar perfluorinated membranes such as Flemion[®] from Asahi Glass and Aciplex[®] from Asahi Chemical differ from Nafion[®] in length, composition, and ionic functionality of the sidechain.[76] The chemical structure of

Nafion[®] is shown in Figure 1.4. Mauritz and Moore recently reviewed Nafion[®] and its fundamental structure–property relationships.[7] Since the introduction of Nafion[®] in 1962, primary uses involved chlor–alkali separations and proton–exchange membranes in fuel cell development. The two main characteristics that set Nafion[®] apart for these applications, as well as in IPTs, are an extremely hydrophobic, semi–crystalline PTFE matrix and microphase separation of the hydrophilic sulfonate functionalities. The semi–crystalline PTFE matrix provides modulus greater than or equal to 100 MPa in the dry state and resistance to dissolution while swelling with hydrophilic diluents.[77] Although the exact state of Nafion[®]'s morphology still remains under debate, most theoretical and empirical models suggest the formation of multiplets and/or aggregates of the sulfonate groups within a matrix of PTFE.[32, 78, 79] These ionic aggregates provide a physical network in the dry state[80] and a pathway for ion–associated transport to achieve ionic conductivities on the order of 100 mS/cm when swollen with hydrophilic diluents.[46, 81]

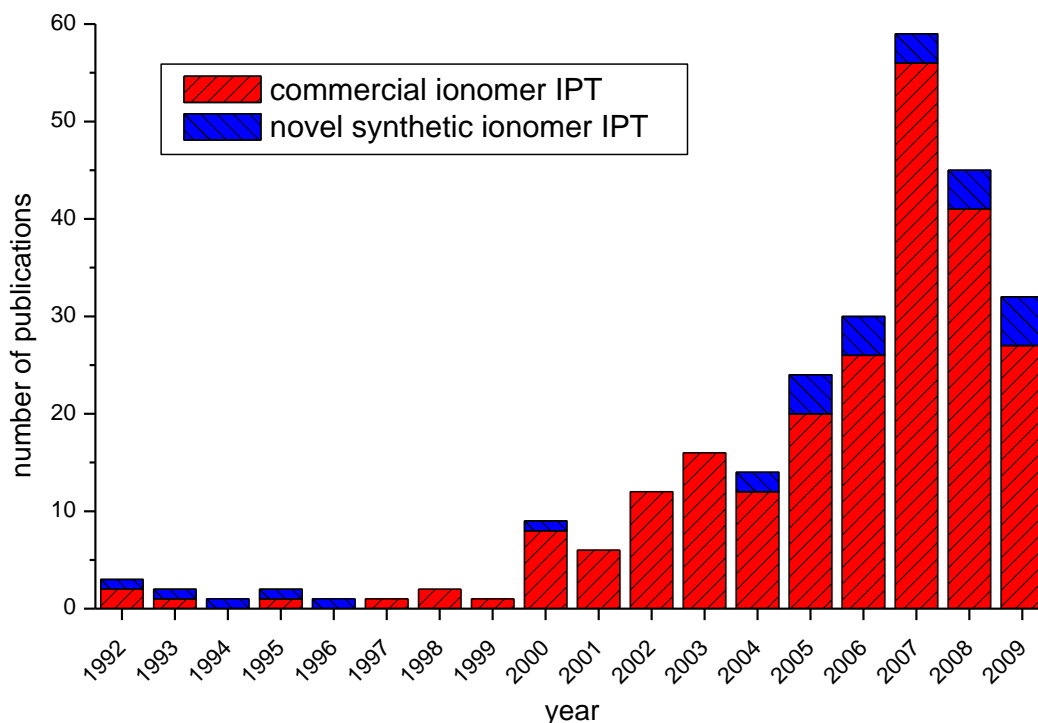


Figure 1.3: IPT publications (peer reviewed) employing commercial or synthetic ionomers

Perfluorinated membranes such as Nafion[®] established the basis of IPT technology and continue to drive research and development toward applications, especially in medical devices

and artificial muscle research.[1, 82, 83] The continued importance of this commercial ionomer is evident in multiple recent advances concerning IPTs and their components. The most common IPT electrode geometry results from an electroless deposition method where the ionomer membrane is repeatedly impregnated with a metal salt followed by addition of a reducing agent to deposit a dendritic high surface area metallic layer near the surface.[84, 85] Recent advances in this impregnation-reduction process (IRP) revealed that reversing the technique distributed controlled electrode gradients across the thickness of the membrane instead of high concentrations at the outside surface.[86] This new approach allowed for greater actuation lifetimes for submersed IPTs under large applied potential (5 V). Jeon *et al.* also extended the electroless plating technique with lithography and electroplating to create patterned metal electrodes that allowed increased actuation with multiple degrees of freedom to mimic the swimming motions of fish.[87]

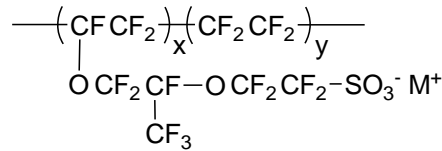


Figure 1.4: The chemical structure of Nafion[®] in the sulfonate salt form

Asaka, Onishi, *et al.* earlier demonstrated a correlation between high electrode interfacial area with the ionomeric membrane and increased strain with Flemion[®]-IPTs and a gold electroless plating technique.[84] Further investigation by Akle, Leo, and coworkers revealed that increased surface area-to-volume ratio of conducting powders in IPT electrodes increased strain in a direct correlation with increased capacitance.[20, 54] Those studies led to the development of a method termed the direct application process (DAP) for tuning electrode composition for optimal performance with RuO₂ or single walled carbon nanotube (SWCNT) conducting powders, regardless of the composition of the central ionomer membrane.[60] In this case, dispersions of the conducting particles were created with solutions of the target ionomer and painted or sprayed onto decals or the central membrane itself. Water-based IPTs created with the DAP method require a subsequent IRP step. Surface resistance of ionic liquid-based IPTs is reduced through melt-press application of several layers of gold leaf. Similar to the previously established capacitive relationship to peak strain, a percolation threshold existed in through-

thickness electrical conductivity of the electrodes when related to strain rate. Figure 1.5 depicts the cantilever bending response of an ionic liquid–swollen Nafion[®]–IPT, constructed with the DAP method, with varied magnitude of the input voltage. Akle *et al.* also recently extended the DAP method to create hybrid electrodes from combinations of SWCNT and RuO₂. [55, 88] Tuning of the electrode composition with these two components led to strain rates (2.7 % / s) and peak strains (10.6 %) for IPTs greater than those with single component electrodes and operational in air. Other researchers have also pursued water-based immersion-type Nafion[®]-IPMCs with CNTs. Baughman *et al.* demonstrated that sheets grown exclusively from pristine carbon nanotubes could act as high energy density electromechanical actuators. [89] This discovery initiated a new and quickly expanding division of electroactive materials, carbon nanotube actuators, which due to their electrostatic transduction mechanism were recently combined with IPMC technology to create hybrid ionic electromechanical transducers. [90-93] Homogeneous dispersion of the CNTs throughout the ionomer film created composite actuators with performance heavily dependent on the loading of CNT. Better performance with low loadings led to the conclusion that these composites benefitted from increased mechanical and electrical properties of the CNTs but that their individual electromechanical actuation was limited by the surrounding polymer matrix. [94]

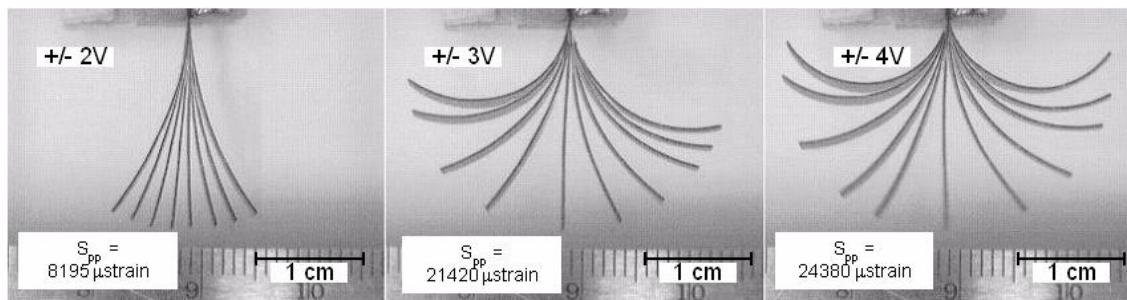


Figure 1.5: Deflected shapes for an ionic liquid–swollen Nafion[®]–IPT as a function of voltage amplitude for a square wave potential input. [20] "Reprinted from *Sens. Actuators, A: Phys.*, 126, Akle, B. J., Bennett, M. D., and Leo, D. J., High strain ionomeric–ionic liquid electroactive actuators, p.173–181, Copyright (2006), with permission from Elsevier."

Notably, these electrode advances were developed with Nafion[®] as a model IPT membrane but are directly applicable to other ionomers as well. A consistent observation for application of the impregnation-reduction method to other ionomers is that efficiency, depth, and homogeneity of metal deposition increase with higher ion exchange capacity (IEC) of the membrane. This is

likely due to the balance between well-defined microphase separation and an increased population of ionic aggregates that exchange cations with the metal salt. Use of carbon nanotube fillers throughout or at the membrane surface was also found to hinder metal electrode deposition. Specific modifications to the DAP method for use with sulfonated polysulfones (sBPS) will be discussed in Chapter 3 of this dissertation.

Performance augmentation and fundamental understanding of the diluent's role in IPT operation were also recently highlighted. Farinholt and Leo performed a parametric study to examine the effects of counterion size and diluent viscosity and dielectric constant on actuation and sensing performance of Nafion[®]-IPTs.[95] The common metric for performance was variation in the IPT electrical impedance where higher values led to decreased performance. Bennett, Leo, and coworkers also observed that cation size and ionic liquid interactions with Nafion[®] influenced morphological stability, charge transport, ionic conductivity, and actuation speed.[61] Nafion[®]-IPT construction with a hydrophobic ionic liquid led to a swelling of the PTFE matrix and disruption of the cluster network. The lack of morphological stability for this combination of membrane and diluent decreased ionic conductivity of the IPT and resulted in slower transducers when compared to those constructed with a hydrophilic ionic liquid. Flemion[®]-IPTs were also investigated with glycerol and various ionic liquids as environmentally stable diluents.[58, 96] Overall, employment of encapsulation methods or non-volatile diluents in IPT design enabled long-term actuation in air with minimal loss of performance and a significant decrease in back relaxation when compared to water-based Nafion[®]-IPTs.[57, 97, 98] Akle, Leo, *et al.* also demonstrated within an electrode study that increased uptake and decreased viscosity of the IPT diluent led to higher response speeds in Nafion[®]-IPTs, likely due to increased ion mobility.[60] In water-based Flemion[®]-IPTs, similar trends were observed where actuation speed and charge-specific displacement depended on cation size and the related amount of freezable water in the IPT.[81] These actuation tests were performed under a constantly varied peak-to-peak voltage (triangle wave) to impose a constant current. Neither Flemion[®] nor Nafion[®]-IPTs demonstrated back relaxation under these conditions when constructed with identical electrode materials. Earlier studies demonstrated that Flemion[®] differed from Nafion[®] through the absence of back relaxation during actuation under application of a step in dc potential.[23] The different actuation character was attributed to the effect of different pK_a values of the anions bound to the otherwise similar polymer backbones.[99] The pK_a of Nafion[®]'s

sulfonate salt, similar to trifluoromethane-sulfonic acid, is approximately -6 while the pK_a of the carboxylate salt, analogous to trifluoromethane-acetic acid, in Flemion[®] is nearly 0.5. During dc step actuation, a large excess of cations enter the ionic aggregates in the cathode boundary layer. Stronger acidity of the bound anion was hypothesized to impose a larger dipole and increase the driving force for rearrangement of the excess charges. This rearrangement led to a decrease in electro-osmotic pressure and expulsion of excess diluent at the cathode to manifest back relaxation. Triangle wave excitation of the IPT likely avoids back relaxation, regardless of the ionomer, through a gradient accumulation of charge similar to a series of infinitely small steps.

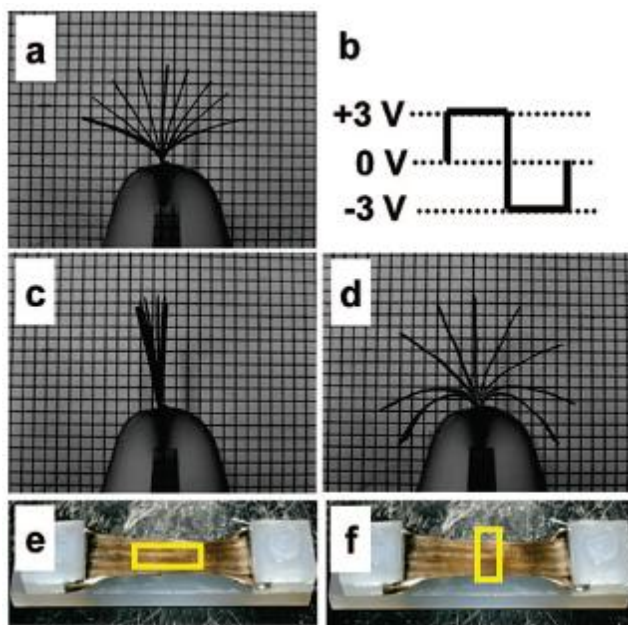


Figure 1.6: Actuation of Nafion[®]-IPTs (a) unoriented, (b) 3 V square-wave at 0.1 Hz, oriented and cut (c) parallel to draw, (d) perpendicular to draw. Membrane orientation fixture with indicator of IPTs cut (e) parallel to draw and (f) perpendicular to draw.[100] “Reprinted with permission from Park, J. K. and Moore, R. B., 2009, Influence of Ordered Morphology on the Anisotropic Actuation in Uniaxially Oriented Electroactive Polymer Systems, *ACS Appl. Mater. Interfaces*, 1, 697-702. Copyright 2009 American Chemical Society.”

Customized Nafion[®]-IPT geometry and response was recently made possible through development of solution and melt processing methods to modify Nafion[®] membranes for increased IPT actuation in bending.[101] Recent studies from Moore *et al.* demonstrated methods for orientation of the membrane, which resulted in varied morphological structures and distinctly anisotropic actuation of water-based IPTs in air.[100, 102] As shown in Figure 1.6,

uniaxial orientation of the IPT membrane prior to the cutting step produced distinct results for actuation. Small-angle X-ray scattering (SAXS) results indicated preferential orientation of the microphase-separated morphology concurrent with the membrane orientation. Induced directionality of the morphological structure was concluded to hinder (parallel to draw) or enhance (perpendicular to draw) actuation, especially for high input voltages. Samples cut at a 45° angle to draw were even found to manifest twisting motions during actuation. Nafion®–IPT performance improvements are also possible through a distinctly different route. Combinations of field-activated or other ionic EAPs with IPTs are termed hybrid electromechanical transducers. For example, the formation of conducting polypyrrole on the surface of Nafion® before IPT construction led to increased blocked force, free displacement, and actuation bandwidth.[103] A similar study bonded a ferroelectric EAP membrane, poly(vinylidene fluoride) (PVDF), to a Nafion®–IPMC, which resulted in simultaneous actuation and sensing capabilities.[104] The research trends and performance enhancements developed through optimization of IPT components with Nafion® provide a benchmark that influences the design, synthesis, development, and final application of novel ionomers in IPTs.

1.2.3 Step-growth ionomers

Ionic transport, elastic modulus, processability, and chemical and thermal stability are critical to both IPT and proton–exchange membrane fuel cell (PEMFC) performance. Perfluorinated ionomers including Nafion® set the benchmark in PEMFCs before their consideration as IPT membranes. Examples of novel step–growth ionomers that were synthesized for PEMFC applications include sulfonated and carboxylated versions of poly(arylene ether sulfone)s, polyetherketones, polyimides, polybenzimidazoles, and polyphosphazenes.[105, 106] Design of charge transport membranes has focused on modification of stable hydrophobic polymers with controlled levels of polar functionality. This contrast in chemical composition, similar to that found in Nafion®, facilitates microphase separation that is advantageous for charge transport. In a similar fashion to the development of IPTs, PEMFCs are multi–component composites that depend on the optimization of electrode–ionomer interfaces, mechanical properties, diluent characteristics, and charge transport for performance. Due to these similarities, several synthetic PEM step–growth ionomers are under investigation as possible IPT membranes.[107, 108]

Currently, only a few studies exist concerning novel step-growth ionomers for IPTs and most efforts have concentrated on sulfonated polysulfones.

Poly(arylene ether sulfone)s (PAES) are engineering thermoplastics that are thermally, mechanically, hydrolytically, and oxidatively stable.[109] These properties, as well as relatively high glass transition temperatures compared to Nafion[®], originate from the aromatic chemical structure and corresponding rigidity of the polymer backbone. The vast majority of polysulfones are amorphous due to the kinked nature of the sulfone linkage in the backbone.[109] Sulfonated polysulfones are tunable ionomers that offer high ionic conductivity (~80 mS/cm) and the ability to form tough, ductile films from solution ($E_{hydr} \approx 640$ MPa). These ionomers are typically subject to solution processing in aprotic organic solvents but lack adequate melt processability in the neat state due to the strength of their physical crosslinks. Present synthetic efforts for fuel cell membranes have catalyzed novel compositions for IPTs.[110, 111] The polysulfone ionomers that have received attention as potential electromechanical transducers included both sulfonated poly(arylene ether sulfone) (SPAES or BPSH) and sulfonated poly(arylene thioether sulfone) (SPATS). The chemical structures of these random copolymers are provided in Figure 1.7. IEC, hydrated elastic modulus, and ionic conductivity for these ionomers are provided for comparison with relevant commercial and chain growth ionomers employed for IPTs in Table 1.1. These sulfonated poly(arylene ether)s were synthesized through a nucleophilic aromatic substitution reaction in an aprotic solvent, in the presence of weak base, under dry conditions, at approximately 165 °C to attain high molecular weight.[112] As observed in the structure of both macromolecules, the flexible linkages are the ethers and thiols in SPAES and SPATS respectively. SPAES is considered more rigid since there is one less linkage in between the aromatic rings of the backbone. Biphenol was chosen as the starting monomer for SPAES instead of the more common bisphenol-A to increase chain rigidity, resulting in a higher glass transition temperature, higher elastic modulus, increased blocked force, and possibly increased energy density of the IPT dependent on preservation of free deflection. McGrath, Harrison, *et al.* provided details on the synthesis and characterization of SPAES with different bisphenol monomers.[113] Although SPATS is less rigid than SPAES, one intended benefit of the thiol in the backbone was increased adhesion to gold at the polymer-electrode interface[114] to extend IPT lifetime and performance limits.

Akle, Leo, and coworkers performed electromechanical characterization of water-based linear SPAES and SPATS–IPTs in comparison with Nafion[®]–IPTs that were electroded with the impregnation–reduction process (IRP).[115, 116] The ionomer series was designed with a higher ion exchange capacity (SPAES: 1.3 – 1.7, SPATS: 1.17 – 1.51), higher water uptake, fully amorphous phase, higher glass transition temperature and higher modulus compared to Nafion[®]. Transducers prepared from each ionomer were optimized for reducing agent concentration where electrodes were applied with the IRP. All transducers were characterized for blocked force production, free deflection, capacitance, and sensitivity. Except for the lowest IEC sample of SPATS, the SPAES and SPATS–IPTs outperformed the Nafion[®]–IPT in blocked force and free displacement actuation at frequencies up to 10 Hz (IRP). Since all of the ionomers were in the sulfonate salt form and saturated with water, characteristic back relaxation occurred for all step responses (1 V). However, the SPAES series experienced less back relaxation (% of peak strain) and demonstrated greater steady-state strain than the SPATS series which was comparable to Nafion[®]. The larger pK_a of the sulfonate salt (weaker acid) on SPAES and SPATS decreased the magnitude and speed of back relaxation in comparison to Nafion[®]. Similar to Nemat-Nasser’s studies of back relaxation in water–swollen sulfonate ionomers, such as Nafion[®]–IPTs,[117] these SPAES and SPATS–IPTs show back relaxation under dc step potential inputs[115] and would not outperform similar transducers constructed with Flemion[®] in the realm of precision movement and motion control. Regardless, SPAES and SPATS outperformed Nafion[®] in every IPT response to ac/dc potential inputs except for low frequency sensing, where the values were comparable.

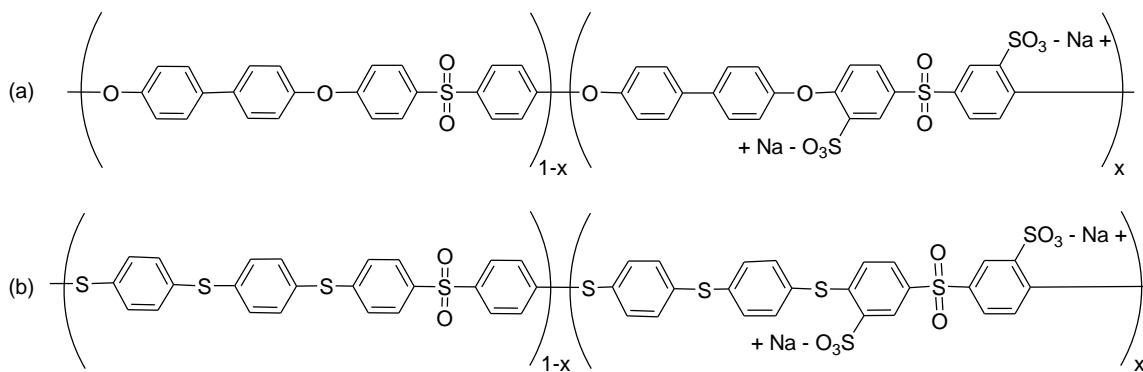


Figure 1.7: Chemical structures for (a) SPAES (b) SPATS

The study of SPAES and SPATS–IPTs was further extended to compare water-based transducers from the series constructed with both the IRP and DAP methods.[108] A sample of the frequency response functions for the novel IPT study is shown in Figure 1.8. Although the two electrode methods employ the same ionomers, there is significantly less spread in the data for the DAP method. This occurrence likely originated from the composition of the electrodes rather than the ionomer selection, since the DAP–IPTs used a Nafion[®] electrode matrix interfaced with the polysulfone central membranes. For the IRP samples, the ionomer is only present in the electrode at the interface with the central membrane. The effect of the electrode composition within the DAP technique is most noticeable for the capacitance results. Overall, IPTs constructed with the DAP method displayed greater actuation at low frequency while those based on the IRP method dominated at high frequency. Electrodes based on the DAP method

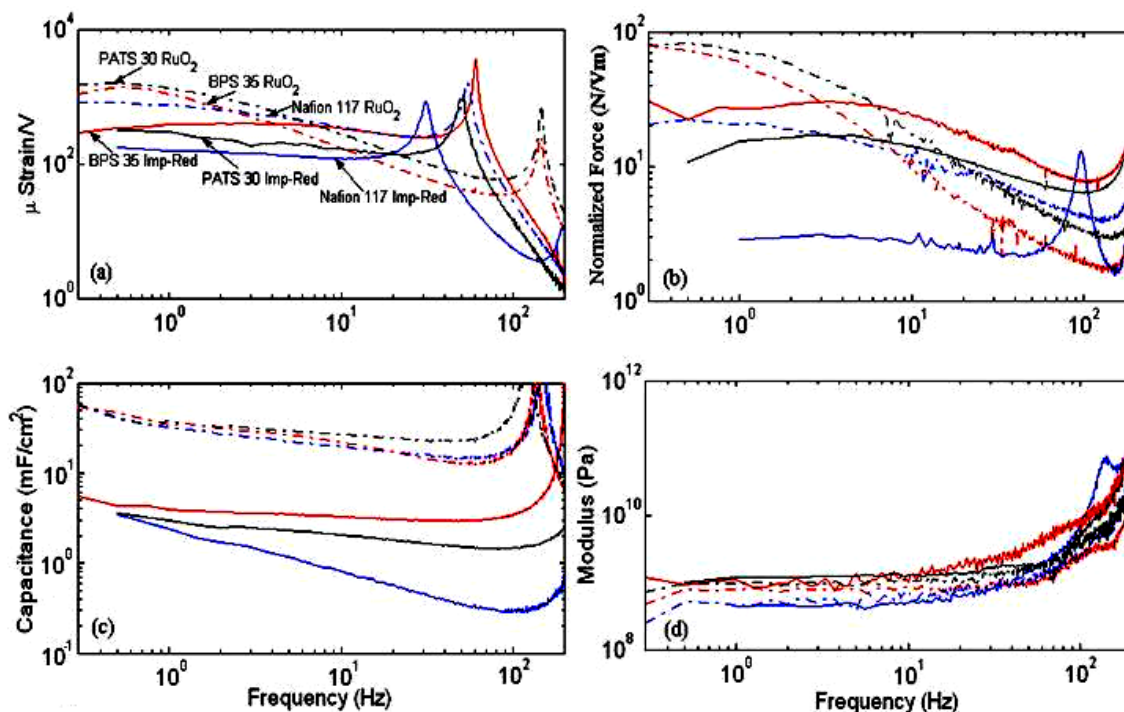


Figure 1.8: (a) Microstrain per volt (b) normalized force (c) capacitance and (d) modulus versus frequency for BPS 35 (red), PATS 30 (black), and Nafion[®] 117 (blue) to construct IPTs using impregnation–reduction and RuO₂–based direct assembly electrodes[108] "Reprinted from J. Electrochem. Soc., 154, Wiles, K. B., Akle, B. J., Hickner, M. A., Bennett, M. D., Leo, D. J., McGrath, J. E., Directly Copolymerized Poly(arylene sulfide sulfone) and Poly(arylene ether sulfone) Disulfonated Copolymers for Use in Ionic Polymer Transducers, p. P77-P85. Copyright (2007), with permission from the Electrochemical Society."

also provided larger capacitance (up to 50x) than the IRP technique with platinum for all ionomer compositions investigated.[108] Figure 1.8 also shows that regardless of the electroding technique employed, SPAES and SPATS–IPTs outperformed Nafion[®]–IPTs in actuation across the majority of the frequency range investigated for microstrain per volt, modulus, and force output. Specifically the larger force output of SPAES and SPATS than Nafion[®] was expected based on much higher values of hydrated modulus for these ionomers. Below 10 Hz, SPAES and SPATS–IPTs each displayed increased free deflection and blocked force resulting in a higher peak energy density than for the Nafion[®]–IPTs. Between the two novel ionomers, SPAES performed best within the IRP sample set due to its higher ionic conductivity and capacitance. This trend combined with the higher capacitance of all IPTs constructed with the DAP method further accentuated the importance of charge storage ability for maximum electromechanical performance across commercial and novel ionomers. For further extension of step-growth ionomer–IPTs, the studies included in this dissertation introduce controlled levels of branching into SPAES to observe the effect of controlled topology on morphological development and IPT performance.[118-121] The transition is also made from water-based to ionic liquid-based transducers. Those experiments and results compose Chapters 3 – 5.

1.2.4 Chain-growth ionomers

During the initial development of IPTs, perfluorosulfonated ionomers such as Nafion[®] and sulfonated polystyrene (sPS) crosslinked with divinylbenzene emerged as leading candidates. Sulfonated polystyrene did not experience the extent of development associated with Nafion[®]–IPTs. However, the availability of commercial variations on sPS, Selemion[®] (Asahi Glass) and Neosepta[®] (ASTOM Co.), have encouraged more development of IPT technology with chain growth ionomers.[122-127] This subset of IPTs seemingly arose from the efforts of Kuhn and Katchalsky concerning chemomechanical transducers from polymeric acid networks in 1949.[128-130] Fifteen years passed before these transducers were discovered to also have electrochemomechanical properties.[131] This discovery combined with similar research on reconstituted collagen fibrils led to the development of soft ionic polymers and hydrogels for artificial muscles.[132-134] Typically these polymers were lightly crosslinked polyelectrolytes that operated while either submerged or encapsulated in an electrolyte environment. The level of crosslinking was varied to achieve balance between increased rigidity and decreased swelling.

Table 1.1: Physical properties of commercial and synthetic IPT membranes (H₂O hydrated)

ionomer [ref]	bound/free	ion exchange		hydrated	ionic
	ion form	capacity (meq/g)	uptake (wt %)	modulus (MPa)	conductivity (mS/cm)
Nafion [®] -117 [108]	SO ₃ ⁻ / Na ⁺	0.91	22	120	110
Flemion [®] [41]	CO ₂ ⁻ / Na ⁺	1.45	24	169	8.5[81]
Aciplex [®] A-172 [135]	NR ₄ ⁺ / Cl ⁻	0.185	n/a	n/a	n/a
SPAES [108]	SO ₃ ⁻ / Na ⁺	1.53	40	640	80
SPATS [108]	SO ₃ ⁻ / Na ⁺	1.17	20	1040	60
PVA-co-AA [63]	CO ₂ ⁻ / H ⁺	n/a	31[136]	n/a	2[136]
SSEBS [137, 138]	SO ₃ ⁻ / Li ⁺	1.59[141]	164[141]	n/a	382[141]
SPS-co-AA + PVA [139]	SO ₃ ⁻ -co- CO ₂ ⁻ / Na ⁺	1.21	210	289	7.53x10 ⁻¹⁰
PVA + PAMPS [140]	SO ₃ ⁻ / Na ⁺	1.05	110	n/a	8.75
PE-co-VA-SSA [142]	SO ₃ ⁻ / H ⁺	0.36 (min) 1.18 (max)	36 82	n/a	n/a
PE-co-VA-g-SPEO [143, 144]	SO ₃ ⁻ / K ⁺	1.32 (min) 1.93 (max)	n/a	n/a	0.304 1.65
FA-co-AA [145]	CO ₂ ⁻ / Li ⁺	1.47	50	n/a	n/a
[146]	CO ₂ ⁻ / Na ⁺	1.47	15		
FMA-co-AA [147]	CO ₂ ⁻ / H ⁺	1.63	15	0.63	n/a
FMA-co-SA [148]	SO ₃ ⁻ / Li ⁺	0.905	94	0.25	n/a
FMA-co-SA-co-HEMA [149]	SO ₃ ⁻ / H ⁺	1.34	41	0.71	n/a
FMA-co-AMA [150]	NR ₄ ⁺ / Cl ⁻	1.23	7	1.41	n/a
PS-alt-MI + PVDF [151]	SO ₃ ⁻ / Li ⁺	1.41	14	n/a	56
[152]		1.56 1.64	25 40		79 88
PVDF-g-SNEC [153]	SO ₃ ⁻ / H ⁺	n/a	25	n/a	138
(PVDF-co-HFP)-g-SPS [154]	SO ₃ ⁻ / Na ⁺	2.89	186	n/a	75.6
(PE-co-TFE)-g-SPS [154]	SO ₃ ⁻ / Na ⁺	2.83	194	n/a	81.2
(PTFE-co-HFP)-g-SPS [154]	SO ₃ ⁻ / Na ⁺	1.65	88	n/a	13.6
FEP-g-SPS [155]	SO ₃ ⁻ / Li ⁺	1.20 1.70 2.3	sat. sat. sat.	140 104 55.3	n/a

These two properties typically related to the transducer's ability to perform as force and bending actuators respectively.[156]

In 1992, the first formal study summarizing the concept and dynamics of using ionic polymeric gels such as polyacrylamide and poly(vinyl alcohol-*co*-acrylic acid) (PVA-*co*-AA) as IPTs appeared in the literature.[63] The most important aspect of this study in terms of IPT operation was the concept of encapsulating the ionomeric gel and electrolyte within an electroded compliant container.[157] Containment of the IPT membrane and diluent facilitated the creation and control of geometries where actuation force and bending were applied without submersion in the presence of large boundary electrodes.[158, 159] Furthermore, encapsulation led to the first observation in IPTs of mechanoelectric sensing with ionomeric gels[160-162] and their increased development in IPT technology.[163] Recent studies employed the commercially available hydrogel sulfonated poly(styrene-*b*-ethylene-*co*-butylene-*b*-styrene) (SSEBS) crosslinked with vinyl silanes to design low-cost transducers in comparison to Nafion[®]-IPTs.[137] Actuation results were based on electroless deposition of the electrodes and submersion in aqueous solution. This cost-effective substitute operated in water to achieve a maximum tip displacement of ~1 mm in response to an applied dc potential of 2 V. Employment of para-substituted sulfonated polystyrene blocks provided a sufficiently weak acid to significantly reduce back relaxation in comparison to Nafion[®]-IPTs. Subsequent studies demonstrated that low loadings of multi-walled carbon nanotubes (MWCNT) or carbon nanofibers (CNF) further increased displacement and response speed in cantilever bending, especially for ac input voltages at higher frequency.[138, 164]

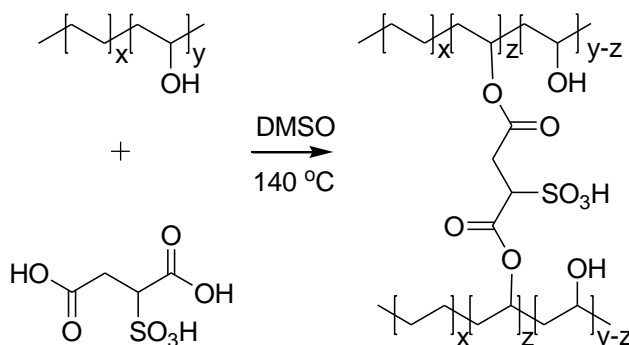


Figure 1.9: Synthetic scheme for crosslinking EVOH with sulfosuccinic acid

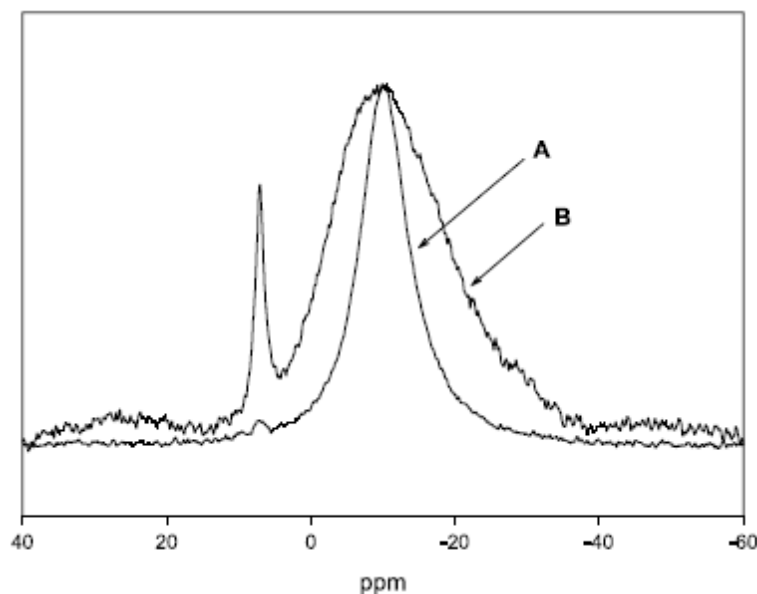


Figure 1.10: Solid-state ^{23}Na NMR spectra of (a) as received Nafion[®] 117 and (b) 15 wt % sulfosuccinic acid modified PE-*co*-VA.[142] "Reprinted from *Polymer*, 46, Phillips, A. K. and Moore, R. B., Ionic actuators based on novel sulfonated ethylene vinyl alcohol copolymer membranes, p.7788–7802, Copyright (2005), with permission from Elsevier."

Phillips and Moore synthesized poly(ethylene-*co*-vinyl alcohol) crosslinked with sulfosuccinic acid (PE-*co*-VA-SSA), as depicted in Figure 1.9. The ionomeric membrane's morphology was examined on the nanometer and angstrom length scales with small-angle X-ray scattering (SAXS) and ^{23}Na nuclear magnetic resonance (NMR) spectroscopy respectively. As shown in Figure 1.10, ^{23}Na -NMR revealed isolated sodium sulfonate ion pairs (5 ppm) and a wide distribution of ion pairs that aggregated into multiplets (-10 ppm) for the 15 wt % SSA modified PE-*co*-VA. SAXS results only detected a very broad ionomer peak for 63 wt% SSA modified PE-*co*-VA. The corresponding results for Nafion[®] displayed a narrower distribution of multiplets in ^{23}Na NMR and a more distinct ionomer peak in SAXS. Characterization of PE-*co*-VA-SSA-IPT performance revealed decreased actuation speed and comparable peak strain and blocked force compared to Nafion[®]. Water-based PE-*co*-VA-SSA-IPTs performed similarly to Nafion[®]-IPTs but without back relaxation at identical conditions. The absence of back relaxation again matches the notable difference in acidity between Nafion[®] and PE-*co*-VA-SSA due to the location of the sulfonic acid functionality. These results coupled with NMR measurements of diffusion coefficients (i.e., Nafion[®] > PE-*co*-VA-SSA) suggested that a more diffuse morphological structure directly related to decreased actuation performance, regardless of the specific ionomer.[142] The diffuse morphology likely results from the limited mobility of the

sulfonate salts that are bound on a short chain between two cross-link (i.e., branch) points. However, without modification to the location of the SSA functionality or the molecule's topology, increased levels of sulfonation above 15 wt % only leads to mechanically unstable hydrogels unsuitable for IPT fabrication and actuation.

Separately, poly(ethylene-*co*-vinyl alcohol) with controlled molecular weight poly(ethylene oxide) grafts placed at the vinyl alcohol sites were designed as IPT membranes. The grafted PEO chains were then sulfonated through a ring opening of 1–3 propane sultone in the presence of potassium *tert*-butoxide to create ionomers (PE-*co*-VA-*g*-SPEO) of varied ion exchange content for IPT construction.[143] This study provided polymer architecture analogous to the short-chain branches on Nafion[®] and was one of the few studies to investigate the effect of ionomer topology on actuation performance. Location of the sulfonate salt at the end of the PEO graft caused the IEC to significantly decrease with longer graft lengths. Increased graft lengths led to morphological changes detected with AFM and XRD, decreased ionic conductivity, and lower actuation performance overall.[144] However, a local maximum was detected in the conductivity and bending stress with increased graft length that possibly indicated an optimal branch length for microphase separation and charge transport. Du *et al.* performed a different approach to grafting for increased IPT performance where poly(sodium 4-styrenesulfonate-*co*-acrylic acid) (SPS-*co*-AA) was employed to surface modify MWCNTs.[139] The polymer-grafted MWCNTs were then dispersed in a mixture of PVA and SPS-*co*-AA to cast CNT composite membranes for IPTs.

Composition matching between the matrix and the filler enhanced the physical crosslinking of the system to increase hydrated modulus and augment electrical conductivity. However, increased stiffness due to CNT loading (10-20 wt %) decreased the ac actuation response of the transducers by 40 % in comparison to the IPT with 0 % CNT. Back relaxation was not observed for these IPTs that combined sulfonate and carboxylate salts in the ionomer charge transport pathway. Dai *et al.* carried out a similar study and referred to the physically cross-linked mixture of ionomers as a semi-interpenetrating network comparable to those formed with mixtures of covalently cross-linked networks. Their work used mixtures of PVA and poly(2-acrylamido-2-methyl-1-propanesulfonic acid) (PAMPS) with carboxylated MWCNTs (0.1-3 wt %) to form CNT composites for IPTs. For this lower range of CNT loading, a percolation threshold was observed at 1 wt % as a maximum in ionic conductivity that further corresponded to maximum

values of bending angle and tip force. Both studies created water-based CNT–IPTs after treatment with the IRP method that avoided back relaxation, produced comparable actuation to Nafion[®], and allowed for tuning of IPT metrics based on CNT loading. Instead of the use of fillers for property enhancement, Lu *et al.* created hybrid transducers from poly(styrene-*alt*-maleimide) (PS-*alt*-MI) cross-linked with a sulfonated linker in the presence of PVDF (Figure 1.11).[151, 152] The inclusion of PVDF in the system was meant to provide a contrast in polarity with the charge functionalities on PS-*alt*-MI while increasing overall thermal, mechanical, and chemical stability of the composite. Tip displacements were much greater than Nafion[®] and did not demonstrate characteristic back relaxation. However, high water uptakes led to blocked force performance ~50 % less than comparable Nafion[®]–IPTs.

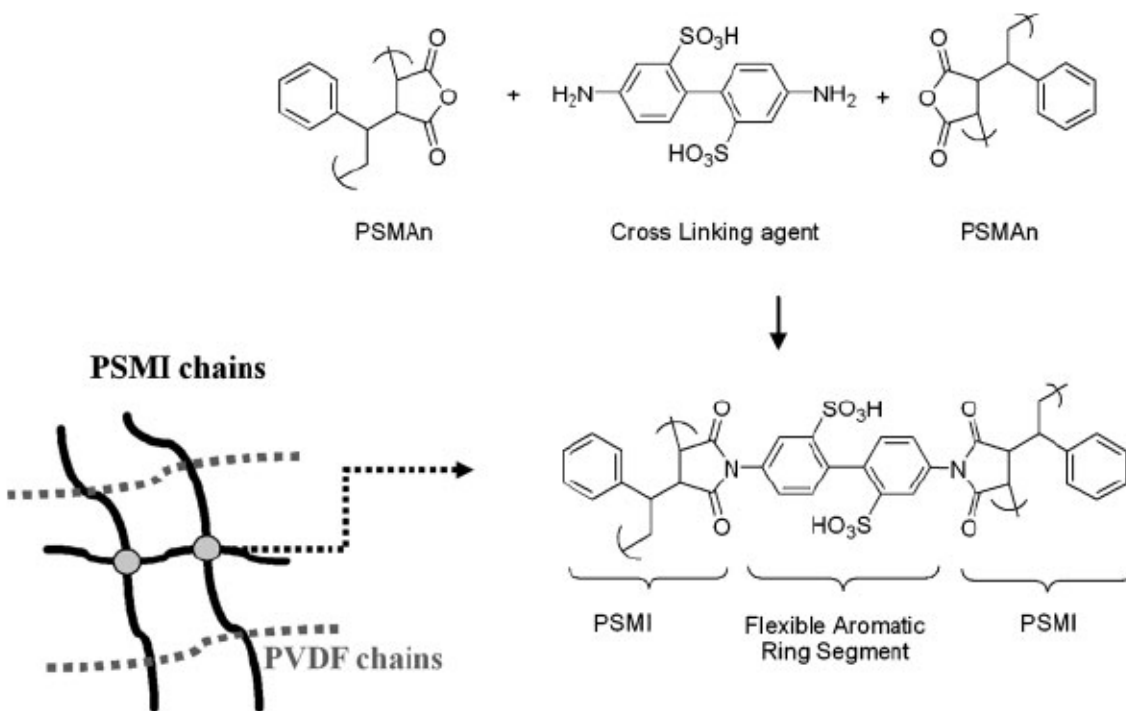


Figure 1.11: Schematic representation and chemical structures of the ionic networking membrane composed of cross-linked PS-*alt*-MI and PVDF [152] Lu, J., Kim, S.-G., Lee, S., Oh, I.-K.: A Biomimetic Actuator Based on an Ionic Networking Membrane of Poly(styrene-*alt*-maleimide)-Incorporated Poly(vinylidene fluoride). *Adv. Funct. Mater.* 2008. 18. p.1290–1298. Copyright Wiley-VCH Verlag GmbH & Co. KGaA. Reproduced with permission.

Partially fluorinated IPT membranes were also developed with chain-growth polymerization as analogues to the chemical composition of Nafion[®]. The radical copolymerization of

fluoroalkyl acrylate (DuPont Zonyl TA-N, FA) and acrylic acid (AA) resulted in novel IPT membranes.[145, 146] Variation of the AA content demonstrated the need to balance swelling behavior with IEC to achieve maximum actuation. Likely due to the choice of a carboxylate salt, copolymers with 35 – 50 mol % AA displayed significant actuation without back relaxation in force and bending respectively. AA levels above 50 mol % led to soft gels with water uptakes above 500 wt % and little or no actuation capabilities. Similar synthetic IPT studies included the copolymerization of fluoroalkyl methacrylate (DuPont Zonyl, FMA) with monomers such as acrylic acid (AA), 2-acrylamido-2-methyl-1-propanesulfonic acid (SA) (crosslinking of SA with varied percentages of 2-hydroxyethyl methacrylate (HEMA)), and 2-(dimethylamino) ethyl methacrylate (AMA). The objective was to provide melt processability (typically unavailable with Nafion[®]) through variation in polymer composition for control of thickness and shape of the IPT membrane. The FMA-*co*-AA and FMA-*co*-SA were both weak acid-based ionomers swollen with water that displayed significant actuation in bending without back-relaxation. IPT performance again displayed a maximum based on ion content. At ion contents greater than those associated with the observed maximum displacement, the level of water uptake caused cracks in the electrodes likely associated with decreased actuation. Blocked force was not measured but decreased modulus with increased ion content implied that this parameter would also have a maximum.[147, 148] In a subsequent study, incorporation of up to 6 wt % HEMA effectively provided sites to crosslink the copolymers (FMA-*co*-SA-*co*-HEMA) at constant ion content, thus swelling in water decreased. Increased crosslinking monotonically decreased current and displacement responses, however, covalent network formation increased the available actuation force. The force maximum, approximately 300 % of the value for FMA-*co*-SA, resulted from incorporation of only 1 wt % HEMA. Furthermore, the current and strain rate only decreased 10 % in comparison to a decrease of nearly 80 % for the highest level of crosslinking.[149] In this case, polymer topology through covalent crosslinking reduced swelling in a high IEC polymer to achieve a significant increase in the energy density of this class of novel IPTs. The copolymerization of FMA and AMA introduced a seldom investigated parameter into IPT construction, i.e. anion transport (FMA-*co*-AMA) based on a fixed quaternary ammonium counterion. Similar to the acid-form ionomer studies, a maximum in bending and force actuation based on ion content was observed without back relaxation.[150] Anion transport in IPTs reverses the response direction to the applied potential and was

originally reported using a version of the commercial perfluorinated ionomer Aciplex A-172[®]. [135]

IPT performance was further investigated through construction of hybrid transducers with ionic groups grafted to ferroelectric polymers. Operation of the hybrid-IPTs was performed with voltages (~2 V DC) much too low to induce conformational changes and electromechanical transduction based on the ferroelectric polymer mechanism. Chen *et al.* received a patent for a hydrophobic fluorinated matrix combined with a polar ionic phase through radiation grafting of N-ethylene carbazole to preformed poly(vinylidene fluoride) with subsequent sulfonation (PVDF-*g*-SNEC). Compared to a similarly constructed Nafion[®]-IPT, the platinum-electroded hybrid-IPT achieved 25 % greater free displacement and 200 % larger blocked force with a 70 % increase in ionic conductivity and 25 % greater swelling ratio. IEC and modulus were not reported. [153] Jho, Han, and coworkers also employed this approach through radiation grafting of polystyrene sulfonic acid to the ferroelectric polymers poly(vinylidene fluoride-*co*-hexafluoropropylene) ((PVDF-*co*-HFP)-*g*-SPS), poly(ethylene-*co*-tetrafluoroethylene) ((PE-*co*-TFE)-*g*-SPS), and poly(tetrafluoroethylene-*co*-hexafluoropropylene) ((PTFE-*co*-HFP)-*g*-SPS). Hybrid-IPTs were constructed from these modified EAPs and were compared to performance of a Nafion[®]-IPT. The water uptake and final ionic conductivity of the hybrid-IPTs was much greater than for the Nafion[®]-IPT. The bending actuation results are depicted in Figure 1.12. Total free deflection scaled with increased IEC, while ionic conductivity and strain rate did not follow the IEC and were proportional to water uptake. All of the hybrid transducers displayed at least ten times greater tip displacement without back relaxation however, the blocked force of the Nafion[®]-IPT was greater. In contrast to typical IPTs, blocked force of the hybrid-IPTs increased with increasing water uptake. [154, 165] Although hydrated moduli were not reported, dry moduli of the ferroelectric polymers is approximately equal to the elastic modulus of dry Nafion[®]. In this case, modification of the IPT chemical composition resulted in a five-fold increase in energy density based on charge transport without a dramatic loss of mechanical properties. However, Rao *et al.* reported on water-swollen IPTs composed of fluorinated ethylene-propylene copolymers radiation grafted with styrene and post-sulfonated (FEP-*g*-SPS). [155] In this case hydrated moduli were reported and decreased with higher levels of grafting (i.e., higher IEC) from 480 MPa (0 % grafted) to 55 MPa (46 % grafted). A more typical

tradeoff was observed where increased IEC resulted in higher water uptake, lower modulus, and greater actuation speed and strain in free displacement.

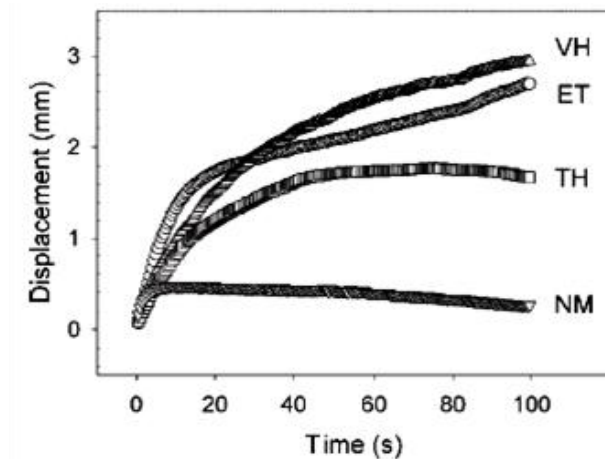


Figure 1.12: Displacement of PVDF-co-HFP (VH), PE-co-TFE (ET), PTFE-co-HFP (TH), and Nafion® (NM) IPMCs recorded for 100 s with an applied DC voltage of 2 V [154] Han, M. J., Park, J. H., Lee, J. Y., Jho, J. Y.: Ionic Polymer-Metal Composite Actuators Employing Radiation-Grafted Fluoropolymers as Ion-Exchange Membranes. *Macromol. Rapid Commun.* 2006. 27. p.219-222. Copyright Wiley-VCH Verlag GmbH & Co. KGaA. Reproduced with permission.

1.2.5 Summary

As highlighted in this chapter, a foundation of Nafion®-based IPT technology is well established despite the ionomer's complex morphology, cost, and processing challenges. Growth of potential and commercial applications of Nafion®-IPTs motivated further exploration into the benefits of tailoring membrane properties for performance. An ionomeric membrane optimized for IPT application must exhibit mechanical integrity, a stable chemical composition, and consistent physical properties over long cycling lifetimes when swollen with an electrolyte diluent. A high performance IPT membrane in bending and force actuation typically requires an ionic conductivity greater than 100 mS/cm and a hydrated modulus greater than 50 MPa. The emerging goal is to fundamentally understand the significance of each ionomer parameter as it relates to electromechanical transduction and performance. Synthetic polymers designed specifically to address the effects of molecular weight distribution, chemical composition, stereochemistry, topology, morphology, and the interface with varied IPT components will provide fundamental structure – property relationships. The effects on transduction performance

in IPTs will direct engineering design for specific applications while operating within a balance where synthetic efforts can tailor electrical and mechanical properties of the ionomeric membrane.

Despite the use of many commercial polymer starting materials, chemical composition is so far the most extensively investigated polymer parameter and had significant effect upon every aspect of the membrane's properties and device performance. The most significant trend was the designation of acid strength of the bound anion as the largest contributor to the origins of back relaxation. The importance of charge storage at the interface between the electrode and ionomer to total strain existed regardless of the chemical composition of the ionomeric membrane. However, the link between chemical composition and morphological structure to IPT performance was clarified through investigation of ionomers tailored for comparison. Results of those studies suggested that well-defined microphase separation enabled more efficient charge transport and increased nucleation of electrode particles which led to higher interfacial surface area. These investigations suggested that increases in capacitance and ionic conductivity are both achievable based on morphology and lead to greater performance. The typical tradeoff in transducer performance for electroactive polymer transducers exists between blocked force production and free displacement. Opportunities for IPT performance gains without this tradeoff were shown through increased energy density and energy conversion efficiency of the transducer.[166] Adjustment of polymer topology through controlled crosslinking enhanced blocked force production while allowing for increased mechanical integrity at high IEC levels. Higher IEC is typically required for sufficient ionic conductivity in ionomers with less distinct microphase separation. Optimization of branched topologies while preserving the IEC could similarly lead to increased modulus, better solubility/processability than crosslinked systems, enhanced functionality for compatibility, and a tuned morphological structure. This bottom-up approach, as the subject of this dissertation, will further enable methods for attaining increased performance through geometry and optimized IPT components, as was demonstrated for piezoelectric transducers.[167] The specific polymer parameters of molecular weight and stereochemistry remain available for IPT tuning and to this point are relatively unexplored. Fundamental investigation of IPT membrane design will also contribute to extensive efforts to establish understanding of solid-state ionomer properties,[48, 49] especially at the interface with ionic liquids.[168] Systematic variations in membrane properties will reveal more details of the

mechanism for electromechanical transduction in these charge transport based composite devices. Feedback between design and performance will create a cycle where fundamental understanding of ionomer design and structure – property characterization facilitate improvement and enable further commercialization of IPTs in the future.

1.3 Motivation

After more than fifteen years of research and development on IPT technology the majority of understanding is based upon the model platform, Nafion[®]-IPTs. In the water-swollen form these devices display large strain rates and peak strains but decreased steady-state strain due to back relaxation. Recent advances with the use of ionic liquids provided an alternative to this long-standing disadvantage. Negligible vapor pressure, high electrolytic limits, and increased viscosity inherent to ionic liquids enabled increased lifetimes of actuation, greater peak strain, and reduction or elimination of back relaxation with Nafion[®]. Extensive advances in electroding techniques have also served to increase actuation lifetime, free strain, and blocked force through the use of semi-conducting ceramic powders and carbon nanotubes (CNT). Optimization of conducting particle loading both in membrane composites and IPT electrodes has achieved increased energy density of the devices due mainly to enhanced electrical and mechanical properties of the fillers/conductors. Fundamental understanding of the processes that result in electromechanical transduction in these devices has increased and driven further development of applications. However, efforts to tailor the ionomer membrane itself are limited, especially for step-growth ionomers. The majority of chain-growth ionomer studies either includes commercial non-perfluorosulfonate membranes or purchased ionomers/polymers that are then further functionalized.

The logical next step at this stage of research for IPT technology is to begin fundamental investigations of the ionomeric membrane and matrix. Fundamentally, IPT operation requires the presence of free ions for charge transport within the polymer matrix. The most common approach is use of ionomers with microphase separation on the basis of bound hydrophilic functionalities and a more hydrophobic backbone composition. However, the sole presence of microphase separation based on charged functional groups is not sufficient to qualify a polymer for application in IPTs. The combined presence and population of charge carriers are critical to the design of high-performance IPTs. The success of Nafion[®] as an IPT membrane highlights

that increased organization of this morphological structure to form distinct interconnected phases relates to maximum charge transport and electromechanical transduction. At least one phase of the polymer should be continuous and allow for transport of the membrane's charge carriers. Furthermore, increased connectivity of the charge containing phase should decrease the total number of required charge carriers for sufficient electromechanical transduction. Design of the ionomer should essentially concentrate on the efficiency of charge transport based on tailoring the combined mechanism, chemical composition, morphological structure, and diluent effects. A synthetic study of ionomers with direct control over the degree of charged functional groups will enable systematic variations in ion exchange capacity (IEC), especially in the case of polymer systems that are predicted to have less distinct microphase-separation. Step-growth polymerization is a well-established fundamental technique to produce engineering thermoplastics. These polymers typically demonstrate significant toughness, stability, and elastic modulus. All of these properties would benefit IPT design, especially considering that the vast majority of transducers to date have demonstrated low force-production when swollen with the necessary diluent. The low blocked force capabilities of present IPTs limit the available applications for this technology.

Design of an ionomer series starting with the monomers allows for tuning of other important polymer properties than just the chemical composition. Investigations into the effects of polymer topology are limited and mainly concentrated on the difference between linear and cross-linked systems. Synthetic methods are available to control the degree of branching to produce polymers with topologies ranging from linear to slightly branched, hyperbranched, and dendritic. This range of control allows for the potential to tune solubility, melt processability, microphase separation, ionic conductivity, and hydrated modulus of the IPT membrane. Increases in the number of endgroups associated with branching also provide the potential to post-functionalize the ionomer for increased compatibility with other IPT components. All of these properties have been deemed desirable for tuning based on previous IPT development. Furthermore, no studies have emerged beyond Nafion[®] and Flemion[®]-IPTs that employ ionic liquids in IPTs. Due to the large benefits associated with this diluent, studies beyond perfluorosulfonated ionomers are warranted. The DAP method has been extended to include ionic liquid diluents, but is also not yet proven beyond Nafion[®]-IPTs. These two significant advances in the field provide solid

points of reference to investigate the influence of controlled polymer topology on the performance of IPTs.

1.4 Research objectives

The primary objective of this research is to investigate the effects of polymer topology on electromechanical transduction in ionic polymer transducers. To achieve this objective, three primary research thrusts were pursued. (i.) Initially is the synthesis of a series of novel ionomers with controlled degrees of branching and ionic content. Step-growth polymerization provided direct control over the molecular weight of the branches to be combined and an oligomeric $A_2 + B_3$ method for production of the branched polymers. Design of IPTs with these novel ionomer requires extensive chemical, structural, and physical characterization of the base polymers. (ii.) The confirmed series of ionomers is then employed with current state-of-the-art techniques and materials to construct ionic liquid-swollen ionic polymer transducers. Interactions between the novel ionomers and the individual IPT components are also characterized for indicators of device performance. (iii.) Characterization of electromechanical transduction through actuation of the fully fabricated devices is the final objective. Observation of actuation performance allows for correlations between transduction in the final device and properties/interfaces that originate with the polymer topology tailored to the novel ionomer series.

1.5 Contributions

The research described in this dissertation encompasses the full breadth of materials design to materials application. These efforts are put forth to increase the fundamental understanding of macromolecular architecture as relates to electromechanical transduction in ionic polymer transducers. Polymer synthesis and characterization was performed to produce a branched series of ionomers suitable for IPT development with ionic liquids and the DAP method. Specific contributions from this line of research are:

- Highly branched and linear sulfonated polysulfones were synthesized according to an oligomeric $A_2 + B_3$ polymerization to provide a soluble series for all subsequent investigations.

- The sulfonated polysulfones were fully characterized to provide material properties necessary for design and understanding within IPT applications.
- The DAP method was extended and modified to account for use of sBPS and high-boiling aprotic solvents to fabricate IPT electrodes.
- Two distinct methods were developed to target ionic liquid uptake into sBPS membranes.
- Model sample sets were fabricated to characterize the interface between the ionomer and the ionic liquid as well as the ionomer and the conductor of the electrode.
- A technique employing through-thickness EIS was developed to characterize and model the impedance and capacitance of IPT components and fully fabricated IPTs.
- Characterized the electromechanical transduction properties for an optimized series of linear and branched sBPS–IPTs with targeted uptakes of ionic liquid.
- Demonstrated the first series of IPTs employing 100 % novel ionomer in all components of the device to be fabricated with the DAP method. The series of sBPS – IPTs is also the first reported novel ionomer to fully compose IPTs designed with ionic liquids.

1.6 Document organization

The research encompassed in this dissertation is organized in to five primary chapters that describe the efforts used to establish the above described contributions. The present chapter reviewed the scientific rationale behind the original hypothesis and the supporting literature for further development of novel ionomeric membranes for application in ionic polymer transducers. Progress to address the specific research objectives is described in the remainder of the document. Chapter 2 covers the synthesis and characterization of the series of polymers that form the basis for investigation of the effect of macromolecular architecture on IPT performance. Development of the synthetic method to produce the target ionomers as well as extensive characterization of chemical composition, structure, solution properties, membrane properties, and morphology are provided. Chapter 3 presents the initial studies to design IPTs with a novel branched sulfonated polysulfone. Interaction of the ionomer with the conducting particles both in isolated model electrodes as well as full-scale transducers was elucidated with EIS, equivalent circuit modeling, and evaluation of electromechanical actuation. The volumetric ratio of the conducting particles to ionomeric matrix was varied while the content ratio of ionic liquid to

ionomer was kept constant. Chapter 4 concentrates on the interface of the ionomer with the ionic liquid through isolation of the system as model central membranes. Two distinct techniques were employed to imbibe the membranes with the ionic liquid. Evaluation of the effect of this interaction was primarily dependent on characterization of charge transport with EIS. The electrolyte combination of the ionomer and ionic liquid was also evaluated in terms of hydrated modulus and thermal transitions with DMA. Chapter 5 encompasses the design, fabrication, and evaluation of an optimized set of IPTs based on the techniques developed above. Optimized interfaces between the ionic liquid, conducting particles, and the ionomer were employed to create transducers with anticipated maximum performance. The sample set was also designed specifically to use a branched ionomer and its linear analogue for two levels of sulfonation. Performance of the resultant transducers confirmed that branching did influence electromechanical transduction and could be an addition to the effect of increased sulfonation. Chapter 6 provides an overall summary and conclusions associated with the project as a whole. Suggestions for future work are also included. Appendices follow with the results of important collaborations and research performed with colleagues at the U.S. Army Research Laboratory.

Chapter 2 OLIGOMERIC $A_2 + B_3$ SYNTHESIS OF BRANCHED POLYSULFONE IONOMERS

*This chapter is primarily derived from and expanded upon: [169] Duncan A J, Layman J M, Cashion M P, Leo D J and Long T E 2010 Oligomeric $A_2 + B_3$ synthesis of highly branched polysulfone ionomers: novel candidates for ionic polymer transducers *Polymer International* **59** in press

The present chapter discusses the synthesis and characterization of oligomeric $A_2 + B_3$ polysulfones and their linear analogues. As previously discussed, very few novel polymers have been synthesized for specific application in ionic polymer transducers. Although versions of linear poly(arylene sulfone)s have been investigated, no comparison was made on the basis of polymer topology. Also, the IPTs constructed with BPSH and PATS only employed the novel ionomer in the central membrane, regardless of the electroding technique. The DAP method requires use of the ionomer matrix in the electrodes and in those cases was filled by Nafion[®] in the active volumes of the transducer. Synthesis of the IPT membranes from the monomer stage allows for direct control over the ion exchange capacity (IEC) through chemical functionalization to target sufficient ionic conductivity for performance of the device. This control is important in consideration of the increased elastic modulus of BPS in comparison with Nafion[®] and the anticipated increase in bending stiffness that will contribute to overall displacement in actuation. The materials synthesized at this stage served as the basis for all subsequent characterization of interactions with the chosen IPT ionic liquid and electrode materials through production of a series of transducers based on the DAP method. For this reason, extensive characterization of the series of sulfonated polysulfones was carried out and is detailed here. Of specific importance is characterization of the degree of branching, molecular weight, thermal transitions, and elastic modulus. These synthetic efforts resulted in a series of

ionomers with degrees of sulfonation ranging from 0 – 40 mol % and topologies described as linear to highly branched.

2.1 Motivation

The influence of branching on the physical properties of macromolecules is well established.[170-173] Increases in the degree of branching (DB) typically reduce chain mobility near the branch point and affect polymer properties based on reduction of crystallinity and entanglement density coupled with increased free volume due to a greater population of end groups.[174, 175] AB_n and $A_2 + B_n$ synthetic methods result in hyperbranched polymers that typically have poor solid-state properties, which are indicative of a high modulus coupled with low mechanical strength and minimal elasticity.[176, 177] Decreased hydrodynamic volume and increases in the number of chain ends due to branching typically lowers the solution and melt viscosities to facilitate easier, less energy-intensive processing.[178, 179] An increased number of end groups also allows for secondary functionalization to modify surface properties, intermolecular interactions, and morphological structure.[180, 181] $A_2 + B_n$ branching reactions performed without careful control over the monomer addition order or percent monomer conversion can lead to infinite molecular weight and the development of various hyperbranched and network structures, when only low molar mass products are predicted before the gel point.[182-184] This likelihood increases as the functionality of “n” on the B monomer increases.[185] An alternative route to branched polymers with control of the distance between branch points is the reaction of oligomeric A_2 units with B_3 monomers. The oligomeric $A_2 + B_3$ method was demonstrated for a variety of polymer compositions and for polymerizations in both the melt state and dilute solution.[119, 186-191] Solution polymerizations were demonstrated with (i) A_2 and B_3 mixed initially, (ii) A_2 added slowly to B_3 , and (iii) B_3 added slowly to A_2 . Experimental results and computational studies demonstrated that the mode of monomer addition affected the tendency for gelation, polymer topology, molecular weight development, and the polydispersity index (PDI).[184, 192] Formation of high molecular weight soluble polymers in the absence of gelation is dependent on dilute concentration and the formation of cyclic structures for all three modes of monomer addition. Oligomeric $A_2 + B_3$ polymers benefit from A_2 units with controlled molar mass above the molecular weight for entanglement. This characteristic was shown to significantly augment the stress-strain properties of oligomeric $A_2 +$

B₃ polyurethane ureas over their hyperbranched analogues.[193, 194] Furthermore, control of the molecular weight of A₂ oligomers allows for tuning of processability based on the zero shear viscosity and shear thinning behaviors that result from either short-chain or long-chain branches and branch density along the effective backbone.[171] Present use of the DAP method to fabricate IPTs relies heavily on melt pressing steps. Control of the length of the A₂ unit between branch points and as branch lengths therefore provides the ability to create a library of polymers with incremental variation between linear and hyperbranched topologies. The ability to tune melt processability based on branching (per a thorough rheological study) could further optimize the DAP for reduction of the macroscopic interface between the electrodes and the central ionomeric membrane.

The fundamental performance mechanism of these devices depends on the capability of the film to facilitate ion transport, most often mobile cations, to an electric double layer formed at the interface of the ionomer and the electrode.[54, 73] For this reason, ionomers and solid polyelectrolytes are the most common materials synthesized and employed as IPTs. The association of ionic functionalities to form nanoscale morphological structure is well documented in many ionomer systems, yet remains a topic of intense research.[33, 48, 49, 79, 195] Ionic association within the polymer matrix typically leads to increased T_g , higher modulus, and augmented ionic conductivity.[196-198] As reviewed previously the majority of investigations and developments concerning IPT actuators and sensors are centered on DuPont's Nafion[®] ion-exchange membrane.[35, 61, 64, 199] Introduction of branching to IPT ionomeric membranes is anticipated to serve many purposes during the construction and lifetime of the device. The increased number of end groups may modify the polymer solubility, interaction with the diluent, and vary the melt viscosity of the membrane during processing. Increased processability allows for tailoring of the ionomeric membrane dimensions as well as its shape. However, the strength of ionic associations may compete with the effect of branching on melt processability since these associations are likely to act as dynamic physical crosslinks even in the melt. Particularly in the case of ionic liquids, melt rheological studies would be necessary to isolate branching effects during melt pressing where the diluent screens or reduces the strength of these polymer-based ionic associations. Furthermore, recent studies demonstrated that controlled variation of branching in sulfonated polymers resulted in corresponding changes in the microphase separated morphological structure and ionic conductivity.[200-202]

Charged poly(arylene ether)s are already well established as potential membranes for ion-conducting devices such as fuel cells.[105] This specific study describes the synthesis and characterization of a series of linear and highly branched sulfonated polysulfones through step-growth polymerization and an oligomeric $A_2 + B_3$ methodology. Characterization of the polymers with nuclear magnetic resonance spectroscopy (NMR), dynamic light scattering (DLS), and size exclusion chromatography (SEC) provides confirmation of chemical composition and structure, DB, solution size distribution, and relative molecular weight. Membranes cast from the ionomers are also subjected to stress-strain analysis. Thermal transitions and thermomechanical properties were investigated with thermogravimetric analysis (TGA), differential scanning calorimetry (DSC), and dynamic mechanical analysis (DMA). Morphological characterization of the dry membranes is performed with small angle X-ray scattering (SAXS). This combination of characterization techniques provides the essential material properties for application of sBPS membranes to the construction and performance of IPTs. Establishment of structure–property relationships based on DB and ionic content will also serve to establish the isolate the effect of controlled polymer topology on electromechanical transduction in sBPS – IPTs.

2.2 Experimental methods

2.2.1 Materials

4,4'-biphenol (BP, 97 %, Aldrich) was dissolved in the presence of activated carbon and refluxing acetone, recrystallized, and dried *in vacuo* at 60 °C for 24 h. This process was performed in triplicate. 4,4'-dichlorodiphenylsulfone (DCDPS, monomer grade, Solvay Advanced Polymers) was used as received. The sulfonated comonomer 3,3'-disulfonate-4,4'-dichlorodiphenylsulfone (SDCDPS) was synthesized and purified to a known weight fraction of NaCl according to a reported method (Figure 2.1).[203, 204] Anhydrous K_2CO_3 (≥ 99.0 %, Fluka) was dried *in vacuo* along with DCDPS and SDCDPS at 120 °C for 24 h. 1-bromo-4-fluorobenzene (99 %), Mg, and PCl_3 (99.9+ %) were purchased from Aldrich and used without further purification to synthesize tris(4-fluorophenyl)phosphine oxide (TFPPO), according to a previously reported procedure (Figure 2.2).[205] Anhydrous N,N-dimethylacetamide (DMAc, 99.8 %, Aldrich) and toluene (≥ 99.5 %, EMD) were used as received and stored over molecular sieves under N_2 until use.

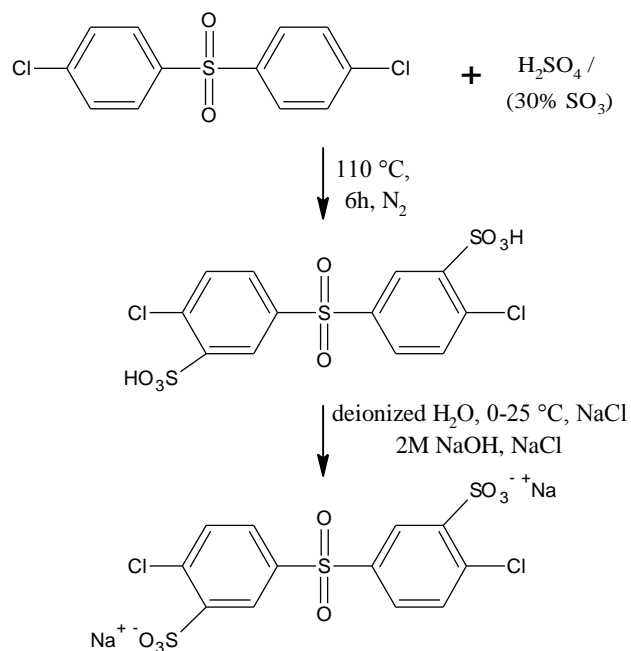


Figure 2.1: Synthesis of the disulfonated DCDPS monomer

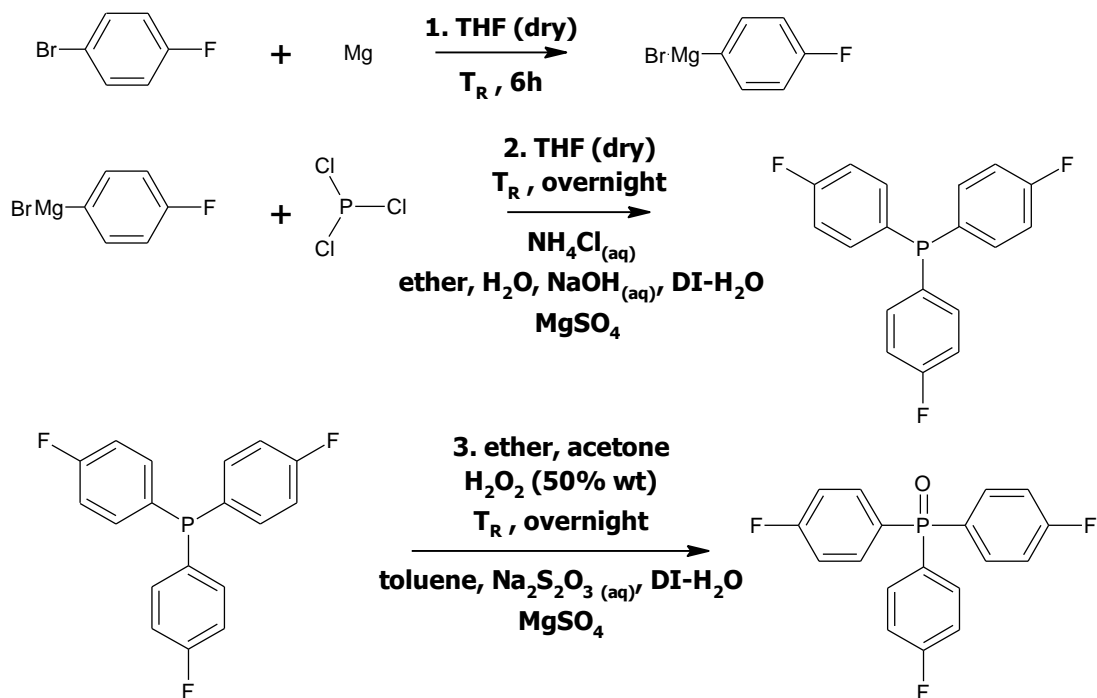


Figure 2.2: Synthesis of the TFPPPO branching agent (B₃)

2.2.2 A₂ oligomer synthesis

A typical polymerization to target a 3 000 g/mol oligomer with 20 mol % disulfonation charged BP (4.08 g, 21.9 mmol), DCDPS (4.36 g, 15.2 mmol), and SDCDPS (1.86 g, 3.79 mmol) into a 100 mL three-neck, round-bottomed flask at 20 wt % solids in DMAc (30 mL). K₂CO₃ (3.01 g, 21.8 mmol) and toluene (15 mL) were also added to the reaction flask. The reaction setup was equipped with an overhead mechanical stirrer, a dry nitrogen inlet (with condenser), and a Dean-Stark trap attached to a reflux condenser. The system was purged with N₂ for 0.5 h before immersion in a constant temperature bath at 145 °C for 4 h to reflux the toluene/water azeotrope. Dropwise removal of the azeotrope was performed during a temperature ramp to 165 °C. The reaction at 165 °C was allowed to proceed for 12–24 h. The reaction solution was cooled to ambient temperature under a slow N₂ purge. The reaction mixture was vacuum-filtered to remove excess salt introduced with the SDCDPS and produced during the reaction. The resulting 0 and 20 mol % disulfonated oligomers were precipitated into stirred deionized water and the 40 mol % disulfonated oligomers were precipitated in 10/1 IPA/H₂O (v/v). The precipitated oligomers were extracted in their precipitation medium at 60 °C for 12-16 h to aid further removal of salt impurities. The oligomers were vacuum filtered and dried *in vacuo* at 120–170 °C for 24 h. The A₂ oligomers are designated as Xk-BPSH-YY where Xk is the target molecular weight (g/mol) in thousands and YY represents the target mol % disulfonated repeat units.

2.2.3 A₂ + B₃ polymerization of sulfonated polysulfones

For a typical branching reaction a 3 000 g/mol, 20 mol % disulfonated oligomer (3.01 g, 0.892 mmol), and TFPPO (0.296 g, 0.892 mmol) were charged into a 100 mL three-neck, round-bottomed flask at 10 wt % solids in DMAc (32 mL). K₂CO₃ (0.142 g, 1.02 mmol) and toluene (16 mL) were also added to the reaction flask. The reaction assembly was identical to that used for synthesis of the A₂ oligomers. The system was purged with N₂ for 0.5 h before immersion in a constant temperature bath at 145 °C for 4 h to reflux the toluene/water azeotrope. Dropwise removal of the azeotrope from the Dean-Stark trap was performed during a temperature ramp to 160 °C over 1 h. The bath temperature was held at 160 °C for 0.5 h before a temperature ramp to 165 °C. The branching reaction was monitored for development of high molecular weight (0–2 h), indicated through a large increase in the solution viscosity of the reaction mixture. Synthesis of the highly branched sulfonated polymers employed a further step in bath temperature to 170

°C and 4–28 h to complete the reaction. The concentration (wt %) of the reaction mixture was diluted to one-half the original with additional DMAc to lower the solution viscosity during filtration to remove the salt residue. Subsequent steps for isolation of the polymer were similar to those used for the A₂ oligomers. The highly branched poly(arylene ether sulfone) products are designated as HB-XkBPS-YY where Xk is the A₂ oligomer target molecular weight (g/mol) in thousands and YY represents the target mol % disulfonation of A₂ repeat units.

2.2.4 Characterization techniques

¹H NMR and ¹⁹F NMR analysis were performed on a Varian INOVA 400 MHz spectrometer at ambient temperature. Low molecular weight nonsulfonated oligomers, sulfonated oligomers, and highly branched sulfonated polysulfones were analyzed in DMSO-d₆. Nonsulfonated oligomers above 3 000 g/mol and highly branched nonsulfonated polysulfones were analyzed in CDCl₃. ³¹P NMR analysis of the highly branched polysulfones was performed on a JEOL 500 MHz spectrometer.

Dynamic light scattering was performed with a Malvern ZetaSizer Nano equipped with a 633 nm He–Ne laser light source. Each solution was analyzed five times. Solutions were made at a concentration of 1 mg/mL in N-methylpyrrolidone (NMP) containing LiBr (0–0.2 M). Size exclusion chromatography was performed at 50 °C in NMP for nonsulfonated polymers. Ionomers were analyzed in NMP that contained 0.2 M LiBr. A Waters system composed of three in-line Polymer Laboratories PLgel 5 µm MIXED-C columns and an autosampler was fitted to a Waters 2414 Refractive Index detector and a Wyatt Technologies miniDAWN multiangle laser light scattering (MALLS) detector to provide dual detection. \overline{M}_w and \overline{M}_n were calibrated based on dRI retention volumes/times for a series of linear polystyrene (PS) standards (Polymer Laboratories, 8 standards, $M_p = 5\ 000, 9\ 860, 28\ 500, 766\ 000, 186\ 000, 426\ 600, 1\ 226\ 000, 3\ 390\ 000$ g/mol).

Membranes were cast on level glass plates underneath a glass cover from 5–10 wt % solution of the polymer in DMAc. Removal of the solvent proceeded over approximately 24–48 h under an IR heat lamp. The films were released from the plates during submersion in deionized water. After surface drying, the films were dried *in vacuo* during a temperature ramp from RT–250 °C, isothermal step at $T_g + 5$ -10 °C for 1 h, and cooled to room temperature under reduced pressure. Stress-strain analysis was performed with a 5500R Instron universal testing instrument at a

cross-head speed of 12 % /min at ambient conditions. Five samples for each composition were cut from larger membranes with an ASTM D3368 die and tested. Thermal transitions were detected with a TA Instruments Hi-Res Thermogravimetric Analyzer 2950 (N₂, 10 °C/min) and a TA Instruments Q1000 differential scanning calorimeter (N₂, 20 °C/min). Dynamic mechanical analysis was performed on a TA Instruments Q800 (5 °C/min) in tensile mode based on an imposed linear deformation of 15 μstrain at 1 Hz. Due to the high temperature nature of the tests, all DMA characterization for the neat membranes was performed in air.

Small angle X-ray scattering (SAXS) was performed at the Brookhaven National Laboratory on the Advanced Polymer Beamline (X27C) at the National Synchrotron Light Source. The wavelength of the X-ray beam was 1.366 Å and the sample-to-detector distance 867 mm. Two-dimensional SAXS images were recorded using a Mar CCD camera with an intensity uncertainty on the order of 2% and analyzed using the POLAR software developed by Stony Brook Technology and Applied Research, Inc. All scattering intensities were corrected for transmission and background scatter due to air and Kapton windows and represented in arbitrary, relative intensity units as a function of the scattering vector, q , which is a function of the scattering angle through the relationship

$$q = \left(\frac{4\pi}{\lambda} \right) \sin \theta \approx \frac{2\pi}{d} , \quad (2.1)$$

where λ is the wavelength of X-ray beam (1.366 Å), θ is half of the scattering angle (2θ), and d is the distance between the centers of scattering domains according to Bragg's Law. Data within the two-dimensional scattering profiles was smoothed with a Level 15 Loess Algorithm in the program PeakFit v4.12. The curve that resulted was fit with a linear baseline and a second derivative method with Gaussian peaks to estimate the locations of features in the profile.

2.3 Results and Discussion

2.3.1 A₂ sulfonated polysulfone oligomers

Synthesis of poly(arylene ether sulfone)s based on various bisphenols and aromatic sulfone monomers was previously demonstrated in the presence of the weak base K₂CO₃. [113, 206, 207] Sulfonation of the monomer DCDPS was performed in the presence of fuming sulfuric acid to obtain SDCDPS with quantitative disulfonation *ortho* to the chlorine functionalities of

DCDPS.[112] This method achieves direct control over ionic content and avoids side reactions and degradation typically associated with post-sulfonation techniques.[208] Controlled reaction of BP with varied ratios of DCDPS and SDCDPS in the presence of K_2CO_3 proceeded in DMAc and toluene. The initial toluene reflux serves as an azeotrope for the removal of water residue from monomers and water produced in the reaction. The synthetic scheme to produce A_2 oligomers of 3 000, 5 000, and 10 000 g/mol that contain 0, 20, and 40 mol % disulfonation and a functionality of two is depicted in Figure 2.3. Molecular weight control of the hydroxyl terminated oligomers, as calculated with the Carothers relationship

$$\bar{X}_n = \frac{1+r}{1-r} \quad , \quad (2.2)$$

is obtained with a stoichiometric imbalance based on a molar excess of BP; where $r = N_a / N_b$ such that N_a and N_b represent the moles of chlorine and hydroxyl end groups respectively in the polycondensation reaction.[175] The above relationship assumes complete conversion (100 %) for the reaction.

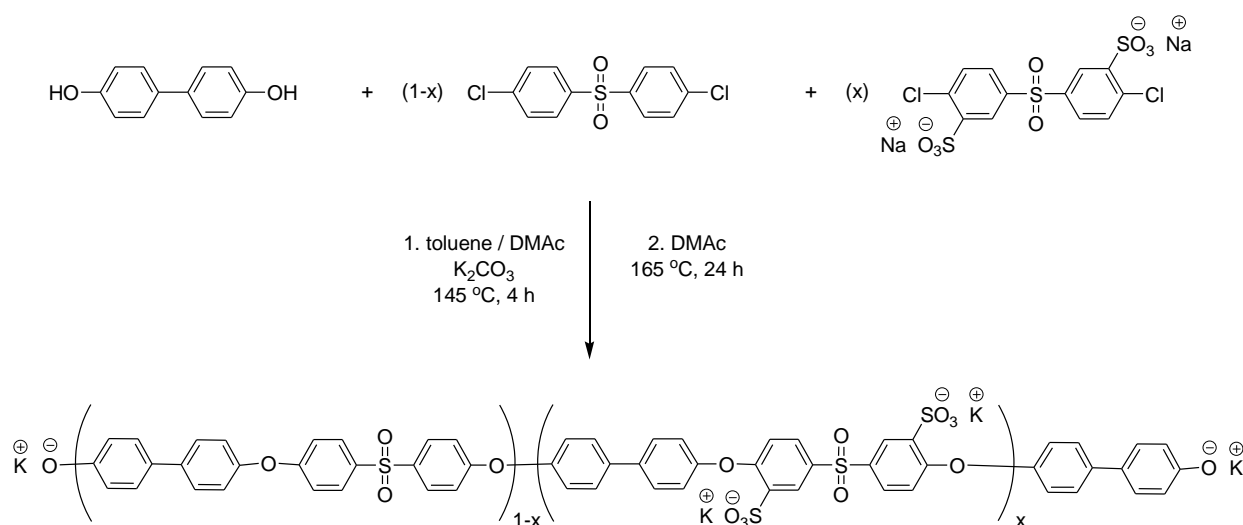


Figure 2.3: Synthesis of controlled molecular weight hydroxyl terminated A_2 oligomers

Figure 2.4 provides an overlay of the 1H NMR spectra for A_2 oligomers with a target \bar{M}_n of 3000 g/mol that contain 0, 20, and 40 mol % disulfonated repeat units. The peak that represents the hydrogens on the aromatic ring adjacent to the sulfone of DCDPS appears at 7.91 ppm. Upon inclusion of SDCDPS into the polymer backbone, the oligomer displays distinct shifts in the 1H

NMR spectrum at 8.27, 7.81, and 6.95 ppm for the hydrogens on the same aromatic ring as the carbon that is bonded to the potassium sulfonate salt. The ratio of the average area determined from integration of these three SDCDPS peaks to those of DCDPS is used with

$$\text{degree of sulfonation} = x = \frac{[(\int c + \int d + \int e)/3]/2}{[(\int c + \int d + \int e)/3]/2 + (\int b)/4} \quad , \quad (2.3)$$

to determine the degree of sulfonation (x) of the oligomer. A broad multimodal peak with varied intensity present at 6.78 ppm represents the hydrogens on the aromatic carbons adjacent to the hydroxyl/phenoxide end group. The peak characteristics, as well as the appearance of a peak at 9.51 ppm for the hydroxyl hydrogen, indicate incomplete conversion of the potassium phenoxide salt to a hydroxyl functionality during isolation of the oligomers. Calculations of molecular weight were based on integration of the full peak width of approximately 0.11 ppm to account for both end group species. Under the assumption that the stoichiometric imbalance of BP results in two hydroxyl end groups on every chain, the number average molecular weight (\overline{M}_n) of each A_2 oligomer is estimated with the experimentally determined degree of sulfonation and peak integrations from ^1H NMR end group analysis according to

$$\overline{M}_n = \left(\frac{\int h, m}{\int a} \right) [x(MW_{di-sulf\ RU}) + (1-x)(MW_{nonsulf\ RU})] + (MW_{end\ groups}) \quad . \quad (2.4)$$

The A_2 oligomer target and experimental \overline{M}_n , degree of sulfonation, and ion exchange capacity (IEC)[207] are presented in Table 2.1. There is good agreement between the target and experimental \overline{M}_n for the full series of A_2 oligomers. The targeted degree of sulfonation is also met for each oligomer within ± 6 mol %. Successful synthesis of the targeted compositions and molecular weights for the A_2 oligomers confirms that use of the presulfonated DCDPS does not significantly alter the linear step-growth reaction and results in random oligomeric ionomers.

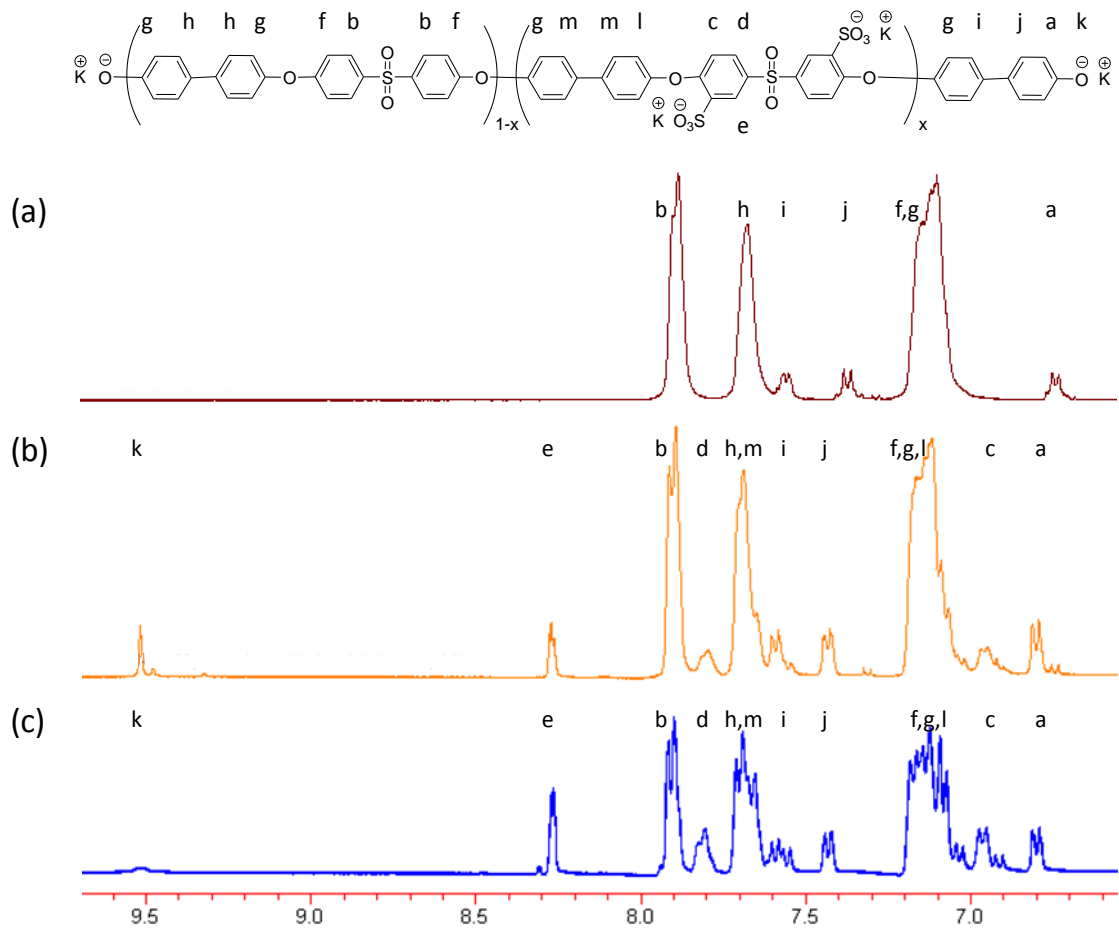


Figure 2.4: ^1H NMR spectra and assignments for polysulfone A_2 oligomers with a target \overline{M}_n of 3 000 g/mol and target degrees of sulfonation of (a) 0 % (b) 20 % (c) 40 %

Table 2.1: Results of ^1H NMR analysis for A_2 oligomer \overline{M}_n and degree of sulfonation

target oligomer	monomer molar ratio (A : B)	target \overline{M}_n ^{a)} (g/mol)	target degree of sulfonation ^{b)} (%)	degree of sulfonation ^{b)} (%)	\overline{M}_n ^{c)} (g/mol)	IEC [K ⁺ form] ^{d)} (mequiv/g)	\overline{X}_n
3k-BPSH-00	1.00:1.14	3 000	0	0	4 400	0.00	22
3k-BPSH-20	1.00:1.16	3 000	20	19	3 000	0.85	13
3k-BPSH-40	1.00:1.17	3 000	40	36	3 500	1.49	15
5k-BPSH-00	1.00:1.08	5 000	0	0	4 900	0.00	24
5k-BPSH-20	1.00:1.09	5 000	20	18	6 400	0.81	29
5k-BPSH-40	1.00:1.10	5 000	40	38	5 100	1.54	21
10k-BPSH-00	1.00:1.04	10 000	0	0	8 100	0.00	40
10k-BPSH-20	1.00:1.04	10 000	20	17	12 600	0.77	57
10k-BPSH-40	1.00:1.05	10 000	40	46	11 300	1.80	45

a) calculated with Equation 2.1

b) determined with ^1H NMR and Equation 2.2

c) determined with ^1H NMR and Equation 2.3

d) Ion exchange capacity; calculated based on Li *et al.*

2.3.2 $\text{A}_2 + \text{B}_3$ sulfonated polysulfones

Several previous studies investigated the synthesis and characterization of hyperbranched,[209, 210] dendritic,[211] and crosslinked [212] poly(arylene ether)s. Under dilute solution conditions oligomeric $\text{A}_2 + \text{B}_3$ reactions can develop high molecular weight and a high DB without gelation. Unal *et al.* used slow addition of A_2 oligomers to a solution of B_3 monomer to polymerize highly branched poly(urethane urea)s and poly(ether ester)s.[188, 192] An effect of A_2 oligomer molecular weight on the onset of gelation was not detected. Lin *et al.* initially mixed the A_2 oligomers with the B_3 monomer to synthesize highly branched bisphenol-A based poly(arylene ether)s.[119] In those polymerizations increased molecular weight of the A_2 oligomer decreased cyclization and resulted in gelation at shorter times. A_2 oligomers also appeared to promote a kinetic excluded volume effect after reaction with B_3 monomers.[213]

Reactivity of the remaining fluorines on the B_3 monomer seemed to decrease after reaction with an A_2 oligomer. Increased molecular weight of the oligomeric A_2 chains increased shielding

of the B₃ monomer to decrease the extent of conversion for the branching reaction and effectively delay gelation. Overall, time to gelation decreased due to the greater impact of decreased cyclization than lowered reactivity of the B₃ monomer. Lower solution concentrations were necessary to sufficiently increase cyclization and achieve a balance between the two effects to obtain high molecular weight branched polymers.

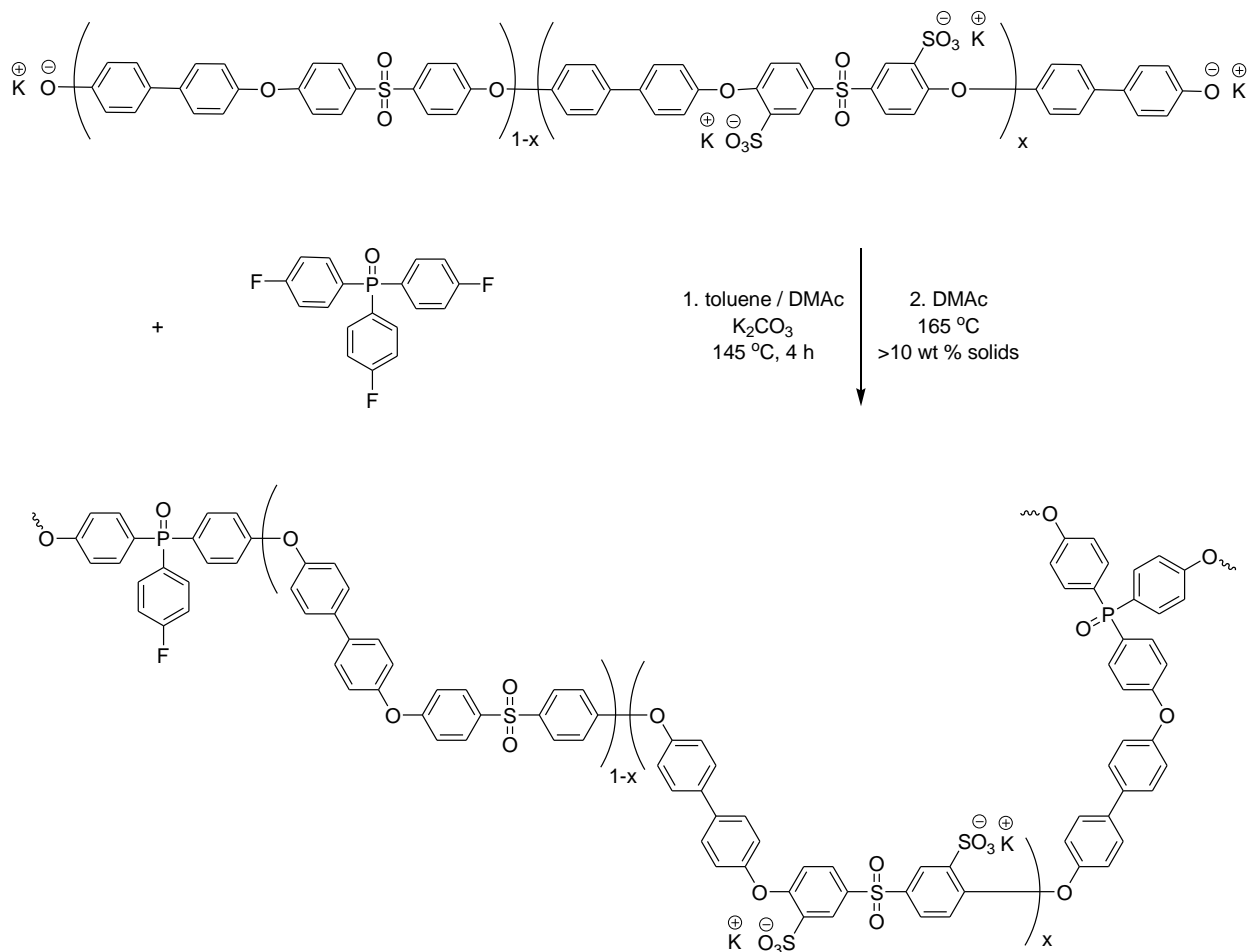


Figure 2.5: Synthesis of highly branched poly(arylene ether sulfone) ionomers through an oligomeric A₂ + B₃ method

2.3.2.1 Composition, structure, and molecular weight characterization

The highly branched sulfonated polysulfones presented here are well defined and form ionomeric membranes suitable for application in IPTs. The target \overline{M}_n of the A₂ oligomers are incrementally greater than the entanglement molecular weight of nonsulfonated 4,4'-biphenol based

polysulfones (1 500 g/mol) [214, 215] to preserve or increase the mechanical properties of the highly branched polymer in comparison to its hyperbranched analogue.[187] The condensation reaction of hydroxyl terminated A_2 oligomers of varied molecular weight and degree of sulfonation with the B_3 monomer, TFPPPO, is depicted in Figure 2.5. As a control, linear polysulfones were synthesized in the same manner as the A_2 oligomers but with a 1:1 stoichiometric balance of BP and DCDPS/SDCDPS. The TFPPPO branching unit provides three highly reactive fluorine sites for nucleophilic aromatic substitution while the phosphine oxide acts as a spectroscopic tag. After reaction with A_2 oligomers the TFPPPO molecule displays three distinct shifts in the ^{31}P NMR spectrum. The peak positions in Figure 2.6 indicate the presence of TFPPPO in the polymer as a dendritic (D), linear (L), terminal (T), or monomer (M) unit with zero, one, two, or three unreacted fluorines respectively. The unreacted fluorines that remain in the polymer were also detected with ^{19}F NMR as a secondary source of information concerning the extent of conversion of the branching reaction. The DB for the highly branched polysulfones in the present study is calculated with

$$DB_{\text{Fréchet}} = \frac{D+T}{D+L+T} \quad (2.5)$$

$$DB_{\text{Frey}} = \frac{2D}{2D+L} \quad (2.6)$$

$$DB_{\text{global}} = \frac{D+T}{D+L+T+L_{A_2}} \quad \text{where: } L_{A_2} = \overline{X}_n \frac{[A_2]}{[B_3]}, \quad (2.7)$$

which are here expressed as the Fréchet,[216] Frey,[217] and global[119, 188] degrees of branching respectively. The first two methods (i.e. $DB_{\text{Fréchet}}$ and DB_{Frey}) are generally applied to hyperbranched systems while DB_{global} includes a term, L_{A_2} , to account for the separation of branch points in the polymer due to oligomeric A_2 units instead of single monomers. DB_{global} has a value of 50 % and is theoretically equal to $DB_{\text{Fréchet}}$ for a hyperbranched polymer produced with a conventional $A_2 + B_3$ reaction. The value of DB_{global} decreases to reflect a less branched topology as the molecular weight of the A_2 oligomer increases.

These quantifications of DB aided in evaluation of the extent of conversion for polymers produced during adjustment of the $A_2 + B_3$ reaction conditions for varied $A_2 \overline{M}_n$ and degree of

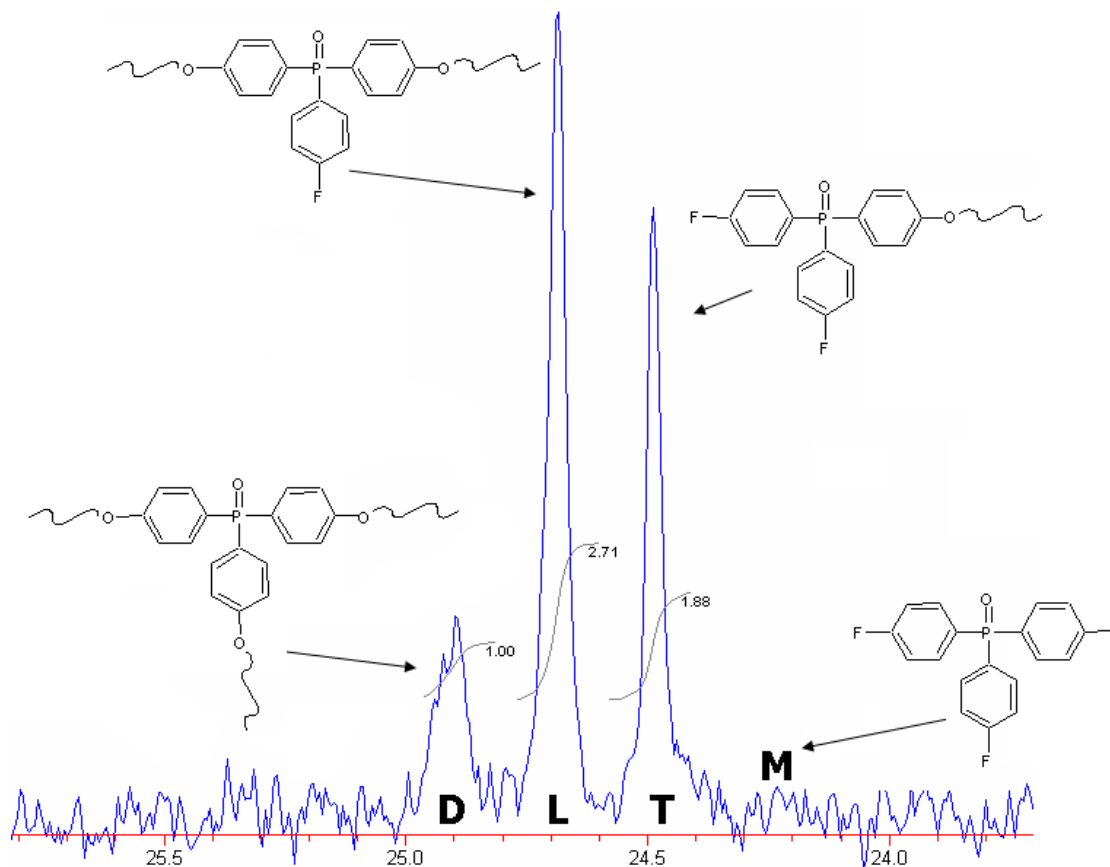


Figure 2.6: ^{31}P NMR spectrum of a highly branched 20 mol % disulfonated polysulfone synthesized with a 10 000 g/mol oligomeric spacer between dendritic (D), linear (L), and terminal (T) branch points [M indicates shift for TFPPPO monomer]

sulfonation. For a typical reaction of a 5 000 g/mol A_2 oligomer with 0 % disulfonation at a 1:1 molar ratio of A_2 to B_3 and 23 wt % solids, gelation (95 %) occurred at 3 h. The monomer concentration was decreased to 6 wt % and the reaction resulted in a moderate gel fraction (38 %) after 12 h. A further reduction of concentration to 3 wt % solids avoided gelation even after 24 h. These conditions resulted in low molecular weight products with a high fraction of terminal units, as detected with ^{31}P NMR, that indicated A_2 oligomers end capped with B_3 monomer. Based on this knowledge of the 5 000 g/mol A_2 reactivity, an increase to 12 wt % solids and stepwise increases in temperature from 160 °C to 170 °C resulted in a high viscosity reaction mixture in just over 1 h. As shown in Table 2, HB-5kBPS-00 displayed a 42 % conversion of the B_3 monomer to dendritic units, and a 48 % $\text{DB}_{\text{Fréchet}}$, 62 % DB_{Frey} , and 1.8 % $\text{DB}_{\text{global}}$. The high $\text{DB}_{\text{Fréchet}}$ reflects a high extent of conversion for the branching reaction while the high DB_{Frey} suggests development of high molecular weight based on removal of the terminal unit

contribution to the DB calculation. The sensitivity of the reaction to monomer concentration is likely due to the effect upon the development of cyclic structures. Cyclics were observed previously for other oligomeric $A_2 + B_3$ and hyperbranched polysulfones, although smaller A_2 molecular weights were used and no charge was present in the backbone of the polymers.[119, 218] An analogous process revealed the reaction conditions necessary to achieve a high DB without gelation for the other nonsulfonated A_2 oligomers in the series. Increased \overline{M}_n of the nonsulfonated A_2 oligomer required increased reaction concentration to achieve similar extent of conversion without gelation for the same reaction times. As expected for polymers with similar values of $DB_{\text{Fréchet}}$, increased \overline{M}_n of the A_2 oligomer decreased the DB_{global} value.

Table 2.2: Polymer topology characterization for $A_2 + B_3$ polysulfones with varied oligomeric spacer lengths and ionic content

Sample	$A_2 M_n$ (g/mol)	[M] (mol/L)	$A_2 : B_3$ (mol:mol)	t (h)	$D^a)$	$L^a)$	$T^a)$	L_{A_2}	DB (%)		
									Fréchet	Frey	global
HB-3kBPS-00	4 400	0.04	1:1	1	0.24	0.50	0.26	22	50	49	2.19
HB-3kBPS-20	3 000	0.06	1:1	6	0.17	0.51	0.32	15	49	40	3.03
HB-3kBPS-40	3 500	0.05	1:1	28	0.16	0.50	0.34	18	50	39	2.69
HB-5kBPS-00	4 900	0.05	1:1	1	0.42	0.52	0.06	26	48	62	1.79
HB-5kBPS-20	6 400	0.04	1:1	12	0.13	0.51	0.36	28	49	34	1.72
HB-5kBPS-40	5 100	0.03	1:1	98	0.04	0.25	0.71	26	75	24	2.81
HB-10kBPS-00	8 100	0.04	1:1	1	0.37	0.47	0.16	71	53	61	0.74
HB-10kBPS-20	12 600	0.04	1:1	12	0.18	0.48	0.34	57	52	43	0.90
HB-10kBPS-40	11 300	0.04	1:1	28	0.15	0.54	0.31	48	46	36	0.93

a) determined with ^{31}P NMR

Reaction conditions and complete DB values are provided for the branched polymer series in Table 2.2. The reaction parameters developed for each target \overline{M}_n of nonsulfonated A_2 oligomer were directly applied to the oligomeric $A_2 + B_3$ synthesis of sulfonated highly branched polysulfones. Consequently, a correlation appeared between increased mol percent disulfonation of the A_2 oligomer and increased reaction time necessary to achieve a high DB. Increased charge along the backbone causes chain extension due to electrostatic repulsion between repeat units commonly known as the polyelectrolyte effect.[219] Extension of the polymer contour length is

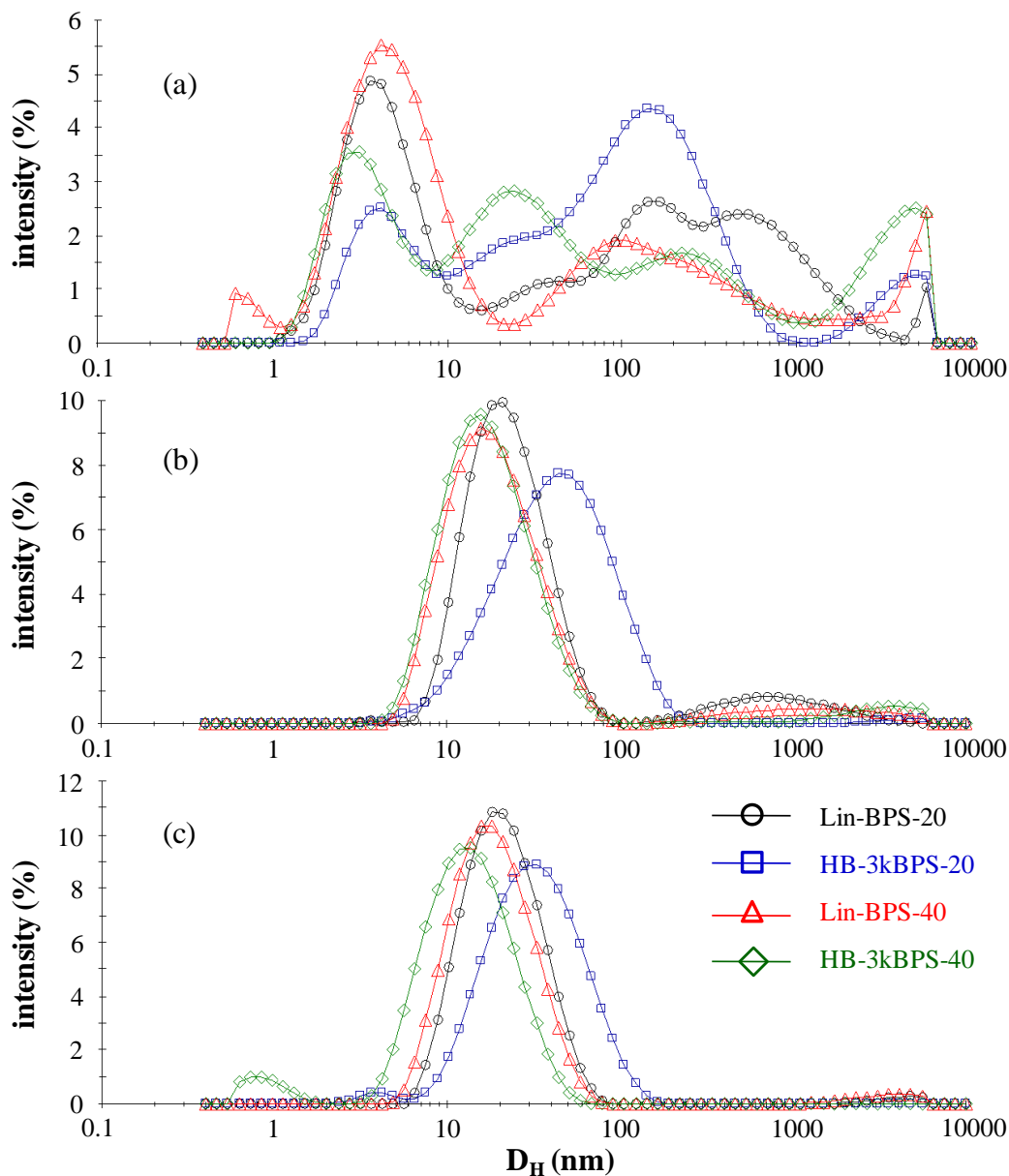


Figure 2.7: DLS size distributions by intensity for linear and branched sulfonated polysulfones in NMP, (a) 0 M LiBr (b) 0.01 M LiBr (c) 0.2 M LiBr.

likely to limit cyclization and branching due to a decreased number of configurations and limited availability of the end groups to react.[213] Although a value of approximately 50 % $DB_{\text{Fréchet}}$ was achieved for nearly all highly branched ionomers the DB_{Frey} values diminished with increased sulfonation of the A_2 oligomer employed in the reaction. This trend suggests lower molecular weight of the branched ionomers based on a larger fraction of terminal units with

increased A_2 sulfonation. Furthermore, for each discrete A_2 \overline{M}_n , DB_{global} increased slightly for greater degrees of sulfonation. DB_{global} decreased with increased \overline{M}_n of the A_2 oligomer as predicted for all degrees of sulfonation. Overall, these results indicate that increased ionic content of the A_2 oligomers significantly modified the balance between cyclization, the kinetic excluded volume effect, and the extent of conversion of the oligomeric $A_2 + B_3$ reaction. The final polymer series displays topologies between linear and moderately branched (HB-3kBPS) where DB_{global} would equal 50 % for a hyperbranched analogue.

DLS was performed on solutions of linear and highly branched ionomers in NMP/LiBr to determine size distributions and the tendency for the ionomers to aggregate in solution. This characterization is necessary to qualify potential SEC mobile phases as applicable to the full series of ionomers regardless of topology or ionic content.[220] LiBr was chosen as the charge screening agent based on DLS experiments that confirmed its increased effectiveness over glacial acetic acid for prevention of aggregation in this ionomer series. Results from the DLS intensity signal are provided in Figure 2.7a for linear and branched polysulfones of both 20 and 40 mol % disulfonation. The distribution displays significant aggregation for all four ionomers across a wide range of hydrodynamic diameters in NMP when no LiBr is present. However, addition of 0.01 M LiBr (Figure 2.7b) significantly reduces aggregation and hydrodynamic size to display a bimodal distribution. This result is characteristic of the anti-polyelectrolyte effect for charged polymers in the presence of salts or other charge screening species.[221, 222] Samples that contained either branching or an increased degree of sulfonation required a greater concentration of LiBr to limit aggregation. Overall, DLS of the linear and branched samples was performed in NMP solutions of 0, 0.01, 0.025, 0.05, 0.1, and 0.2 M LiBr. As shown in Figure 2.7c, only solutions of 0.2 M LiBr prevented significant aggregation regardless of topology or ionic content.

Based on the assumption of minimal aggregation in solution SEC in NMP, 0.2 M LiBr was performed for the full series of linear and branched ionomers. Nonsulfonated polymers were analyzed with SEC in neat NMP although HB-5kBPS-00 and HB-10kBPS-00 were not analyzed due to incomplete solubility in the chosen mobile phase. The traces from the refractive index detector are shown in Figure 2.8 for the full sBPS ionomer series, at both degrees of sulfonation. The traces appear normal with minimal tailing present that would indicate undesired polymer-stationary phase interaction or aggregation. The branched samples display typical broad,

multimodal peaks previously seen in similar branched polymers.[119] Molecular weight distributions (MWD) for the linear samples are approximately equal to two as expected for an $A_2 + B_2$ step growth reaction. The branched samples display MWD values greater than two with a maximum of 4.17 for HB-3kBPS-00. For each distinct oligomer series increased sulfonation of the A_2 oligomer appears to lower the MWD of the final polymer. Again, with respect to typical hyperbranched polymers, SEC results classify the series as moderately branched ionomers with systematic changes in topology toward the provided linear analogues.

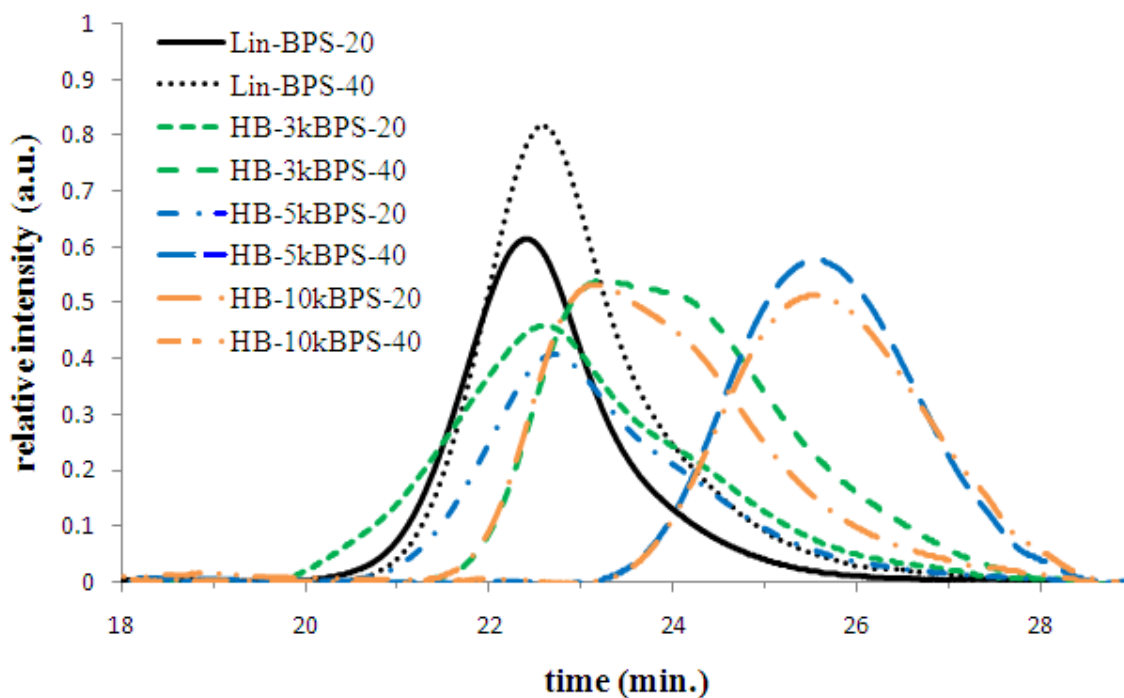


Figure 2.8: SEC chromatogram showing the RI traces for the series of linear and branched ionomers (NMP, 0.2 M LiBr, 50 °C)

Notable in the analysis is the fact that calibration with linear PS standards underestimates the molecular weight of branched polymers due to their reduced hydrodynamic diameter.[223] SEC confirmed that relative molecular weights (\overline{M}_n , Table 2.3) of greater than 20 000 g/mol were achieved for all linear and branched ionomers except for HB-5kBPS-40 and HB-10kBPS-40. Possible fractionation during isolation of the oligomer and limited conversion in the branching reaction due to a high degree of sulfonation likely combined to produce artificially narrow molecular weight distributions for these two samples. The lower molecular weight of these two

samples emphasizes the effect of increased A₂ oligomer \overline{M}_n and increased degree of sulfonation on the extent of conversion, as previously noted for DB. Overall, \overline{M}_n values of the branched and linear polymers decrease for each A₂ oligomer molar mass as the degree of sulfonation increases. Also, as the branched polymers become more linear (larger A₂ \overline{M}_n , smaller DB_{global}) \overline{M}_n values decrease for each respective degree of sulfonation.

Table 2.3: Molecular weight characterization for polysulfones with varied oligomeric spacer lengths and ionic content

Sample ^{a)}	\overline{M}_n (g/mol)	\overline{M}_w (g/mol)	$\overline{M}_w / \overline{M}_n$	degree of sulfonation ^{b)} (%)	IEC [K ⁺ form] (mequiv/g)
HB-3kBPS-00	35 600	148 300	4.17	0	0.00
HB-3kBPS-20	47 600	165 300	3.47	18	0.84
HB-3kBPS-40	25 000	49 500	1.98	36	1.53
HB-5kBPS-00	--	--	--	0	0.00
HB-5kBPS-20	44 700	102 700	2.30	18	0.81
HB-5kBPS-40	11 200	14 400	1.29	43	1.74
HB-10kBPS-00	--	--	--	0	0.00
HB-10kBPS-20	29 300	56 200	1.92	19	0.86
HB-10kBPS-40	11 100	14 400	1.30	45	1.81
Lin-BPS-00	104 200	219 600	2.11	0	0.00
Lin-BPS-20	83 300	153 700	1.85	18	0.83
Lin-BPS-40	56 500	116 100	2.05	38	1.54

a) When YY = 00, SEC performed in NMP, 50 °C, MW determined with MALLS detection. When YY = 20 or 40, SEC performed in NMP, 0.2 M LiBr, 50 °C, MW based on PS equivalent MW from dRI retention volumes and times.

b) determined with ¹H NMR

2.3.2.2 Characterization of mechanical and thermal properties

Stress–strain experiments were performed for the linear and most highly branched materials (HB-3kBPS). Films were cast from solution and formed tough, flexible, transparent membranes with a distinct yellow color, especially for the sulfonated ionomers. Curves representative of the average for five repetitions at each composition are plotted in Figure 2.9 and the tensile

properties are summarized in Table 2.4. For each respective degree of sulfonation, the linear polymers demonstrated the greatest elongation at break. Introduction of branching to the polysulfones, even for the low DB_{global} levels, significantly decreased the strain at break of the membranes. Although the A_2 oligomer \overline{M}_n of HB3kBPS is greater than the molecular weight for entanglement, the linear polymers are more prone to entangle at multiple sites along the backbone with other chains and result in increased elongation. Regardless of the topology, incorporation of sulfonate salts into the backbone of the polymer increased the available range of strain up to approximately 40 % and for the linear polymers resulted in a significant increase in both ultimate tensile strength (UTS) and tensile modulus (E). For the branched polymers, the increase in modulus due to sulfonation was smaller in comparison to the increase due to the branched nature of the polymer. HB-3kBPS-40 displays a lower elongation at break than HB-3kBPS-20, although this may also be due to a difference in molecular weight beyond the change in degree of sulfonation. Overall, the series of polysulfones displays tensile moduli of 1-2 GPa in the dry state, similar to values reported in the literature.[224] The full series displays yield points between 5 – 10 % strain, after which the membranes do not elastically recover. Regardless, the

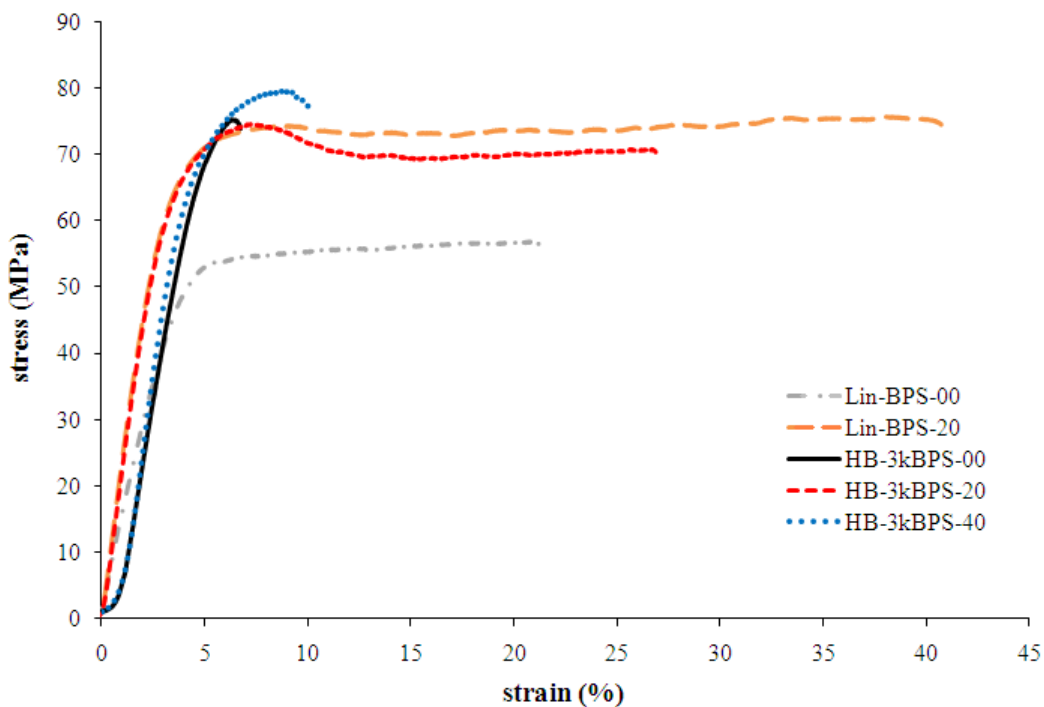


Figure 2.9: Comparison of stress–strain behavior for linear and highly branched polysulfones (A_2 $\overline{M}_n = 3\,000$ g/mol) with varied degrees of sulfonation as indicated

detected elastic region is sufficient for the typical range of strain experienced during IPT actuation.

Thermal stability of linear and branched polymers was established with TGA in N₂ at 10 °C/min as summarized in Table 2.5. Nonsulfonated polysulfones are thermally stable up to a 5 % weight loss temperature ($T_{d,5\%}$) of approximately 500 °C and experience a single degradation step that leads to significant char yield typical of highly aromatic polymers. Introduction of the TFPPO branch unit and adjustment of the molecular weight between branch points does not significantly affect the maximum thermal stability of the series. Linear and branched ionomers in the sodium sulfonate form display high thermal stability (> 450 °C), although increased degree of sulfonation typically decreases the $T_{d,5\%}$. Figure 2.10 depicts an example of this trend with the weight % versus temperature curves for the HB-3kBPS series. Despite this decrease, the lowest recorded $T_{d,5\%}$ for all polymers was 458 °C for HB-3kBPS-40. Initial weight loss is due to degradation of the sodium sulfonate groups. This assignment fits the trend although the initial step overlaps the final degradation of the polymer backbone at high temperature and was not quantitatively resolved based on degree of sulfonation. Dynamic investigation of thermal stability for the series in air demonstrated a regular decrease in the $T_{d,5\%}$ of approximately 25 °C with a corresponding decrease of 50 % in the char yield.

Table 2.4: Stress – strain properties for polysulfones as a function of topology and degree of sulfonation

sample	modulus (GPa)	ultimate tensile strength (MPa)	elongation at break (%)
Lin-BPS-00	1.40 ± 0.13	56.0 ± 4.6	22.0 ± 3.7
Lin-BPS-20	2.18 ± 0.33	73.1 ± 3.2	43.7 ± 6.9
Lin-BPS-40	n/a	n/a	n/a
HB-3kBPS-00	2.08 ± 0.28	78.8 ± 9.2	6.9 ± 1.2
HB-3kBPS-20	2.37 ± 0.29	80.2 ± 9.7	22.9 ± 9.5
HB-3kBPS-40	2.44 ± 0.08	74.3 ± 5.5	10.3 ± 4.2

Table 2.5: Thermal transition temperatures for the series of linear and branched polysulfones measured with DSC, DMA, and TGA

Sample	T_g	T_α	T_β	$T_{d\ 5\%}$
	[DSC] ^{a)}	[DMA] ^{b)}	[DMA] ^{b)}	[TGA] ^{c)}
	(°C)	(°C)	(°C)	(°C)
HB-3kBPS-00	230	---	242	518
HB-3kBPS-20	255	277	246	482
HB-3kBPS-40	298	312	259	458
HB-5kBPS-00	230	---	244	516
HB-5kBPS-20	254	280	255	489
HB-5kBPS-40	322	n/a	n/a	479
HB-10kBPS-00	229	---	245	493
HB-10kBPS-20	241	261	228	479
HB-10kBPS-40	327	n/a	n/a	465
Lin-BPS-00	235	---	245	512
Lin-BPS-20	271	280	243	480
Lin-BPS-40	311	359	231	485

a) based on deriv. heat flow (W/g/°C), second heat, 20 °C/min

b) loss modulus signal, 5 °C/min, 1 Hz

c) temperature associated with 5 % weight loss, 10 °C/min

Thermal transitions and thermomechanical behavior were investigated with DSC and DMA respectively. The results are summarized in Table 2.5 for all synthesized polymers. Glass transition temperatures (T_g) were detected for the entire polymer series with DSC based on peaks in the derivative heat flow (W/g/°C) of the second heat cycle. T_g remained relatively consistent despite changes in polymer topology. However, increased ionic content resulted in higher T_g values of approximately 2 °C for each 1 % disulfonation of the polymer. A resolvable β -transition was not detected with DSC between 25–350 °C for any ionomer in the series. DMA experiments were performed for all samples that formed tough, ductile films. Narrow molecular weight distributions and low \overline{M}_w values for HB-5kBPS-40 and HB-10kBPS-40 did not allow formation of free-standing membranes. The storage modulus (E'), loss modulus (E''), and $\tan \delta$ versus temperature curves for the polymers in the HB-3kBPS series are shown in Figure 2.11. α -

transitions detected in the loss modulus (E'') signal with DMA (also present in $\tan \delta$) were an average of 19 °C higher than those determined from derivative heat flow measurements with DSC. The nonsulfonated polysulfones displayed a single transition in the E'' signal at approximately 245 °C. Introduction of sulfonation into the polymer significantly raised the α -transition to >300 °C for samples with 40 mol % disulfonation. A β -transition occurred only in sulfonated polymers and appeared as a low temperature shoulder overlapping the α -transition in the E'' and $\tan \delta$ signals at approximately 244 °C for the full series of ionomers. A third peak at ~146 °C (average) regularly appeared in temperature sweeps of the ionomers. However, the area under this peak and the peak temperature varied with the degree of sulfonation and annealing. Due to this variability, the transition's proximity to 100 °C, the minimal appearance in $\tan \delta$ and realization of these high temperature experiments in air the peak was assigned to the loss of free water from the membrane. Further scans of dry samples run under a N₂ purge (Section 4.3.1.2) displayed a further decrease in the peak temperature and area, supporting this assignment.

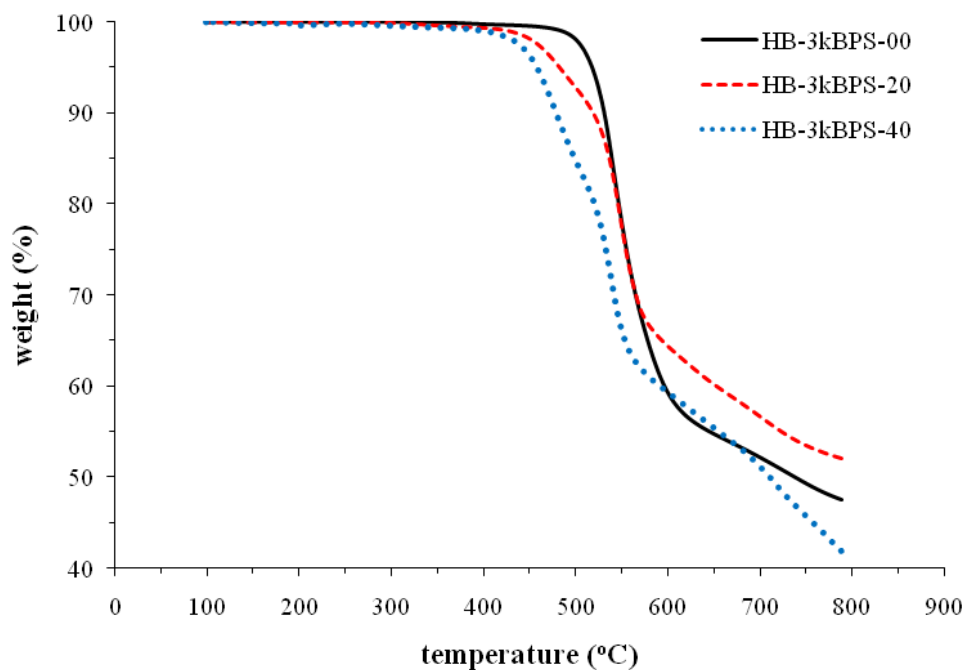


Figure 2.10: TGA for thermal stability of highly branched polysulfones ($A_2 \overline{M}_n = 3\,000$ g/mol) with various degrees of sulfonation as indicated (N₂, 10 °C/min)

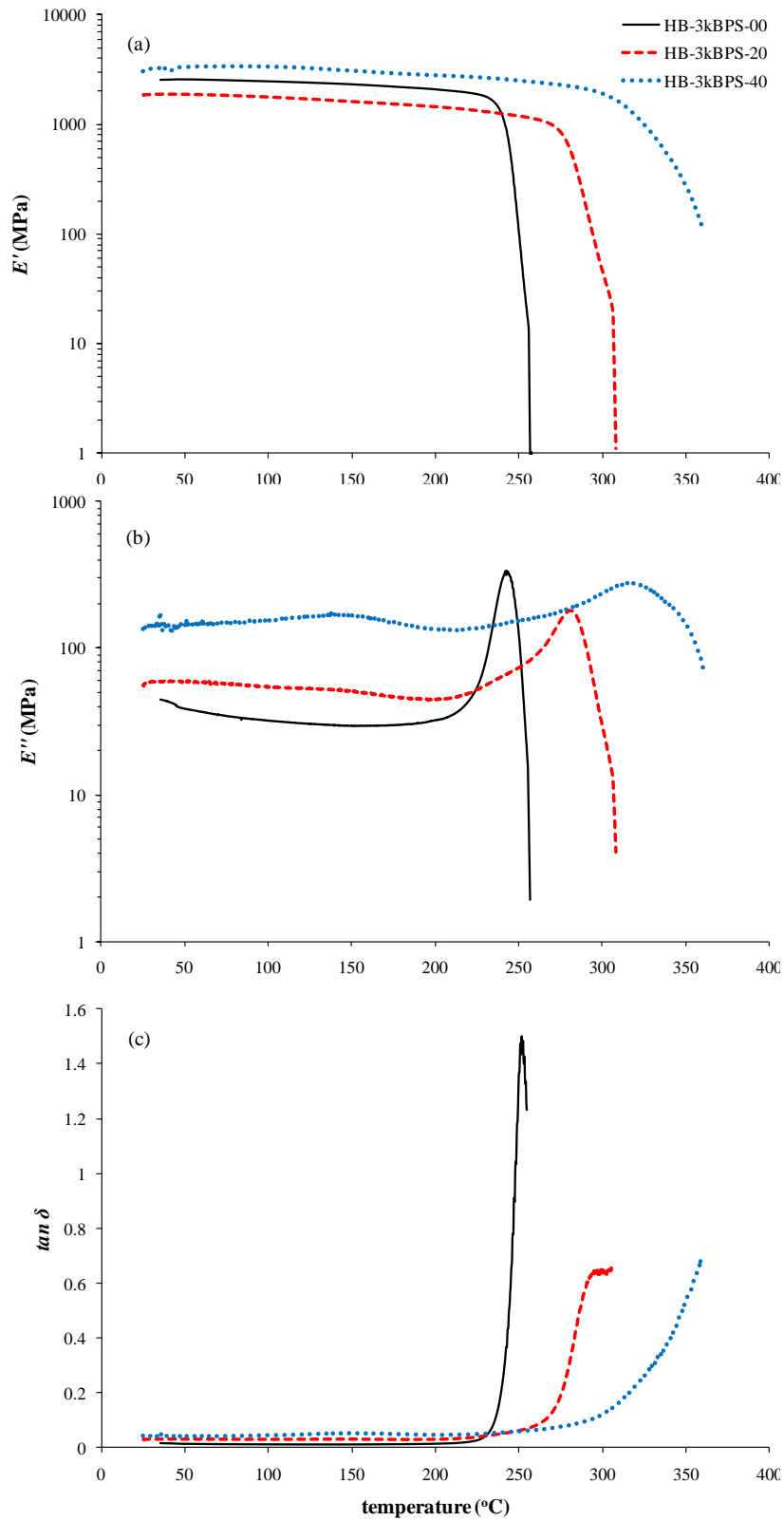


Figure 2.11: (a) E' (b) E'' (c) $\tan \delta$ versus temperature for highly branched polysulfones ($A_2 \overline{M}_n = 3000$ g/mol) of varied degrees of sulfonation as indicated (5 °C/min, 1 Hz)

The consistency and slight increases of the β -transition in DMA due to higher sulfonation suggests that it is actually the glass transition temperature of the non-sulfonated polymer matrix ($T_{g,m}$). Also, the peak for the non-sulfonated samples aligns well in temperature with the shoulders (β -transition) that appear in the ionomer samples. Association and microphase separation of ionic functional groups from the bulk polymer matrix is commonly observed in ionomers and is often referred to as a cluster morphology.[48] Groupings based on ionic association vary in population from isolation in the bulk to multiplets, aggregates, and clusters that display their own disassociation temperature ($T_{g,cl}$). For the present series of linear and branched sulfonated polysulfones the average difference between $T_{g,m}$ and the α -transition is 51 °C. However, the α -transition consistently displays large shifts to higher temperature due to increased levels of sulfonation. This trend combined with the constant values of $T_{g,m}$ resulted in assignment of the α -transition to disassociation of sodium sulfonate ionic aggregates. This assignment makes further sense due to the fact that these sulfonated polysulfones do not demonstrate the typically wide rubbery plateau associated with DMA of most ionomers where $T_{g,m}$ precedes $T_{g,cl}$ by a large temperature difference.[49] Flow is detected for all temperatures above the α -transition in DMA (e.g. E') and increased sulfonation decreases the slope of the curve after $T_{g,cl}$, likely due to the increased population of ionic associations continuing to act as a dynamic network of effective crosslinks which retards the rate of change of the modulus.[225]

As shown in Table 2.6 for these amorphous polysulfones, the E' and E'' measured with DMA (35 °C) increase based on the presence of sulfonation in the backbone. The DB introduced with the oligomeric $A_2 + B_3$ strategy does not have a traceable effect on modulus values in comparison to changes that result from variation in the degree of sulfonation. This trend from dynamic testing is different than the results from tensile testing that displayed a definite increase in modulus of the linear polymers due to sulfonation. However, at 35 °C, the full series of polymer films display a storage modulus of at least 1 GPa, similar to the values found with tensile testing. Ionomers benefit from the ionic associations that act as physical crosslinks to increase both E' and E'' with greater ionic content; here to a maximum of approximately 3.2 GPa and 0.14 GPa respectively. These modulus values for membranes in the dry state are advantageous for IPT design where higher degrees of sulfonation will likely provide greater hydrated modulus simultaneous with augmented ionic conductivity.

Table 2.6: Storage and loss moduli for the series of linear and branched polysulfones

Sample	E' [DMA] ^{a)} (MPa)	E'' [DMA] ^{b)} (MPa)
HB-3kBPS-00	2 600	40
HB-3kBPS-20	1 900	60
HB-3kBPS-40	3 200	140
HB-5kBPS-00	1 900	50
HB-5kBPS-20	2 200	100
HB-5kBPS-40	---	---
HB-10kBPS-00	800	30
HB-10kBPS-20	1 300	60
HB-10kBPS-40	---	---
Lin-BPS-00	1 700	20
Lin-BPS-20	2 700	110
Lin-BPS-40	1 500	60

b) storage modulus signal, 35 °C

b) loss modulus signal, 35 °C

2.3.2.3 *Small-angle X-ray scattering for morphological investigation*

Due to the charge-transport based performance of IPTs, verification of a pathway for charge movement through the membrane is essential. Sulfonated polysulfones in this case were designed to contain targeted amounts of bound anions that previously were shown to cause phase separation in the presence of a hydrophobic matrix of the base polymer.[226] Differences in polarity between the sulfonate salts and the aromatic backbone of the polysulfone aid phase separation to form hydrophilic domains that contain physical crosslinks. These crosslinks are bound through electrostatic dipole-dipole interactions between the sulfonate salts. Association of three to four sulfonate pairs constitutes a multiplet. When these multiplets further aggregate they create features termed ionic aggregates or clusters. Some groups proposed that the clusters contain a small fraction of backbone material and are surrounded with a hard shell of uncharged

polymer backbone that has limited mobility based on covalent bonds to the bound ions.[45] This phase separation creates regions of varied electron density based on the presence or absence of the free cations. In this case Na^+ , in comparison to the surrounding polymer matrix, provides sufficient contrast in electron density for scattering characterization when bombarded with X-rays. Initial characterization of sBPS with SAXS at the U.S. Army Research Laboratory displayed small scattering intensities that required long exposure times to acquire sufficient data for analysis. Those results are found in Appendix B including analysis of both the nonsulfonated and sulfonated (Na^+ and H^+) BPS. The scattering results discussed here were obtained by Jong Keun Park and Dr. Robert B. Moore during beamtime at the Brookhaven National Laboratory on the Advanced Polymer Beamline (X27C) at the National Synchrotron Light Source.

The 2-D scattering profiles for sBPS ionomers of the series that contain 20 mol % disulfonation are presented in Figure 2.12. On initial inspection the profile features are fit with peaks that represent adjacent hard spherical domains that scatter the incident X-rays. The distance between the centers of the scattering domains is termed d as is determined from Bragg's Law in relation to the scattering vector, q , and the scattering angle, θ (Equation 2.8). There are two distinct peaks in each scattering profile shown in Figure 2.12. A minor peak of lower intensity and width appears at higher values of q ($0.2 - 0.3 \text{ \AA}^{-1}$) and is present due to the use of Kapton in the background for the experimental setup. The peak of greater intensity and width that appears at lower values of q is typically referred to as the ionomer peak for analysis of charged polymers. The appearance of this profile characteristic confirms the presence of hydrophilic / hydrophobic phase separation into clustered domains of sulfonated salts organized through electrostatic associations in sBPS. The ionomer peak varies in breadth and appears in a range of q just below a value of 0.1 \AA^{-1} that corresponds to a domain spacing of approximately 6–10 nm. These values are consistent with the literature for ionic clusters found in other statistically random ionomers.[227-229] The results of peak fitting to estimate domain sizes for the sBPS series are shown in Table 2.7.

For the series of 20 mol % sBPS the introduction of branching into the polymer backbone has a significant effect on the scattering profile. Lin-BPS-20 displays a very broad peak/shoulder in the SAXS profile that indicates a wide range of distances between scattering centers (i.e. clusters) and a peak value of 9.79 nm. The branched ionomers with 3 000 – 10 000 g/mol oligomeric spacers display sharper peaks in the SAXS profile, especially in the case of HB-

5kBPS-20. The peaks for the branched ionomers are also shifted to higher q values indicating a decreased Bragg spacing to an average of 7.51 nm. Narrower peaks indicate a smaller distribution of cluster sizes which may originate with increased mobility of the bound charges on polymer branches as compared to those on the linear macromolecules. The ability to more efficiently organize based on polar functionality combined with polymer topology may also explain the decreased cluster size. Decreased A_2 oligomer molecular weight for the branched series does appear to cause a slight increase in cluster spacing, however an increased number of samples would be necessary to fully confirm this trend due to the small differences between members of the series.

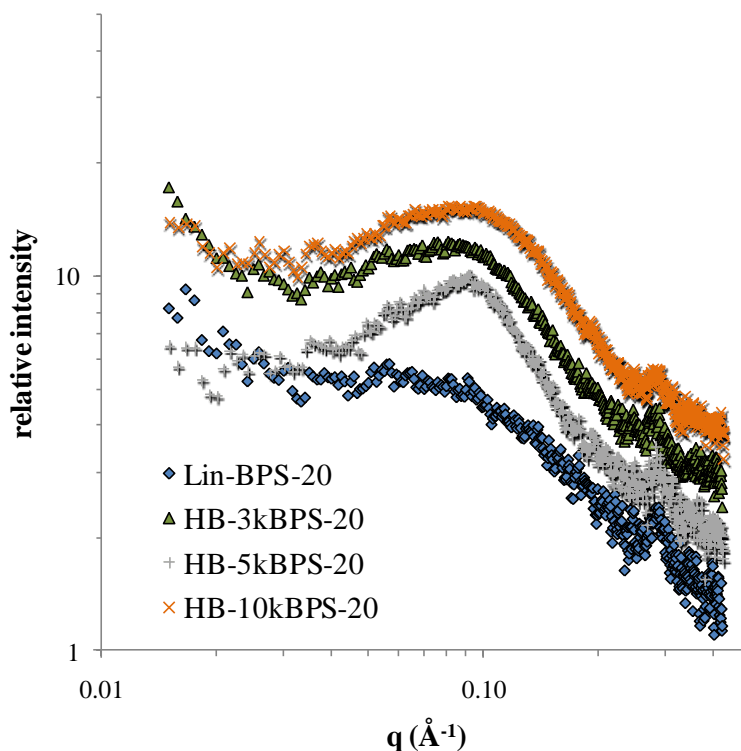


Figure 2.12: 2-D SAXS profiles for comparison of linear versus branched sBPS membranes containing 20 % disulfonation

Increased mobility due to the entropy associated with chain ends may allow for better organization of the sulfonated repeat units near those ends into hydrophilic clusters within the local polymer volume during membrane formation. Tsang *et al.* observed this effect through a comparison of P(VDF-*co*-HFP)-*b*-SPS ionomers where the SPS was either designated as a block or a series of grafts.[230] The ionic block copolymers organized into a lamellar morphology

while the graft copolymers formed an interconnected cluster morphology. Saito *et al.* also noted that polymer architecture significantly affected the ability of sulfonated acrylic graft copolymers to form aggregates.[202] Ionomers with sulfonated blocks near the graft point did not form detectable aggregates based on the charge content. However, when the sulfonated blocks were located at the graft end increased mobility allowed for ionic aggregation within the existing lamellar morphology (primary morphological structure). Although Nafion[®] only contains a single sulfonate per branch, the location of the anion at the branch terminus similar to Saito's study has also been highlighted for its affect on the efficient formation of ionic aggregates.[7] Finally, Asano *et al.* noted that the introduction of low degrees of branching to sulfonated polyimides decreased the distribution of and distance between ionic domains in comparison to linear analogues.[200] Consequently branching appeared to increase connectivity which resulted in higher ionic conductivity. Asano's study synthesized random ionomers similar to the random sBPS copolymer series investigated here. Random distribution of the charged functionalities along the branch lengths appears to contribute to that connectivity where SAXS indicates that the distances between scattering centers are decreased.

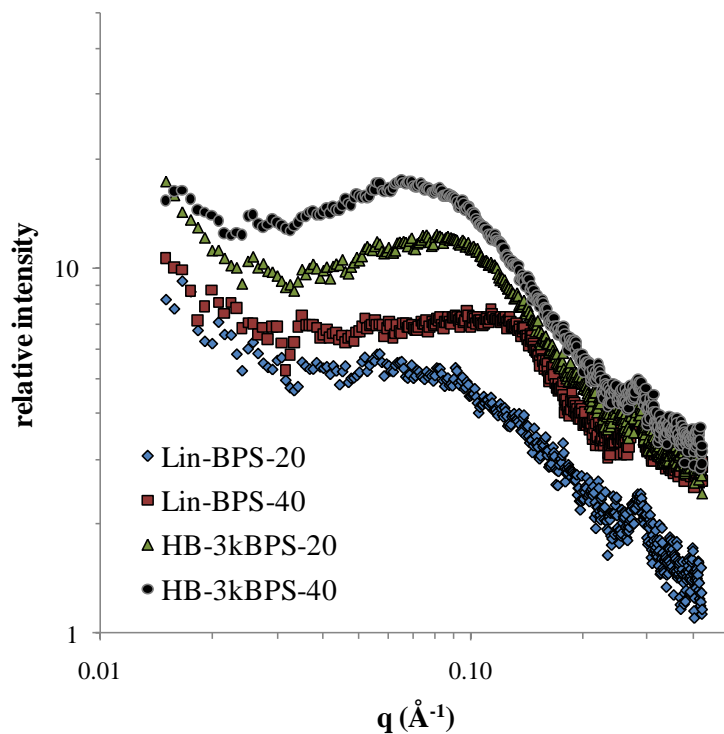


Figure 2.13: 2-D SAXS profiles for comparison of linear versus branched sBPS membranes containing 20 % or 40 % disulfonation

Figure 2.13 displays the comparison between scattering profiles of sBPS ionomers that vary both in degree of sulfonation as well as polymer topology. In this case, the degree of sulfonation is the distinguishing factor for the effect of topology on the phase-separated morphology. For 20 mol % sulfonated samples, as previously discussed, introduction of branching narrows the ionomer peak and shifts it to higher q . sBPS containing 40 mol % sulfonation displays the opposite trend, where the ionomer peak for the linear sample displays a higher q value than the branched sample. HB-3kBPS-40 demonstrates a primary Bragg spacing 157 % larger than Lin-BPS-40. Notably, the peak is still very broad in comparison to the branched sample. These opposing trends suggest that the effect of an increased population of sulfonated repeat units on the cluster morphology is very different for varied polymer topologies. Increased sulfonation was already identified as a determining factor in the development of branching and molecular weight for the oligomeric $A_2 + B_3$ reaction. The present SAXS studies confirm that these two variables also interact during phase separation to influence the morphology of the charge transport network that will enable application of these sBPS membranes in IPTs.

Table 2.7: Scattering vector positions and corresponding Bragg spacings for the ionomer peak present in SAXS analysis of linear and branched polysulfones

sample	peak position, q (\AA^{-1})	Bragg spacing, d (nm)
Lin-BPS-20	0.064	9.79
Lin-BPS-40	0.107	5.86
HB-3kBPS-20	0.080	7.86
HB-3kBPS-40	0.068	9.20
HB-5kBPS-20	0.085	7.40
HB-10kBPS-20	0.086	7.27

2.4 Summary

Highly branched poly(arylene ether sulfone)s of varied ionic content were successfully synthesized through an oligomeric $A_2 + B_3$ method without gelation. The synthesis of A_2 oligomers with targeted \overline{M}_n provided the ability to control the DB_{global} in branched polymers with otherwise identical $DB_{\text{Fréchet}}$. Variation in the percent sulfonation of the controlled molecular

weight A_2 oligomers revealed a significant effect of ionic content on the extent of conversion of the $A_2 + B_3$ branching reaction and development of high molecular weight; likely due to a kinetic excluded volume effect augmented by electrostatic interactions. Characterization of molecular weight distributions and DB_{global} indicated topologies that ranged from moderately branched (e.g. HB-3kBPS) to slightly branched (e.g. HB-10kBPS) when compared to the linear controls. The identified molecular weights were indicative of the film forming capabilities of the sBPS series and resulted in high modulus membranes with sufficient tensile elongation for the chosen application. Higher degrees of sulfonation resulted in large increases in $T_{g,cl}$, E' , and E'' with minor decreases in thermal stability. Investigation into the effect of branching on the thermal and mechanical properties revealed that the achieved DB_{global} displayed a more subtle effect on thermal transitions, E' , and E'' than the overall degree of sulfonation. However, the changes in DB_{global} provided a topologically discreet series of polymers whose thermal and mechanical properties were comparable to their linear analogues. The effects of polymer topology and the degree of sulfonation were both significant contributors to the development of a hydrophilic / hydrophobic phase separated morphology. Such a series now enables fundamental investigation into the effect of polymer topology on the interaction of the ionomer with IPT components and the performance of the resultant IPTs.

Chapter 3 INVESTIGATION OF THE IONOMER – CONDUCTOR INTERFACE IN SBPS ELECTRODES AND TRANSDUCERS

*This chapter is primarily derived from and expanded upon: [121] Duncan A J, Sarles S A, Leo D J, Long T E, Akle B J and Bennett M D 2008 Optimization of active electrodes for novel ionomer-based ionic polymer transducers *Proceedings of SPIE-The International Society for Optical Engineering* **6927** 69271Q/69271-69271Q/69212

As well as: [231] Duncan A J, Long T E and Leo D J 2009 Design for optimized electromechanical transduction in ionic polymer transducers fabricated with architecturally controlled ionomers *Proceedings of ASME: Conference on Smart Materials, Adaptive Structures and Intelligent Systems* **2 1-9

3.1 Motivation

Other than the single study involving sPAES and sPATS by Wiles *et al.*, [108] nearly every investigation for development of the ionomer-conductor interface has been performed with commercial perfluorosulfonate ionomers and the impregnation-reduction process. [23, 44] The studies reviewed in Chapter 1 of novel ionomers synthesized for application in IPTs exclusively employed the IRP method. Even hybrid transducers with carbon nanotubes dispersed in a matrix of the ionomer were typically electroded with the IRP method after formation. [90, 91] This trend in development is partially due to the fact that most IPT research presently employs water as the diluent, which coincides well with the electroless plating process of the IRP method. Also, the IRP method is well-established and proven in both the fuel cell and IPMC literature despite a few associated limitations. [43] Delamination of the metal electrodes due to solvent electrolysis and blistering is a common difficulty, although it is decreased when the IPT is submersed in a diluent reservoir and avoided below the diluent electrolytic limit. Electrode wear is primarily in the form of cracking and flaking on the microscopic level, increasing the resistance of the electrodes while

forming telltale discolorations on the surface of the transducer. Increased surface resistance decreases the efficient application of the input voltage down the length of the IPT. Breakdown of a constant electric field applied through the thickness of the transducer then reduces the driving force for actuation. Use of metals with the IRP method also increases the tendency for further oxidation and reduction of species on the surface and at the interface with the ionomer, which increases stiffness and at times decreases capacitance which has been directly linked to actuator performance.[47, 54] Deposition of those metals is also dependent on diffusion of the specific metal salts into the ionomeric membrane to exchange with the bound ions of the ionomer and then undergo reduction. This method works well with repeated cycles to form dendritic, high surface area electrodes at the surface of Nafion[®] which demonstrates very well-defined microphase separation on the basis of the charged functional groups that participate in the exchange. Formation of the IRP electrodes on ionomeric membranes with compositions that do not microphase separate as distinctly as Nafion[®] typically require much larger IEC values to facilitate sufficient deposition.

Recent development of the direct application process (DAP) extended the number of available techniques for producing IPT electrodes.[60] The DAP method allows for the use of nearly any ionomer, conducting particle, and diluent combination to form electrodes where the conducting particles are dispersed in a matrix of the diluent-swollen ionomer. This geometry maximizes the interfacial area between the conductor and the ionomer to allow for compositional tuning around the percolation threshold of the conducting particle. The DAP method also enables control of the thickness of the electrodes. In combination with the use of soluble ionomers, this characteristic allows tailoring for dimensions of all three layers within the IPT. Tuning of the thicknesses within the trimorph structure provides the opportunity to minimize the thickness of the central layer, which primarily serves for charge transport and equilibration of the distributions that develop out from the electric double layer at the ionomer–conductor interface in the electrodes. The electrodes are the active volume within the IPT that manifests transduction. Use of the DAP allows for increases to this active volume without the addition of further passive metal as in the IRP method. Also, incorporation of the base ionomer into the DAP electrodes increases compositional homogeneity and adhesion between the layers to aid processing and prevent delamination at high strains and extended lifetimes.

Stand-alone electrodes and a corresponding series of complete IPTs were fabricated with varied loadings of RuO₂ in the electrodes. The DAP method specifically enabled the investigation of well-defined changes in the electrodes at the interface of the conducting particles with the ionomeric matrix. Model stand-alone electrodes were evaluated in the absence of the macroscopic interface with the central ionomer membrane. The DAP method was modified to allow production of RuO₂ containing electrodes with these soluble ionomers and a defined content of ionic liquid diluent. Although many different ionomers have been investigated as membranes for these transducers, we believe these are the first IPTs reported where the trimorph structure is 100 % fabricated with a novel ionomer using the DAP method. This chapter also includes the first report of novel IPTs constructed to operate with ionic liquids as the diluent. Isolated electrodes and IPTs were characterized for their electrical properties with through-thickness electrical impedance spectroscopy (EIS) to provide estimations of charge transport in the primary dimension employed for actuation. The impedance results were fit with an equivalent electrical circuit model that provided estimations of the component electrical parameters. A method was also developed with analysis of the impedance data to allow for estimation of an effective capacitance of the device. Variation in the volumetric ratio of the ionomer and conductor revealed a percolation threshold that was reflected in both ionic conductivity and electrical capacitance. The built IPTs were also characterized for bending actuation in response to step voltage inputs. Post-actuation, the IPTs were examined with SEM to observe the cross-sections and verify the targeted dimensions based on the DAP method.

3.2 Experimental materials and methods

3.2.1 Materials

The ionomer chosen to serve as the electrode matrix and central membrane for fabrication of the isolated electrodes and IPTs was HB-3kBPS-20. The chemical structure of this soluble highly branched ionomer is provided in Figure 3.1a. Due to the synthetic strategy described in Chapter 2, this ionomer contains ~3 000 g/mol chains between phosphine oxide branch points. 20 mol % of the repeat units in the backbone contain disulfonated monomers in the Na⁺ salt form that provide an IEC (sBPS = 0.84 mequiv/g) comparable to Nafion[®] (sBPS = 0.91 mequiv/g).

The ionic liquid, 1-ethyl-3-methylimidazolium trifluoromethanesulfonate (EMI-Tf) (Merck, high purity), was used as received for the diluent electrolyte during IPT fabrication and testing. The chemical structure of EMI-Tf is shown in Figure 3.1b.

RuO_2 (Alfa Aesar, $\geq 99\%$ anhydrous) was used as received for construction of the electrodes in a similar manner to the DAP method. These high surface area conducting particles allow for more flexibility in processing and enabled the construction of well-defined electrodes with varying volumetric ratios of the conductor to the ionomeric matrix. Several layers of gold leaf (~ 100 nm) served as the surface electrode for the purpose of lowering the surface resistance of the device.

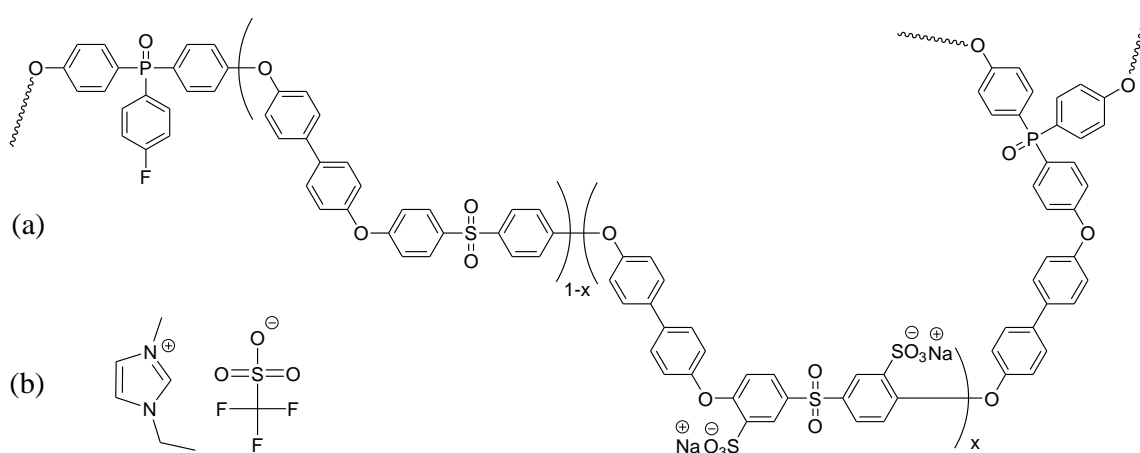


Figure 3.1: Chemical structures for (a) HB-3kBPS-20 and (b) EMI-Tf

3.2.2 Electrode and transducer fabrication

Fabrication of stand-alone electrodes and analogous IPTs employed in this study was carried out based on a modified version of the DAP method. Membrane and electrode casting allowed for similar conditions to be applied during fabrication of all layer components of the IPT device. A casting technique was also better suited for targeted uptake of defined amounts of ionic liquid into the ionomeric membrane. Calculation of the necessary amount of dry ionomer was based on the desired volume (electrode or central membrane), volumetric ratio with RuO_2 , and estimated polymer density (1.29 g/cc, Radel). All electrodes and ionomeric membranes began with HB-3kBPS-20 dissolved at 5 wt % in dimethylacetamide (DMAc) in glass vials. EMI-Tf was then added to the solution based on the desired final uptake of ionic liquid (75 wt % for all samples)

in the dry, cast membrane. RuO₂ was weighed out for the dispersions according to its reported density (6.96 g/cc) to provide electrodes with volumetric loadings of conducting particles from 0 – 45 vol %. The volume of RuO₂ in each fabricated electrode was kept constant while the volume of ionomer was varied to produce the target volumetric ratios. Membrane solutions and electrode dispersions were stirred for 12 h at 25 °C with a magnetic stir-bar at 200 rpm. Immediately prior to casting, the solutions and dispersions were sonicated for 5 min and stirred for 10 min at 400 rpm in alternating steps for 1 h followed by a continuous sonication step for 30 min.

Kapton film was chosen to construct rectangular casting molds (w = 16 mm, l = 36 mm, h = 10 mm) due to its flexibility and low surface energy in comparison to typical polysulfones. The casting molds were sealed with silicone rubber and secured to a level glass plate during the fabrication process to reduce thickness variation in the resulting films and electrodes. The solutions and dispersions were transferred to the casting molds inside a fume hood by syringe in a stepwise fashion. This layer-by-layer approach combined with the use of an initially higher temperature (~50 °C, IR heat lamp) attempted to minimize settling of the RuO₂ particles during casting. Compositions with less ionomer solution were further diluted to a constant volume of DMAc to enable the layer-by-layer process. Dispersions for the isolated electrodes contained polymer concentrations between 0.5 – 5.0 wt % where the ionomer concentration decreased as the target RuO₂ content increased. Similar preparation applied to the electrodes for the built IPTs, although the polymer concentration range was between 3.0 – 5.0 wt %. Central membranes for the IPTs were also cast in Kapton molds, although in a single step instead of the layer-by-layer approach used for the electrodes. After distribution of the dispersions to the molds over 1 h at higher temperature, the membranes and electrodes were allowed to dry for 12 h at ~35 °C in the fume hood while under a ventilated glass cover. All films were further dried *in vacuo* during a 1.5 h ramp from 25 – 140 °C, 0.5 h hold at 140 °C, and a 12 h ramp from 140 – 25 °C. The Kapton casting substrates were peeled away from the dried films before melt processing.

Prior to application of gold leaf to the stand-alone electrodes or IPTs, a single thin layer of HB-3kBPS-20 / EMI-Tf solution (0 % RuO₂) was painted on the outside surfaces of the DAP electrodes. This layer was allowed to dry under the IR lamp in the fume hood at ~35 °C for 1 h to facilitate the removal of DMAc. Stand-alone electrodes were fabricated by melt-pressing three layers of gold leaf (Falcon Brand, t ≈ 100 nm) onto both surfaces of the cast DAP electrode

films. Pressing conditions were 150 °C, 4 MPa (~600 psi), and 20 s for each layer of gold leaf applied. The fabricated electrode was then cut into 1 cm² samples for testing. Thicknesses of the stand-alone electrodes ranged between 0.12 – 0.26 mm. Electrodes for the full IPTs were cast in a single sheet that was cut in half before fabrication of the transducer. The electrodes were melt-pressed onto both sides of the central ionomeric membrane before further melt pressing to apply the outer layers of gold leaf. Melt-pressing conditions were the same as those for the stand-alone electrodes. The fabricated IPT was then cut into 3 mm x 30 mm samples for testing. Thicknesses of the IPTs were in the range between 0.19 – 0.45 mm.

3.2.3 Electrical impedance spectroscopy

Electrical properties of the cast HB-3kBPS-20 / EMI-Tf films, stand-alone electrodes, and built IPTs were characterized with EIS using an Autolab PGSTAT12 Potentiostat/Galvanostat with FRA2 Impedance Module for a frequency range of 1 MHz – 0.1 Hz and an HP-4192A Impedance Analyzer from 15 MHz – 100 Hz. Both instruments were operated to test from high frequency to low frequency in potentiostatic mode to apply a single 100 mV rms sine wave while calculating the complex impedance response of the sample based on measured current. A custom fixture with conductive aluminum contacts was designed to allow for through-thickness EIS characterization of all samples. A pressure of 4 kPa (~0.6 psi) was applied from a load placed on top of the fixture to ensure consistent and constant contact between the surface of the sample and the fixture electrodes. All measurements were performed inside a custom-built Faraday cage after a minimum of 12 h equilibration in air at room temperature and relative humidity (except those labeled “dry”). Ionic conductivity values σ (S cm⁻¹) were calculated from the expression

$$\sigma = \frac{h}{R \cdot l \cdot w} \quad , \quad (3.1)$$

based on the through-thickness geometry of each sample where h (cm) is the sample thickness, l (cm) is the sample length, w (cm) is the sample width, and R (ohm) is the bulk real resistance estimated from the kinetic portion of the Nyquist plot where the imaginary impedance approaches zero.

3.2.4 Electromechanical transducer characterization

All fully fabricated IPTs were characterized for their electromechanical response based on configuration as a clamped cantilever beam (Figure 3.2). The clamped length (L_c) between two

gold electrodes was 10.45 mm, allowing for an average IPT free length (L_f) of 19.5 mm. Free displacement $\delta(t)$ (μm) of any point along the length of the transducer defined as L_f (mm) was measured with a non-contact laser vibrometer. These parameters along with the thickness t (mm) of the sample are used in

$$\varepsilon(t) = \frac{\delta(t) h}{L_f^2}, \quad (3.2)$$

to calculate the strain $\varepsilon(t)$ response in the time domain. Any prebend in the sample was angled away from the laser vibrometer to maximize the range of motion detection. The noise in the measured displacement provided by the laser vibrometer was approximately 2 μm . Voltage input signals were provided by a DSpace ControlBoard and routed through an HP 6826A power amplifier. Actuation responses in the time domain were measured as displacement resulting from step input voltages of varying magnitude (1, 1.5, 2, 2.5 V) and directionality (\pm), typically over 300 s. Strain is normalized to the full step duration as well as the applied voltage to provide the average strain rate $\dot{\varepsilon}$ (s^{-1}) and the normalized strain rate $\dot{\varepsilon}^*$ ($\text{s}^{-1}\text{V}^{-1}$).

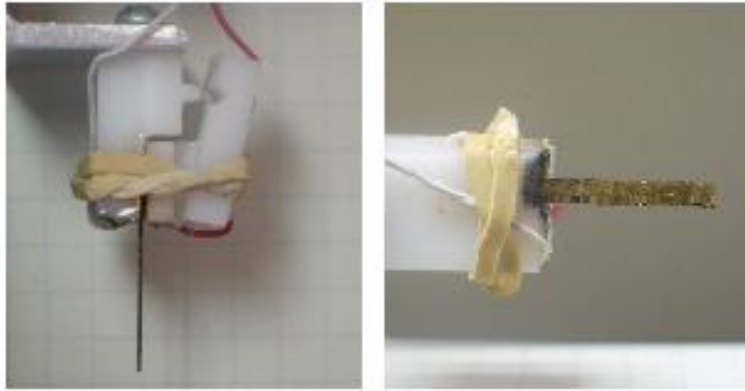


Figure 3.2: Bending actuation setup for a novel IPT fabricated from HB-3kBPS-20, EMI-Tf, and RuO_2

3.3 Results and discussion

3.3.1 Stand-alone IPT components

The initial section of this chapter concentrates on the fabrication and characterization of samples representative of the individual components of the ionic polymer transducer. Central ionomeric

membranes were cast in the presence of EMI-Tf to take advantage of the ionic liquid's near-zero volatility and provide direct control over uptake. During solvent evaporation (DMAc), the swollen membranes displayed a distinct opacity as compared to the transparency of the sample with zero EMI-Tf uptake. The change in transparency is likely due to microscopic heterogeneities formed during casting (ref. Ch. 4). Drying conditions for the swollen membranes were established by detection of the plasticized glass transition temperature (T_g) with differential scanning calorimetry (DSC). DSC results indicated a significant decrease in the T_g from the neat value of 255 °C (0 wt % uptake, Ch. 2) for HB-3kBPS-20 to 132 °C for uptake of 4.9 mol EMI-Tf / mol SO_3^- . Thermogravimetric analysis (TGA) was used to confirm the removal of free-water from the samples after drying at 140 °C. The same drying conditions were applied for all further electrode and IPT samples based on this ratio of ionomer to ionic liquid. The ionic liquid-swollen ionomer was first characterized for ionic conductivity as a function of diluent uptake. A full study of the casting method with four sBPS ionomeric membranes formed in the presence of varied uptakes of EMI-Tf follows in Chapter 4.

From these results, the cast HB-3kBPS-20 sample with an uptake of 4.9 mol EMI-Tf / mol SO_3^- was used for all further studies. Construction of stand-alone electrodes was performed to isolate and investigate the effects of specific changes in the composition of the IPT active area. Volumetric RuO_2 content was varied from 7.5 – 70 %, although only compositions up to 45 vol % are reported here. Electrodes with greater than 45 vol % RuO_2 were successfully cast but were too fragile for accurate impedance testing or subsequent fabrication of IPTs. Without the contribution of the central ionomer membrane, through-thickness EIS was performed in the absence of the two macroscopic interfaces inherent to the trimorph geometry. The impedance data was then fit with an equivalent circuit model to estimate contributions of the electrode components to the overall electrical properties.

3.3.1.1 Electrical impedance spectroscopy

EIS was performed through the thickness of EMI-Tf swollen HB-3kBPS-20 ionomeric membranes with different uptake levels of the ionic liquid. Although the bulk of this study concerns the DAP electrodes, it is important to establish a range of working electrical properties for the HB-3kBPS-20 ionomer since it serves as the matrix interfacing with the conducting particles. This measurement is also important to provide a baseline for the matrix conductivity

measured in the same dimension (through-thickness) as the subsequent tests for the electrodes and transducers. Ionic conductivity data as calculated from the Nyquist plot is displayed in Figure 3.3. The semi-log plot of the data displays that initial uptake of EMI-Tf results in a dramatic increase in conductivity over the neat membrane with linear increases due to further uptake of ionic liquid. Overall, through-thickness conductivity of non-electroded samples was found to underestimate the values in comparison to those established with in-plane conductivity fixtures. The lower conductivities are believed to originate with increased contact resistance associated with the fixture's electrodes. Data presented here primarily establishes trends with EMI-Tf uptake and a baseline for comparison to the other IPT components. A more thorough investigation of ionomer-ionic liquid membrane conductivity in-plane is provided in Chapter 4.

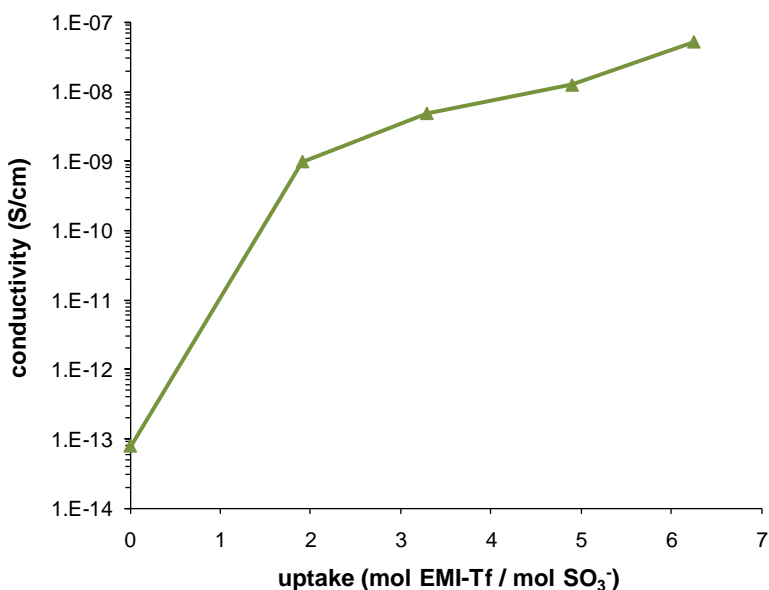


Figure 3.3: Through-thickness ionic conductivity versus molar uptake of EMI-Tf in cast HB-3kBPS-20 membranes

Construction of stand-alone IPT electrodes was performed based on a casting version of the DAP method for samples containing 0 – 45 vol % RuO₂. The ionomer to ionic liquid ratio was kept constant at an uptake of ~4.9 mol/mol while the total volume of RuO₂ was also constant. EIS was performed to provide the frequency dependence of the impedance (Figure 3.4) in the through-thickness direction. All impedance characterization was performed in this dimension of the IPT to better relate the results to existing models and theories on the relationship of free-ion charge mobility to electromechanical transduction.[47, 66, 232]

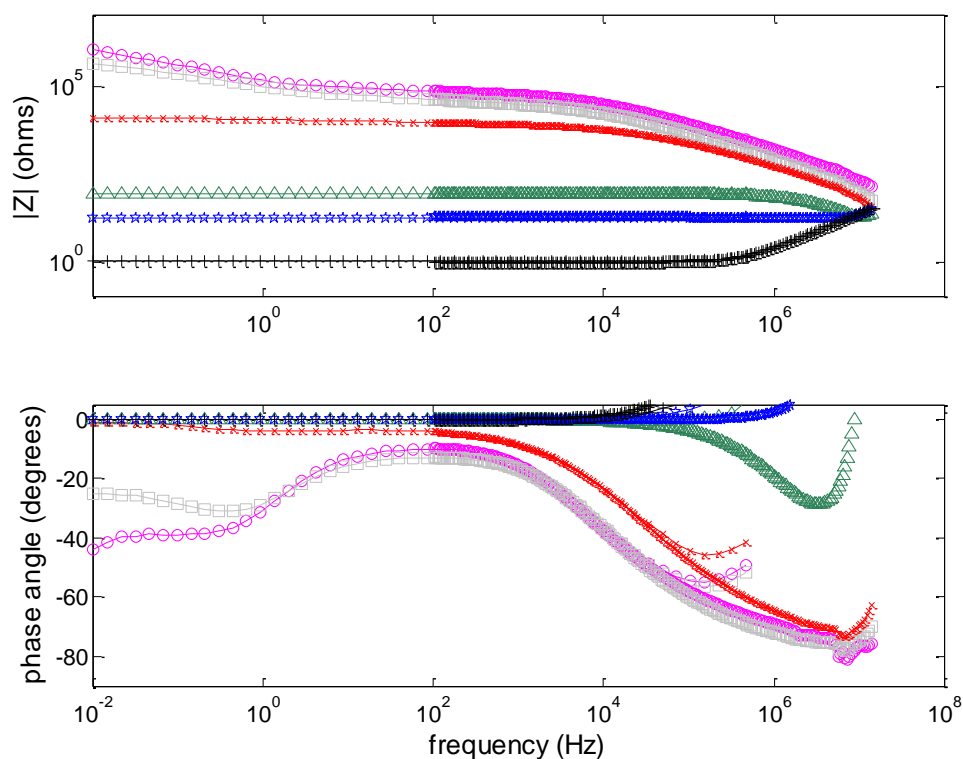


Figure 3.4: Bode plot for the impedance of stand-alone electrodes constructed with varied volumetric loading of RuO₂ (LEGEND: 7.5%, pink circle; 15%, grey square; 22.5%, red X; 30%, green triangle; 37.5%, blue star, 45%, black cross)

The magnitude of the impedance versus frequency data (Figure 3.4) for the stand-alone electrodes reveals a direct relationship between the volumetric loading of conducting RuO₂ particles in the electrode and the resistance of this IPT layer. From 7.5 – 45 vol % RuO₂ the magnitude of the impedance systematically decreases with increased loading of conducting particles. Low frequency impedance and phase data indicate a strong capacitive component in the samples with up to 15 vol % RuO₂. Phase data approaching 45° for these samples indicates that the conductivity is based on diffusion-limited mass transport at very low frequencies.[233] For this series of samples, the data at 100 Hz in the Bode plot is a good indicator of the bulk resistance of the isolated electrode in the through-thickness direction. At this frequency, samples with less than 30 vol % RuO₂ display a phase angle less than zero, indicating contribution of some capacitive component. However, for loadings of 30 vol % RuO₂ and above the phase is nearly constant at zero across the full frequency range, indicative of purely resistive behavior. This transition based on loading of conducting particles is also reflected in the large decrease in

resistance between 22.5 and 30 vol %. Percolation between the RuO₂ particles lowers total resistance to the flow of current through the electrode. As the loading of conducting particles increases, the electrode transitions from an ion-conductor to an electrical resistor.

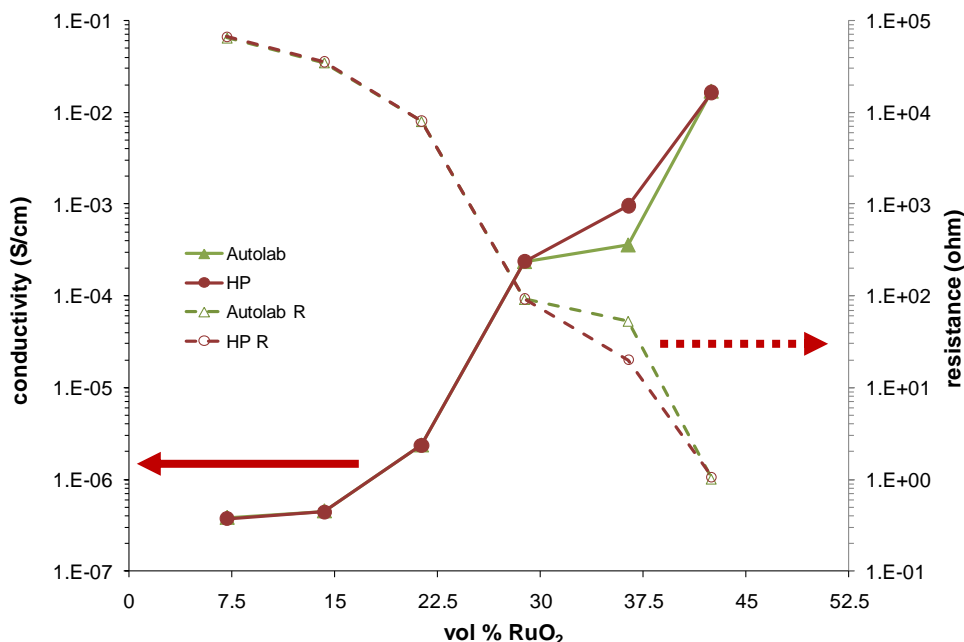


Figure 3.5: Bulk resistance and ionic conductivity versus RuO₂ loading in stand-alone electrodes as characterized with both the Autolab and HP Impedance Analyzers

The percolation behavior of the electrodes that was observed for the impedance data is also apparent in the plot of ionic conductivity versus electrode composition (Figure 3.5). Up to 22.5 vol % RuO₂ the ionic conductivity increases at most by one order of magnitude. However, between 22.5 – 30 vol % RuO₂ the ionic conductivity increases by two orders of magnitude followed by further increases up to 16.4 mS/cm at 45 vol % RuO₂. The percolation threshold in ionic conductivity for Nafion[®]–EMI-Tf–RuO₂ stand-alone electrodes was estimated to be 19 vol % by Akle *et al.*[60] Based on the change in slope between 15 – 22.5 vol % RuO₂, extrapolation places the percolation threshold of this sBPS–EMI-Tf–RuO₂ system at approximately 18 vol %. Fabrication of stand-alone electrodes with higher loadings of conducting particles was attempted but the brittle nature of the electrodes containing so little ionomer matrix caused excessive fracture that did not allow for further characterization

3.3.1.2 Equivalent electrical circuit modeling

The impedance data for the stand-alone electrodes obtained from EIS was modeled with an equivalent electrical circuit to estimate identities and magnitudes of the electrical properties associated with the materials and interfaces that compose the IPT electrode. Previous studies have identified the electrodes as the electromechanically active volume of the IPT where formation of an electric double-layer with characteristic capacitance directly correlates with peak strain in several modes of actuation.[39, 54] The chosen equivalent electrical circuit model is depicted in Figure 3.6, herein referred to as EC-1. The model is composed of a resistor (R_1) and constant phase element (CPE, Q_1) in parallel where that total unit is in series with another resistor (R_2). Q_1 is a pseudo-capacitor element whose contribution to the magnitude of the impedance is represented by the variables Y_1^0 ($S \cdot s^{n_1}$) and n_1 . As n_1 values approach unity, Q_1 equals a pure capacitor.

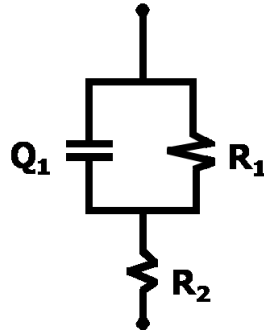


Figure 3.6: EC-1: equivalent circuit model for stand-alone electrodes

The complex impedance for EC-1 is shown in

$$Z_{EC-1}^* = \frac{R_1}{1 + R_1 Y_1^0 (i\omega)^{n_1}} + R_2 . \quad (3.3)$$

The model fit to the experimental data is accomplished by an unconstrained nonlinear optimization using the MatLab *fminsearch* function. Minimization of the error between the experimental data and model predictions is an iterative process based upon initial estimates of the model variables. Boukamp's method for weighting the error is applied based on the inverse square of the calculated complex impedance.[234] Figure 3.7 shows selections of the EIS data and model fits based on RuO_2 loading (15 – 37.5 vol %) at levels before and after percolation for the stand-alone electrodes. The fits display good agreement with the data for the frequency range

from 0.1 – 1000 Hz. Discrepancies in the fit near 1000 Hz for samples below percolation is due to the presence of a second high frequency capacitive element that is not accounted for in EC-1.

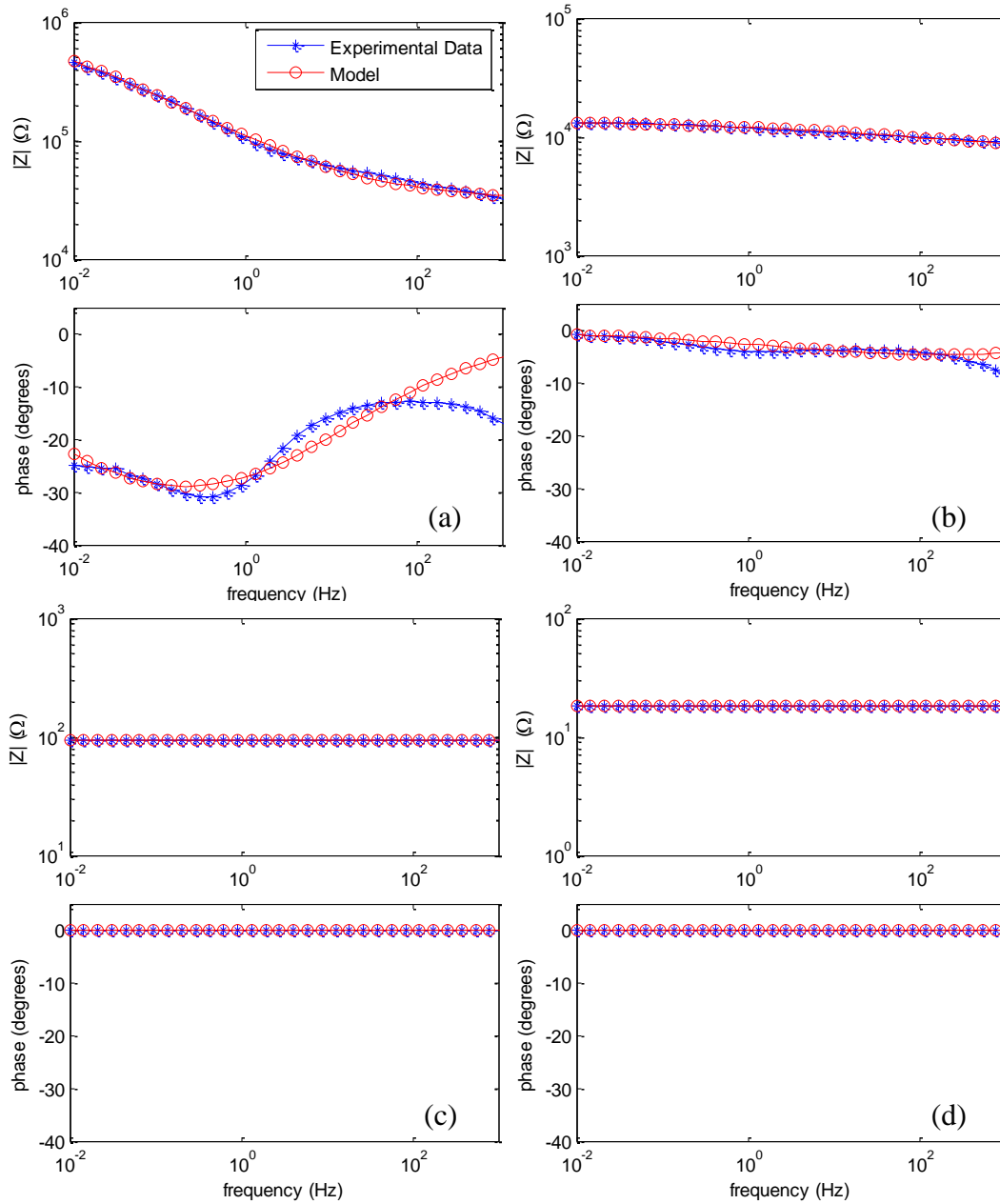


Figure 3.7: Representative fits of EC-1 to experimental EIS data for stand-alone electrodes with RuO₂ volumetric loading of (a) 15 % (b) 22.5 % (c) 30 % (d) 37.5 %

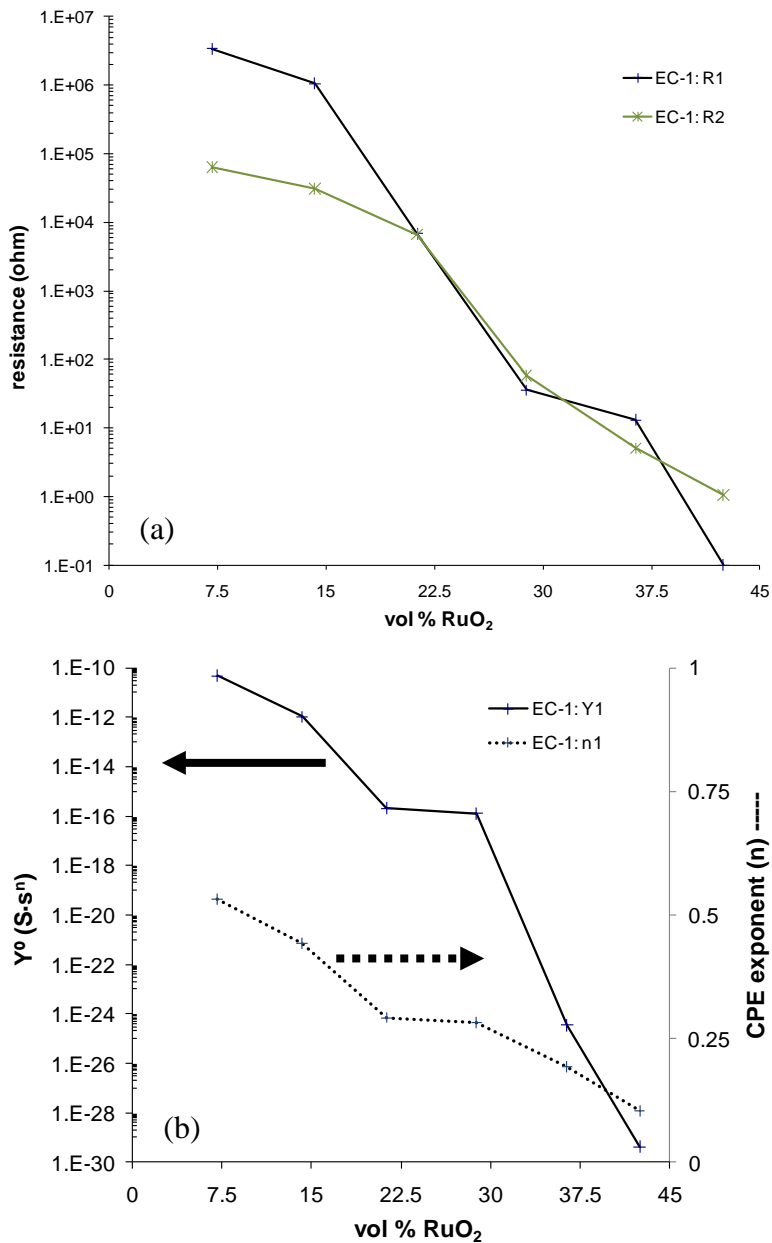


Figure 3.8: Equivalent circuit parameters for (a) resistor and (b) capacitive elements of EC-1 as determined from fits and calculations based on impedance data for stand-alone electrodes

Figure 3.8a provides the optimized values of the circuit model parameters corresponding to the best fit to the experimental data. Resistance values demonstrate a percolation similar to the trends seen in the ionic conductivity data. The trends and estimated magnitudes of R₁ and R₂

from the circuit model suggest that they represent a charge transfer resistance at the RuO₂ / HB-3kBPS-20 interface and the bulk resistance of the composite respectively. The fit values of R₁ and R₂ demonstrate an intersection within the range of RuO₂ loadings investigated. The crossover detected at 22.5 vol % shows that at lower loadings of RuO₂ the interfacial charge transfer resistance, R₁, dominates the cumulative resistance (R₁ + R₂) of the electrode. As the loading of RuO₂ increases above 22.5 %, less ionomer matrix separates the conducting particles and allows for longer electrically conducting percolation pathways to form. Under these conditions, R₂ dominates the overall resistance. The magnitude of the contribution of the ionomer – ionic liquid electrolyte to the resistance (R₂) above percolation is unclear. Although the total resistance decreases dramatically, percolation is not extensive enough at the loadings investigated to approach the resistance of a 100 % RuO₂ layer (5.33 μΩ; σ = 3500 S/cm). This aspect of the electrical transition in the electrodes is not presently captured with EC-1. Several attempts were made to calculate an effective capacitance for the stand-alone electrode series. The equivalent electrical circuits employed were not sufficient to fully capture the transition of the composite from an ionic conductor to an electrical resistor presently, as is shown for the correspondingly large decrease in the capacitive elements shown in Figure 3.8b.

3.3.2 Fully constructed IPTs

After observing and modeling the electrical characteristics of the isolated IPT electrodes based on loading of RuO₂ the logical next step was to build a corresponding series of transducers from EMI-Tf swollen HB-3kBPS-20. Variation in the volume percent of RuO₂ in the IPT electrodes was consistent with the stand-alone electrode samples. EIS was used to determine the frequency dependent impedance of the built IPTs. Although the same equivalent circuit used to model the electrodes could be applied to the full transducers, the available parameters were not sufficient to describe all of the processes observed for the full frequency range. This insufficiency also prevented accurate estimation of an effective capacitance with EC-1. Therefore, an extended equivalent circuit is introduced to model the full available frequency range and allow for capacitance estimation. To observe the effect of varied RuO₂ loading in the electrodes on the performance of these novel transducers, bending strain responses to step input voltages were recorded.

3.3.2.1 *Electrical impedance spectroscopy*

Impedance analysis was performed in the through-thickness direction for the series of fully constructed IPTs having electrodes of varied volumetric loading of RuO₂ from 0 – 45 %. As in the stand-alone electrodes, the uptake ratio of EMI-Tf to HB-3kBPS-20 was kept constant at ~4.9 mol/mol during construction of the outside electrode as well as the swollen central ionomeric membrane. The Bode plot displaying magnitude of the impedance and phase angle versus frequency is provided in Figure 3.9.

The magnitude of the impedance and phase angle of the built IPTs display very similar trends to the data for the stand-alone electrodes, showing steadily decreasing impedance with increasing content of RuO₂ in the electrodes. However, the most immediately noticeable difference is that the average IPT impedance for the series of RuO₂ electrode variations is on much higher and only spans a single order of magnitude between 0.1 – 1 GΩ. The stand-alone electrodes displayed a similar maximum in the low-frequency impedance but had a range of impedances over 5 – 6 orders of magnitude. At 100 Hz, this difference reflects that the presence of the central membrane in the IPTs is the common source of increased bulk resistance. The electrodes only display comparable impedance at compositions less than the percolation threshold. All built IPTs within the series display some capacitive behavior, observed as phase values less than zero at low frequencies. Increased RuO₂ content up to 45 vol % approximates pure electrical resistors at the bounds of the central membrane as the impedance in this frequency range approaches the value displayed for the bulk ionomer resistance. This observation highlights the opportunity for ionomer design to increase charge transport of the base polymer and decrease impedance of the structure directly. Although essentially serving as a passive element, the central ionomeric membrane's charge transport is essential to manifest performance in the electrodes and is further explored in Chapters 4 and 5. At high frequency the series of curves collapse and display phase that approaches -90°. Only the stand-alone electrodes with compositions of RuO₂ below the percolation threshold displayed this behavior which appears to reflect some capacitive component due to the electrolyte combination of sBPS and EMI-Tf.

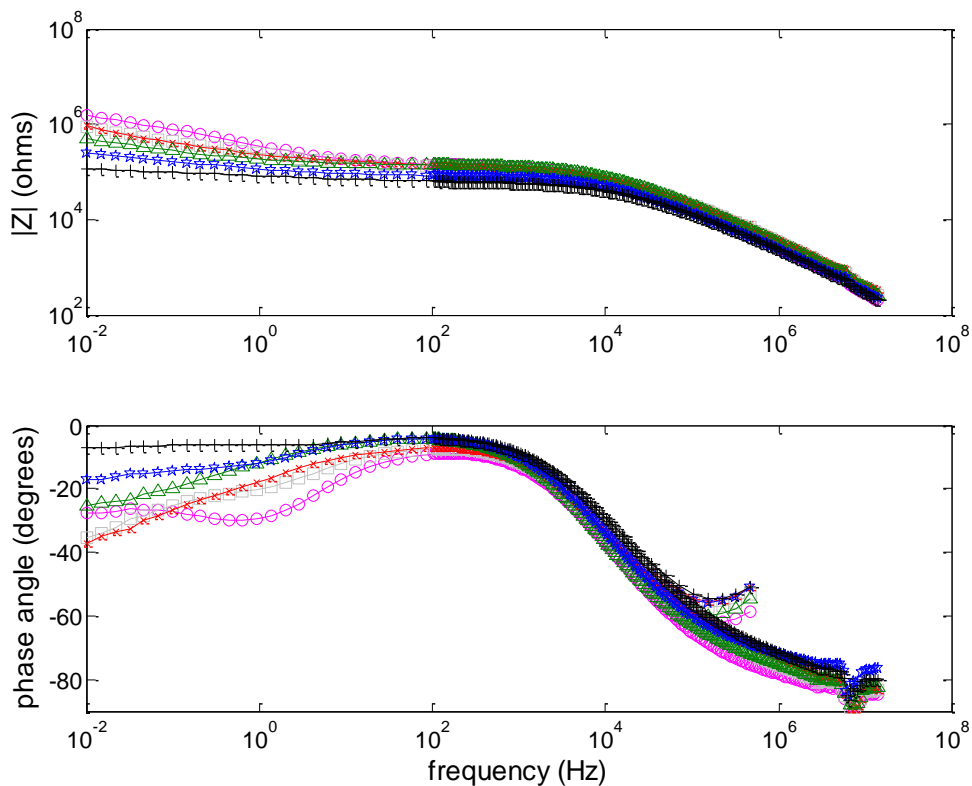


Figure 3.9: Bode plot for the impedance of built IPTs constructed with varied volumetric loadings of RuO₂ in the electrodes (LEGEND: 7.5%, pink circle; 15%, grey square; 22.5%, red X; 30%, green triangle; 37.5%, blue star, 45%, black cross)

Figure 3.10 presents the calculated ionic conductivity of the built IPTs versus RuO₂ loading of the device electrodes. The range of ionic conductivity for the IPTs is less than a single order of magnitude in comparison to the stand-alone electrode conductivities that spanned five orders of magnitude. This behavior is expected since as mentioned above, the bulk conductivity of the IPT is primarily dependent on the impedance of the central membrane. In the case of the IPTs, percolation is still present but only in the electrodes. Relatively constant bulk conductivity for the series is a direct reflection of the constant ratio between ionomer and ionic liquid employed for fabrication of all components in the IPTs. Approximately one order of magnitude difference is evident between the ionic conductivity of the IPT series and the value determined from EIS of the bare cast HB-3kBPS-20 membrane with 75 wt % uptake of EMI-Tf. As mentioned previously, this difference is attributed to decreased contact resistance for the through-thickness measurement with the electrodes of the IPT compared to the surface of the bare membrane.

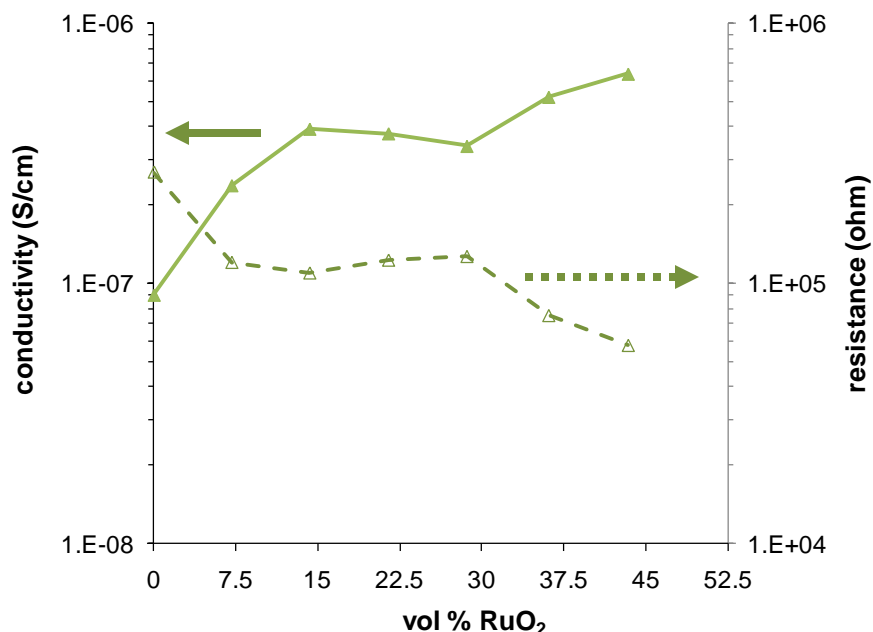


Figure 3.10: Bulk resistance and ionic conductivity versus RuO₂ electrode loading in novel HB-3kBPS-20 / EMI-Tf – IPTs

3.3.2.2 Equivalent electrical circuit modeling

Due to the importance of capacitance as an indicator for maximum strain in IPTs, a more complex equivalent circuit model was necessary for its estimation in the IPTs than for the stand-alone electrodes. Examination of the composition and processes inherent to the IPT led to the extended equivalent circuit model, herein referred to as EC-2, shown in Figure 3.11. Essentially, EC-2 places a CPE-modified Randle's circuit in series with the elements that were present in EC-1. The Randle's circuit is a well known electrochemical element that combines parameters to model the parallel capacitive and faradaic processes that occur in an electrical double layer (EDL).[233] Modification of the traditional Randle's circuit to include a CPE was justified due to the pseudocapacitive behavior shown in EIS[235] and the rough nature of the solid, high surface area RuO₂ employed in the electrodes.[236, 237] Further examination of EIS data for bare ionomer membranes swollen with diluents suggested that EC-1 was a better suited model for less complex components and/or a narrower frequency range. This was also confirmed by its ability to fit the low frequency data associated with the isolated electrodes. In the case of the extended circuit, EC-1 is now assigned to describe impedance for the high frequency range associated with the electrolyte (i.e., ionomer and ionic liquid).

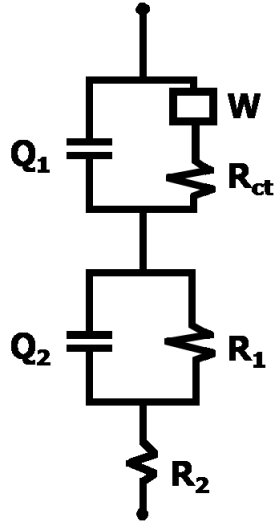


Figure 3.11: EC-2: extended equivalent circuit model for built IPTs

The estimation of the complex impedance for EC-2 (Z_{EC-2}^*) is shown in

$$Z_{EC-2}^* = \frac{Z_f^*}{1 + Q_1^* Z_f^*} + \frac{R_1}{1 + R_1 Y_2^\circ (i\omega)^{n_2}} + R_2 \quad (3.4)$$

where:

$$Z_f^* = \frac{1}{Y_w^\circ (i\omega)^{0.5}} + R_{ct} \quad (3.5)$$

and:

$$Q_1^* = Y_1^\circ (i\omega)^{n_1} . \quad (3.6)$$

Implementation of the EC-2 model accounted for all materials and interfaces present in the IPT. This fact allowed the model's application to the full range of frequency data obtained from the combined EIS analyzers (0.01 Hz – 5 MHz). The same fitting procedure using the MatLab *fminsearch* function was also employed to minimize the weighted error between the EC-2 model estimation and the experimental data. Application of the EC-2 model provided excellent fits to the full frequency range and displayed sufficient flexibility to account for changes in RuO₂ content for the full range of IPTs analyzed.

Both Figure 3.12a and b display experimental data for IPTs with electrodes that contain ~37.5 vol % RuO₂ with EC-2 fits that are representative of the quality for the full sample series. The Bode plot shown in Figure 3.12a displays the ability of EC-2 to accurately fit both the magnitude of the impedance and the phase for the full frequency range. Even with a reduced frequency range EC-1 was unable to attain this quality of fit, especially in regards to the phase

data. The Nyquist plot in Figure 3.12b demonstrates excellent fits to the kinetic portion of the curve that would otherwise require a separate fit to estimate the bulk conductivity of the ionomer.

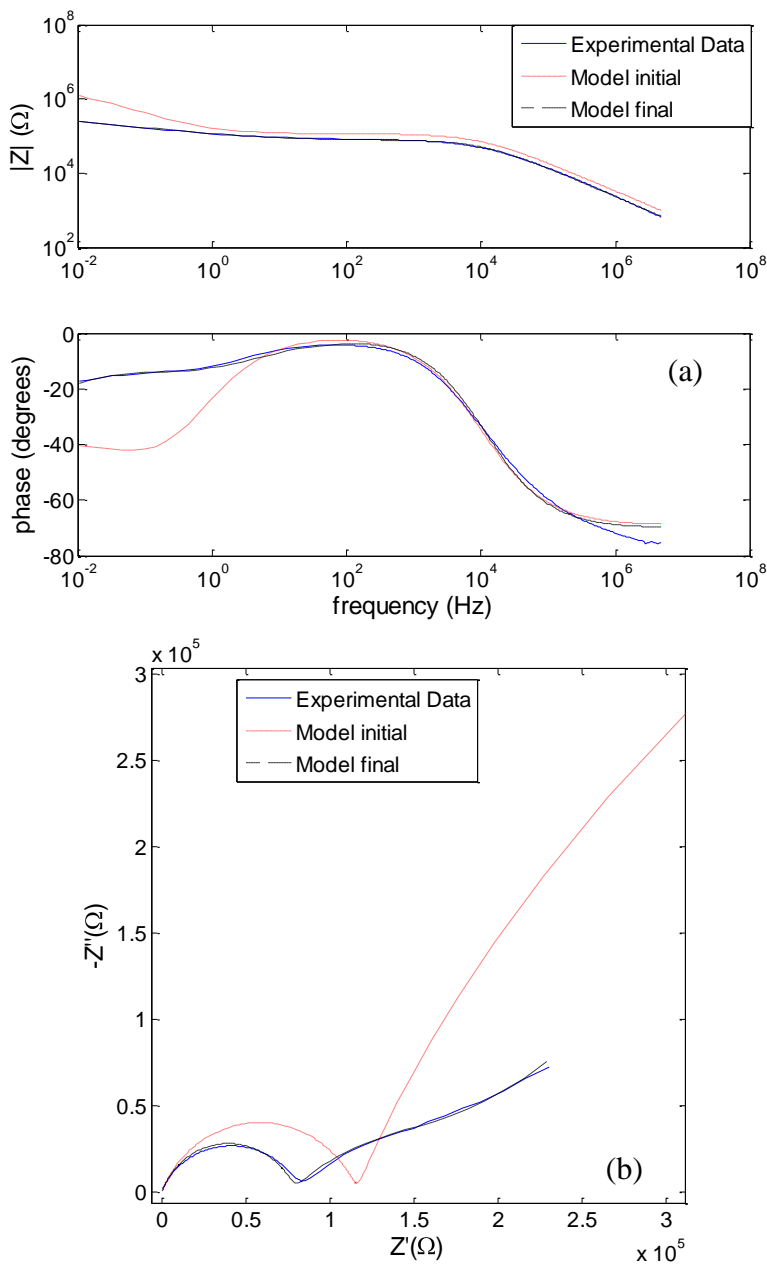


Figure 3.12: (a) Bode plot and (b) Nyquist plot from EIS characterization and modeling with EC-2 of an IPT with 37.5 vol % RuO₂ electrodes

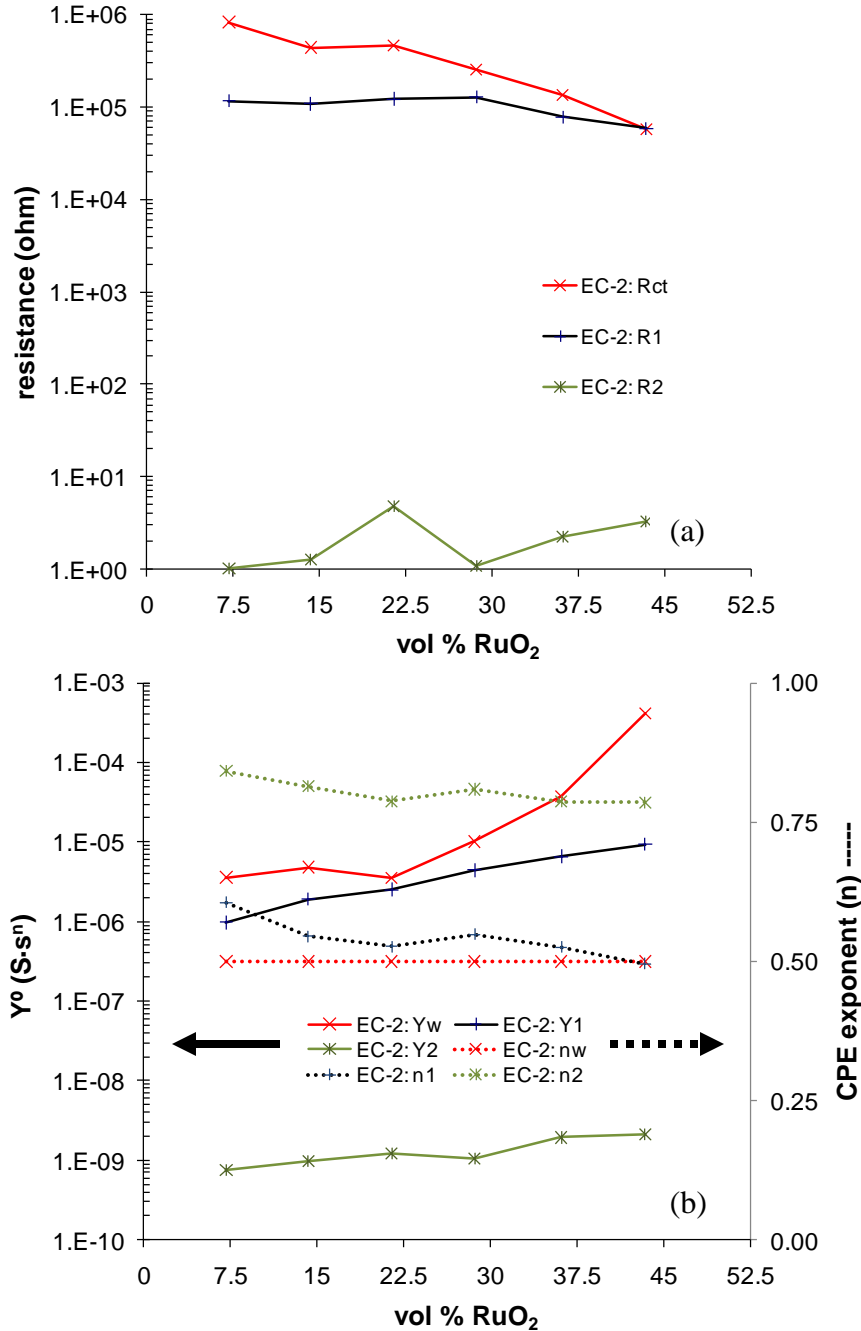


Figure 3.13: Equivalent circuit parameters for (a) resistors and (b) CPEs in EC-2 as determined from fits and calculations based on impedance data for IPTs

The ability of EC-2 to provide excellent fits to the impedance data for a wide frequency range allowed for better estimation of the processes and materials associated with the circuit parameters. The Randle's circuit appears to accurately account for a charge transport resistance (R_{ct}) associated with the bulk ionomer (55 – 92.5 vol %) and ionic liquid contained in the electrodes. The Warburg diffusion impedance (W) also provides good estimation of the

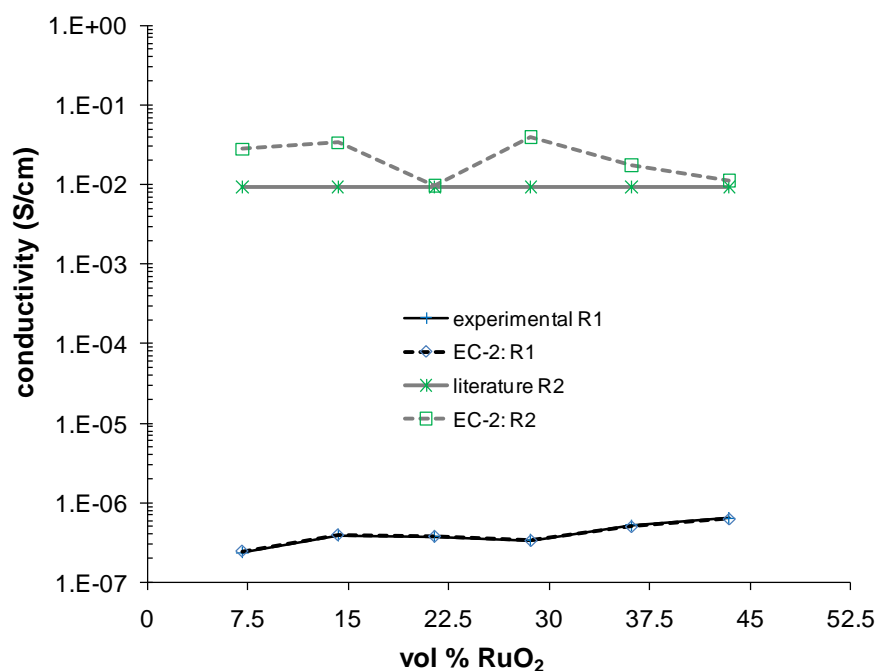


Figure 3.14: Ionic conductivity of R₁ and R₂ components as calculated from experimental results and EIS modeling with EC-2

resistance to ion transport as they approach the EDL that forms at the RuO₂ surface. In accordance with the initial parameter inputs, the Randle's circuit impedance primarily contributes in the low frequency range, from ~0.01 – 1000 Hz. Assignment of the EC-1 components to the high frequency range (1000 – 10⁶ Hz) accurately models the electrolyte-swollen ionomer (R₁, Q₂) and the ionic liquid (R₂). Variation in the EC-2 parameters with RuO₂ loading of the IPT electrodes is shown in Figure 3.13. The decreasing trend for the values of R_{ct} aligns with percolation in the electrodes that was detected in the isolated electrode study between 22.5 – 30 vol % RuO₂. At this composition the electrode begins to transition from a mainly ionic resistor to an electronic resistor through connectivity of the RuO₂ particles. R_{ct} decreases markedly beyond 22.5 vol % RuO₂ such that its value is nearly equal to the bulk resistance of the ionomer (R₁) at 45 vol % RuO₂. The values of R₁ are also nearly constant in relation to the changing composition of the electrodes, which is expected for the resistance of the bulk ionomer. R₂, assigned to the resistance of the ionic liquid electrolyte, displays a very low resistance in the bulk and only a slight dependence on the electrode composition. Figure 3.14 demonstrates that in relation to the experimental geometry of the IPT samples, the values of R₁ and R₂ from EC-2

provide excellent estimates of the bulk conductivity for the swollen ionomer and the electrolyte at all electrode compositions, confirming the accuracy for application of the model. The nearly constant values for the calculated ionic conductivities also provide an indirect indication of processing consistency and low variation in the IPT samples since the ratio of sBPS to EMI-Tf was kept constant for the study.

3.3.2.3 *Estimation of an effective capacitance from IPT impedance*

Both the accurate fitting and phenomenological correlations of EC-2 with the impedance spectra of the sBPS–IPTs justify the model’s use for estimation of the double-layer capacitance ($C_{dl} = C_1$) associated with the interfaces in the RuO_2 electrodes of IPTs. The capacitance associated with the ionic liquid-swollen ionomer (C_2) is also notable considering the depressed semi-circle displayed in the Nyquist plots for the IPTs indicative of a CPE. Capacitance in the solid-liquid electrolyte (sBPS/EMI-Tf) is of interest due to the bound charges on the polymer backbone in the presence of both the cations and anions of the ionic liquid. However, the frequency dependence of the CPEs in both elements of the equivalent circuit requires further calculation for true effective capacitance than just use of the Y° parameter.[238]

A previously employed method to account for the frequency dependence of the IPT capacitance was estimation with the imaginary part of the circuit impedance as shown in Equation 3.7. This method was mainly applied to a resistor and capacitor in series as a model for the IPT.[54] However, application to the present system results in the data labeled $C(Z'')$ in Figure 3.15 when normalized for the cross sectional area of the IPT.

$$C_{RC} = \frac{1}{Z''(\omega) \cdot \omega} \quad (3.7)$$

With a larger number of parameters in EC-2 it is desirable to deconvolute the contributions of the CPEs (Q) that represent C_1 and C_2 . Each Q is in parallel with at least one impedance, R_{ct} and R_1 respectively. Calculation of the true effective capacitance for each pair of Q and R elements in parallel assumes a distribution of time constants as shown in

$$T^n = Y^\circ R \quad (3.8)$$

In the case where $n = 1$ for an ideal capacitor, $T = RC$. Substitution of this case back into Equation 3.8 leads to the true effective capacitance for Q||R as described with[239]

$$C = \frac{(Y^\circ R)^{1/n}}{R} . \quad (3.9)$$

The results for C calculated using Y_1° and R_{ct} , according to Equation 3.9, are shown in Figure 3.15 as $C(R_{ct})$. However, for the application of the Q||R elements within EC-2 there are other impedances in series with R that could contribute to the overall capacitance, including some that are frequency dependent. Shervedani and Mozaffari estimated that in the case of a CPE-modified Randle's circuit the effective capacitance is calculated according to [240]

$$C = \left[Y^\circ \left(\frac{1}{R_{eff}} \right)^{n-1} \right]^{1/n} \quad (3.10)$$

where:

$$\frac{1}{R_{eff}} = \frac{1}{R_s} + \frac{1}{R_{ct}} . \quad (3.11)$$

Equation 3.11 is based on the zero point break frequency in $|Z|$ representative of the transition between the two contributing resistances and provides equality between Equations 3.9 and 3.10. For calculation of C in the frequency range associated with the EC-2 model, R_{eff} in Equation 3.10 could include contributions from Z_w , R_{ct} , R_1 , Z_{Q_2} , and R_2 . Equations 3.12 – 3.15 represent potential variations on R_{eff} . The frequency dependencies of these contributors are plotted with those previously mentioned in Figure 3.15.

$$\frac{1}{R_{eff}} = \frac{1}{R_1} + \frac{1}{R_{ct}} \quad (3.12)$$

$$\frac{1}{R_{eff}'} = \frac{1}{R_1} + \frac{1}{R_{ct} + |Z_w|} \quad (3.13)$$

$$\frac{1}{R_{eff}''} = \frac{1}{|Z(R_1 Q_2)|} + \frac{1}{R_{ct}} \quad (3.14)$$

$$\frac{1}{R_{total}} = \frac{1}{|Z(R_1 Q_2)|} + \frac{1}{R_{ct} + |Z_w|} \quad (3.15)$$

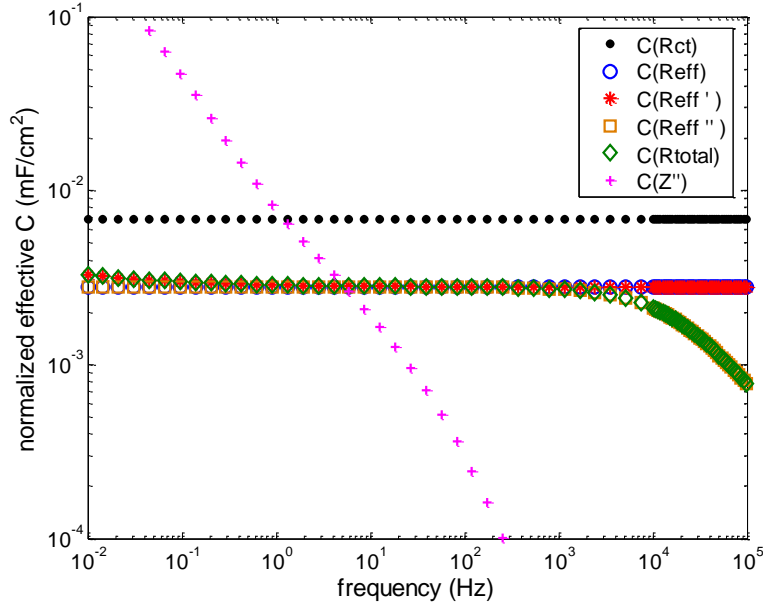


Figure 3.15: Frequency dependence for the normalized effective capacitance when calculated with various components of EC-2 for an IPT with 37.5 vol % RuO₂ electrodes

The zero point break frequency for the IPT sample analyzed in Figure 3.15 was estimated to have a value of ~5 Hz. All other samples in the series displayed break frequencies in a similar range. In this range of frequency, representative of the transition for C_1 (C_{dl}), R_{eff} is nearly constant for all estimations except for $C(Z'')$. $C(R_{ct})$ appears to overestimate the effective capacitance since it does not account for the contribution of R_1 . Based on these results, Equations 3.10 and 3.12 were employed to calculate the effective capacitances C_1 and C_2 for the IPT series. The capacitance for the EDL and ionomer-ionic liquid electrolyte versus RuO₂ content of the electrodes is plotted in Figure 3.16. C_1 , assigned to the double layer capacitance in the electrodes, increases with greater RuO₂ content and appears to plateau at a maximum value of 2.75 μF immediately after percolation (22.5 – 30 vol %). C_2 , indicative of the capacitance of the ionic liquid-swollen ionomer, displays a much lower effective capacitance of approximately 10 pF that appears to remain constant regardless of electrode composition. The results of this analysis provide several distinct advantages in the design and evaluation of IPTs. First, the method establishes through-thickness EIS as a tool to characterize the effective capacitance of IPTs. Second, assignment of the parameters within EC-2 to materials and processes inherent to IPT performance allows for a more thorough understanding of the material interactions and

processing effects on the final device. Finally, in the case of sBPS / EMI-Tf / RuO₂ IPTs the optimum electrode composition to maximize capacitance is approximately 42 %.

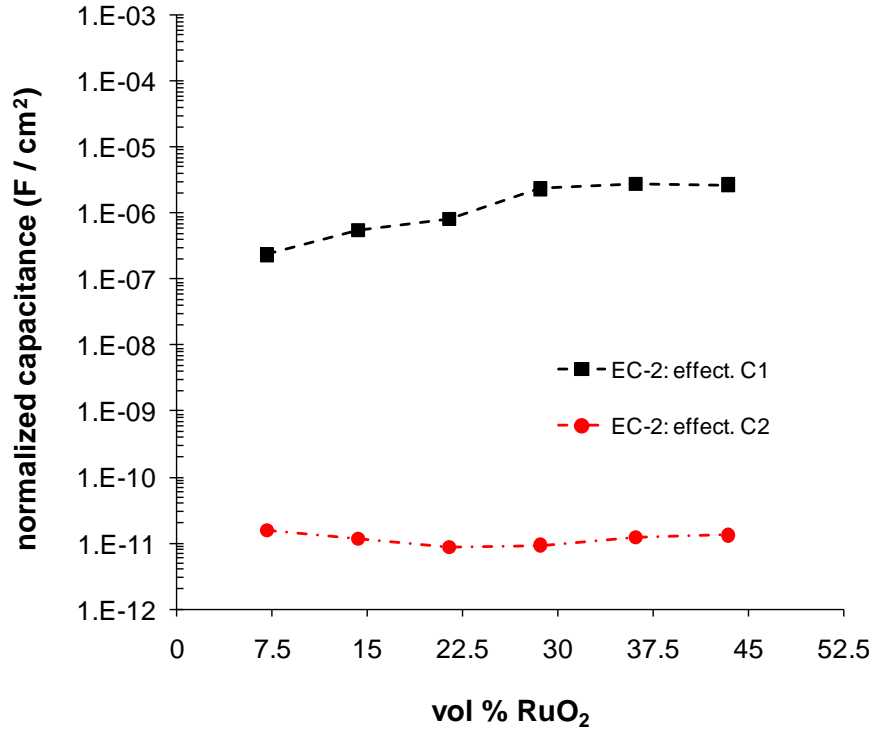


Figure 3.16: Calculated effective capacitance associated with each CPE in EC-2 from fits of impedance data for built IPTs

3.3.2.4 Electromechanical actuator performance

The fully fabricated IPTs with varied electrode loadings of RuO₂ were characterized for their performance as bending transducers in response to step voltage inputs. Application of the driving voltage for actuation was initially in the negative direction for a period of 300 s before switching the voltage to the same magnitude in the opposite direction for a further 300 s. A sample step-response for an EMI-Tf swollen HB-3kBPS-20fd-IPT with 45 vol % RuO₂ electrodes is shown in Figure 3.17. For the range of step input voltages applied to this specific sample, 1 – 2.5 V, the IPT demonstrated between 15 – 42 μm displacements respectively. The curves in Figure 3.17 are raw data acquired through use of a non-contact laser vibrometer that enabled detection of such small displacements. The value at 300 s was typically taken as the peak displacement, although the curves indicate that the transducer would continue actuation at longer times. The

displacement response curves also indicate that after the initial response to the applied voltage the IPT displays a constant strain rate with no sign of back relaxation over the time period investigated. Previous demonstrations of water-swollen SPAES and SPATS–IPTs did demonstrate back-relaxation, although decreased in magnitude as compared to Nafion[®]–IPTs.[108] The absence or significant reduction of back-relaxation as compared to water-swollen IPTs was previously established for ionic liquid-swollen Nafion[®]–IPTs.[57] Although the displacements for these novel HB-3kBPS-20 IPTs are much smaller than those for similar Nafion[®]–IPTs, this series is the first demonstration of novel IPTs that employ ionic liquid as the diluent and correspondingly avoid back relaxation.

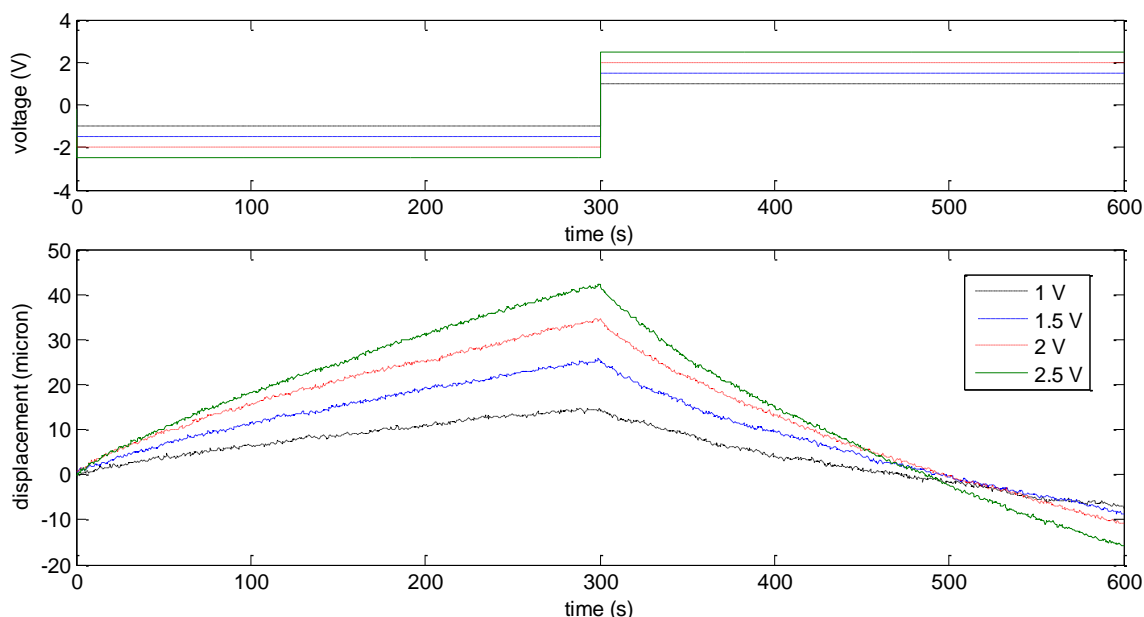


Figure 3.17: Displacement response curves to step input voltages of varied magnitude and direction for an EMI-Tf swollen HB-3kBPS-20–IPT with 45 vol % RuO₂ DAP electrodes

Figure 3.18a shows the peak microstrain as calculated from Equation 3.2 for the full series of transducers actuated with varied step-inputs. Figure 3.18b plots the voltage-normalized strain rate versus electrode loading of RuO₂. The resistive nature of these IPTs led to slow strain rates that remained relatively constant over the period of interest. The reported strain rate is an average over the 300 s period of actuation. Furthermore, normalization of the strain rate to the applied voltage causes the data to collapse to approximate a single curve across the entire range of electrode loadings. Any discrepancy remaining in the actuation results due to the direction of the

applied voltage is most likely due to a pre-bend that indicates residual mechanical strains in the IPT from fabrication. Peak strain displays an approximately linear increase with increased step inputs. Both strain and strain rate correlate well with the percolation behavior detected through EIS analysis. Percolation of the actuation response occurs for IPTs with electrodes that contain between 22.5 – 30 vol % RuO₂. Based on the equivalent circuit modeling, IPTs with higher loading of RuO₂ beyond the percolation threshold have nearly equal effective capacitance. Further increases in strain and strain rate beyond percolation are likely due to the subsequent increases in conductivity that were shown within the isolated electrodes.

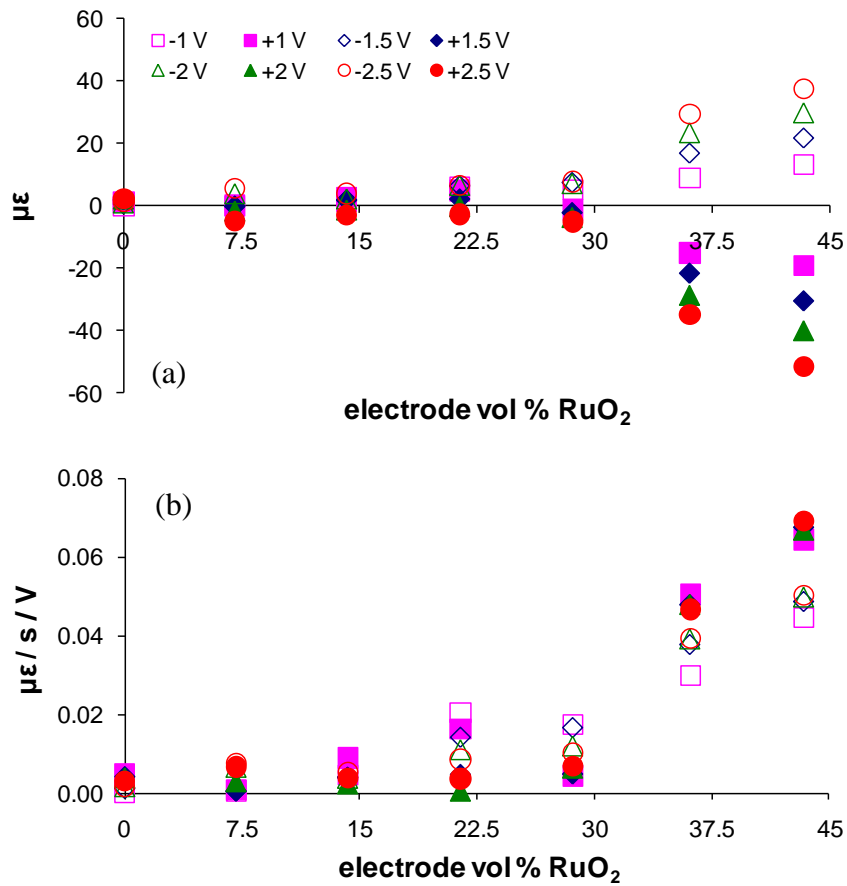


Figure 3.18: (a) peak strain achieved within 300 s and (b) normalized strain rate resulting from step input voltages of varied magnitude and direction for IPTs with varied vol % RuO₂ electrodes

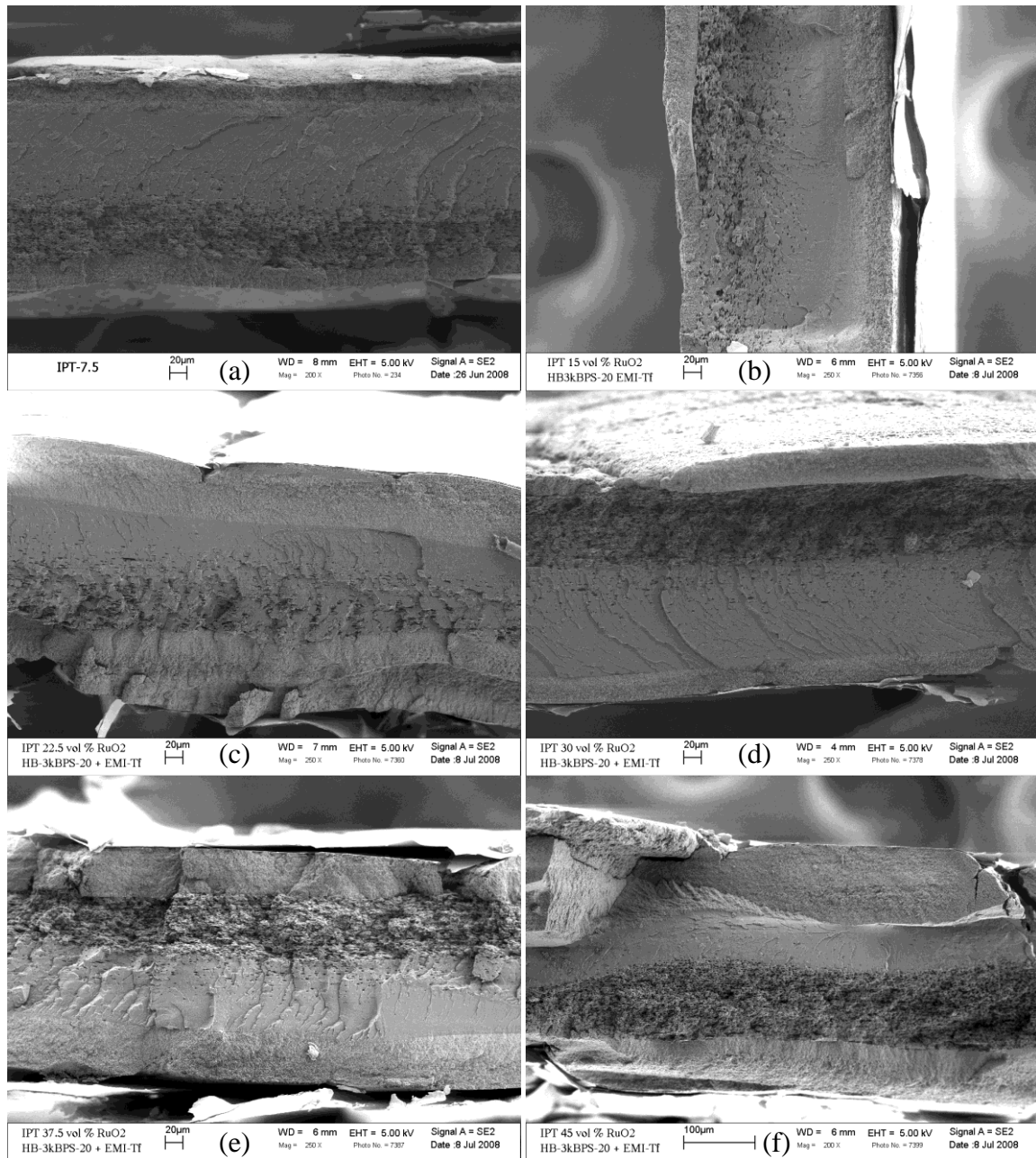


Figure 3.19: SEM micrographs of HB-3kBPSS-20 – IPTs designed with electrodes containing (a) 7.5 (b) 15 (c) 22.5 (d) 30 (e) 37.5 (f) 45 vol % RuO₂

After actuation, each of the IPTs was freeze-fractured across the width to analyze the cross-section with SEM. This characterization allows for detailed observation of the trimorph structure to confirm successful design and processing of the IPT with the DAP method. SEM micrographs of each of the transducers are shown in Figure 3.19a-f. Note that the thin outer layer which appears as bright white in SEM is the gold leaf of the transducer. A minimum of three

measurements were taken per transducer cross-section for each electrode and the central membrane. The average thickness of the IPT and its components are reported in Table 3.1. Upon inspection of the SEM micrographs, the first immediately noticeable characteristic is the difference in the fracture surface through the thickness of the central membrane for all samples. This transition from a smooth, solid surface to one that contains a high density of pores is likely due to the casting process in the presence of the ionic liquid. This hypothesis is further explored in Chapter 4. On average for the series of IPTs the central membrane was approximately 162 μm thick, which within error is very close to the target of 183 μm for analogous Nafion[®] membranes. The electrodes were on average 45 μm thick, although the error and range of thicknesses was much larger for this component than the central membrane, thus the observation of some asymmetry in the paired electrodes for each IPT. The variation is likely due to the decision to keep the RuO₂ volumetric loading equal for all electrodes. Necessary adjustments in the volume of ionomer to produce the desired volumetric ratios caused variation in electrode thickness, which may have contributed some of the variability to the actuation results. Regardless, the electrodes appear homogeneous with good dispersion of the RuO₂ particles in the ionomeric matrix through use of the casting DAP method.

Table 3.1: Average HB-3kBPS-20–IPT layer thickness \pm one standard deviation

RuO ₂ content (vol %)	electrode 1 (μm)	central membrane (μm)	electrode 2 (μm)	total IPT (μm)
7.5	35 \pm 3	167 \pm 7	25 \pm 5	228 \pm 15
15	38 \pm 10	142 \pm 15	41 \pm 9	221 \pm 34
22.5	46 \pm 21	160 \pm 37	46 \pm 38	252 \pm 96
30	31 \pm 12	199 \pm 12	33 \pm 13	263 \pm 37
37.5	47 \pm 16	132 \pm 17	66 \pm 12	244 \pm 46
45	90 \pm 45	170 \pm 5	60 \pm 10	320 \pm 64

3.4 Summary

In this chapter a highly-branched ionomeric polysulfone (HB-3kBPS-20) was employed as an IPT membrane to construct the first 100 % novel DAP electrodes and corresponding IPTs reported. Fabrication of the series of well-defined, stand-alone electrodes for EIS characterization was enabled by the DAP method and carried out with a defined uptake of ionic liquid, also a first for novel IPT membranes. The study varied volumetric loading of RuO₂ conducting particles in the electrodes and the corresponding full IPTs. A percolation threshold in ionic conductivity was defined at 18 vol % RuO₂ for the stand-alone electrodes. Equivalent circuit models were identified for both the electrodes and the built IPTs that provided excellent fits for the impedance spectra and phenomenological correlation between the device composition and the circuit parameters. Estimates of the circuit parameters indicated that the interfacial charge transfer resistance between the conducting particles and the ionomeric matrix dominates the electrical response prior to percolation. Beyond percolation in the electrodes, the bulk resistance of the ionomer – ionic liquid electrolyte accounts for the majority of the total IPT resistance. A method for calculation of an effective capacitance from impedance data was shown to be robust for IPTs with wide variation in the electrode compositions. For this series of novel IPTs, an electrode composition of ~42 vol % RuO₂ was identified as optimal for maximized capacitance of the device. Bending actuation of the fabricated IPTs further demonstrated percolation behavior in peak strain and strain rate with larger displacements occurring at higher electrode loadings of the conducting particles. Consistency of the casting derivation of the DAP method was confirmed with observation of the IPT cross-sections with SEM. Actuation performance correlated well with the optimal electrode composition identified to maximize capacitance. Despite successful construction and evaluation of the series, final IPTs demonstrated very low actuation capability and very resistive behavior in comparison to the standard Nafion[®]-IPT. The limiting factor was deemed as the ionomer – ionic liquid combination. Chapter 4 discusses direct efforts to augment the ionic conductivity of ionic liquid swollen sBPS. Chapter 5 then outlines the fabrication of optimized IPTs to demonstrate performance improvements over the series investigated here.

Chapter 4 METHODS FOR AUGMENTATION OF CHARGE TRANSPORT AT THE IONOMER – IONIC LIQUID INTERFACE

*This chapter is primarily derived from and expanded upon: [241] Duncan A J, Akle B J, Long T E and Leo D J 2009 Ionomer design for augmented charge transport in novel ionic polymer transducers *Smart Materials and Structures* **18** 104005

As well as: [242] Duncan A J, Leo D J, Long T E, Akle B J, Park J K and Moore R B 2009 Electromechanical performance and membrane stability of novel ionic polymer transducers constructed in the presence of ionic liquids *Proceedings of SPIE-The International Society for Optical Engineering* **7287 728711

4.1 Motivation

As mentioned in Chapter 1, one of the most significant recent advancement in IPT technology is replacement of the water diluent with various molten salts, also referred to as ionic liquids.[57] These materials have a melting temperature generally far below room temperature and are completely composed of ions. The organic nature of the ions in ionic liquids creates materials with high thermal and electrolytic stability, high ionic conductivity, and a negligible vapor pressure. The back-relaxation response of Nafion[®]-IPTs was eliminated when water was replaced with the ionic liquid 1-ethyl-3-methylimidazolium trifluoromethanesulfonate (EMI-Tf), however the response speed was slower due to increased viscosity of the fluid.[57] Ionic liquids generally have a much higher viscosity (~50 cP) than water (~1 cP). For actuation at greater than 1.23 V, electrolysis was observed in IPTs swollen with water that resulted in blistering and delamination of the applied electrodes. The higher electrolytic limit of ionic liquids allows for higher peak strain due to a larger available range of voltage (e.g., EMI-Tf, ± 4 V) without inducing diluent degradation.

In light of their many benefits ionic liquids do have drawbacks in terms of interfacing with the IPT ionomer. One major drawback is that Nafion[®] membranes swell more slowly and to a lesser extent with ionic liquids as compared to water. Bennett *et al.* identified a critical uptake (f_c) of ionic liquid where the molar ratio of ionic liquid to bound charge sites on the ionomer was sufficient to displace all of the ionomer's free ions. Uptake of ionic liquid above f_c provided sites for fast ion exchange through the bulk electrolyte diluent and corresponded to a large change in conductivity and strain rate of IPTs. With the recent emergence of ionic liquids in IPTs, Nafion[®]-EMI-Tf is presently the only system with a reported f_c (Na⁺ form, 0.69 mol IL / mol SO₃⁻).[61] For increased performance of IPTs a mixture of methanol and ionic liquid was used to expand the available swelling levels. Methanol aids in swelling the Nafion[®] membrane to allow entrance of the ionic liquid. The methanol is then removed with heat *in vacuo* to leave the ionic liquid in the membrane. Bennett *et al.* further suggested that hydrophilic ionic liquids reside mostly in the hydrophilic cluster-channel network of Nafion[®] while hydrophobic ionic liquids tend to disrupt this network by swelling the hydrophobic polymer matrix. Differences in polarity between the ionic liquid and the microphase separated ionomer led to varied levels of morphological stability. This link translated directly to the performance of IPTs built with the corresponding ionic liquid-swollen membranes.[61]

This chapter concentrates on efforts to expand the use of ionic liquids to sBPS ionomers and to optimize charge transport of the imbibed membranes. The ionomeric membrane provides the pathway through the thickness of the device for charge transport and equilibration of the mobile ion redistribution that occurs under the applied potential within the electrodes. Since charge transport based on microphase separation of the ionomeric membrane is central to the operation of IPTs, investigation of various techniques and parameters for the incorporation of ionic liquids into the membrane is critical.[243] Here, use of sulfonated polysulfones in the presence of EMI-Tf requires verification that a charge transport pathway is sufficiently formed that will remain intact during processing and performance of subsequent IPTs. The ionomeric membranes are both swollen and cast in the presence of EMI-Tf. The casting method targets sBPS membranes with exactly defined uptakes where the membrane is formed in the presence of the ionic liquid. The morphology is examined with small-angle X-ray scattering (SAXS) for comparison between a neat membrane and one formed in the presence of ionic liquid. The thermomechanical properties of the cast membranes were evaluated with dynamic mechanical analysis (DMA) as a

function of uptake magnitude and ionomer composition, primarily to establish thermal transitions and hydrated elastic modulus. Electrical impedance spectroscopy (EIS) was performed for all ionic liquid containing membranes to determine their ionic conductivity. This measure of charge transport serves as an indirect indicator of the degree of microphase separation based on differences in polarity for various ionomers.[196, 244, 245] Swelling studies varied time, temperature, and co-diluent content to maximize the uptake of EMI-Tf into sBPS while optimizing the total ionic conductivity of these model central membranes for IPTs.

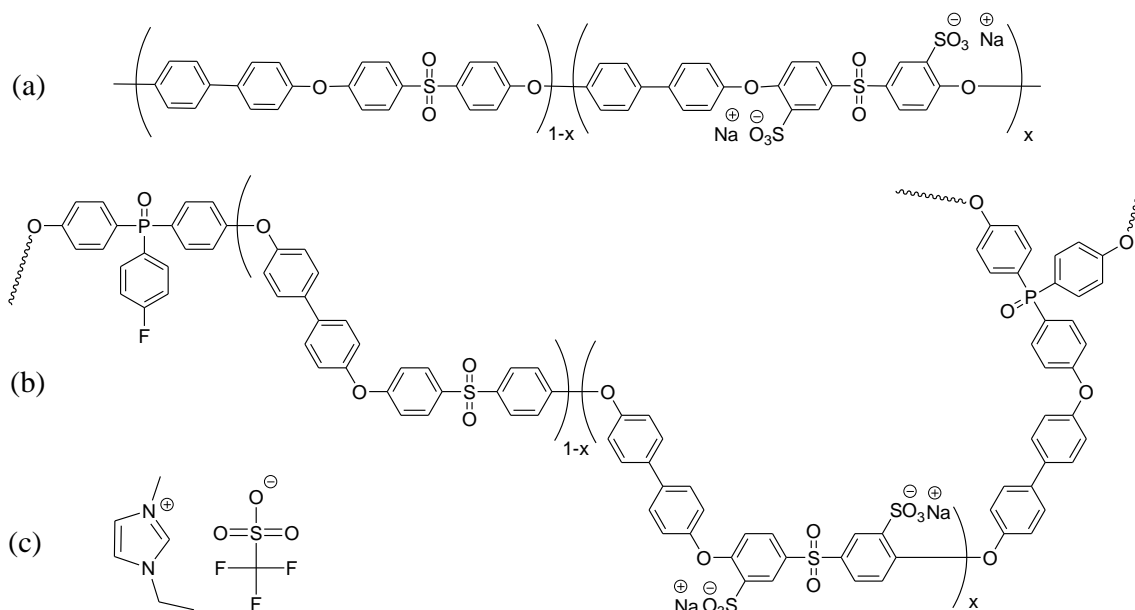


Figure 4.1: Chemical structures for (a) Lin-BPS-YY, (b) HB-XkBPS-YY and (c) EMI-Tf

4.2 Experimental

4.2.1 Materials

Linear (Lin-BPS) and branched samples (HB-3kBPS) of 20 and 40 mol % sulfonation are included in the present study. For comparison, the chemical structures for the linear and branched ionomers are depicted in Figure 4.1a and Figure 4.1b respectively. Equivalent weight (EW), ion-exchange capacity (IEC), global degree of branching (DB_{global}), and the glass transition temperature (T_g) as reported in Chapter 2 are summarized for the applicable samples in Table 4.1. Membranes were cast from a 10 wt % solution in dimethylacetamide (DMAc, Sigma

Aldrich, 99%). All ionomeric membranes were exchanged to the sodium (Na^+) sulfonate form through immersion in 0.5 M NaCl for 24 h before drying and characterization.

The ionic liquid chosen for the diluent uptake study is 1-ethyl-3-methylimidazolium trifluoromethanesulfonate (EMI-Tf, Merck, high purity) and was used as received. The chemical structure of EMI-Tf, is shown in Figure 4.1c. Methanol (MeOH, Sigma Aldrich, 99% pure) was employed as a co-diluent and was used as received for membrane swelling.

Table 4.1: Chemical and physical properties for sBPS employed in the EMI-Tf uptake study

	EW	IEC	DB _{global}	T_g
	(g/eq)	(meq/g)	(%)	(°C)
Lin-BPS-20	1 200	0.83	0	271
Lin-BPS-40	650	1.54	0	326
HB-3kBPS-20	1 200	0.84	3.0	255
HB-3kBPS-40	650	1.53	2.7	309

4.2.2 Methods

Uptake of ionic liquid into the ionomeric membranes was accomplished with one of two methods. The first method directly cast membranes from a solution of the polymer and ionic liquid together. Stock polymer solutions at 10 wt % in DMAc were combined with the target uptake of EMI-Tf, between 0 – 100 % of the total dry polymer weight to create casting solutions. Both the stock ionomer solution and EMI-Tf were filtered through a 450 nm PTFE syringe filter into clean containers to create the casting solution. These solutions were stirred at RT overnight to achieve complete dissolution. Casting solutions were poured into level molds composed of a glass substrate with silicone rubber walls (15.5 mm x 36 mm) and placed beneath a heat lamp (~50 °C) in a fume hood under a ventilated glass cover to gradually evaporate the DMAc for 12-24 h. All films were further dried *in vacuo* with a 1 h ramp from 25 – 85 °C, 12 h hold at 85 °C, and an 8 h cool from 85 – 25 °C. Thermogravimetric analysis (TGA, TA Q500, N₂, 10 °C/min) and differential scanning calorimetry (DSC, TA Q1000, N₂, 10 °C/min) indicated the presence of significant DMAc residue and higher glass transition temperatures (T_g) than 85 °C respectively. A second annealing step was performed *in vacuo* at 250 °C for 1 h followed with a slow cool to

RT overnight. Cross-sections of the cast membranes (post-IPT fabrication) were observed as freeze-fractured samples (liquid N₂) with a Leo 1550 field-emission scanning electron microscope (FESEM). The samples were sputter coated with an 8 nm layer of Au/Pt to reduce charge accumulation on the sample surface.

For the second method, a series of swelling tests was performed to measure the amount of EMI-Tf ionic liquid (IL) absorbed into the ionomeric membranes with variations in time, temperature, and presence of a second diluent. Uptake was quantified through measurement of the swollen weight (*wt*) of the membrane in comparison to its original dry weight using Equation 4.1 and 4.2, where MW_{IL} is the molecular weight (g/mol) of the ionic liquid and EW is the equivalent weight of the dry ionomer membrane (eq SO₃⁻ / g). In the case where a second diluent was used the membrane was removed from submersion and dried *in vacuo* at 90 °C for 12 h, leaving only EMI-Tf in the membrane due to its negligible vapor pressure.

$$uptake(wt\ %) = \frac{wt_{swollen} - wt_{dry}}{wt_{dry}} * 100\ % \quad (4.1)$$

$$uptake\left(\frac{mol\ IL}{mol\ SO_3^-}\right) = \frac{(wt_{swollen} - wt_{dry})/MW_{IL}}{wt_{dry}/EW} \quad (4.2)$$

Small angle X-ray scattering (SAXS) data is a part of the characterization performed at the Brookhaven National Laboratory on the Advanced Polymer Beamline (X27C) at the National Synchrotron Light Source. The methods employed to attain and process the data are the same as those described for the neat membranes in Chapter 2.

Dynamic mechanical analysis (DMA) was performed on a TA Instruments Q800 (3 °C/min) in a two point clamped tensile mode based on an imposed linear deformation of 15 μstrain at a frequency of 1 Hz. Sample dimensions were measured prior to the drying step. Distance between the clamps was set to ~10 mm unless sample size required a smaller setting to a minimum of 6 mm. The screw fittings on the clamps were set to a torque of 6.0 in-lb. If the sample was soft and tore or buckled the torque was decreased to as little as 0.5 in-lb. The temperature range observed was between 20 °C and the flow temperature displayed for a sample. Testing for the full range of temperature was performed under a N₂ blanket. Estimates of RT storage modulus (E') were made at 25 °C. Thermal transitions were estimated based on peak positions in the loss modulus (E'') signal. Each sample was repeated at least two times.

Electrical properties of the swollen and cast sBPS–EMI–Tf membranes were evaluated through EIS with an Autolab PGSTAT12 Potentiostat/Galvanostat and FRA2 Impedance Module over a frequency range of 1 MHz – 0.1 Hz. The instrument was operated in potentiostatic mode to apply a single 100 mV rms sine wave while measuring the complex impedance response of the sample. A custom fixture aligned two parallel rectangular brass rods at a defined separation of 0.3 cm to allow for in-plane impedance measurements with a maximum sample length of 3 cm. A load placed on top of the fixture ensured consistent and constant contact between the surface of the sample and the electrodes. All measurements were performed inside a custom-built Faraday cage and a humidity chamber at room temperature (RT) with controlled relative humidity (RH) of 42 ± 2 %. Ionic conductivity values (σ , S/cm) were calculated

$$\sigma = \frac{t}{R \cdot l \cdot w} \quad , \quad (4.3)$$

based on the in-plane 2-point measurement geometry and an estimate of the bulk membrane resistance (R , Ohm) where t (cm) is the sample thickness, l (cm) is the sample length, and w (cm) is the sample width. The Autolab FRA software was employed to fit a circle to the kinetic portion of the complex impedance data (Nyquist plot) to extrapolate the bulk membrane resistance as the low frequency x -intercept where the imaginary component of the impedance equals zero.[233, 244] After mounting each sample, the impedance was measured to detect equilibration of the membrane with the chamber humidity. Measurements for calculation of the conductivity were not recorded until the change in impedance with time was less than 0.75 % per minute. At this point three to five impedance measurements were performed sequentially. The average value of the bulk impedance was used to calculate the membrane conductivity. One standard deviation typically represented no more than 10 % error from the average value. Error was significantly smaller for less hygroscopic membranes, typically with lower ionic liquid uptake.

4.3 Results and discussion

The process of tuning novel synthetic polymers for application as ionic polymer transducers (IPT) requires attention to the interfaces of all components in the device. Results discussed in Chapter 3 for sBPS–EMI–Tf–RuO₂ IPTs highlighted the fundamental importance of interactions between these components in the electrodes to the optimization of electromechanical

transduction. The transducers were constructed with HB-3kBPS-20 and EMI-Tf through the casting process at 75 wt % uptake. Despite observations of percolation in ionic conductivity and increased capacitance through a range of RuO₂ loading, bending actuation was relatively slow and maximum strain was limited. The most direct method to achieve performance increases in subsequent sBPS–IPTs is the addition of linear and branched samples that contain a higher ion exchange capacity (IEC) to the experimental matrix, along with higher uptake levels. In this chapter, ionomers with approximately 20 and 40 mol % disulfonated repeat units in the backbone of the polymer are imbibed with the ionic liquid diluent through casting and co-diluent swelling methods. Due to the high bulk ionic conductivity of EMI-Tf (~9 mS/cm [246]), increased uptake within the polymer membrane serves to augment total ionic conductivity which is typically proportional to strain rate in bending actuator performance.[50] However, this relationship only remained valid with preservation of the membrane’s microphase separated morphology and homogeneous dispersion of the ionic liquid within the polymer.

4.3.1 IPT membranes cast in the presence of ionic liquids

Although not used previously for construction of IPTs, encapsulation/distribution of ionic liquids through casting from polymer solutions was performed with electrospinning[247] and membrane formation for fuel cells.[248, 249] Containment of the ionic liquid within the bulk polymer was an effective method to increase the ionic conductivity of the composite above that of the neat polymer. The study described in Chapter 3 was an initial attempt to construct novel IPTs with sBPS and EMI-Tf through a casting method but low strains and small strain rates even at optimized electrode compositions resulted. The performance was further supported with EIS measurements that revealed low ionic conductivity (~0.1–1 μ S/cm) through the thickness of the transducers for the full range of RuO₂ loaded electrodes. Model electrodes built in the absence of a central membrane demonstrated similar ionic conductivity up to the percolation threshold for RuO₂ content (22.5–30 vol %). Beyond percolation, conductivity of the electrodes increased to a maximum of 16 mS/cm at 42.5 vol % RuO₂. The primary difference between the two sample sets is the presence of the central membrane, which appears to be the origin of decreased conductivity in the built IPTs. The SEM micrograph in Figure 4.2a displays a cross-section of the first IPT constructed with the modified DAP method that used HB-3kBPS-20, EMI-Tf (75 wt % uptake), and RuO₂ (40 vol %) in the electrodes. The sample shown in the SEM micrograph is the first

recorded IPT constructed with 100 % novel ionomer and the DAP method. It is also the first recorded novel (non-commercial) synthetic IPT that employs ionic liquid as the diluent electrolyte.

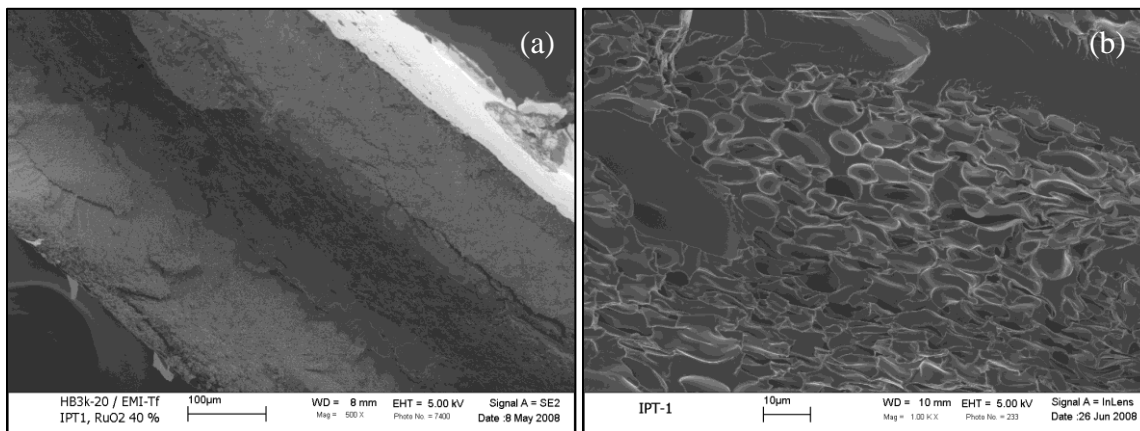


Figure 4.2: SEM micrographs of (a) the cross-section of an sBPS–IPT and (b) its central membrane cast from HB-3kBPS-20 solution and 75 wt % EMI-Tf uptake

Initial inspection of the IPT cross-section revealed that this specific sample has an approximate thickness of 450 μm , evenly distributed between the two outer electrode layers and the central ionomeric membrane. Based on the dimensions of the electrodes this was the thickest sample constructed. Samples from the percolation study in Chapter 3 averaged closer to 250 μm total due to improvement in the DAP casting method. Generally in IPTs with high ionic conductivity and sufficient electrical capacitance thickness of the electrodes should not limit transduction performance unless they become vanishingly small in comparison to the central membrane. This case would limit the active volume available for the formation of the electrical double layer, charge storage, energy transfer, and electromechanical transduction. Based on this assumption, insufficient ionic conductivity of the IPT was apparently the source of limited performance. Charge transport within the IPT is primarily dependent on the combined conductivities of the ionomeric membrane and the ionic liquid. Further inspection of the central layer in Figure 4.2a revealed a porosity gradient through the thickness (bottom left to top right). Higher magnification was employed to observe this area, as shown in Figure 4.2b. The pores are generally circular and appear to have an average diameter of 5-8 μm . This scale is much larger than the ionic aggregates (1-10 nm) typically associated with microphase separated

ionomers.[48] Central membrane porosity was not observed previously in SEM characterization of Nafion[®]-IPTs swollen with ionic liquids. Based on the casting steps for formation of the central membrane, the pores most likely originated from early separation of the ionic liquid from the sBPS-EMI-Tf casting solution. During solution preparation the hydrophilic ionic liquid demonstrated reduced solubility in DMAc solutions of HB-3kBPS-20 compared to neat DMAc. EMI-Tf ($\rho = 1.39 \text{ g/cc}$) also has a higher density than DMAc ($\rho = 0.937 \text{ g/cc}$) and after separation may settle toward the bottom of the casting solution. A gradient of encapsulated ionic liquid through the thickness of the central membrane formed as the DMAc evaporated and polymer concentration increased to approach the solid state. Indirect effects of the ionic liquid distribution gradient were observed during construction of further IPTs. As the amount of ionic liquid encapsulated increases through the thickness of the membrane, the elastic modulus should decrease based on local plasticization of the polymer. This occurrence may produce asymmetric actuation in the device. Plasticization of the central membrane due to IL uptake is characterized with DMA and will be discussed shortly. Presence of an ionic liquid distribution gradient in the electrodes may also create local variations in RuO₂ dispersion, morphology and ionic conductivity along the z-axis, the primary direction for charge transport during transduction, although this was not visible with SEM.

Operation of IPTs during electromechanical transduction is a combination of synthetic design, nanoscale organization, and microscale interfaces to create macroscopic motion and perform work. Regardless of their configuration, mode, or whether IPTs are leveraged as actuators or sensors; efficient charge transport is necessary for optimized performance. Although the introduction of ionic liquids into IPTs has many benefits with Nafion[®], it is necessary to confirm that those benefits remain with novel synthetic ionomers such as the sBPS series in this dissertation. Both Nafion[®] and sBPS contain the same sulfonate salt composed of a bound anion and a free cation. However, there are several distinct differences between the two polymers when considered in terms of their association, organization, and interaction with EMI-Tf ionic liquid. First, the fluorocarbon backbone of Nafion[®] is much more hydrophobic than the aromatic hydrocarbon backbone of sBPS. Also, the presence of electron withdrawing perfluoroether groups adjacent to Nafion[®]'s sulfonate salt make the anion much more acidic and polar than the same charged functional group in sBPS. The sulfonate salt of Nafion[®] is also located at the terminus of a short-chain branch off the backbone of the polymer while the sulfonate salts of

sBPS are placed directly on the aromatic rings in the backbone. These differences in acidity, polarity, and functionalization between Nafion[®] and sBPS are theorized to have direct effects on the degree and distribution of microphase separation within the ionomers that directly correlates with charge transport. The polytetrafluoroethylene (PTFE) matrix of Nafion[®] is also semi-crystalline whereas sBPS is fully amorphous. The presence of crystalline domains is known to enhance the solvent resistance in many polymer systems. EMI-Tf is considered a hydrophilic ionic liquid and could serve to either plasticize and/or dissolve sBPS. The below characterization techniques were used to investigate variations in morphological, mechanical, and electrical properties based on discrete uptake of EMI-Tf in sBPS through casting.

4.3.1.1 *Small-angle X-ray scattering*

To observe the effect of ionic liquid uptake on the microphase separated morphology of an ionomer it is first necessary to establish the presence of that structure in the absence of the diluent. The desired phase separated morphology based on ionic and nonionic domains was established in Chapter 2 for all samples of sBPS using small-angle x-ray scattering. The series of four sBPS ionomers investigated varied in both composition and polymer topology to produce matched pairs based on either parameter. Samples were prepared corresponding to the four ionomer compositions of interest for systematic IL uptakes with both casting and co-diluent swelling. However, limited sample time and beamline technical difficulties with two synchrotron attempts prevented data acquisition for the full series. Presently scattering data is only available for a single sample that was cast in the presence of EMI-Tf. Comparison between the 2-D SAXS scattering patterns of a dry HB-3kBPS-20 sample and its counterpart with 25 wt % uptake is shown in Figure 4.3. The previously identified ionomer peak of HB-3kBPS-20 ($q \approx 0.1 \text{ \AA}^{-1}$) experiences a large shift to lower q values due to a 25 wt % uptake of IL and begins to overlap with the feature referred to as the low angle upturn. Peak estimation indicates that the domain spacing (center-to-center) increases approximately 37 % at this uptake level. The domain separations that result are larger than any detected in the dry state for the full sBPS series. Values for Bragg scattering associated with the ionomer peak are provided in Table 4.2.

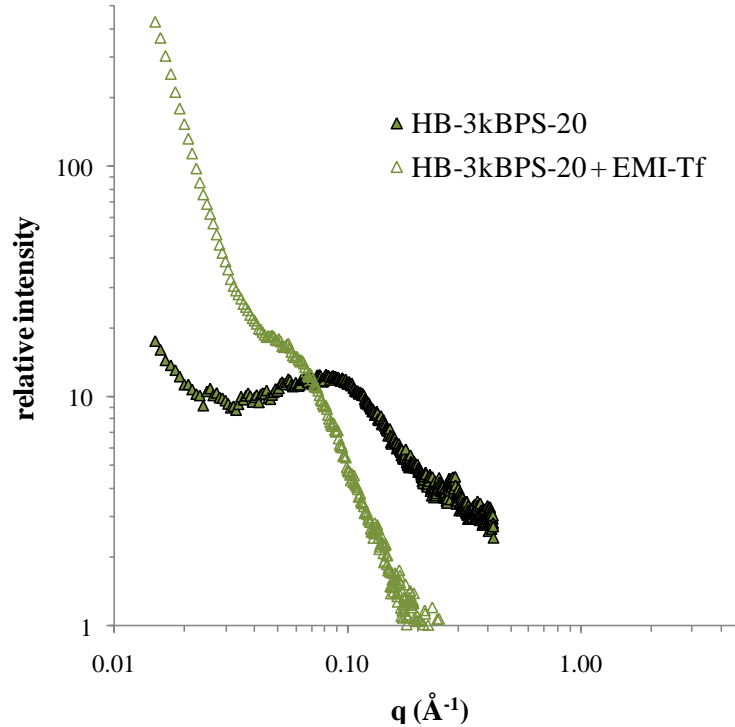


Figure 4.3: 2-D SAXS profile for HB-3kBPS-20 cast in the presence of 0% EMI-Tf (filled triangles) and 25 % EMI-Tf (open triangles)

On initial inspection, the size of the swollen ionomer domain appears to correlate well with a system where a hydrophilic diluent is selectively swelling the ionic domains of the host membrane. However, since the membrane was cast in the presence of ionic liquid, the ionic domains formed in the presence of a polar, non-volatile secondary component. Swelling in this case is not expected to mimic the uptake of a diluent into a microphase separated domain that was formed from a true solution. Association of the ionic liquid with the sulfonate salts and polar functionalities of the sBPS backbone during membrane formation may have affected the local polarity along the polymer backbone and frustrated microphase separation. This situation would lead to larger scale morphological structures and potential inhomogeneity in the distribution of sulfonated repeat units within the bulk matrix. Detection of these membrane characteristics with SAXS are typically associated with the low q upturn and have been investigated extensively for ionomeric and non-ionomeric polymer systems.[250-256] Scattering data for the imbibed sample at q values between $0.01\text{--}0.03 \text{ \AA}^{-1}$ displays a power law regression of -3.5 followed by a brief region from $0.03\text{--}0.04 \text{ \AA}^{-1}$ that has a slope of -1.7 . In comparison, the neat ionomer displays a regression of -1.25 for the same range of q . The presence of high electron density functionalities

on EMI-Tf as well as its ability to exchange cations with the sulfonate salts of sBPS create a complex environment for scattering analysis. Detection of possible reservoirs of EMI-Tf encapsulated within the bulk of sBPS with SEM may correlate with the very large scale inhomogeneities that begin to appear at low q and overlap with the distribution of ionic scattering centers for membranes formed in the presence of ionic liquid. Li *et al.* detected similar low q regression values and trends for a series of sulfonated polystyrene ionomers that indicated long-range inhomogeneities based on chemical composition and foreign particles (i.e., metals from neutralization).[257]

Table 4.2: Scattering features from peak fits of 2-D SAXS experiments with uptake

sample	uptake	ionomer peak		Porod slope (α)
	(wt %)	q (\AA^{-1})	d (nm)	$I \sim q^{-\alpha}$
HB-3kBPS-20	0	0.0800	7.86	1.25
	25	0.0583	10.8	3.49

While the similar trends from different characterization techniques are interesting, correlation will require extensive further scattering and microscopy studies beyond the present data and associated sample sets to distinguish between the effects of the uptake methods. The full morphological study should include samples from all four ionomers imbibed with both the casting and co-diluent methods. Uptake levels should include a large number of samples between 0 – 25 wt % to observe the evolution between the two curves shown above with a corresponding comparison to swelling with co-diluents. Characterization techniques should include multi-angle X-ray scattering (i.e., USAXS, SAXS, WAXS) to investigate large scale heterogeneities, variations in the ionomer peak, and effects of any ionic liquid in the hydrophobic matrix on the amorphous halo. Scattering studies with variable temperature sweeps may aid in correlation with transitions detected in DMA. Scattering studies should also be coupled with high-angle annular dark field scanning transmission electron microscopy (HAADF-STEM) in an effort to correlate ionic aggregate size similar to the work of Winey *et al.*[195, 258] Additional techniques shown to be effective for investigation of ionomer morphology and charge transport include atomic force microscopy,[259, 260] FTIR,[61] and NMR.[80, 142, 261, 262]

4.3.1.2 *Dynamic mechanical analysis*

One of the primary reasons for investigating sBPS as potential IPT membrane is its high elastic modulus combined with the ability to synthesize target degrees of sulfonation for high ionic conductivity and the potential for IPTs with increased energy density. Thus, each of the four target ionomer compositions was cast in the presence of target uptakes of ionic liquid (0, 25, 50, 75, and 100 wt %) to form free-standing membranes. The uptake series creates a range of membranes from neat sBPS to essentially a 50/50 w/w sBPS–EMI-Tf membrane. DMA was employed to characterize the sBPS–EMI-Tf series for the magnitude of change in E'_{hy} and the corresponding thermal transitions with IL uptake.

Table 4.3: Thermal transitions from DMA of sBPS ionomers cast with EMI-Tf

sample	uptake (wt %)	T_{γ} (°C)	T_{β} (°C)	T_{α} (°C)	T_{plateau} (°C)	T_{flow} (°C)
Lin-BPS-20	0	55	261	313	330	368
	25	59	124	188	208	224
	52	63	125	157	196	228
	76	59	120	146	187	243
	100	51	114	136	182	237
Lin-BPS-40	0	69	270	358	417	450
	25	76	121	216	246	263
	50	52	123	148	186	209
	75	57	118	138	179	198
	98	59	114	134	173	224
HB-3kBPS-20	0	63	242	281	296	306
	25	78	128	182	213	225
	50	59	123	157	187	198
	76	60	116	143	174	207
	108	56	126	150	178	197

The full experimental results for all detected thermal transitions versus uptake from DMA of the sBPS series are provided in Table 4.3. Data is unavailable for the HB-3kBPS-40-EMI-Tf series since these membranes were too fragile to withstand placement in the clamps of the tension fixture for DMA. Figure 4.4a, b, and c are representative of the temperature dependence of E' , E'' , and $\tan \delta$ respectively for varied EMI-Tf uptakes in cast membranes of Lin-BPS-20. The trends observed for all three DMA signals were similarly reflected for runs with HB-3kBPS-20 and Lin-BPS-40. All ionomers investigated displayed five distinguishable thermal transitions similar to those reported in Chapter 2. Beginning at high temperature and working down, weak rubbery plateaus were observed for each ionomer-ionic liquid combination in the E' signal. The high temperature transition of this plateau region coincided with the onset of flow (T_{flow}) where the supplied thermal and mechanical energy combination was sufficient to overcome all secondary associations, chain entanglements, and molecular friction. However, this is not a melting temperature since these polysulfone ionomers were shown in Chapter 2 to be fully amorphous and the T_m of EMI-Tf is $-10\text{ }^\circ\text{C}$.^[246] The low temperature transition that initiates the plateau was identified as the onset temperature of the plateau region (T_{plateau}), primarily to provide information on the breadth of the plateau with changing composition. This temperature represents polymer interactions that resist flow after the onset of full segmental motion (T_g) in the polymer backbone. In addition to expected effects of molecular weight and polydispersity on entanglements, sBPS contains ionic aggregates that at elevated temperatures can still dynamically act as effective crosslinks.^[48, 263] In decreasing order three further transitions were identified at temperatures below T_{plateau} : T_α , T_β , and T_γ . The E'' signal was primarily employed to identify these three transitions and Figure 4.4b is plotted on a linear scale to aid observation of these lower temperature transitions.

In the case of the neat ionomers, the primary thermal transitions are the same as those identified in Chapter 2 for the full sBPS series. T_α experienced a two to three order of magnitude decrease in E' and displayed the dominant peak in E'' for all three ionomer compositions. These are classic indicators of the onset of polymer segmental motion and the transition was assigned as a T_g . However, due to the variation in the peak temperature with changes in degree of sulfonation T_α was again assigned as a transition of the cluster phase itself ($T_{g,cl}$). Eisenberg *et al.*

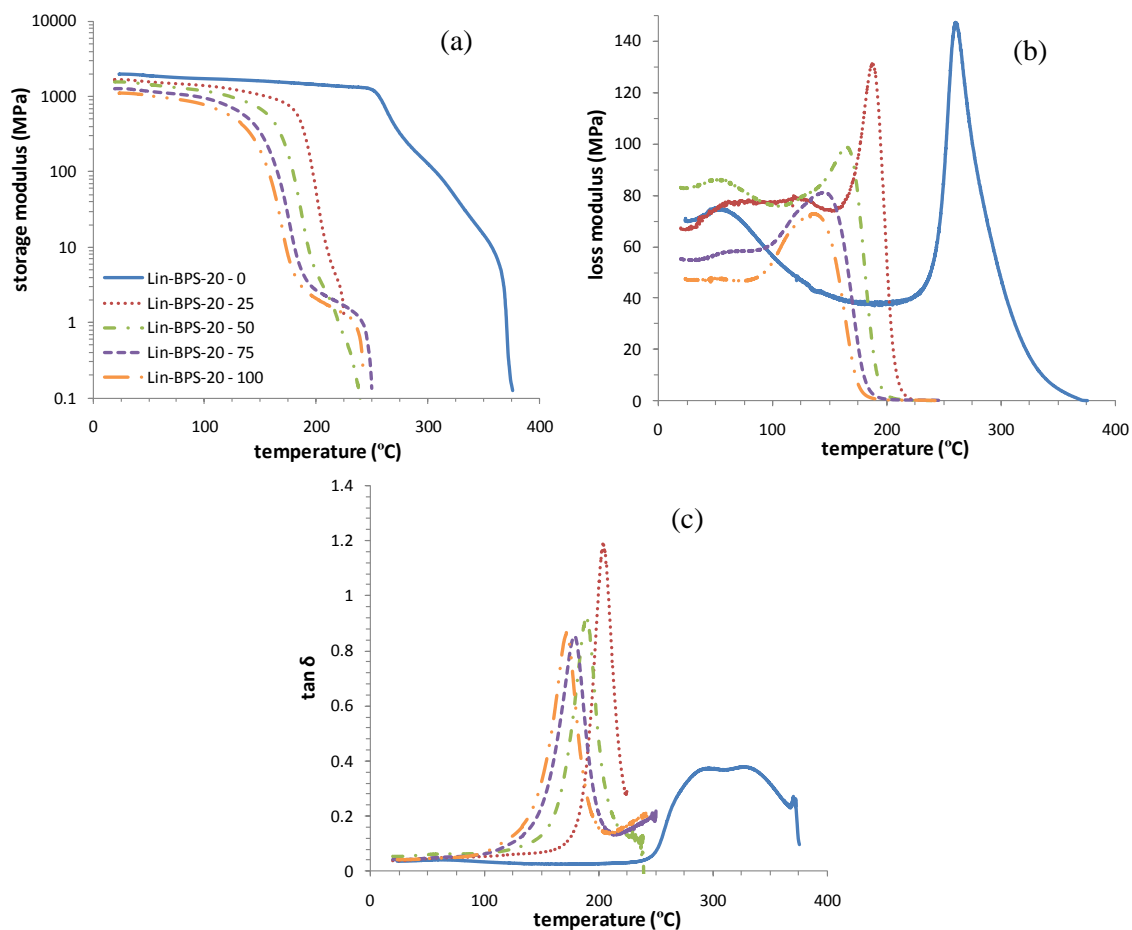


Figure 4.4: DMA (a) E' , (b) E'' , and (c) $\tan \delta$ versus temperature for Lin-BPS-20 cast in the presence of 0 – 100 wt % uptake of EMI-Tf

suggested this transition was a combination of ion-hopping and segmental motion of the chains with reduced mobility within and surrounding the clusters.[45, 228, 264] Overall, $T_{g,cl}$ transitions the physical crosslinks from a static to a dynamic network of associations based on increased temperature.[80] $T_{g,cl}$ for ionomers in the sodium sulfonate form has been reported often between 200-300 $^{\circ}\text{C}$ for DMA studies[80, 226, 228, 265-267] and in this case persisted to temperatures much in excess of 300 $^{\circ}\text{C}$ due to comparatively high levels of sulfonation. T_{β} was assigned to the T_g of the non-sulfonated polysulfone matrix ($T_{g,m}$). As discussed in Chapter 2, the presence of isolated multiplets in the bulk of the hydrophobic phase does increase $T_{g,m}$ above the typical value for non-charged biphenol-based polysulfones (~ 220 $^{\circ}\text{C}$). The high baseline T_g associated with these polysulfones results in a large overlap between $T_{g,m}$ and $T_{g,cl}$ in sBPS ionomers. As seen in the $\tan \delta$ curves for neat Lin-BPS-20 in Figure 4.4c, the $T_{g,cl}$ persists to higher

temperature while $T_{g,m}$ appears as a shoulder at slightly lower temperature. The final consistent transition, T_γ is in the range of temperature from 40-80 °C. Presently it is assigned to the loss of residual water from these hygroscopic membranes. Even after drying, the membranes absorb water during mounting. The same transition was observed in Chapter 2 for neat membranes run in air, where the magnitude of the peak changed with annealing. Notably, T_γ appears at lower temperature for this study where all runs were performed under a N_2 flow.

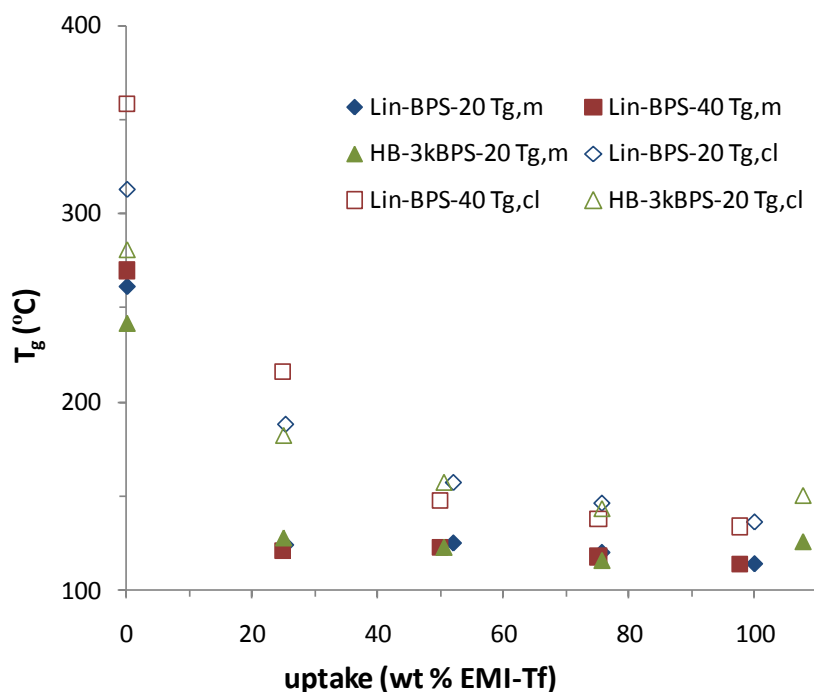


Figure 4.5: Matrix $T_{g,m}$ and cluster $T_{g,cl}$ versus wt % uptake for sBPS cast in the presence of EMI-Tf

Several distinct changes occur in the dynamic mechanical behavior of the sBPS ionomers on introduction of EMI-Tf to the membrane. The most obvious effect is the plasticization and resultant decrease of both $T_{g,m}$ and $T_{g,cl}$ with increased uptake of EMI-Tf. This effect is shown specifically for Lin-BPS-20 in Figure 4.4 and recorded for all three sBPS ionomers in Figure 4.5. At this point it is worthwhile to remember that these membranes have targeted amounts of ionic liquid cast into them, not swollen into a preformed membrane. Therefore, plasticization effects are anticipated to be different from typically swelling experiments due to the fact that microphase separation occurs in the presence of the diluent. Although EMI-Tf is hydrophilic due to its ionic nature, the bulky organic ions also may interact with the ether oxygens and polar

sulfone groups of the nonsulfonated repeat units during membrane formation. As is seen in the plots, $T_{g,m}$ of all three ionomers decreases by a factor of two to a nearly constant value of 120 °C when formed in the presence of 25 wt % uptake or greater of EMI-Tf. The value of $T_{g,cl}$ with uptake decreases at a lesser slope and reaches a plateau value at approximately 50 wt % uptake. Regardless of the degree of sulfonation or polymer topology all three ionomers plateau at the same $T_{g,cl}$ value (~140 °C). Following formation, the membrane series displayed increasing opacity with IL uptake, implying the formation of large scale heterogeneities that were also detected with SAXS and potentially SEM. If those heterogeneities are associated with bulk separation of IL from the matrix and cluster volumes this may contribute to the plateau in T_g values. Also of note is that at higher uptake of EMI-Tf, the length of the rubbery plateau increases. This appears to be a result of the associations/ion exchanges between the sodium sulfonate salts and EMI-Tf that consistently persist to 200-250 °C despite continued plasticization of the bulk ionomer as shown with $T_{g,m}$ and $T_{g,cl}$.

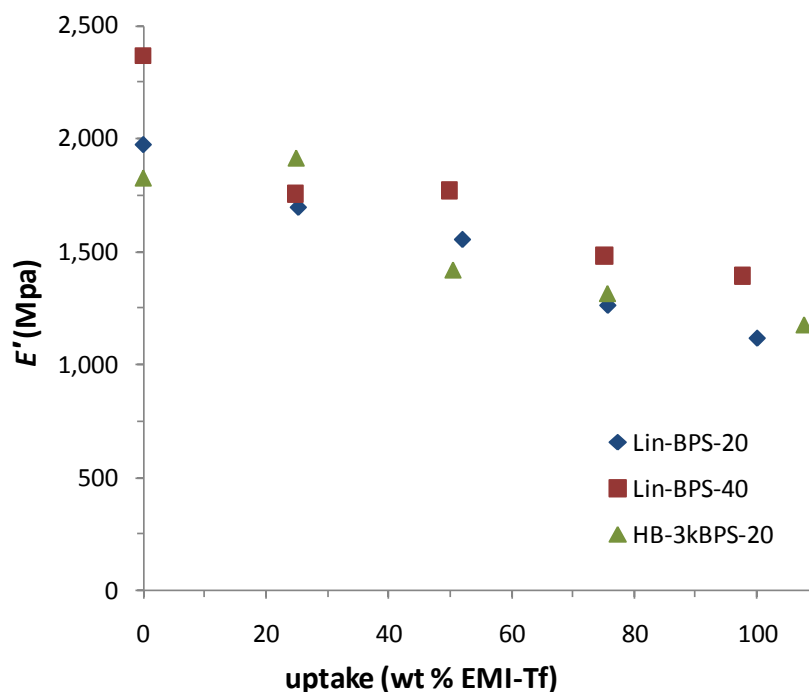


Figure 4.6: Storage modulus (hydrated) versus wt % uptake for sBPS cast in the presence of EMI-Tf

Simultaneous with the trend in the glass transitions the RT E'_{hy} (Figure 4.6) decreased with uptake of ionic liquid. The hydrated modulus did not appear to plateau in the range investigated

but did retain a high value. Even systems that were essentially composed of a 1:1 weight ratio of polymer to ionic liquid demonstrated over 1 GPa of hydrated modulus for all three ionomer compositions. Water hydrated Nafion[®], the present benchmark IPT membrane, has a reported E' of 120 MPa at 22 wt % uptake,[108] ten times less than sBPS membranes cast with EMI-Tf. Nemat-Nasser has reported extensively on micromechanical modeling of the stiffness of Nafion[®] swollen with various diluents.[47, 268] His models correlate with experimental results that demonstrate a $-4/3$ power law regression in both swollen membrane and built IPT stiffness with increased diluent uptake. This exponential decrease in stiffness with increased uptake is not observed here for membranes formed in the presence of the diluent and similar fits did not produce good correlation, likely due to the difference between the casting technique and traditional membrane swelling for uptake of the diluent. Characterization of the cast membranes for ionic conductivity with electrical impedance spectroscopy follows in the next section.

4.3.1.3 *Electrical impedance spectroscopy*

To further probe the effect of casting membranes in the presence of ionic liquid on charge transport, in-plane EIS was performed on the series of samples that targeted 0, 25, 50, 75, and 100 wt % ionic liquid per weight of sBPS. If EMI-Tf separated to form a gradient distribution of heterogeneities during formation then the membrane face that was in contact with the substrate could have greater in-plane ionic conductivity than the face open to the air during DMAc evaporation. The dependence of sBPS ionic conductivity (in-plane) on the molar uptake of EMI-Tf is plotted on both a semi-log and a linear scale in Figure 4.7a and b respectively. Both faces of each sample were tested and are indicated as “A” and “B.” As with DMA, the HB-3kBPS-40 samples with uptake above 25 wt % were too fragile for consistent characterization in the fixture employed for the rest of the series and are not shown here. Overall, the face-to-face discrepancies for in-plane conductivity were small but statistically real and accentuated at higher uptake, indicative of a concentration gradient of ionic liquid distribution through the thickness of the membrane. The difference in conductivity between faces of the same membrane is also more prevalent in the 20 % sulfonated ionomers than the 40 % sulfonated samples. Higher hydrophobic content in the polymer backbone at lower levels of sulfonation likely decreased compatibility with the hydrophilic ionic liquid to cause lower solubility of the components during membrane formation. On the time scale of membrane formation, this was observed as

earlier appearance of opacity in the 20 mol % disulfonated series than for the 40 mol % disulfonated samples. Despite the presence of these heterogeneities as detected with SAXS, DMA, and EIS the difference in conductivity between faces of the same membrane is much smaller than the overall change in charge transport achieved for each increased target of IL uptake with the casting method.

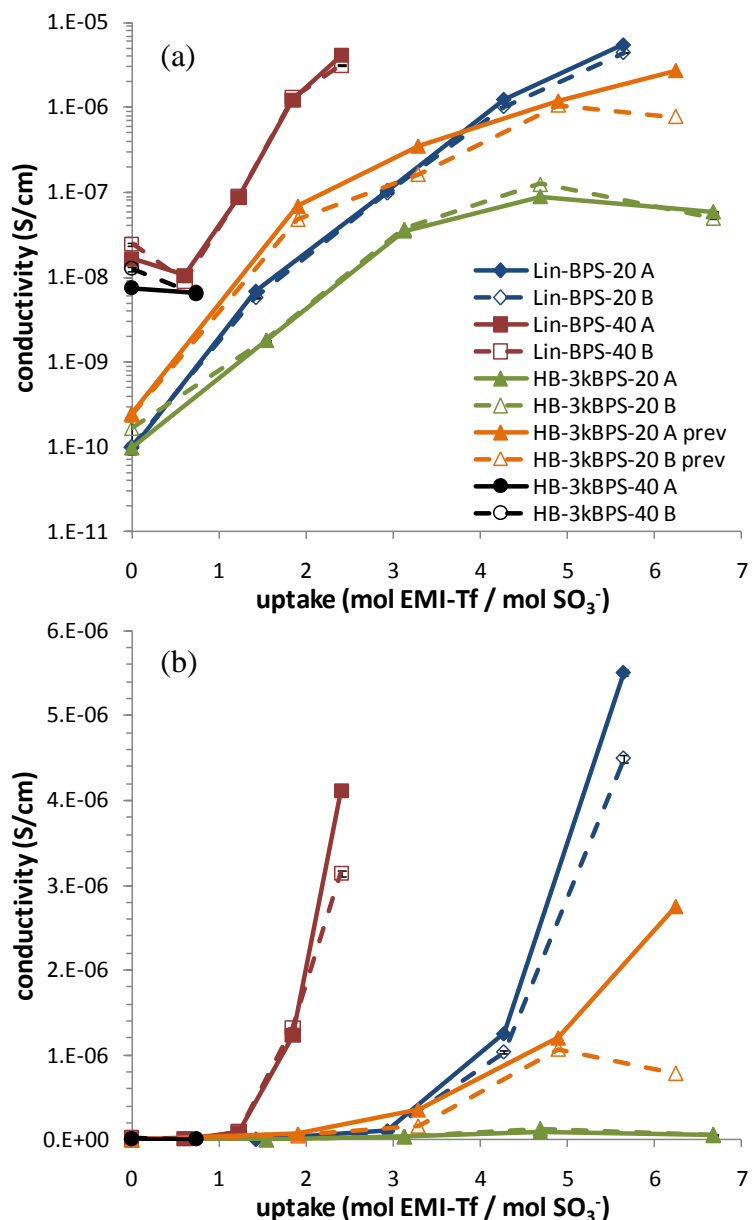


Figure 4.7: (a) Semi-log and (b) linear plots of in-plane ionic conductivity versus molar uptake for sBPS membranes cast in the presence of EMI-Tf. “prev” indicates data for comparison from a previous study. A and B represent the faces of the ionomer membranes tested.

Despite minor gradient formation, the initial introduction of ionic liquid to sBPS results in a significant increase in conductivity above the level of the dry membrane and reproducibly meets the targets for each ionomer composition. However, there is a small decrease in conductivity of the 40 % sulfonated membranes before the upturn in conductivity. Both the linear and branched membranes at this sulfonation level display a higher conductivity in the neat state than membranes cast in the presence of 25 wt % ionic liquid. This trend implies that the equilibrium microphase separated morphology associated with the neat ionomer is optimal for charge transport and is not formed during casting in the presence of ionic liquid. For these ionomers statistical placement of sulfonated repeat units during reaction causes fluctuations in local polarity along the polymer backbone that lead to formation of charge transport pathways. Association of the hydrophilic ionic liquid with these random copolymers during membrane formation appears to reduce the driving forces for microphase separation and therefore affect the conductivity of the final membrane. However, uptake levels above 25 wt % for Lin-BPS-40 provide bulk conductivities that surpass those of the neat ionomer by more than two orders of magnitude. This inflection point in conductivity is not detected with EIS for the 20 % sulfonated samples. The much lower conductivity of the neat membranes at the lower sulfonation level enhances the difference between the bulk conductivity of the ionomer and the ionic liquid. The conductivity gain based on 25 wt % uptake of ionic liquid is apparently greater than the decrease in charge transport due to a less defined microphase separation of the ionomer. Although not investigated in this dissertation, these trends suggest that further development of the casting method to maximize stable morphologies formed in the presence of the ionic liquid would likely achieve large gains in ionic conductivity. Tuning parameters could potentially include addition of surfactants, multi-step procedures, annealing regimens, and co-solvents.

Two distinct polymer-to-polymer trends stand out in the conductivity data. First, the influence of branching appears to consistently decrease the attainable conductivity of cast sBPS – EMI-Tf. This trend appears for both levels of sulfonation, although more data is required for HB-3kBPS-40 before confirmation. Regardless, the values for the present series of membranes formed with HB-3kBPS-20 are consistently lower than those for Lin-BPS-20. The two ionomers have nearly the same ionic conductivity in the dry state but respond differently to the introduction of ionic liquid. The branched polymer appears to reach a plateau in conductivity with increased uptake. HB-3kBPS-20 values from a previous study (indicated “prev”, triangles)

where the cast membranes were annealed (1 h plus cool) at temperatures just above the distinct $T_{g,cl}$ for each sample also show similar trends at high uptake. In contrast, the primary sample set discussed here was annealed (i.e. residual DMAc removal) at 250 °C for 1 h followed by a slow cool. As was shown with DMA, this annealing temperature is higher than both the $T_{g,m}$ and $T_{g,cl}$ for all cast membranes except for the neat samples (0 wt % uptake). The higher annealing temperature appears to decrease the difference in face-to-face conductivity. However, this may be due to increased homogenization of the membrane's morphology that overall results in lower conductivity. Subsequent tests would benefit from use of the lower annealing temperature to increase conductivity beyond the levels displayed here. Secondly, the degree of sulfonation of the ionomer has a direct effect on the achieved ionic conductivity per molar uptake. Lin-BPS-40-100 and Lin-BPS-20-100 demonstrate nearly the same ionic conductivity although they differ in molar uptake by a factor of 2.35. One mol of EMI-Tf per one mol of SO_3^- in Lin-BPS-40 results in higher conductivity than the same molar ratio in Lin-BPS-20. This result suggests that the bulk conductivity of cast membranes at high uptake levels (>25 wt %) is dependent on the interaction of the ionic liquid with the ionomer as a whole, not just the available free cations as was pertinent for Nafion[®].

At uptakes corresponding to greater than 50 wt %, differences in conductivity based on ionomer composition are more visible on the linear plot in Figure 4.7b. A critical uptake (f_c) was previously described in terms of its important link to increased Nafion[®]-IPT actuation with ionic liquids.[61] With EIS, f_c is typically detected as an inflection point in the linear plot of ionic conductivity versus molar uptake, similar to the curves in Figure 4.7b. Phenomenologically this parameter was defined as the amount of free bulk ionic liquid available for charge transport within an ionic liquid swollen membrane. This free ionic liquid is considered to be in excess of the diluent that participates in the initial ion exchanges with the bound anions of the ionomer. For the combination of Nafion[®] and EMI-Tf, the ionic liquid was concluded to preferentially swell the hydrophilic phase of the ionomer. As determined from Figure 4.7b the critical uptakes for Lin-BPS-20, Lin-BPS-40, HB-3kBPS-20, and HB-3kBPS-20prev are 2.94, 1.23, 3.13, and 3.29 mol EMI-Tf / mol SO_3^- respectively. These values were used to normalize the molar uptake and produce the relationships shown in Figure 4.8a and b. The conductivity values for ionomers of different degrees of sulfonation and different polymer topologies collapse to nearly a single

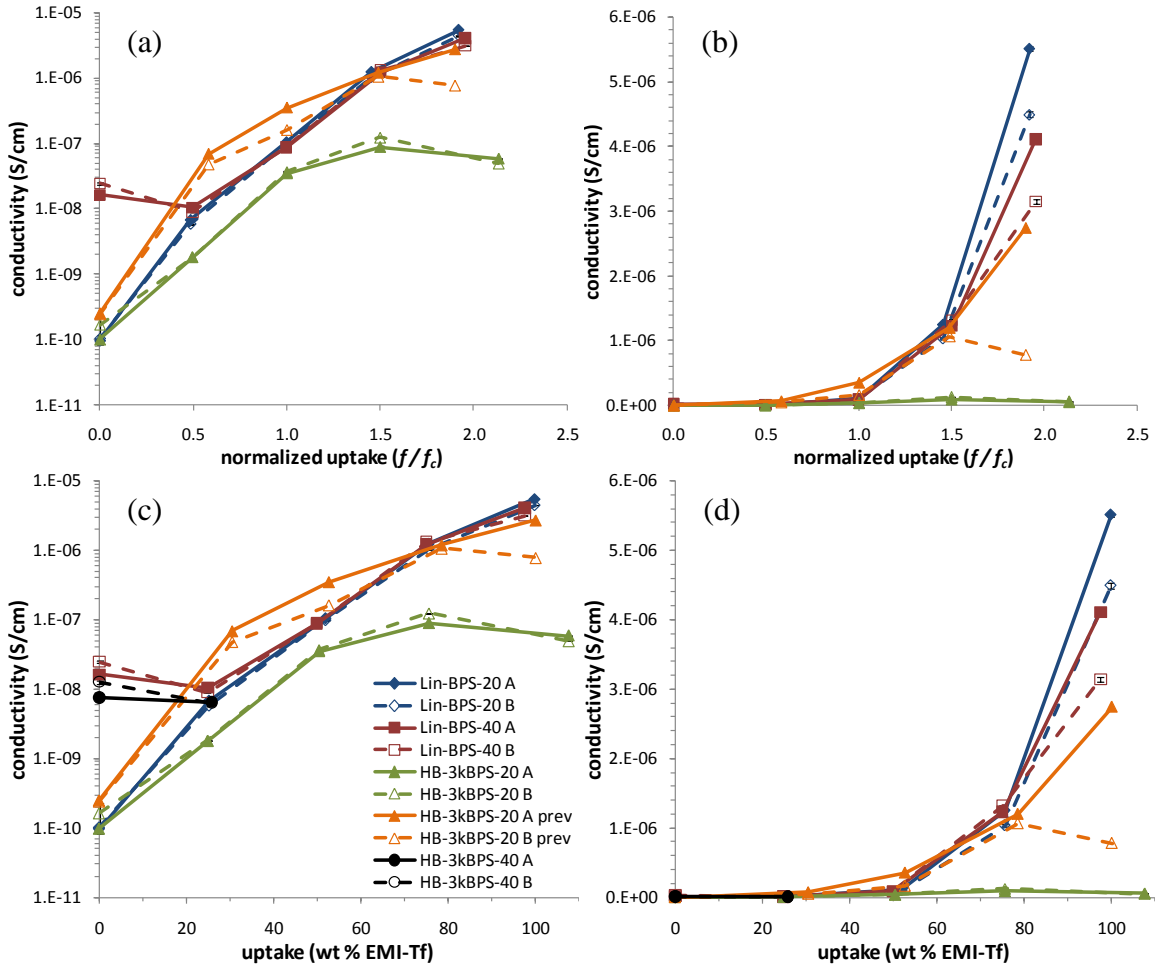


Figure 4.8: Semi-log and linear plots of in-plane ionic conductivity versus (a & b) normalized molar uptake (c & d) wt % uptake for sBPS membranes cast in the presence of EMI-Tf. “Prev” indicates comparison data from a previous study.

curve based on this normalization. The difference in conductivity with normalized uptake is minimized for the linear samples in comparison to the branched ionomers, especially above 25 wt % uptake. Also notable is a similar trend to collapse conductivity per uptake when the series is plotted versus wt % uptake. Both methods accounts for the amount of ionic liquid encapsulated in the membrane, with no distinction as to its location, association with a specific phase, or the composition of the host membrane. These two treatments for the conductivity data confirm that the amount of ionic liquid in the membrane is the dominant parameter for conductivity and is emphasized by a large increase in conductivity beyond some percolation threshold. Interestingly, that percolation threshold in conductivity aligns with the uptake level (50 wt %) where $T_{g,m}$ and $T_{g,cl}$ reached a plateau. Decrease in the T_g implies local plasticization

of the ionomer chains by direct interaction with the ionic liquid. If the heterogeneities detected in SEM and SAXS are indicative of porosity that contains bulk EMI-Tf, then it is likely that percolation indicates increased connectivity between these pores and a less tortuous path for charge transport by the ions of EMI-Tf. The branched topology of HB-3kBPS-20 is likely to increase swelling due to a lower number of chain entanglements. If more of the free ionic liquid is absorbed into the polymer matrix this may create a more tortuous path for charge transport and reflect the decreased conductivity at all uptake levels. The uptake at the percolation threshold is likely a saturation point of the polymer matrix based on absorbance of the ionic liquid. An interesting test of this baseline would be to cast similar loadings of EMI-Tf into non-sulfonated BPS and less sulfonated sBPS to observe if the trend remains. Combination of these results confirms that the conductivity of the ionic liquid dominates the charge transport in membranes that result from the casting method. With this treatment of the data it is straightforward to determine the minimum uptake of EMI-Tf necessary to design an IPT with targeted ionic conductivity for performance, regardless of the ionomer composition.

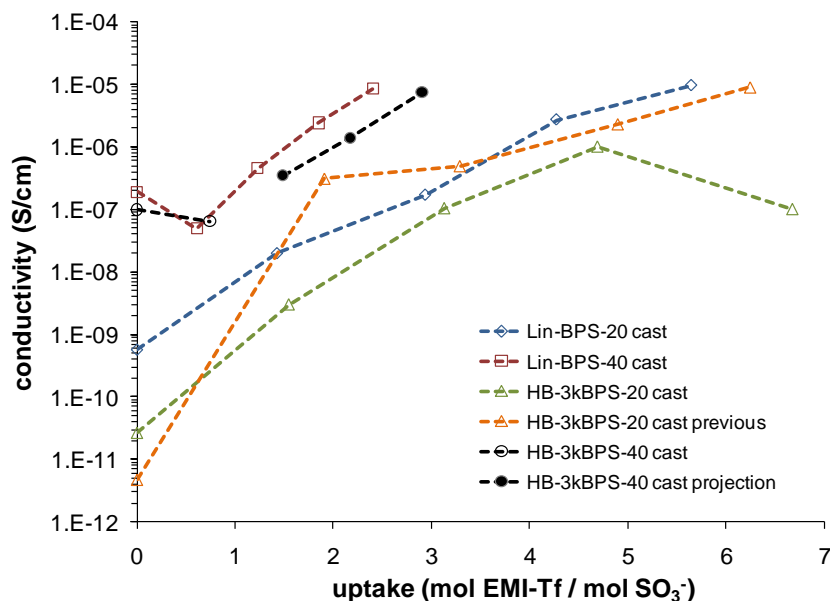


Figure 4.9: Confirmation experiments for ionic conductivity versus molar uptake of sBPS cast in the presence of EMI-Tf

Due to the dependence of conductivity from EIS measurements on environmental parameters the cast series of membranes was retested for confirmation of the above magnitudes and trends. The experimental matrix was randomized per running order and the samples were allowed more time to equilibrate at 40 % RH in the environmental chamber. Noise in the measured signal was minimized with a Faraday cage and improved grounding which was essential for measurements of the 20 % sulfonated samples in the neat state. This set of tests was also included samples produced through the co-diluent method discussed in the next section. The in-plane conductivities versus molar uptake of ionic liquid for confirmation of all four sBPS ionomers are plotted in Figure 4.9. The data points for HB-3kBPS-40 from ~1.5 – 3 molar uptake are noted as projections and due to the time intensive nature of the tests, only a single face of each membrane was tested. The trends discussed previously are preserved, although the overall conductivity of all membranes is slightly increased due to longer residence time in the constant RH chamber. Equilibrium values of impedance were based on a rate of change between measurements of 0.25 % per minute or less and included at least three repetitions. The values shown in Figure 4.9 are those employed for reference to each ionomer composition for the remainder of the dissertation. In its present state, primary benefits of the casting method are predictability of the final uptake, a single step process, increased conductivity greater than the proportional decrease in hydrated modulus, and applicability to target electrode compositions for construction of IPTs.

4.3.2 IPT membranes swollen with ionic liquids

The second direct method used to facilitate uptake of ionic liquids into the ionomeric membrane was immersion in EMI-Tf with time, temperature, and/or some co-diluent. Based on the premise that the diluent enters the fully preformed rectangular membrane through all six faces, anisotropy in the distribution of EMI-Tf is less likely to occur than in the case of membranes cast in the presence of the ionic liquid. However, importance is placed on determination of the path of the ionic liquid during absorption into the membrane and its final location once saturation is reached for the imposed conditions. The preferred final condition would result from the ionic liquid's traversal of the detected microphase separated morphology to swell the hydrophilic phase with minimal disruption of the surrounding hydrophobic matrix. This situation allows for the assumption that the mobile cations associated with the sulfonate salts on the backbone of the polymer are placed in a solvated state and are easily displaced within the defined charge

transport pathway under the application of a driving voltage. Previous studies indicate that the chemical compositions of the ionomer and the ionic liquid, the magnitude of uptake, and the swelling conditions affect the final morphology and ionic conductivity.[50, 269, 270]

Covalently crosslinked polymers are not soluble and swell less than their noncrosslinked compositional analogues due to decreased chain mobility as the crosslink density increases above a value of zero.[263] Neither the highly branched nor the linear ionomers studied here are chemically/covalently crosslinked. In the dry state all of the ionomers contain physical crosslinks due to the association of the sulfonate salts present on the backbone and already discussed.[48] In the swollen state, the presence of a hydrophilic diluent could disrupt the strength of these ionic associations and leave mainly the friction of polymer chain entanglements and compositional solubility parameters to act as the main forces to resist dissolution.

4.3.2.1 Swelling methods applied to sBPS

Attempts to swell the series of linear and branched membranes were initially conducted only in EMI-Tf at RT. These mild conditions were chosen to investigate the possibility that, due to its chemical composition, the ionic liquid could serve as a partial solvent for sBPS when present in large excess. The RT swelling data is presented in Figure 4.10 (solid line, solid symbols). All four ionomers experienced uptakes of 0-10 wt %, where HB-3kBPS-20 consistently displayed the greatest uptake. In the case of HB-3kBPS-20, the branched nature of the polymer limits the ability of its chains to entangle, allowing it to swell more than the linear ionomer (Lin-BPS-20) in EMI-Tf. The uptake values for the 40 mol % sulfonated polysulfones are centered around or below zero across the full period of time. This result likely originates with increased degree of sulfonation that provides higher relative polarity of the membrane in comparison to the ionic liquid. Negative values of uptake were attributed to partial dissolution of the membrane surface balanced with EMI-Tf absorption and error in the measurement of very small mass changes.

After 200 h at RT in EMI-Tf the swelling samples and baths were heated for 2 h to 55 °C before cooling to RT for 4 h. These results are depicted as dashed lines and solid symbols in Figure 4.10. Every ionomer's uptake during this time appeared to increase over the final value observed at RT, although the final levels were not distinguishable from the average RT uptake over after 200 h. In comparison, sBPS swollen over 2.5 h in neat EMI-Tf at 110 °C displayed increased uptake levels. In this case the 40 mol % sulfonated samples had a greater uptake rate

while the 20 mol % sulfonated samples displayed a maximum in uptake after 2 h. These conditions achieved at least 20 wt % uptake for all sBPS membranes where branched ionomers experienced greater uptake than their linear counterparts. A balance of time and temperature to facilitate targeted uptake of neat EMI-Tf into sBPS is justified in the event that morphological stability and ionic conductivity are sufficient for those conditions.

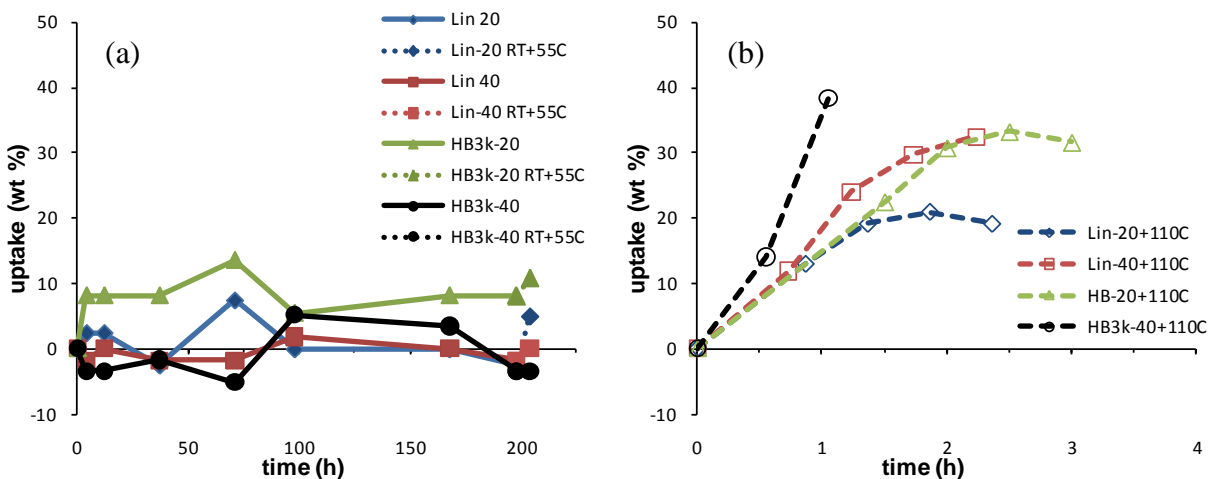


Figure 4.10: Uptake versus time for the sBPS series swollen in 100 % EMI-Tf at (a) RT + 55 °C (b) 110 °C

The primary alternative to long swelling times and application of heat to facilitate uptake is the use of a co-diluent. In this case a second diluent is added to EMI-Tf to enhance swelling of the membrane and allow easier entrance of the ionic liquid into the network of physical crosslinks. Initially the series of sBPS membranes was swollen with a range of potential co-diluents, listed in ascending order of dielectric constant: toluene (TOL), ethyl acetate (EAc), isopropyl alcohol (IPA), methanol (MeOH), water (H₂O), and N-methyl formamide (NMF). Maximum swelling was achieved in NMF, which fully dissolved all membranes in under 8 h. MeOH displayed the largest and fastest uptake for all members of the sBPS series, without dissolution. H₂O performed nearly as well and is a potential non-organic, polar co-diluent that could supplement or replace MeOH in further studies, although not discussed here.

The full series of sBPS ionomers was swollen with EMI-Tf in the presence of MeOH where MeOH composed 20 – 80 wt % of the swelling bath. The EMI-Tf uptake results for all ratios of the co-diluents are shown in Figure 4.11. The first 30 h swelling period was at RT. Further

swelling beyond this point was performed for 2 h at 55 °C plus a 4 h cool to RT. The membranes were removed from the swelling baths and dried in vacuo at 90 °C for 12 h to remove the MeOH. Although this method introduces an extra drying step into the process the uptake results are significantly increased compared to similar heating cycles in 100 % EMI-Tf. Overall, the co-diluent ratios resulted in greater uptake in the 40 mol % sulfonated polymers than the 20 mol % counterparts. HB-3kBPS-40 consistently displayed the greatest uptake, likely due to its branched topology and high degree of sulfonation. Some contribution to the high swelling levels for HB-3kBPS-40 may also originate with the slightly lower molecular weight that was reported in Chapter 2. Due to this potential contribution, an obvious trend in uptake is not apparent based on polymer topology for both levels of sulfonation. Except for Lin-BPS-40 (max uptake at 20 % MeOH), the co-diluent composition of 40/60 w/w MeOH/EMI-Tf provided the maximum overall uptake of ionic liquid for the sBPS polymer series. Full miscibility of the co-diluents appears to reduce the ability of EMI-Tf to dissolve sBPS during swelling. This ratio likely resulted in the maximum uptake for sBPS because of the balance between the ability of MeOH to swell the membranes and the majority content of EMI-Tf left after vacuum removal of MeOH. Application of heat to increase uptake was also successful, although without the use of pressure vessels it is limited to the boiling point of MeOH (b.p. 64.7 °C) and in some cases appears to increase the dissolution rate of already swollen membranes.

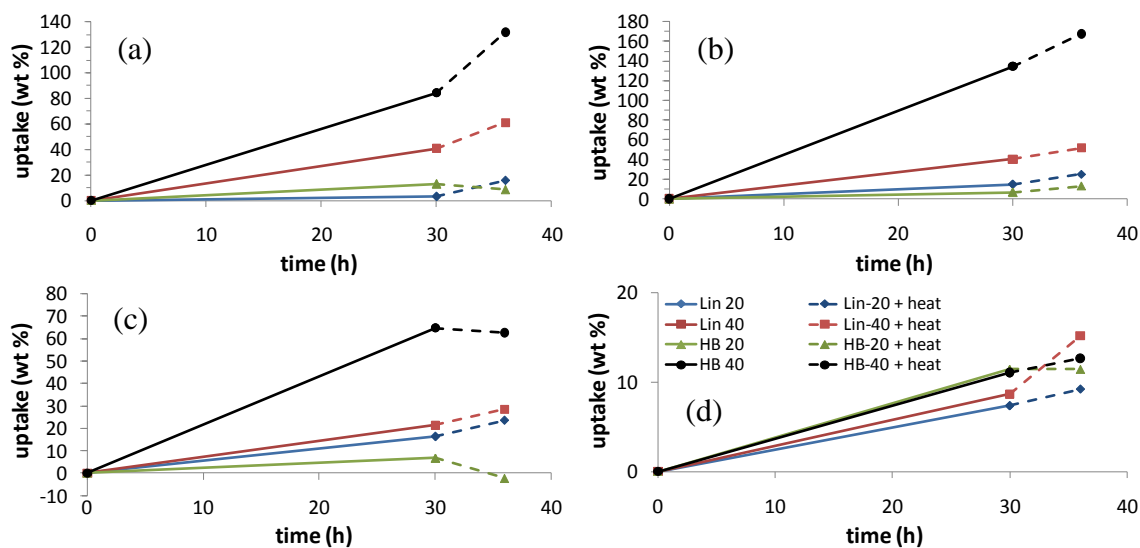


Figure 4.11: EMI-Tf uptake versus time for sBPS immersed in (a) 20/80 (b) 40/60 (c) 60/40 (d) 80/20 w/w MeOH/EMI-Tf

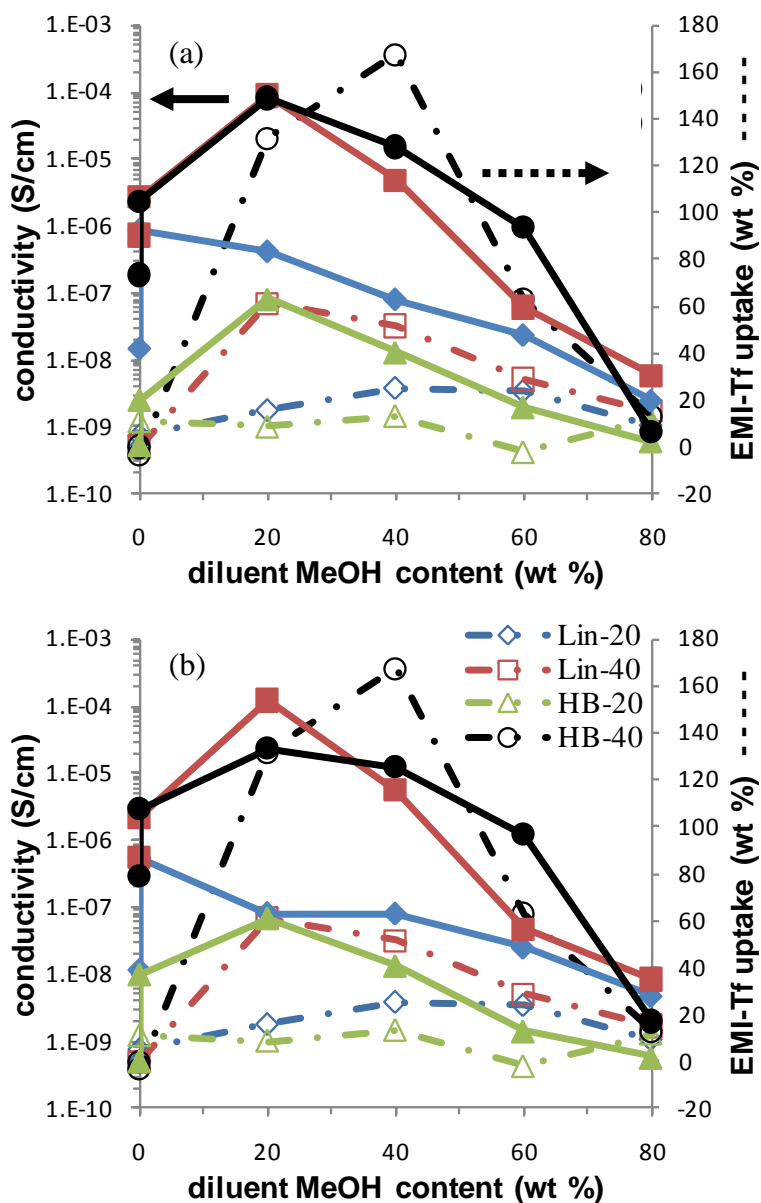


Figure 4.12: In-plane conductivity (left, solid line) and swelling uptake of EMI-Tf (right, dotted line) versus co-diluent ratio of MeOH / EMI-Tf for the (a) A face and (b) B face of sBPS membranes

4.3.2.2 Impedance characterization of swollen membranes

All ionomers swollen with varied ratios of MeOH/EMI-Tf at RT were evaluated for in-plane conductivity with EIS. The results are plotted over wt % uptake values for each co-diluent ratio in Figure 4.12. Note that two values are plotted for each ionomer at 0 % MeOH. The first point

represents a non-swollen membrane while the second point displays uptake and conductivity for a membrane swollen in neat EMI-Tf. Except for Lin-BPS-20 (maximum at 0 % MeOH) the series of sBPS membranes displays maximum conductivity at a co-diluent ratio of 20/80 w/w MeOH/EMI-Tf. The maximum conductivity of the swollen sBPS ionomers precedes the maximum uptake of EMI-Tf in terms of co-diluent ratio. This result implies that uptake of the ionic liquid in the presence of MeOH and the necessary drying step do begin to affect the charge transport properties of the membrane. As further evidence, the 80/20 co-diluent ratio (even at significant uptake) resulted in ionic conductivities equal to or lower than those of the dry sBPS membranes which suggests that the swelling solution begins to negatively affect the microphase separated morphology. Homogenization of the microphase separated polymer morphology may limit the bulk conductivity of the ionic liquid within an increasingly tortuous path to cause a lower value for total charge transport regardless of increased uptake. Shorter times a temperature or removal of heat from the co-diluent swelling conditions could limit this effect similar to the swelling results for sBPS in 100 % EMI-Tf.

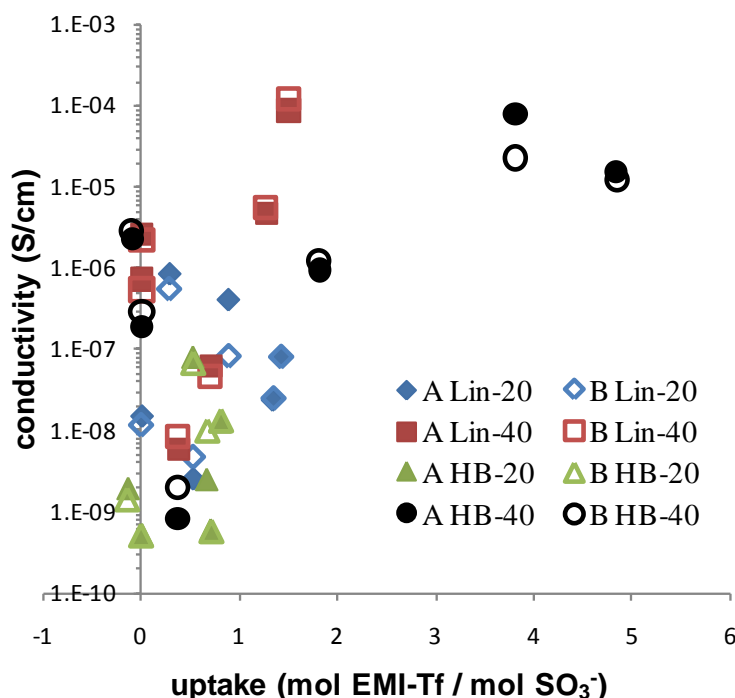


Figure 4.13: Dependence of in-plane ionic conductivity on uptake of EMI-Tf when swollen with varied co-diluent ratios of MeOH to EMI-Tf for the series of sBPS ionomers

Figure 4.13 provides the dependence of ionic conductivity on molar uptake for the series of swollen linear and branched sBPS membranes. Molar uptake accounts for the ratio of charge carriers present between the ionic liquid and the ionomer. The individual points for each ionomer represent the discrete samples subjected to different co-diluent ratios during swelling and the two faces of each membrane. Again, these samples underwent a heat treatment where after 30 h RT swelling the membranes were immersed for a further 2 h at 55 °C and cooled for 4 h to RT. There are very few instances with the co-diluent method where the in-plane conductivities of the A and B faces differ significantly. This trend suggests homogeneous swelling of the ionic liquid into the membranes. Overall, the ionomers with 40 mol % sulfonation display higher maximum ionic conductivities than those with 20 mol % sulfonation per discrete co-diluent ratio. Lin-BPS-20 and HB-3kBPS-20 show uptake and increased ionic conductivity after swelling in neat EMI-Tf. However, the 40 % sulfonated sBPS membranes display increased conductivity for samples with nearly no uptake (swollen in neat EMI-Tf). This trend further confirms the exchange of sBPS for EMI-Tf mass which was previously detected for swelling of highly sulfonated sBPS in EMI-Tf. Uptakes for sBPS membranes other than HB-3kBPS-40 appear to plateau at approximately 2 mol EMI-Tf / mol SO₃⁻. HB-3kBPS-40 achieves more than two times this uptake, although its conductivity is nearly equal to Lin-BPS-40. Absence of increased conductivity due to higher uptake suggests that the bulk conductivity of the ionic liquid is balanced with the homogenization of the membrane's charge transport pathway. The overlap where swollen 20 and 40 mol % sBPS ionomers display nearly equal conductivities at the same uptake level emphasizes that the bulk conductivity of the membrane is heavily dependent on both the integrity of the phase separated morphology as well as the uptake level. For use of these membranes in IPTs, ionic conductivity is essential to performance. The use of co-diluents to achieve higher uptake is a necessary tradeoff to observe the maximum obtainable ionic conductivity for this ionomer–ionic liquid system. As an overall processing parameter the optimal co-diluent ratio is 20/80 w/w MeOH/ EMI-Tf for swelling of sBPS.

As a part of the confirmation tests that were previously discussed for the casting method, the co-diluent samples were also retested under the more controlled set of EIS conditions. The full results of the co-diluent study under the updated EIS methods are combined in Figure 4.14 where the x-axis is the co-diluent ratio, y-axis is the molar uptake of EMI-Tf, and z-axis is the ionic conductivity. On initial inspection the overall trends in conductivity appear as before where the

more highly sulfonated ionomers display the greatest conductivities. The projections in the x-y plane indicate that all four ionomers reach a near maximum uptake of EMI-Tf at a co-diluent ratio of 0.4. In comparison, the maximum in ionic conductivity shown in the x-z plane remains for every ionomer at a co-diluent ratio of 0.2. The combination of these two results is seen in the y-z plane projections where despite an increase in the uptake of ionic liquid, the bulk conductivity of the swollen membranes decreases. This trend continues such that despite a measurable uptake, membranes swollen at a co-diluent ratio of 0.8 display a lower conductivity than the neat/dry membranes. These results suggest that the charge transport pathway originally established through microphase separation is disrupted during swelling in co-diluents with high MeOH content. Confirmation of the results of this study allows for the identification of the co-diluent ratio of 0.2 as the optimum swelling composition to achieve high conductivity for all four sBPS ionomers.

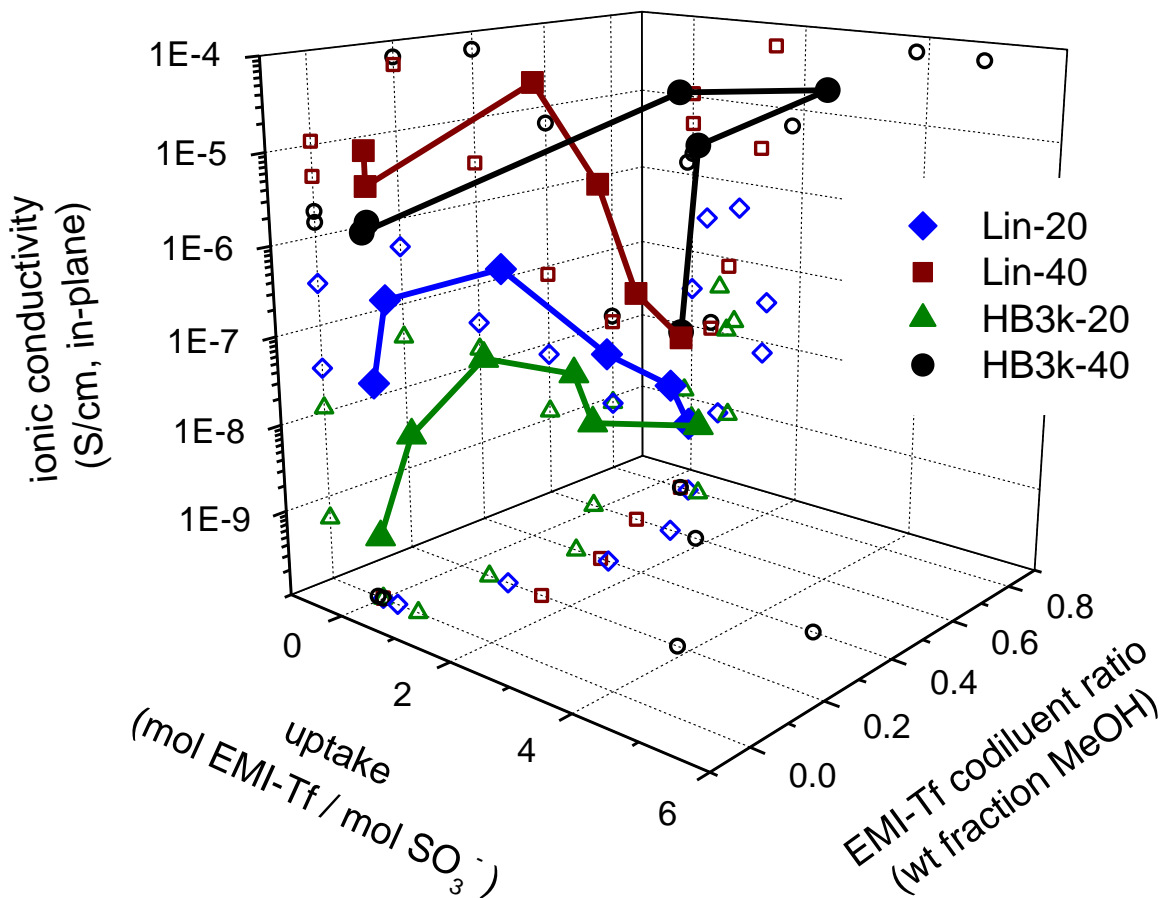


Figure 4.14: 3-D plot (lines) of ionic conductivity vs. uptake of EMI-Tf and co-diluent ratio of MeOH to EMI-Tf for the sBPS series. Open symbols are 2-D projections on each plane.

4.3.3 Comparison of the casting and co-diluent swelling methods

For comparison of the two uptake techniques, Figure 4.15 provides the ionic conductivity of swollen and cast sBPS membranes based on molar uptake of EMI-Tf. The cast samples display a regular trend that targets augmented conductivity with increased content of EMI-Tf. Co-diluent swollen samples demonstrate a maximum in conductivity based on the co-diluent ratio, typically at low MeOH content. At equivalent uptake levels the co-diluent swelling method achieves higher ionic conductivity than the casting method. Specifically for the maxima associated with the co-diluent method, this difference is likely due to swelling of the hydrophilic phase of the membrane at levels of EMI-Tf that do not heavily modify the existing microphase separated morphology. Typically, conductivities associated with co-diluent ratios that appeared to disturb microphase separation are on the order of those produced with the casting method at the same uptake. However, the casting method allows for targeting and creation of sBPS-EMI-Tf membranes at uptakes not possible with the co-diluent method. For 20 mol % sulfonated sBPS those higher uptakes augment the range of conductivities available for those polymer compositions. Further SAXS and ^{23}Na NMR studies of the cast and swollen membranes should clarify the morphological state of the ionomer that corresponds to optimal charge transport. Knowledge of the location of the ionic liquid after uptake will also verify if decreased mechanical stiffness is primarily due to plasticization of the amorphous phase ($T_{g,m}$) or the hydrophilic phase ($T_{g,cl}$) containing the associated sulfonate salts. High conductivity at low uptake will also decrease total plasticization and lead to higher modulus values of the final IPT. The ability to increase the modulus and ionic conductivity concurrently may allow for both increased blocked force and free strain, leading to an increase in the energy density of the device. IPTs designed with optimized sBPS–EMI-Tf combinations using both methods are discussed in Chapter 5.

After analysis of these two studies combined for the individual sBPS compositions, it is interesting to combine the results and compare the effectiveness of the two uptake methods for achieving maximum uptake and conductivity. The results of the co-diluent and casting studies for conductivity versus molar uptake and wt % uptake of the sBPS series are shown in Figure 4.16a and b respectively (based on confirmation tests). In comparison to literature values for Nafion[®] (Na^+ form) swollen with EMI-Tf[61] both Lin-40 and HB3k-40 from the co-diluent series nearly approach the same conductivity and exceed the uptake level. Also, in all cases for

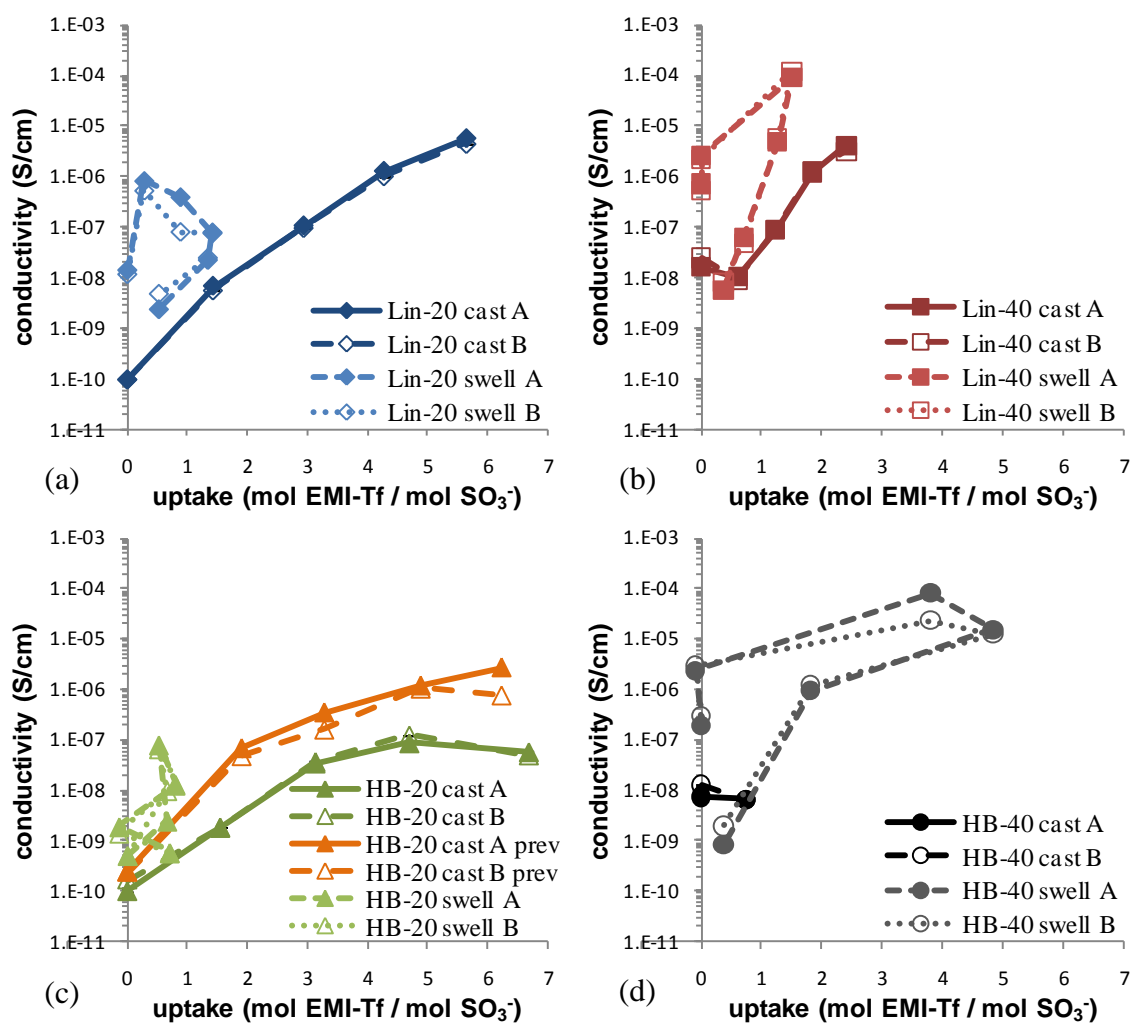


Figure 4.15: Ionic conductivity versus molar uptake for (a) Lin-BPS-20 (b) Lin-BPS-40 (c) HB-3kBPS-20 (d) HB-3kBPS-40 cast in the presence of EMI-Tf or swollen in varied ratios of MeOH / EMI-Tf

sBPS the co-diluent method achieves a greater conductivity per molar uptake than the casting method. This result is likely due to the fact that the co-diluent method swells neat membranes that were formed prior to any interaction with the ionic liquid. This case confirms that formation of an equilibrium morphology prior to swelling with the diluent enhances charge transport in comparison to the percolation of bulk ionic liquid within the tortuous pathway provided by casting. Due to the fact that all of the cast samples achieved the same conductivity at their highest uptake, Figure 4.16b was plotted to see the relation of this trend to the wt % uptake of EMI-Tf. As is seen in the figure, all of the curves for sBPS cast in the presence of EMI-Tf

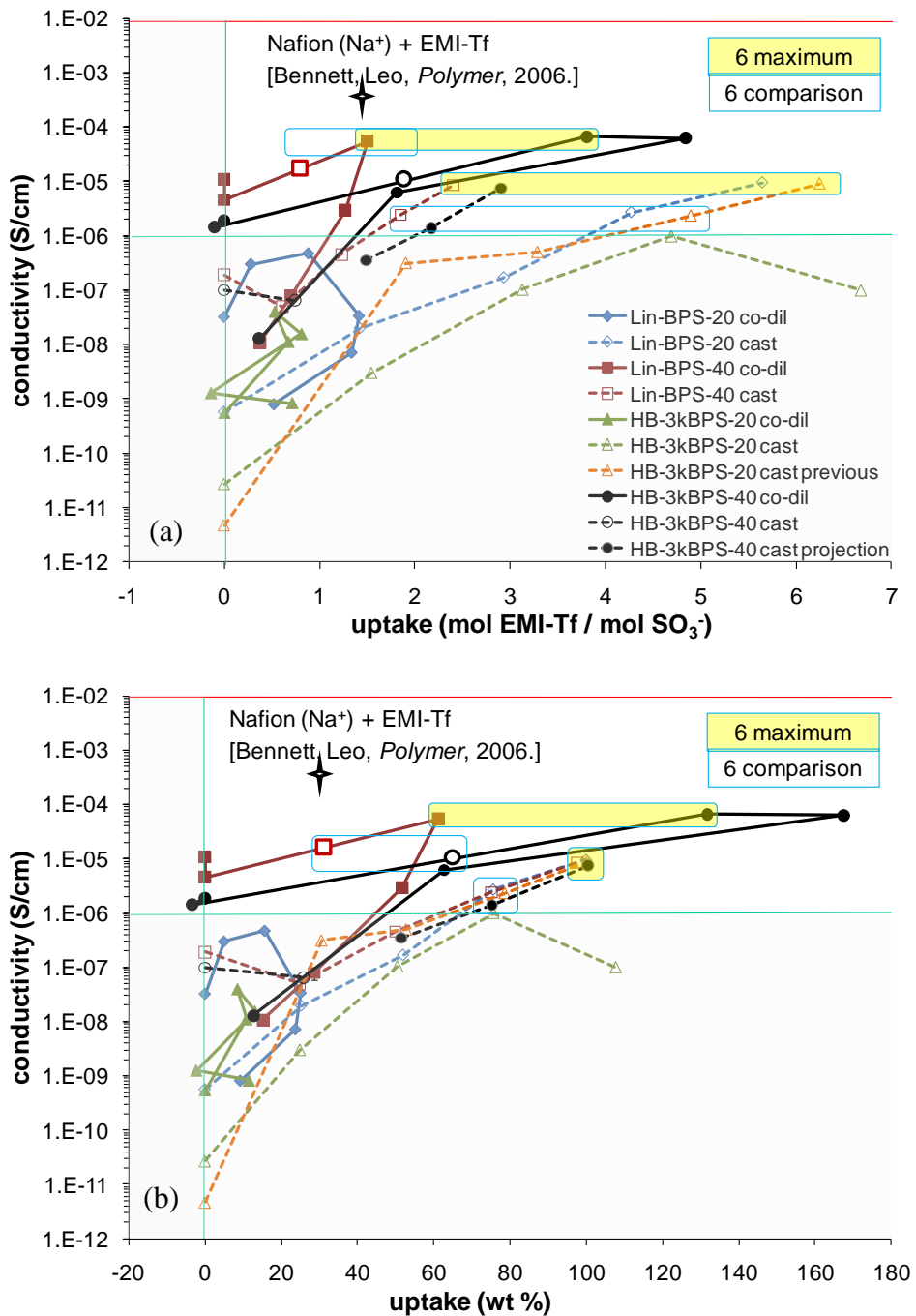


Figure 4.16: IPT design space based on ionic conductivity versus (a) molar uptake (b) wt % uptake for sBPS membranes swollen in co-diluents or cast in the presence of EMI-Tf

overlay at 100 wt % uptake. The curves do not overlay at low uptakes but instead converge with increasing uptake after the 50 wt % uptake percolation threshold. This trend further confirms that the ionic liquid dominates the conductivity response of the membrane for these conditions. At

high uptake, the lack of differentiation on the basis of chemical composition or backbone architecture suggests that the ionic liquid limits ionomer microphase separation that would otherwise be based on distribution of the sulfonated repeat units along the backbone.

The combination of the data from these two studies also provides the distinct opportunity to define IPT design parameters based on available conductivity for the sBPS / EMI-Tf system. Previous actuation of IPTs constructed from HB-3kBPS-20 at 75 wt % uptake demonstrated very slow strain rates, even with optimized electrodes (Chapter 3). This point was taken as the minimum allowable conductivity at approximately 1 $\mu\text{S}/\text{cm}$ (horizontal grey area). Conditions are also not desirable that cause dissolution of the membrane, detected as weight loss or negative uptake. The vertical grey box at zero uptake defines this bound. For the co-diluent study no conditions are presently detected to produce a 20 mol % sulfonated sBPS membrane with sufficient conductivity. However, the casting method confirms that Lin-20 and HB3k-20 at both 75 and 100 wt % uptake are viable candidates for IPT compositions. Thus, the upper right quadrant contains the uptake levels and processing conditions necessary to design higher performance IPTs than those previously demonstrated with sBPS. The clear boxes highlight six compositions available for comparison outside of further developments to the casting and co-diluent swelling methods. The primary data points are highlighted in yellow for maximum conductivity combined with criteria for comparison. IPTs are constructed from these maximum compositions and characterized as electromechanical transducers in bending in Chapter 5.

4.4 Summary

The studies described in this chapter demonstrated two separate methods to imbibe novel ionomeric membranes with ionic liquids in light of their uptakes and final ionic conductivities. Updates to the EIS method for in-plane impedance measurements of ionic liquid-swollen membranes confirmed significant differences in conductivity due to the two uptake methods. The swelling method is a complex combination of co-diluent ratios, time, and temperature but achieves greater ionic conductivity per uptake than the casting method. The optimal co-diluent ratio was identified as 0.2 in terms of conductivity per uptake of EMI-Tf. However, the maximum ionic conductivity attainable through swelling for sBPS with 20 % sulfonation is potentially too low to provide sufficient actuation in IPT form.

Conductivity of membranes cast in the presence of ionic liquids was dominated by the presence of the ionic liquid in comparison to any effects due to chemical composition or polymer architecture. The casting method is straightforward and achieves higher target uptakes easily that for certain polymer compositions are not yet attainable through swelling. SAXS analysis confirmed that a membrane cast in the presence of EMI-Tf displayed much larger distance between ionic domains than the dry sample and the presence of microscopic heterogeneities. DMA studies of the same membranes indicated that the presence of EMI-Tf plasticized the membrane T_g for both phases to an asymptotic value. The combination of these factors resulted in compliant membranes with a hydrated modulus significantly greater than that reported for water-swollen Nafion[®]. EIS indicated only a small degree of face-to-face conductive anisotropy based on the casting technique. The critical uptake was identified for three ionomers in the cast series and revealed a percolation threshold for the ionic liquid that was reflected in the morphological, mechanical, thermal, and electrical properties of the membranes.

Despite the comparably hydrophilic classification of EMI-Tf in relation to other ionic liquids its organic nature is sufficient to partially disrupt microphase separation in sBPS ionomers based on composition and polarity. Homogenization is increased for formation from solution, the presence of heat, and excess organic diluents. Both experiments highlight the importance of tailoring the ionic liquid–ionomer interface for stability even before construction of the final IPT device. The casting method is not presently able to produce membranes with charge transport pathways that are as efficient and well defined as those present in the neat preformed membranes or optimized co-diluent samples. However, bulk conductivity of the composite membrane is also a factor of the amount of ionic liquid present. Combination of the results of these two studies resulted in conductivity versus uptake design criteria for sBPS / EMI-Tf IPTs. Application of these methods in Chapter 5 allows for the construction of IPTs with maximum ionic conductivity for the sBPS–EMI-Tf system.

Chapter 5 DESIGN, FABRICATION, AND CHARACTERIZATION OF OPTIMIZED SBPS IONIC POLYMER TRANSDUCERS

5.1 Motivation

The overall goal of this research is to establish fundamental understanding of the relationship between polymer topology and electromechanical transduction in ionic polymer transducers. Synthesis and characterization of a series of ionomers with controlled branching and charge content was successfully completed to further that goal. Investigation of the neat ionomer series confirmed the synthetic design had produced thermally stable, high T_g , microphase separated, high elastic modulus ionomers capable of forming tough, flexible membranes. Fabrication of an initial set of IPTs with a branched ionomer containing 20 mol % disulfonation was completed simultaneous with an investigation of the percolation threshold of the electrodes for these novel transducers. The percolation study demonstrated that with development the use of ionic liquids and conducting particles through the DAP was viable for sBPS ionomers. Initial actuation testing revealed low peak strain and strain rates despite identification of a maximum in capacitance based on varied composition of the electrodes. EIS characterization of the components and devices themselves revealed that the limiting factor was likely insufficient uptake of the ionic liquid for the chosen ionomer.

A more focused study on the interaction of the ionomer and the ionic liquid revealed that increases in conductivity of the electrolyte matrix were possible. This investigation included other members of the sBPS series with higher degrees of sulfonation and linear analogues to the ionomer used for the percolation study. Two methods were developed around sBPS and the EMI-Tf ionic liquid to maximize conductivity per uptake. Characterization of the imbibed membranes revealed that the ionic liquid dominated the conductivity response at high uptake, although its plasticization effect on the hydrated modulus reached a plateau with uptake. Also,

the presence of the ionic liquid during casting frustrated formation of the microphase separated morphology. Regardless, conditions were identified that produced imbibed membranes with four sBPS compositions displaying maximum conductivity beyond the levels associated with the percolation study.

In this chapter the results of the previous three studies are combined to design and fabricate optimized ionic liquid-swollen sBPS – IPTs with both linear and branched samples. Both the co-diluent swelling method and the casting method are employed to imbibe sBPS with sufficient EMI-Tf to meet the design targets identified in Chapter 4. The casting method is also combined with the DAP to produce RuO₂ electrodes above percolation and maximize capacitance with each sBPS composition. EIS characterization serves as an essential tool to track the effects of fabrication on conductivity in comparison to the desired targets set for the central ionomeric membranes. Finally, the sBPS – IPTs are characterized for bending actuation in free displacement. Increased performance of the sBPS – IPTs demonstrates successful integration of the novel ionomers into the IPT platform in the presence of ionic liquids. Furthermore, knowledge of the exact ionomer properties allows for correlation of transduction with the original design, a process that could be carried out further with this series and other ionomers of interest for tailored performance of IPTs in various applications.

5.2 Experimental materials and methods

Due to the cumulative nature of this research, the materials employed to construct the series of sBPS – IPTs are consistent with those reported in the previous chapters. The ionomer series from Chapter 4 (Lin-BPS-20, HB-3kBPS-20, Lin-BPS-40, HB-3kBPS-40) is also used here to enable tailoring of ionic liquid uptake based on the previous results. These samples also emphasize the largest deviation in topology between the linear and branched ionomers synthesized. The ionic liquid, EMI-Tf, also remains as the sole diluent. Anhydrous RuO₂ serves as the conducting particle of choice based on the previous confirmation of its percolation threshold in a matrix of sBPS and EMI-Tf.

5.2.1 Transducer fabrication

Fabrication of the neat and ionic liquid-swollen central ionomeric membranes for this study was very similar to the process described in Section 4.2.2. Only changes to the process are reported

here. For central membrane casting solutions (10 wt %) 0.25 mL of DMAc solution was found to be the minimum casting volume to wet the entire surface of the mold. Final thickness of the central membrane was tailored to ~ 80 μm based on casting area, total casting volume at the defined 10 wt % concentration, and the reported densities of BPS (1.29 g/cm^3 , Radel) and EMI-Tf (1.39 g/cm^3). The temperature inside the chamber during casting was decreased to ~ 40 $^\circ\text{C}$ for 48 h. The chamber temperature was then raised to ~ 60 - 65 $^\circ\text{C}$ for a final 12 h to further increase the gradual removal of DMAc. After removal from the molds the neat membranes were dried at 250 $^\circ\text{C}$ for 1 h *in vacuo* before a slow cool ramp to RT. Membranes that contained ionic liquid (all targeted to 100 wt % uptake) were dried at 130 $^\circ\text{C}$ for 1 h before a cooling ramp to RT. All samples were stored in a dessicator at 10 % RH until use. Co-diluent swelling was conducted in 20 wt % solutions of MeOH in EMI-Tf on the neat membranes cast with 0 wt % uptake of ionic liquid. Each neat membrane (Lin-BPS-40 and HB-3kBPS-40) was immersed in a separate swelling bath at RT for 48 h. MeOH was removed by drying at ~ 90 $^\circ\text{C}$ for 18 h *in vacuo*, followed by a cooling ramp to RT.

Similar to the steps employed for the percolation study (Chapter 3), the IPT electrodes here were constructed with a casting version of the DAP method. Again, only changes to the method are reported here. Instead of the layer-by-layer approach with large volumes of casting solution (Section 3.2.2), each dispersion was composed of 5 wt % ionomer solution in DMAc, the corresponding IL uptake in wt %, and sufficient RuO_2 to produce the 45 % volumetric ratio with the ionomer. The total casting volume of the electrode dispersion accounts for the volume contributions of the RuO_2 , ionomer, and the intended ionic liquid uptake. The final target thickness of the electrodes was 35 μm . Electrodes applied to cast central membranes and those swollen with the co-diluent method were all created with the DAP casting method at ionic liquid uptakes matched to the central layer content. Two individual electrodes were cast in flexible Kapton molds for each central membrane. Melt press conditions remained as previously described for all samples except the HB-3kBPS-40 co-diluent sample. Due to the very high uptake melt press conditions were reduced to 100 $^\circ\text{C}$ and 1 MPa (~ 150 psi) for two steps of 10 s each. Electrodes containing highly sulfonated ionomers adhered to the Kapton casting boats while the less sulfonated ionomers allowed for easy release of the electrode. In the former case the boat was cut at the corners and flattened out to become the backing for melt pressing. Release from the boat was easily achieved after the initial melt pressing step. Melt pressing conditions for

the gold leaf layers were the same as for the DAP electrodes except reduced to two steps of 15 s each. The IPT sheets were trimmed with a rolling razor blade and cut into multiple transducers with dimensions of approximately 3 mm x 30 mm. Despite trimming, in some cases gold leaf overlapped the edges and created an electrical short through the thickness of the transducer. Near-zero electrical resistance measured with a digital multimeter identified samples that contained shorts. The sources of the electrical shorts were then found under a stereoscope and removed with tweezers or a razor blade.

5.2.2 Electrical impedance spectroscopy

Electrical properties of the central membranes and built transducers were evaluated with electrical impedance spectroscopy (EIS) according to the most updated procedure reported in Section 4.2.2. The two point fixture with parallel rectangular brass rods aligned at a defined separation of 0.3 cm allowed for in-plane impedance measurements of the central membranes. A load (94 – 5094 g) placed on top of the fixture ensured consistent and constant contact between the sample surface and the brass electrodes. Through-thickness EIS characterization of the built IPTs used the custom fixture described in Section 3.2.3, although the aluminum contacts were replaced with two facing 25 μm thick gold foil sheets (on flexible substrates). The maximum sample size for non-electroded samples is a length of 2.9 cm and a width of 0.94 cm. All measurements were performed inside a humidity chamber shielded inside of a Faraday cage at room temperature (RT). An RH sensor in the test chamber provided feedback to a humidifier that adjusted the atmosphere to achieve a constant relative humidity (RH) of approximately 40 %. Ionic conductivity values (σ , S/cm) were calculated with Equation 3.1 based on the measurement geometry, sample dimensions, and an estimate of the bulk resistance (R , Ohm). A minimum of three consecutive impedance measurements were taken for each sample at constant conditions.

5.2.3 Electromechanical transducer characterization

All fully fabricated IPTs were characterized for their electromechanical response as actuators based on configuration as a clamped cantilever beam (Figure 5.1). The fixture clamps were lined with gold foil electrical contacts and spring-loaded to provide constant contact with the electroded surface of the sample. The free length (L_f) was kept at approximately 19 mm and a non-contact laser vibrometer was used to measure the displacement, $\delta(t)$ (μm), of any point along

the length of the transducer as a function of time. Strain, $\varepsilon(t)$, at the outer surface of the IPT was calculated using

$$\varepsilon(t) = \frac{\delta(t)T}{L_f^2}, \quad (5.1)$$

where T is the thickness (mm) of the transducer. Application of Equation 5.1 assumes that the device bends with constant curvature, which has been validated experimentally.[20] The frequency dependence of the actuator's free displacement in response to a random input voltage ($v(\omega) = 0.5 \text{ V}_{\text{rms}}$) was measured with a Tektronix 2630 Fourier Analyzer. As shown in Figure 5.1, a circuit was placed in line with the transducer to measure the voltage drop across a 0.1Ω resistor. Based on the gain of the circuit and this voltage drop the current response, $i(t)$, was measured. The Fourier analyzer calculated the frequency response functions between the displacement and the driving voltage and the current and the applied voltage for experiments that covered a total frequency range of 0.1 Hz – 10 kHz. The frequency dependence of the strain in response to the imposed voltage is calculated using

$$\frac{\varepsilon(\omega)}{v(\omega)} = \frac{(\delta(\omega)/v(\omega))T}{L_f^2}. \quad (5.2)$$

The transfer function between the induced current and applied voltage was also useful to calculate the frequency dependent impedance of the IPT using

$$Z(\omega) = \frac{v(\omega)}{i(\omega)}. \quad (5.3)$$

The strain response in the frequency domain was further normalized with the charge per area according to:

$$\frac{\varepsilon(\omega)}{Q(\omega)} = \frac{\varepsilon(\omega)}{v(\omega)} \left[\frac{v(\omega)}{i(\omega)/j\omega A} \right], \quad (5.4)$$

where A is the area of the transducer in the x-y plane and $Q(\omega)$ is the flow of charge per area in the transducer as a function of frequency. The effective modulus of elasticity (E'_{eff}) for the transducer is calculated from peak associated with the undamped natural frequency (ω_n) in the displacement per volt transfer function. Since the device is clamped in a cantilever configuration the modulus is calculated with the relationship

$$E'_{eff} = \frac{\omega_n^2 \lambda}{k_n^4 I}, \quad (5.5)$$

where λ is the experimentally determined linear mass density of the transducer, I is the moment of inertia for the beam bending axis, and k_n is a factor associated with the first natural frequency.[271] k_n is calculated according to

$$k_n = \frac{1.875104}{L_f}. \quad (5.6)$$

The frequency at which the first peak in the frequency response function appears is the damped natural frequency (ω_d) of the transducer. The damped value is associated with the undamped natural frequency through

$$\omega_n = \frac{\omega_d}{\sqrt{1 - \xi^2}}, \quad (5.7)$$

where ξ is the damping ratio. The damping ratio was estimated from the experimental data in the charge normalized strain response function according to the half-power method[272]

$$\xi = \frac{|\omega_a - \omega_b|}{\omega_d}, \quad (5.8)$$

where ω_a and ω_b are the frequencies associated the intersections of a line, 3 dB below the peak value, with the experimental transfer function.

Actuation responses in the time domain were measured as displacement resulting from step input voltages of varying magnitude (0.5, 1, 2, 3.5 V) and directionality (\pm), typically over 300 s. Step voltages and square wave signals were supplied by a DSpace ControlBoard interfaced with MATLAB Simulink and ControlDesk that also recorded the displacement and current responses of the transducer. Strain rates ($\mu\epsilon/V$) were calculated from the slope of the strain response over the initial 100 ms period following the applied step voltage. Peak strains were recorded for the first maximum in the response and any back relaxation was calculated from the initial minimum as a percentage of the peak strain. Both the fixture used to clamp the IPT and the laser vibrometer employed to measure displacement were fixed to a vibration dampening block during all testing. Room temperature was approximately 22 °C and the relative humidity was on average 45 % \pm 5 %. Any prebend in the sample was angled away from the laser vibrometer to maximize the range of motion detection.

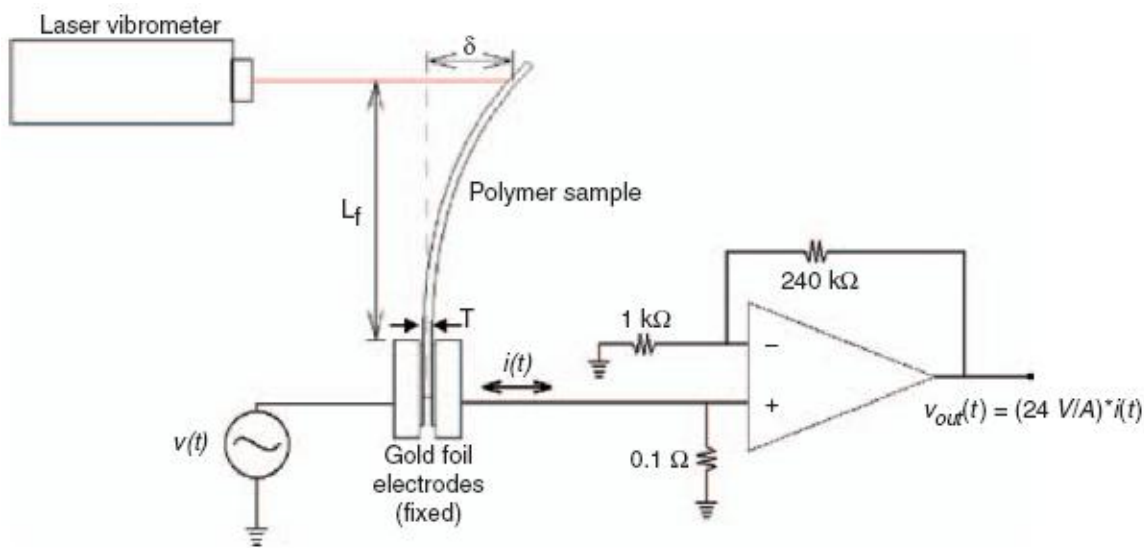


Figure 5.1: Schematic of the experimental setup[88] employed to measure free displacement and current for sBPS – IPTs subjected to voltage inputs. "Reprinted from Akle, B. J. and Leo, D. J.: Single-Walled Carbon Nanotubes – Ionic Polymer Electroactive Hybrid Transducers. *J. Intell. Mater. Syst. Struct.* 2008. 19. p.905–915. Copyright SAGE Publications. Reproduced with permission."

5.3 Results and discussion

5.3.1 sBPS – IPT fabrication

In order to address the effects of polymer branching on electromechanical transduction in IPTs, it is first imperative to fabricate well-controlled devices with a series of ionomers that vary based on topology. The percolation study's use of HB-3kBPS-20 was not sufficient to isolate the effects of branching and primarily demonstrated that the impedance of the ionomer-ionic liquid electrolyte was the limiting factor for performance. In this study, samples are taken from the series of ionomers synthesized in Chapter 2 to construct an experimental matrix which compares two linear ionomers (Lin-BPS-20 and Lin-BPS-40) and two highly branched ionomers (HB-3kBPS-20 and HB-3kBPS-40). In line with the conductivity-based design parameters identified in Chapter 4 each ionomer is individually cast in the presence of 100 wt % uptake of EMI-Tf to form a central membrane. Model central membranes evaluated for ionic conductivity in Chapter 4 demonstrated no discernible difference based on the ionomer composition or topology. The magnitude of the ionic liquid content dominated the response. However, the central membrane of

the IPT has been identified as a passive charge transport pathway within the device. Although this component is critical to operation, the active volumes that manifest transduction reside in the electrodes. Fabrication of sBPS – IPTs with membranes at those compositions and uptakes is intended to determine if the ionomer composition or topology affects performance beyond the contribution of the imbibed ionic liquid. Fabrication of DAP electrodes with different ionomers and matched EMI-Tf uptake is essential to this comparison.

Simultaneous with the investigation of branching effects, this study attempts to optimize the performance of sBPS – IPTs above those previously demonstrated with ionic liquids. During fabrication of the IPTs each step in the DAP was considered for improvement and minimization of variation associated with previous trials. All membranes were cast from 10 wt % solution of the ionomer in DMAc instead of 5 wt % as employed for the percolation study. The higher concentration was used due to comparison of previous results for casting in the presence of ionic liquid at different polymer concentrations. Higher solution concentration with the same uptake of ionic liquid, when formed slowly at lower temperature, generally resulted in higher conductivity. Molds were employed with silicone rubber walls on glass slides (15.5 mm x 36 mm) to provide better control over the membrane dimensions and prevent overflow of the casting solution. The neat membranes used for co-diluent swelling and membranes containing ionic liquid during formation were cast in these molds for consistency within this study and with samples created previously. These extra steps were employed to increase consistency of the central membrane layer while lowering its overall thickness in an effort to reduce the passive volume contained between the active electrodes. Previous use of the casting method in Chapter 3 demonstrated small variability but those central membranes were cut from a single cast film. The casting temperature within the chamber was also lowered slightly from 50 °C to 40 °C simultaneous with an increase in casting time of 200 %. Note that after casting all membranes fabricated in Chapter 4 were annealed at 250 °C for 1 h before the cooling step, regardless of uptake or T_g . The decreased annealing temperature employed here is due to the increased conductivity of the HB-3kBPS-20 samples fabricated in Chapter 3 (labeled “prev”) that were annealed at $T_g + 10$ °C for 1 h before cooling to RT. Neat membranes of the 40 mol % disulfonated samples (linear and branched) were also swollen with co-diluents to facilitate ionic liquid uptake. This comparison for the central membranes demonstrated nearly equal conductivities at very different uptakes. Co-diluent swelling was conducted in 20 wt % solutions of MeOH in EMI-Tf as this was

identified as the optimal swelling combination for uptake of EMI-Tf into sBPS in Chapter 4. Each neat membrane (Lin-BPS-40 and HB-3kBPS-40) was immersed in a separate swelling bath at RT for 48 h. Subsequent heating of the swelling bath was not used here as it was identified as a potential source of instability for the charge transport pathway of sBPS in Chapter 4.

Table 5.1: sBPS – IPT compositions for ionic liquid uptake and electrode RuO₂ loading

ionomer	uptake method	central membrane	CM uptake	electrode uptake	dry electrode ratio RuO ₂	dry electrode ratio RuO ₂	total electrode ratio RuO ₂	total electrode ratio RuO ₂
			(wt %)	(wt %)	(vol %)	(wt %)	(vol %)	(wt %)
Lin-BPS-20	cast	A	100	108	45	81	29	68
		B	100	96	44	81	30	69
HB-3kBPS-20	cast	A	95	110	45	81	28	67
		B	95	117	45	81	28	67
Lin-BPS-40	cast	A	101	110	45	81	29	68
		B	105	106	45	82	29	68
	co-diluent	A	54	59	45	81	35	73
		B	67	68	45	81	33	72
HB-3kBPS-40	cast	A	105	111	45	82	29	68
		B	108	109	45	81	29	68
	co-diluent	A	206	213	45	82	22	59
		B	183	182	45	81	23	61

Since the interface within the electrodes of the IPT is source of electromechanical transduction, differentiation in electrodes is necessary based on composition of the ionomer to make comments about the contribution of polymer properties to actuation performance. The DAP method enables the use of any combination of ionomer, diluent, and conducting particle to construct electrodes for IPTs.[60] Here the DAP method is modified to proceed with a single casting step instead of iterative spraying or painting techniques for the electrodes. Essentially the techniques used for creation of DAP electrodes have only been demonstrated with Nafion[®], which is used as a 5 wt % solution in isopropyl alcohol (IPA). Due to the low boiling point of IPA, application of heat to the fixture during creation of the electrodes is sufficient to remove the solvent quickly and leave a well-defined electrode layer. In the case where the electrode is painted/sprayed directly onto the central membrane, IPA does not dissolve Nafion[®] in its already cast form. In this manner, thickness control and consistent distribution of the electrode over a desired area is achieved. Development of the casting technique was based on necessity with

sBPS since only polar aprotic solvents are available to dissolve sBPS. Spraying and painting techniques were attempted but presently have not produced the consistency found with the casting technique. These methods remain open for development and work best when the electrode dispersion is applied to a decal instead of the central membrane itself. Although direct application eliminates a melt press iteration and the interface associated with that step, the solubilizing ability of solvents such as DMAc typically weakens and/or disturbs the central membrane during application. The spraying method also typically provides better dispersion than painting, although the sustainability and safety associated with fast removal of aerosolized solvents such as DMAc even in a fume hood is likely too dangerous and time-consuming per the benefit in the present state.

Thus, the casting process was applied to fabricate the present set of DAP electrodes composed of the four sBPS ionomers, defined uptakes of EMI-Tf ionic liquid, and RuO₂. As was shown in Chapter 3, capacitance was maximized for a 45 vol % ratio of RuO₂ to dry ionomer in HB-3kBPS-20 IPTs. The same composition was employed here for all transducers based on previous findings that the chemical composition of the ionomer was not the determining factor for electrode capacitance and its subsequent relationship to strain per the applied voltage.[54] Every effort was made to produce consistency in the production of the electrodes. All ionomer solutions were kept at the same concentration regardless of the content of ionic liquid and RuO₂. The total volume of the combined components was also accounted for to increase accuracy of the final thickness of the electrodes per the target of 35 μm. This step also decreased the casting volume by more than a factor of two compared to the percolation study, and thus decreased the casting time to reach a solid electrode. The final compositions of the series of sBPS – IPTs are provided in Table 5.1. The uptake of ionic liquid for the total transducer was based on the design parameters indicated in Chapter 4 and applied to both the central membrane and the electrodes. Again, uptake is defined in terms of the ratio of ionic liquid to dry ionomer. Ionic liquid content for the total transducer was typically within ±10 % of the target. Note that two individual electrode layers were cast for each electrode and the values shown in Table 5.1 are an average of the two layer compositions. The RuO₂ content was also very accurate, as indicated by the dry volumetric ratio (vol %) with a target of 45 vol %. Balance of the electrode components is reflected in the total vol % RuO₂, which accounts for the real volume of the ionic liquid uptake defined for the electrode. For the cast samples, the ionic liquid uptake is constant and so there are

only experimental deviations in the total vol % RuO₂ from a value of 29 vol %. However, the co-diluent samples were designed with a large difference in ionic liquid uptake. The lower uptake of Lin-BPS-40 increases the vol % RuO₂ of the total electrode while the high uptake of HB-3kBPS-40 decreases that value.

5.3.2 Electrical impedance spectroscopy

As previously described, ionic conductivity typically serves as a good indicator for IPT performance, specifically in terms of strain rate.[20, 61] EIS characterization provides this parameter as well as the ability to estimate capacitance, which is the other primary indicator for electromechanical transduction as actuator peak strain. For this study, EIS characterization was performed at each stage of IPT fabrication in addition to estimation of the impedance of fully built transducers. This manner of characterization allows for tracking of the effects of fabrication steps on the conductivity of the IPT and potential identification of the source of increase or decrease for each sBPS composition.

5.3.2.1 *Central membrane*

Uptake targets for the six primary compositions investigated were set based on the maxima in conductivity for model central membranes characterized in Chapter 4. The four sBPS compositions were cast while the two samples with the higher degree of sulfonation were swollen with the co-diluent method. A comparison of the targets and experimental values for uptake is provided in Figure 5.2. These values are also plotted against the resultant in-plane ionic conductivity for the membranes. The casting method produced very good repeatability in terms of the target uptake of ionic liquid. As discussed earlier, the co-diluent method does not show the same level of consistency in uptake and deviation is larger for high uptake targets. Although the uptake for HB-3kBPS-40 was larger than intended, the experimental value incidentally provided a nearly equal molar uptake to the cast linear and branched samples with a lower degree of sulfonation. Conductivity for all central membranes is higher than the values displayed by the targets, although the difference is not a consistent value. Both the target values and those for IPT membranes of this study are based on the updated experimental method for EIS.

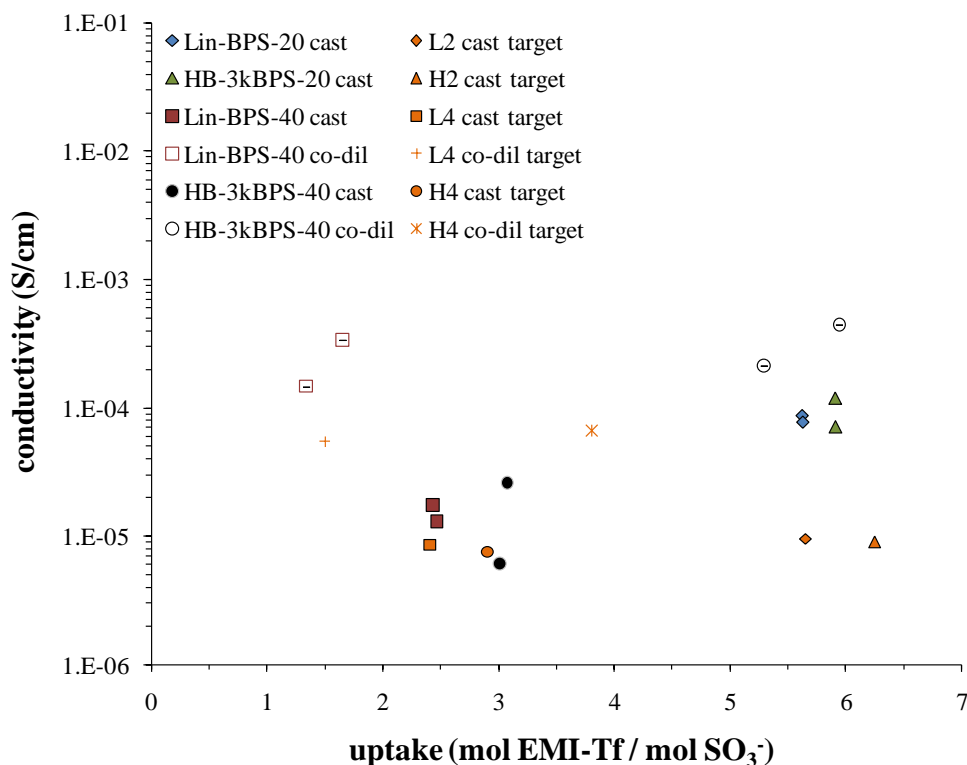


Figure 5.2: Target and experimental ionic conductivity versus molar uptake for central membranes cast in the presence of EMI-Tf or swollen in varied ratios of MeOH / EMI-Tf

The origins of the increased conductivity are most likely associated with the improved casting and swelling conditions employed to imbibe the membranes with ionic liquid. In the cast of the cast samples, longer membrane formation times at lower temperatures may have allowed for several modifications to the membrane. Since the uptake level is very high, the percolated pathway of bulk ionic liquid through the sample is likely present as was suggested in Chapter 4. Increased casting time at lower temperature implies slower evaporation of the casting solvent and a more gradual separation of the ionic liquid from the ionomer to form macroscale heterogeneities. This separation is accentuated with the 20 mol % sulfonated samples because of the decreased compatibility of the ionic liquid with the more prevalent hydrophobic phase. The effect is correspondingly less for the 40 mol % sulfonated samples since the higher number of hydrophilic repeat units increases compatibility with EMI-Tf. The co-diluent samples also display increased conductivity values, although the HB-3kBPS-40 sample values are likely due to the increased uptake. Lin-BPS-40 membranes however display higher conductivity than the target at the same uptake. Again, the difference is attributed to a change in the swelling conditions were time was increased and heat was not applied. The milder conditions may allow

for increased stability to the microphase separated morphology which increases charge transport of the membrane as a whole. Confirmation of this overall hypothesis will require direct morphological investigations of samples cast for both sets of conditions.

5.3.2.2 *IPT processing stages*

During fabrication the IPT progresses through four major stages: ionic liquid uptake in the central membrane (CM), melt pressing of the RuO₂ electrodes onto the CM, melt pressing of gold leaf onto the device, and final sizing to the desired IPT dimensions. For this study, EIS characterization was performed at each stage to track the ionic conductivity of the device as it passed through certain processing steps and conditions. The total process from the separate IPT components to the fully fabricated devices is shown schematically in Figure 5.3. Note, characterization of the central membrane used an in-plane impedance fixture while the other stages were measured with a through-thickness fixture. Again, the experimental data is fit with the FRA measurement program to the Nyquist plot to estimate the real part of the impedance where the imaginary part goes to zero as the bulk resistance of the membrane (R_1). Our previous work demonstrated a larger than expected difference between conductivities resulting from the two measurement geometries for neat sBPS membranes and those containing ionic liquids. The source of the difference was identified as an increased contact resistance between the fixture electrodes and the membrane surface with the through-thickness fixture. Here the through-thickness technique is only applied to samples with RuO₂ or Au electrodes in contact with the fixture. The much higher inherent conductivities of these materials are assumed to minimize the contact resistance and allow for application of a constant potential difference through the thickness of the sample. However, processing-induced morphological changes and anisotropy in conductivity are common to several ionomers and with all other measurement parameters equal often result in higher in-plane conductivity by a factor of 1 – 10.[245, 273-276] Figure 5.4 displays the conductivity at after each fabrication stage for the four sBPS compositions.

As seen in Figure 5.4, the trends that result from fabrication of the IPT are not the same for all sBPS ionomers studied. Before discussing those trends though, the appearance of some very high conductivity values is pointed out, especially those that differ significantly from the other samples of the same composition. For Lin-BPS-20, the values for the second step are a good example and are higher than any other conductivity by at least one order of magnitude. A similar

data point for the completed IPTs using HB-3kBPS-40 approaches 12 mS/cm. These data points are attributed to electrical shorts through the thickness of the membrane. Due to the high electrode loading of RuO₂, any contact between the two electrodes allows a pathway for the current around the central membrane and lowers the overall impedance of the sample. Although external shorts due to edge-overlap of gold leaf are removed, cracks in the central membrane and edge-overlap of the DAP electrodes were also observed. Both cases were typically resolved when the IPT sheet edges were trimmed or finally cut into individual transducers. Contribution to EIS measurements prior to this step was generally unavoidable if the short was large and positioned toward the center of the sheet.

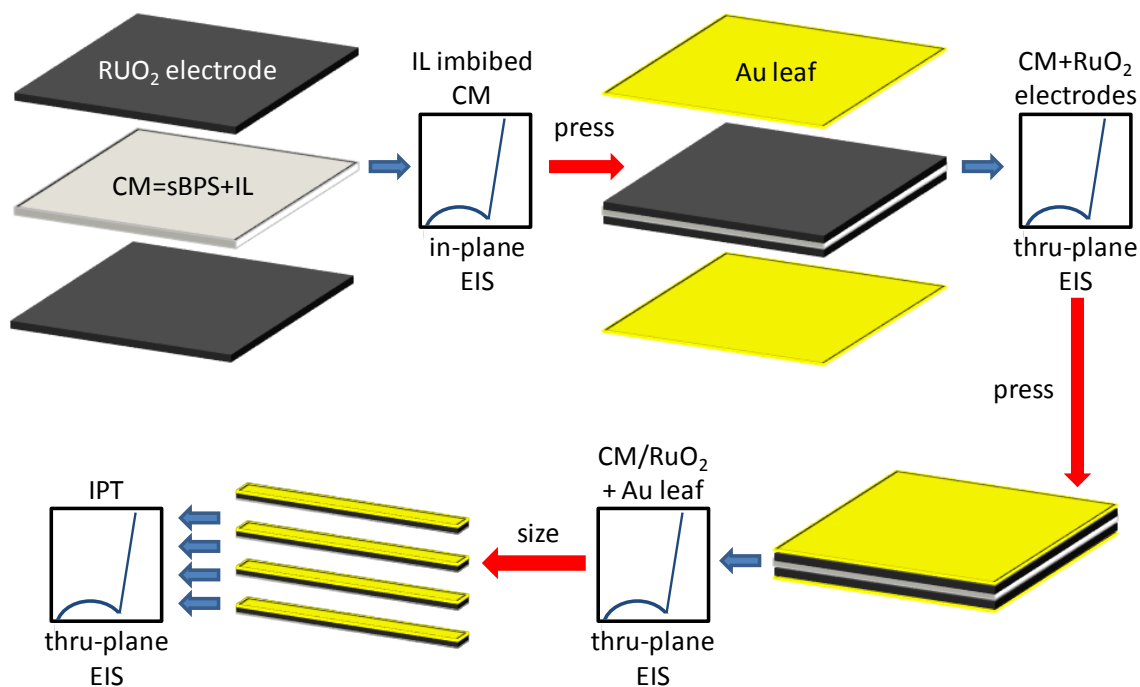


Figure 5.3: Schematic representation of the fabrication stages for IPT construction and EIS characterization points

The overall trend for fabrication of sBPS – IPTs is that the two melt-pressing steps decrease the conductivity in comparison to the original central membrane. Only the membranes with 40 % degree of sulfonation that were cast in the presence of EMI-Tf show increased conductivity through the fabrication process. The cast membranes with lower 20 % degree of sulfonation and the co-diluent swollen samples all decrease conductivity. The variation in conductivity likely has two origins within the fabrication steps. First, the membranes may lose ionic liquid during the

pressing step. Although only small amounts were observed to leach onto the pressing films, the direct dependence of the conductivity on the uptake of EMI-Tf could significantly change with loss of the diluent. The cast samples are more likely to experience losses for this reason if the ionic liquid is macroscopically separated from the ionomer within the membrane. Lower compatibility of EMI-Tf with the more hydrophobic matrix of the 20 % sulfonated samples would increase this effect compared to the 40 mol % sulfonated compositions. The second possibility is that application of pressure at a temperature (140 °C) similar the plasticized thermal transitions of the ionomer ($T_{g,m} \approx 114 - 126$ °C, $T_{g,cl} \approx 134 - 150$ °C, Chapter 4), even for short

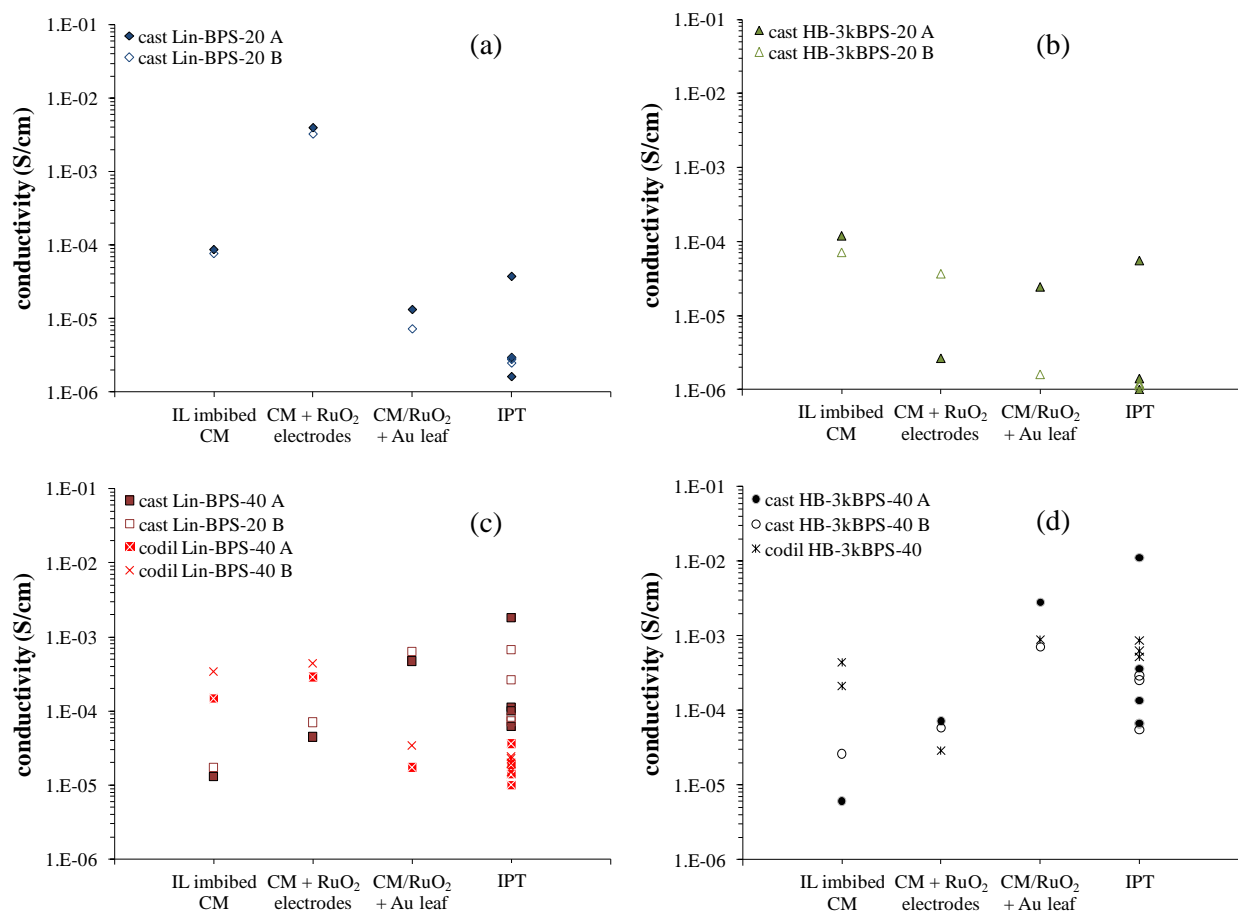


Figure 5.4: Ionic conductivity measured at each stage of IPT fabrication for (a) Lin-BPS-20 (b) Lin-BPS-40 (c) HB-3kBPS-20 and (d) HB-3kBPS-40

durations, may allow sufficient mobility of the ionomer chains to induce further changes to the microphase separated morphology. This effect was even observed without external pressure in the case of heated co-diluent swelling where charge transport did not increase proportional to

increased uptake when heat was applied. If pressure applied in the z-axis causes elongation of domains in the x-y plane this may result in lower through-thickness (z-axis) conductivity, despite increased instability of the charge transport pathway in the presence of the heated ionic liquid.

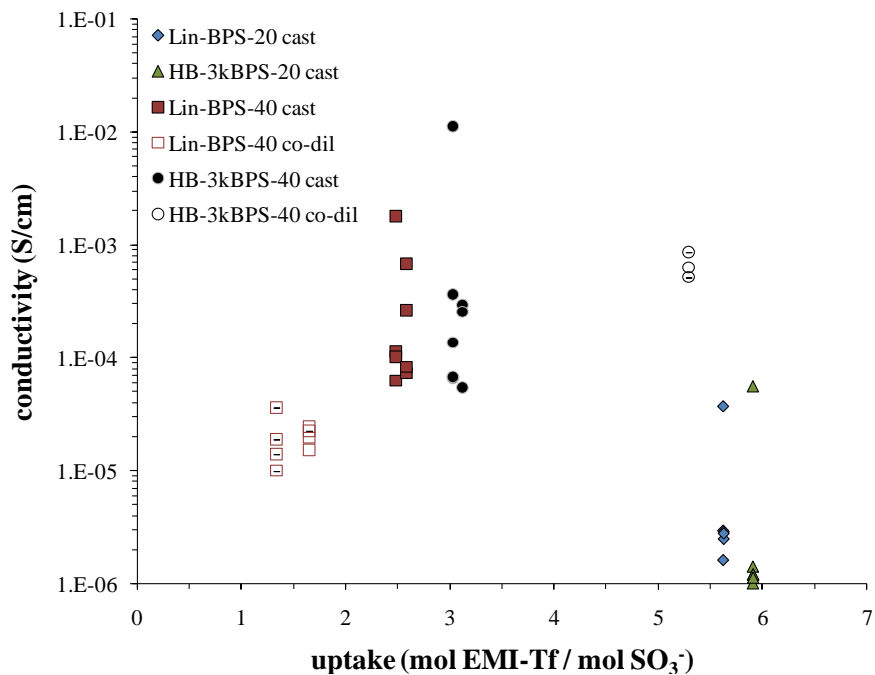


Figure 5.5: Ionic conductivity versus molar uptake for the full series of sBPS – IPTs after fabrication

Despite changes due to the fabrication process, all sBPS – IPTs retain conductivity higher than the design threshold of 1 μ S/cm. Final conductivity for the full series of IPTs is shown in Figure 5.5 based on the original uptake of the central membrane and matched uptakes of the electrodes. For the remainder of Chapter 5 uptake will refer to the values reported for the imbibed central membrane. Although small amounts of ionic liquid may be lost to processing, the fabrication conditions were kept constant for all IPTs and it is assumed that similar losses were experienced for all compositions. Changes in conductivity due to morphological variations with processing are more likely to be dependent on the composition and topology of the ionomer combined with the original uptake method. For IPTs composed of 40 mol % sulfonated ionomer the conductivity appears to increase linearly with uptake of ionic liquid. The linear and branched samples with 20 mol % sulfonation fall outside of this trend despite their originally high molar uptake. The single outliers for these IPTs likely contain shorts that produce high conductivity.

5.3.3 Equivalent circuit modeling for IPT capacitance

As previously shown in Sections 3.3.2.2 – 3, the impedance characterization of the transducers is useful for equivalent circuit modeling and estimation of the device's effective double-layer capacitance. The same EC-2 equivalent circuit model (Figure 3.11) as was fit to impedance spectra in Chapter 3 is applied here based on Equations 3.4 – 3.6 for the complex impedance. Essentially the only changes between the two sample sets are based on ionomer composition, increased ionic liquid uptake, minor processing variations, and dimensional changes. Although it is possible for these differences to be reflected in the model parameter values the geometry, interfaces, and processes on which the model impedance is based do not change. For review, the Randle's circuit including a constant phase element (Q_1), charge transfer resistance (R_{ct}), and Warburg diffusional element (W) is representative of the processes and interfaces inherent to the DAP electrodes. The second constant phase element (Q_2) and resistor (R_1) are in parallel to each other with the total unit in series with the Randle's circuit. $R_1 \parallel Q_2$ was previously assigned to the bulk resistance of the ionomer which contains a pseudocapacitive interface with the bulk ionic liquid (R_2). In this chapter the IPTs were only analyzed with EIS for a frequency range of 0.01 Hz – 1 MHz. Due to the decreased impedance associated with the ionomers at higher uptake, the response shifted to higher frequency and did not resolve the capacitive transition between R_1 and R_2 as well as in Chapter 3. However, the EC-2 model was still successfully fit to the available frequency range and representative fits of the impedance data for a cast sample of Lin-BPS-20 and a co-diluent swollen sample of HB-3kBPS-40 are provided in Figure 5.6a and b respectively.

The Bode and Nyquist plots for these two ionomers are displayed specifically to provide a comparison between the IPTs with the highest and lowest impedances. These samples also allow for comparison of IPTs produced with the casting and co-diluent swelling techniques. The EC-2 model fits the impedance for both cases very well across the entire available frequency range of magnitude and phase with cumulative error below 1 %. The primary source of error which occurs regardless of the magnitude of the impedance is the high frequency upturn toward

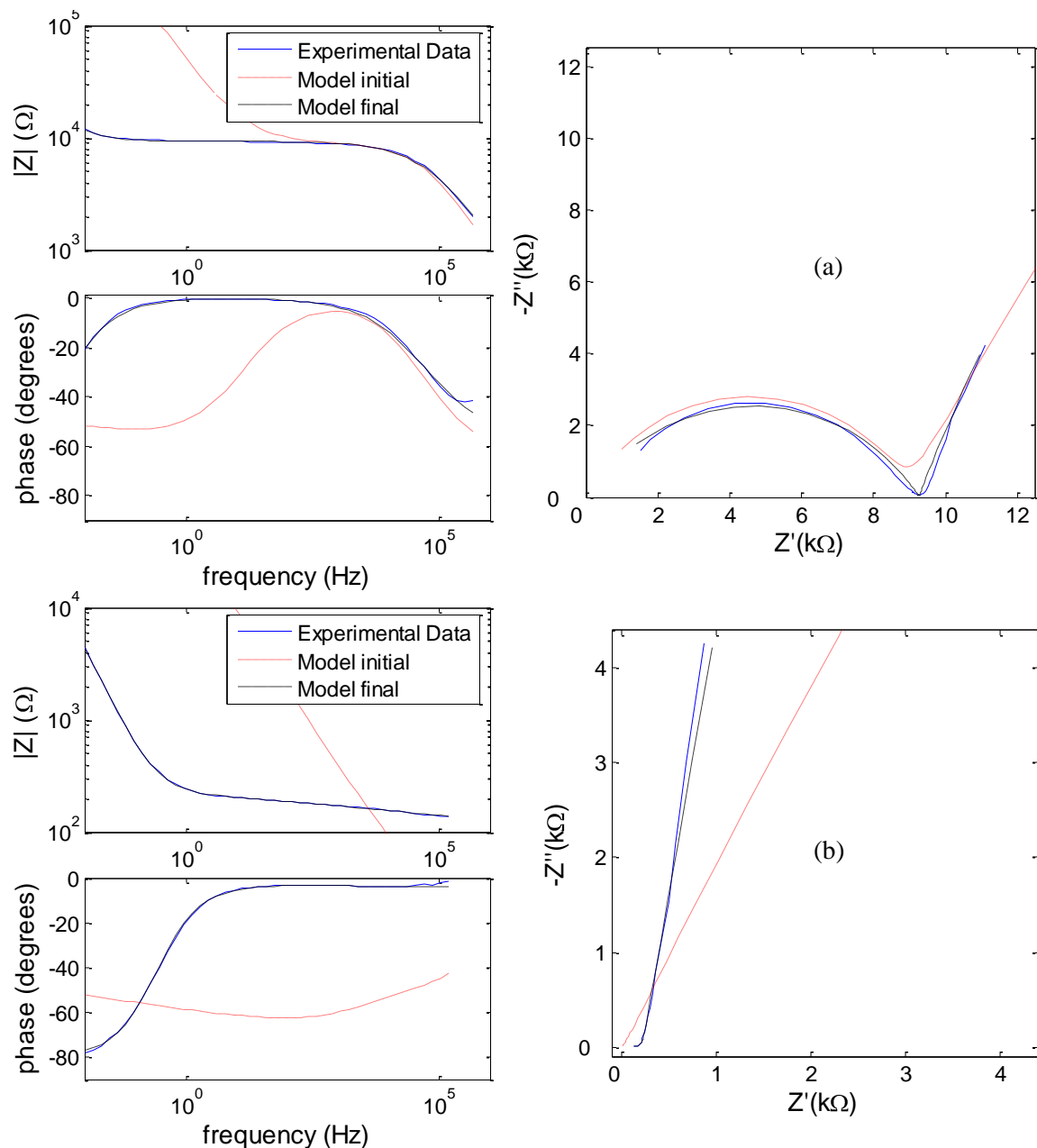


Figure 5.6: Representative fits of EC-2 to experimental EIS data for IPTs fabricated with (a) cast Lin-BPS-20 and (b) co-diluent swollen HB-3kBPS-40

positive phase seen in the Bode plots approaching 1 MHz. Typically this upturn is associated with inductance associated with the measurement so the data was removed from the analysis for phase angles above zero. In the previous analysis from Chapter 3, the high frequency regime was resolved with data from a second impedance analyzer that was not used here. The quality of the fit shown in Figure 5.6 is representative of the fits performed for each of the six primary IPT

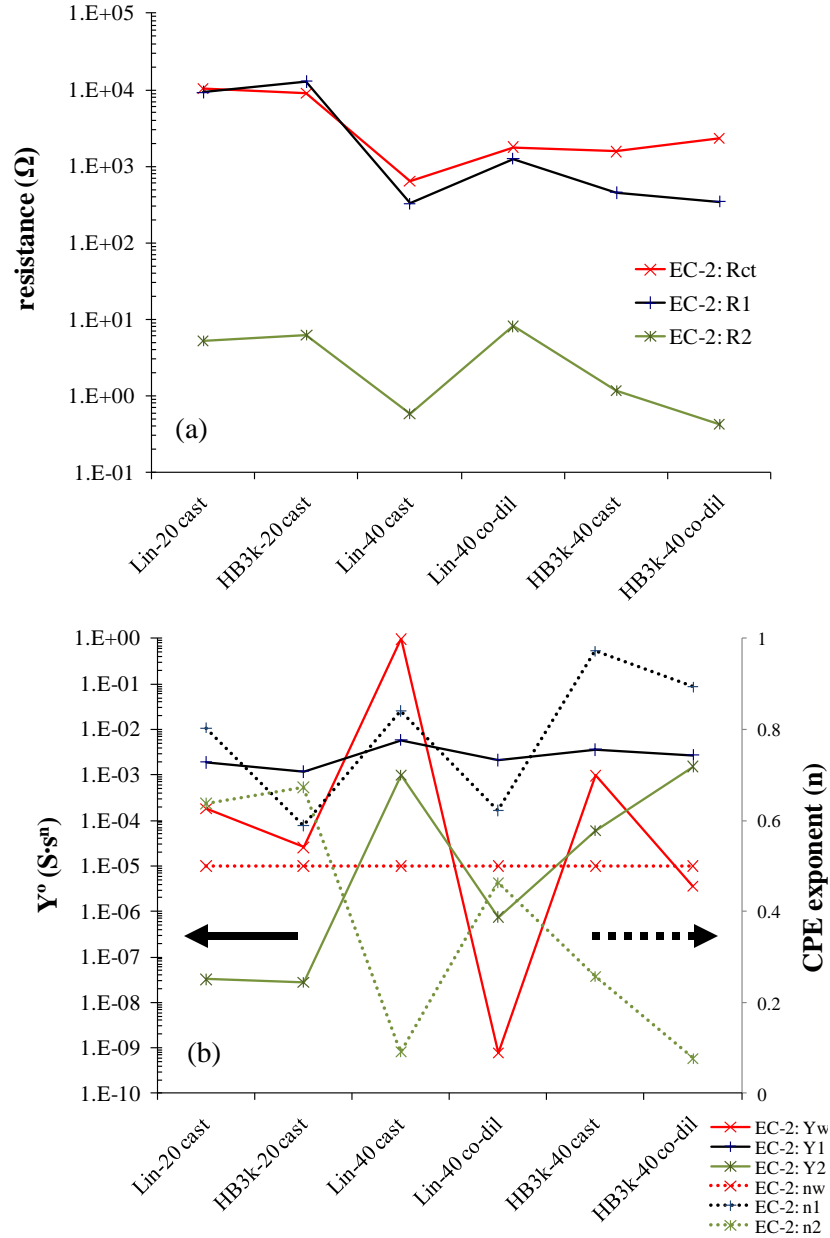


Figure 5.7: (a) Resistive and (b) capacitive equivalent circuit parameters from EC-2 as determined from fits and calculations based on impedance data for sBPS – IPTs

compositions (4 cast, 2 co-diluent). Due to the large range of bulk impedance associated with the different ionomers and uptakes, experimental data from EIS served as the initial guess values for each individual fit. However, constant and equal values of Y_w^o and Y_1^o were used as initial guesses for all samples to prevent any bias in the model's adjustment of these parameters for the fit. This is primarily due to the use of the Randle's circuit parameters to estimate the effective capacitance associated with the double layer developed in the electrodes. The final resistive and

capacitive model parameters that result from the data fits are plotted versus the IPT matrix ionomer in Figure 5.7a and b respectively.

As shown in Figure 5.7a the largest values for the charge transfer resistance (R_{ct}) and the bulk electrolyte resistance (R_1) are displayed by the IPTs constructed with the 20 mol % sulfonated ionomers through the casting process. The values are nearly equal, similar to the trend at 45 vol % RuO_2 for the HB-3kBPS-20 IPTs in Chapter 3. However, the membranes in Chapter 3 demonstrated an order of magnitude higher impedance due to the lower uptake level (75 wt %). The values of R_{ct} and R_1 decrease approximately an order of magnitude for membranes with 40 mol % sulfonation. This change suggests that regardless of the specific ionic liquid uptake, the ion content of the matrix ionomer affects charge transport both in the bulk and in the electrical double layer at the conductor – ionomer interface. The origin of the deviation that appears between the values of R_{ct} and R_1 for the HB-3kBPS-40 IPTs is unclear. Comparison of the cast and co-diluent swollen membranes for Lin-BPS-40 did not reflect the same deviation. Potentially the lack of data at high frequency for these very low impedance samples may have affected the iterations of the fit. Further experiments to higher frequency may resolve the discrepancy. The values of R_2 are relatively consistent for all IPTs investigated. Although some variation is shown for the different ionomers, no conclusions are presently made on the fit of this parameter due to its appearance at very high frequency that was not adequately measured with this set of experiments. Values of R_1 and R_2 are used to calculate the respective conductivities for the bulk ionomer and the ionic liquid shown in Figure 5.8. The model values show relatively good agreement with the experimentally determined conductivity. However, the deviation in values for HB-3kBPS-40 now suggests that R_1 may be overestimated by the model fit, reporting higher impedance that results in a lower conductivity.

Values for the capacitive elements of the EC-2 model shown in are shown in Figure 5.7b for the six IPT compositions. Unlike the resistive elements, the capacitive model parameters do not show a specific trend associated with the ionomer composition of the IPT. Large deviations in the Y_w^o and Y_2^o parameters are potentially due to the nature of the circuit such that estimation of W and Q_2 in series is based on impedance data at the limits of the experimental frequency range. The primary data of interest is the values of n_1 and Y_1^o that contribute directly to the estimation of the double layer capacitance from the Q_1 element of the Randle's circuit. Y_1^o remains relatively constant regardless of the ionomer composition employed for the IPT. n_1 varies

between values of 0.5 – 1 which are associated with a Warburg impedance and a pure capacitor respectively.[233] Values between these limits are a good indicator of the pseudocapacitance described by a constant phase element, which is accurate for this series.

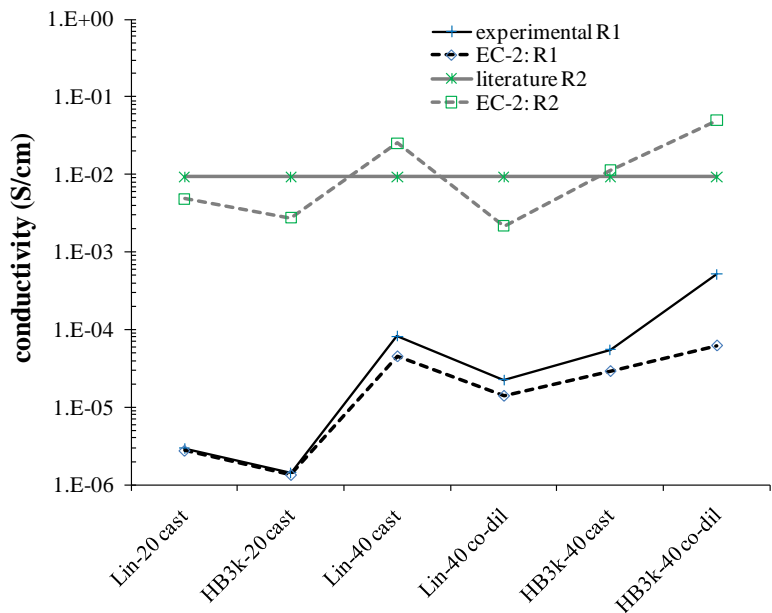


Figure 5.8: Ionic conductivity of R_1 and R_2 components for sBPS – IPTs as calculated from experimental results and EIS modeling with EC-2

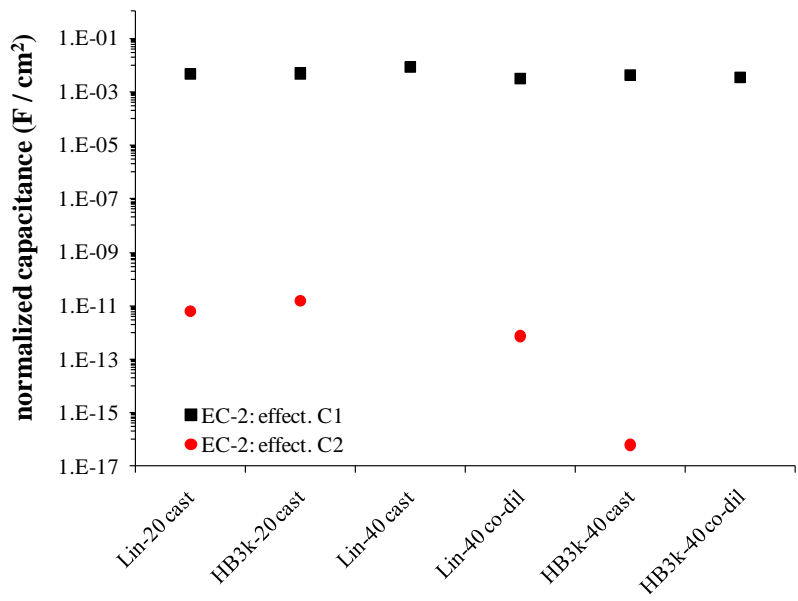


Figure 5.9: Calculated effective capacitance associated with each CPE in EC-2 from fits of impedance data for built sBPS – IPTs

The model parameters were then used to calculate the effective capacitance for the electrical double layer (C_1) and the ionomer – ionic liquid electrolyte (C_2) based on Equation 3.10. The values for the series of IPTs are shown in Figure 5.9. Values of C_2 are included for completeness, although the previously discussed scatter in the model parameters at the limits of the frequency range caused large variations in its estimation. Capacitance of the ionomer – ionic liquid electrolyte is already known to be very small so this result is not unexpected. Values of C_1 , similar to the findings of Akle *et al.*[54] demonstrated that variations in ionomer composition do not significantly vary the device capacitance around an average value of 4.73 mF/cm^2 for the six representative IPTs. However, the values of C_1 calculated here are significantly higher than the effective capacitance of $2.70 \text{ }\mu\text{F/cm}^2$ demonstrated by the HB-3kBPS-20 – IPT with 75 wt % uptake and 45 vol % RuO_2 electrodes in Chapter 3. The lower values of R_{ct} and R_1 for the HB-3kBPS-20 sample in this study were previously attributed to the higher uptake of ionic liquid and do increase the capacitance. However, the capacitive terms (Y_1^o and n_1) showed a more significant difference. For the same ionomer, Y_1^o increased more than two orders of magnitude and n_1 by nearly 120 %, indicating that the transducers in this study demonstrate behavior closer to that of an ideal capacitor than those in the percolation study. As mentioned in Section 3.3.2.3, assumption of the transducer as a network of resistors and capacitors in series allows for calculation of the effective capacitance based on the reciprocal of the imaginary part of the impedance (Equation 3.7).[54] This technique provides a frequency dependent estimation of the capacitance, which is typically reported for low frequencies (e.g., 0.25 Hz). For comparison, C_1 calculated from EC-2 fits of impedance data are plotted versus the capacitance at 0.25 Hz calculated with the reciprocal of the imaginary impedance in Figure 5.10. The agreement between the results of the two calculations is very good. Due to the consistently higher capacitance values and constant RuO_2 loading across the IPT series, the modifications to the casting DAP method are likely the origin of the increased capacitance in comparison to the percolation study. Both this result and the already reported increases in conductivity for the IPT series are expected to produce superior performance to those previously demonstrated with sBPS – IPTs.

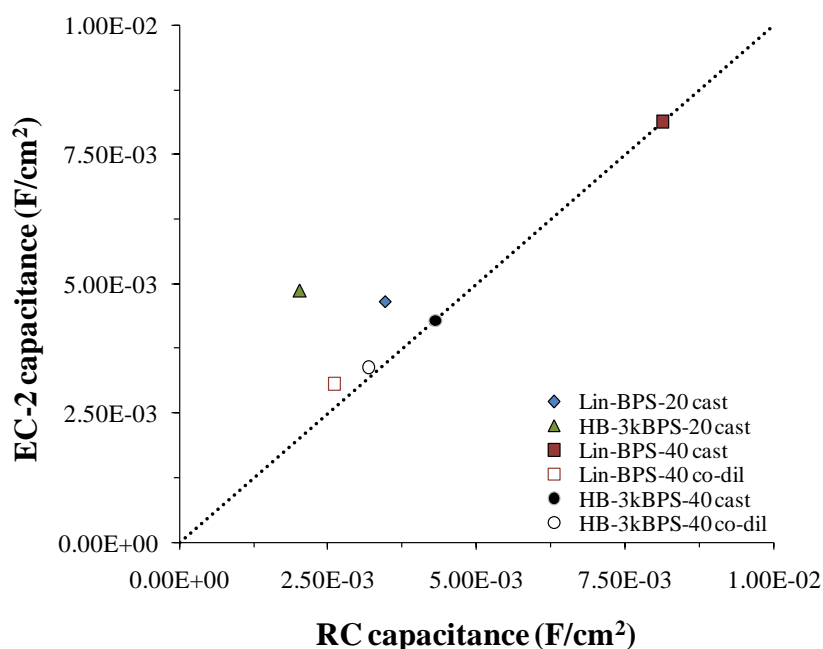


Figure 5.10: Comparison of effective capacitance (C_1) for sBPS – IPT impedance modeled as a series of RC circuits (x-axis, Equation 3.7) or with EC-2 (y-axis, Equation 3.10)

5.3.4 Evaluation of electromechanical transduction for sBPS – IPTs

After establishment of the electrical properties of the IPT series, electromechanical transduction experiments were performed to measure actuation performance based on ionomer composition and the method of ionic liquid uptake. Frequency responses were recorded for the entire series of IPTs to provide a wide range of data on the free displacement per the applied voltage. The results of this method are also employed to calculate the effective bending modulus of the transducer. Based on actuation performance in the frequency domain, two representative IPTs of each composition were then tested for performance in response to step and square wave inputs. The following discussion and corresponding figures primarily concentrates on six representative transducers from the total series. The compositions and dimensions of those IPTs are provided in Table 5.2. The overall goal of this testing is to demonstrate improved actuation performance of sBPS – IPTs and to differentiate between actuation on the basis of the ionomeric matrix composition.

Table 5.2: Representative sBPS – IPT dimensions and densities

ionomer	uptake method	thickness (mm)	width (mm)	free	total	density (g/cm ³)
				length (mm)	length (mm)	
Lin-BPS-20	cast	0.178	2.52	19.1	27.9	2.05
HB-3kBPS-20	cast	0.154	3.09	19.3	29.1	1.89
Lin-BPS-40	cast	0.110	2.75	19.2	27.5	2.44
	co-diluent	0.162	3.09	19.3	29.9	1.93
HB-3kBPS-40	cast	0.112	3.08	19.2	27.7	2.45
	co-diluent	0.170	2.74	19.2	29.1	1.97

5.3.4.1 *Frequency response functions for IPT actuation*

Responses of the IPTs in the frequency domain were obtained through application of a random input voltage with a magnitude of 0.5 V_{rms}. Each transducer was clamped in a cantilever configuration where the displacement of any point along its free length was measured with a non-contact laser vibrometer. Fourier analysis provided transfer functions between the free displacement and the driving voltage as well as the induced current per the applied voltage. These transfer functions were converted to microstrain per volt ($\mu\epsilon/V$) and electrical impedance ($V/A = \Omega$) with Equations 5.2 and 5.3 respectively. Experiments were performed for the following frequency ranges: 0.1 – 10 Hz, 0.25 – 100 Hz, 2.5 Hz – 1 kHz, and 25 Hz – 10 kHz. Similar to previous results with Nafion[®] – IPTs, the first natural frequency of the devices was primarily detected between 0 – 100 Hz. Representative curves for the six IPT compositions tested in this frequency range are provided in Figure 5.11.

In terms of microstrain per volt (Figure 5.11a), the spread in the low-frequency response of the IPTs is based on ionomer composition. IPTs composed of less sulfonated sBPS produce less strain per volt while the more highly sulfonated IPTs display larger responses to the driving voltage. Strain per volt for the series (at 0.25 Hz) is bounded by a maximum of 91 $\mu\epsilon/V$ (HB-3kBPS-40, co-diluent) and a minimum of 2.96 $\mu\epsilon/V$ (Lin-BPS-20, cast). The negative slope of the curve for frequencies below the first resonance peak is typically associated with decreased charge mobility in IPTs.[20] Due to the fact that the mobile charges inside the transducer are not able to track the driving voltage as frequency increases, the total strain response of the device decreases. The average slope of each curve was calculated between 1 – 10 Hz but comparison of

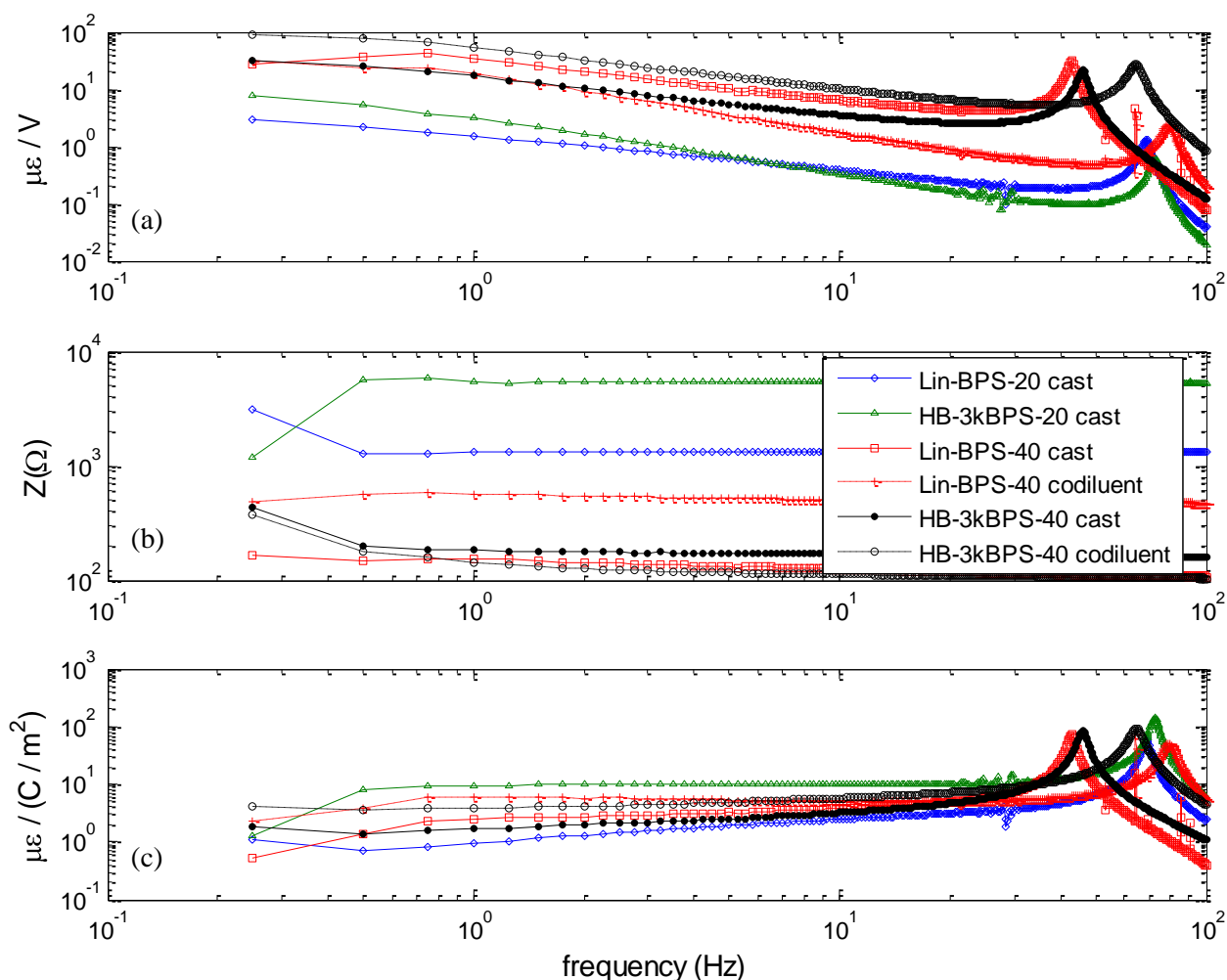


Figure 5.11: Representative frequency response functions for the series of sBPS – IPTs expressed as (a) microstrain per volt (b) impedance (voltage per current) and (c) microstrain per areal charge

the values did not reveal any direct trends with ionomer composition or ionic liquid uptake. However, the trends in microstrain per volt do match well with the impedance values shown in Figure 5.11b. The impedance values result from a combination of the ionomer composition and the ionic liquid uptake. Lin-BPS-20 and HB-3kBPS-20 display the highest impedance due to their lower degree of sulfonation. Interestingly, those samples contain the highest molar uptake of ionic liquid and the same weight percent uptake as the other cast samples with higher degrees of sulfonation. The co-diluent swollen sample of Lin-BPS-40 shows the highest impedance of the 40 % sulfonated samples, which is expected since it contains the lowest overall uptake of the series. The other highly sulfonated samples display similar impedances. The full series displays

resistive behavior across the frequency range investigated and the magnitudes of the impedance match well with the values detected through EIS characterization.

Farinholt and Leo demonstrated through analytical modeling and experimental validation that IPT performance variations are reflected in the impedance response of the transducer.[4] The ability of the device to convert the driving voltage into charge transport is a primary factor in actuation and is directly reflected in the present study as well. Normalization of the frequency dependent strain response with the impedance and geometry of the transducer (Equation 5.4) provides the strain per areal charge, $\mu\epsilon/(C/m^2)$. This unit is also referred to as the strain per electric displacement since it quantifies the strain response of the transducer to the charge transport (i.e., current) that results from the applied voltage, as shown in Figure 5.11c. This normalization of the actuation response decreases the spread in the data at 0.5 Hz from a factor of 35.5 to a factor of 11.75 and also eliminates the low-frequency roll-off that appeared below the natural frequency. The range of strain per electric displacement is between 0.7 – 8.2 $\mu\epsilon/(C/m^2)$ for this series of sBPS – IPTs swollen with EMI-Tf. Although the impedances are generally higher and the strain response is lower here than for previously demonstrated Nafion[®] – IPTs (various diluents and electrodes), the range of $\mu\epsilon/(C/m^2)$ values are very similar if not on the low end of the spectrum. Specifically, the sBPS – IPTs designed and actuated by Akle *et al.* that were water-based with IRP electrodes showed values between 10 – 15 $\mu\epsilon/(C/m^2)$. [20, 54] When Nafion[®] – IPTs (Li⁺) were constructed with RuO₂ (42 vol %) and EMI-Tf (60 wt %), bending actuation produced strain per electric displacement values of 3 – 8 $\mu\epsilon/(C/m^2)$, showing a similar collapse based on areal charge regardless of variance in the IPT design parameters.[39] Presently, no direct correlation between topology or uptake method and actuation performance emerges from the analysis of the frequency response functions. This lack of correlation may be linked to the strain per charge analysis, which indicates that the composition of the electrodes and diluent more directly affects the strain per electric displacement than the composition of the ionomer or the geometry of the IPT.

The data contained in the frequency response functions for $\mu\epsilon/V$ and $\mu\epsilon/(C/m^2)$ is also useful for estimation of the effective modulus of elasticity (E'_{eff}) and the damping ratio (ξ) for the transducers according to Equations 5.5 – 5.8. The calculation was carried out for the full series of forty-two transducers, including a Nafion[®]–IPT that was built with RuO₂ and EMI-Tf at ~60 wt % uptake with the DAP. The values for ξ and E'_{eff} are shown in Figure 5.12 according to the

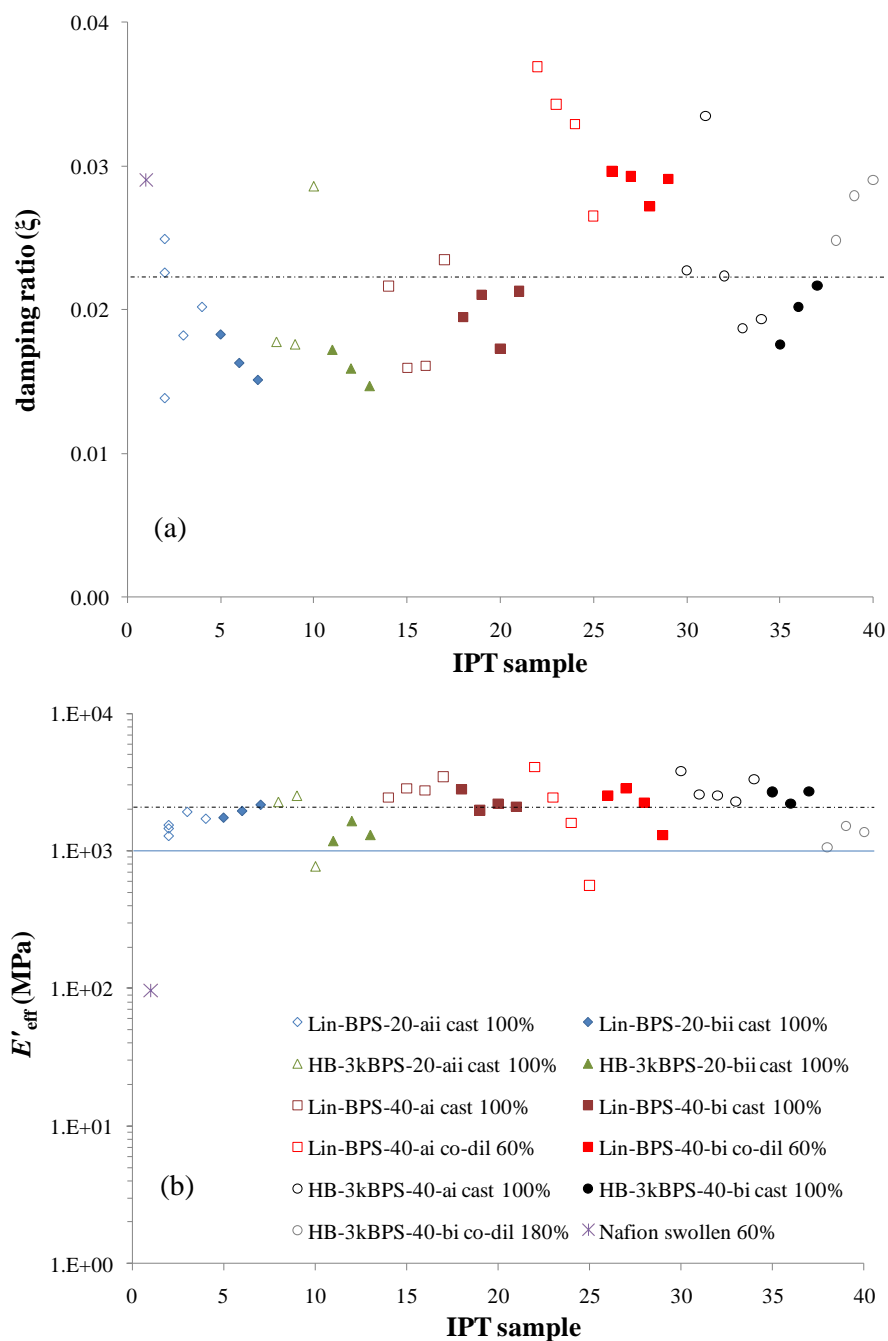


Figure 5.12: (a) Damping ratios and (b) effective bending modulus for the full series of sBPS – IPTs as determined from the frequency response to a random input at 0.5 V_{rms}

ionomeric matrix composition and the uptake method. Observation of the full data set provides a better concept of the variations in mechanical properties for the transducers produced from two independent IPT sheets for each composition. The damping ratios shown in Figure 5.12a are

typical for IPTs and the series has an average value of 0.022 indicated by the dashed line. Note that the Nafion[®] – IPT displays a value just below 0.03. Also of interest is the fact that the co-diluent swollen samples primarily fall above the average while the cast samples fall almost exclusively below the average. The elastic modulus values for the full IPT series are shown in Figure 5.12b. Despite some variations due to processing and application of the electrodes, the IPTs are expected to have relatively consistent modulus based on the trends in plasticization with uptake shown in Chapter 4. Although that study only investigated cast samples, the co-diluent swollen samples follow the general trend. Overall, the series has an average effective modulus of 2.1 GPa, more than an order of magnitude higher than the typical 100 MPa value for hydrated Nafion[®] – IPTs (also shown). Confirmation of increased stiffness for the sBPS – IPTs also explains the overall decrease in actuation strain compared to other previously demonstrated ionomers. Although not addressed experimentally in this dissertation, the combined actuation responses and effective modulus for this series of ionic liquid swollen sBPS – IPTs suggest that these compositions are good candidates for producing significant blocked force.

5.3.4.2 *Actuation responses to step inputs*

Following analysis of the frequency response functions for the series of sBPS – IPTs, two representative transducers were chosen from each composition to test actuation responses in the time domain to step voltage inputs. The experimental setup remained identical to the one used to measure the frequency responses. Each transducer was subjected to a series of step voltage inputs while measuring the free displacement near the end of the device. The applied voltages were ± 0.5 , 1, 2, and 3.5 V for durations of 300 s. Note that the 3.5 V step experiment was not completed for the majority of the 40 % sulfonated IPTs because very large strains for long durations were destructive to the transducer and tended to induce short circuits. In addition to the step responses, each transducer was tested for its free displacement response to a square wave input. The square wave frequency was set to 10 mHz (100 s period) and the peak voltages were ± 0.5 , 1, and 2 V.

Representative actuation responses for the six IPT compositions to a +2 V step input are shown in Figure 5.13. Several important results are observed for this experiment. First, the degree of sulfonation has a direct effect on the time response of the transducer to the applied step voltage. 40 % sulfonated IPTs show much greater peak strains and strain rates in comparison to

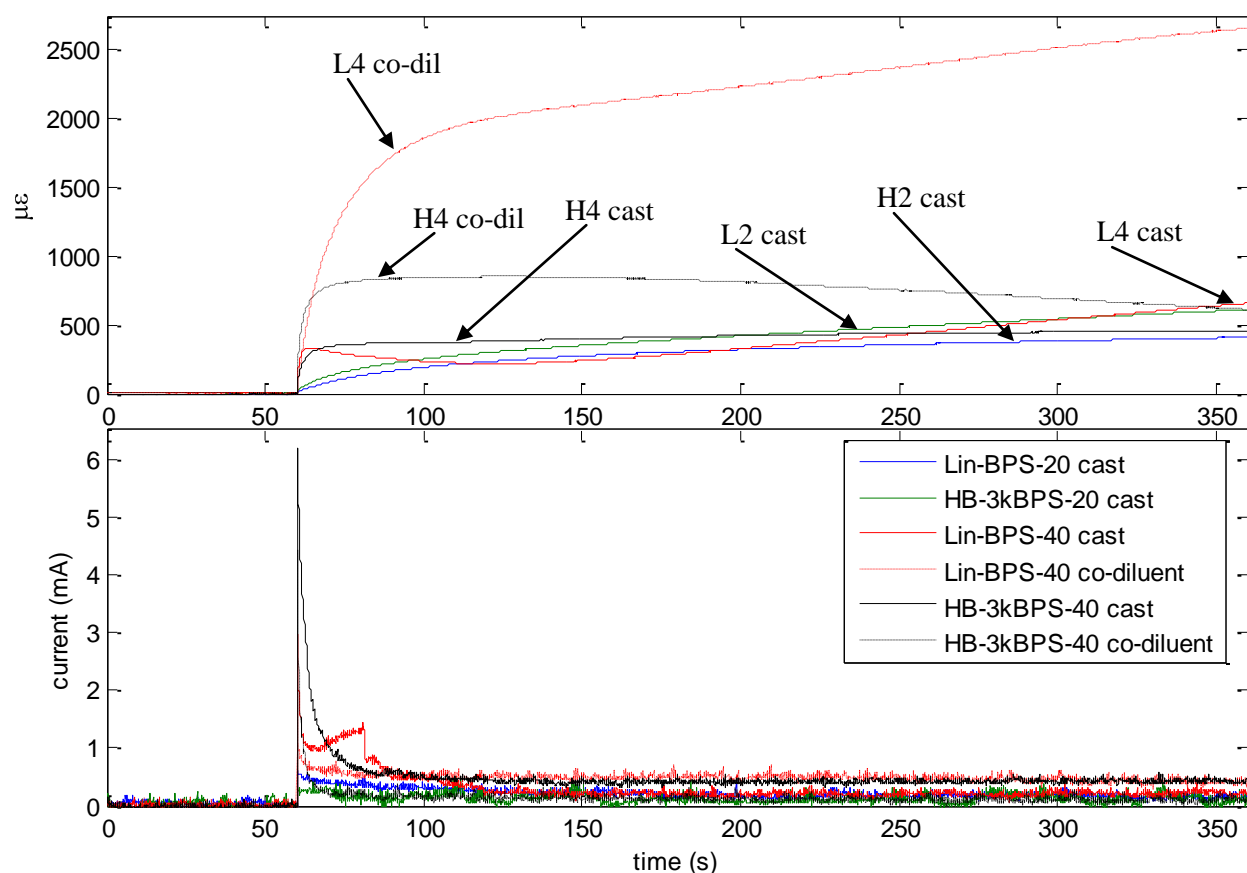


Figure 5.13: Bending actuation response of representative sBPS – IPTs subjected to a +2 V step input for 300 s

the less sulfonated analogues. This difference in performance is also apparent in the current response with time. IPTs constructed with Lin-BPS-40 and HB-3kBPS-40 display a large spike in the current immediately following the step in voltage that decays over time to a steady state value. The transducers fabricated with Lin-BPS-20 and HB-3kBPS-20 through the casting method display a much smaller spike in current that nearly equals the steady state current for the remainder of the test. This more resistive behavior aligns well with the higher impedance detected both with EIS and in the frequency response functions for the built transducers. The other dominant trend in the results is the far greater peak strain and strain rate of IPTs built with the co-diluent swelling method. Notably, these ionic liquid swollen sBPS – IPTs show very little back relaxation for the 2 V step response. This result was expected based on designation of an ionic liquid as the diluent per previous results with ionic liquid swollen Nafion[®] – IPTs.[57, 88] However, over the experimental time frame higher sulfonation of the ionomeric matrix leads to

greater back relaxation of the device. Summation of the differences in response for the six compositions at 300 s unexpectedly results in very similar peak strains ($\sim 500 \mu\epsilon$). Only the co-diluent swollen Lin-BPS-40 IPT shows a significantly different strain than the other transducers at the end of the test.

Peak strain determined for tests of all twelve IPTs due to step voltage inputs of varying magnitude and direction are summarized in Figure 5.14. Due to the detection of some back relaxation combined with possible drift over the period of the test, peak strain was defined for the initial maximum observed in the step response. Again, the Lin-BPS-40 co-diluent swollen IPT is shown to outperform the rest of the sBPS series with a peak response of $\sim 2500 \mu\epsilon$ for a 2 V step input, followed by the branched co-diluent sample. Transducer to transducer the strain response increases relatively linearly with increased magnitude of the step voltage for all samples compositions tested. For the IPTs constructed fully with the casting method (central membrane and electrodes) the peak strain results are all very similar regardless of the degree of sulfonation or polymer topology.

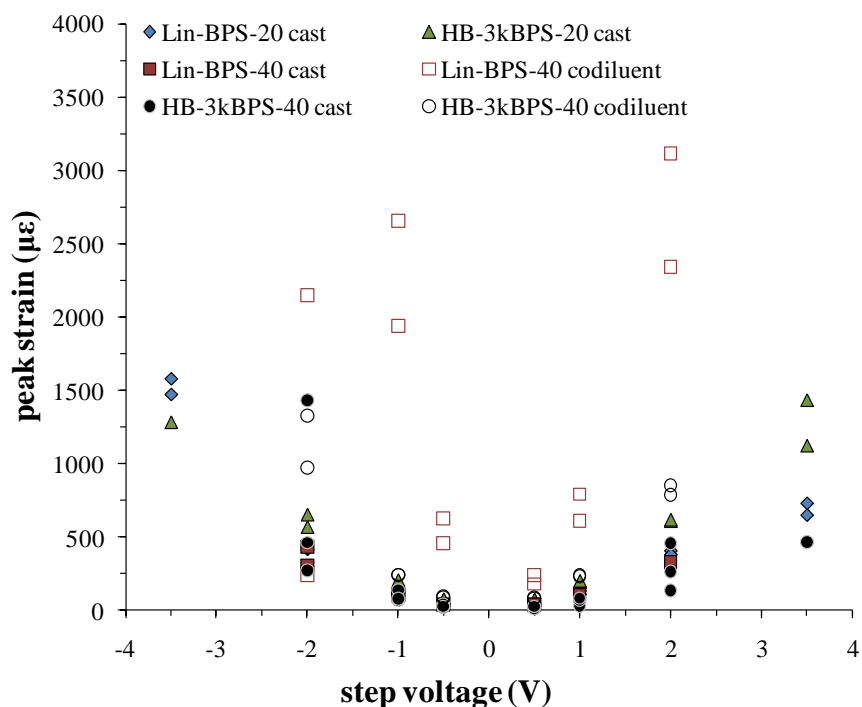


Figure 5.14: Peak strain measured for sBPS – IPT responses to step voltages for 300 s

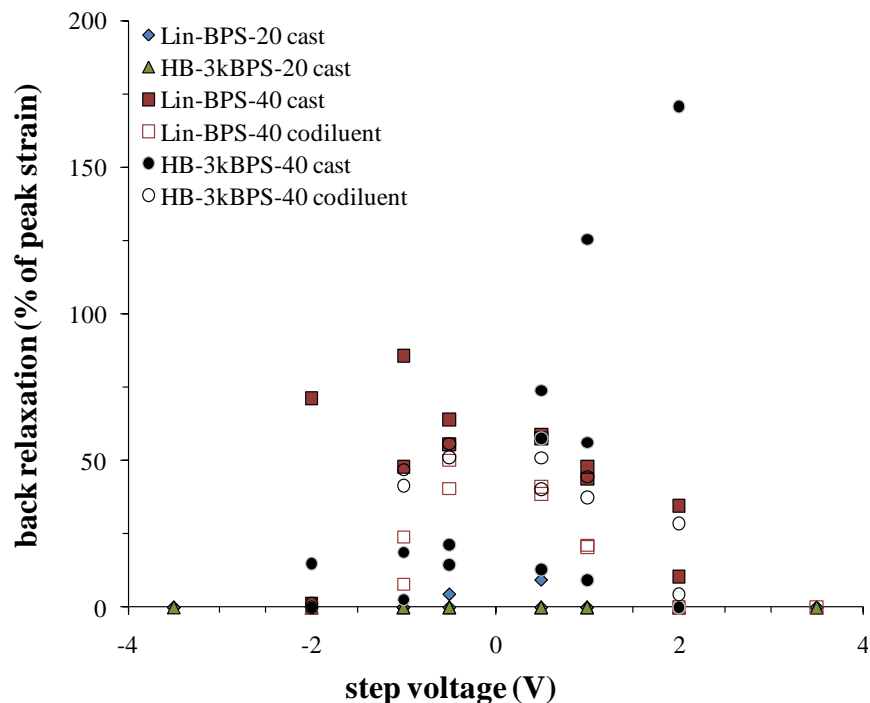


Figure 5.15: Back relaxation as a percentage of peak strain for sBPS – IPT step responses to various voltage magnitudes and directions

In direct relation to the peak strain as a metric for IPT performance is the measure of back relaxation during a step response. In the case of these sBPS – IPTs back relaxation, if demonstrated, was based on the initial minimum shown after the peak response up to 300 s. Quantification of back relaxation is expressed as a percentage of the peak strain and is plotted for all transducers and step voltages tested in Figure 5.15. The trends in back relaxation are nearly inverse in relation to the applied voltage to the trends for peak strain. The largest back relaxations for samples of all compositions are shown at lower applied voltages (~60 %). Note, the apparent outliers from the trend were investigated and found to likely have contained electrical shorts that caused increased back relaxation and drift during continued application of the driving voltage. Although a clear distinction was apparent for peak strain based on the uptake technique, that trend is not reflected for back relaxation. The clear trend is based upon the degree of sulfonation. Less sulfonated IPTs experience almost no back relaxation for all voltages tested while the highly sulfonated IPTs display the majority of back relaxation for the series.

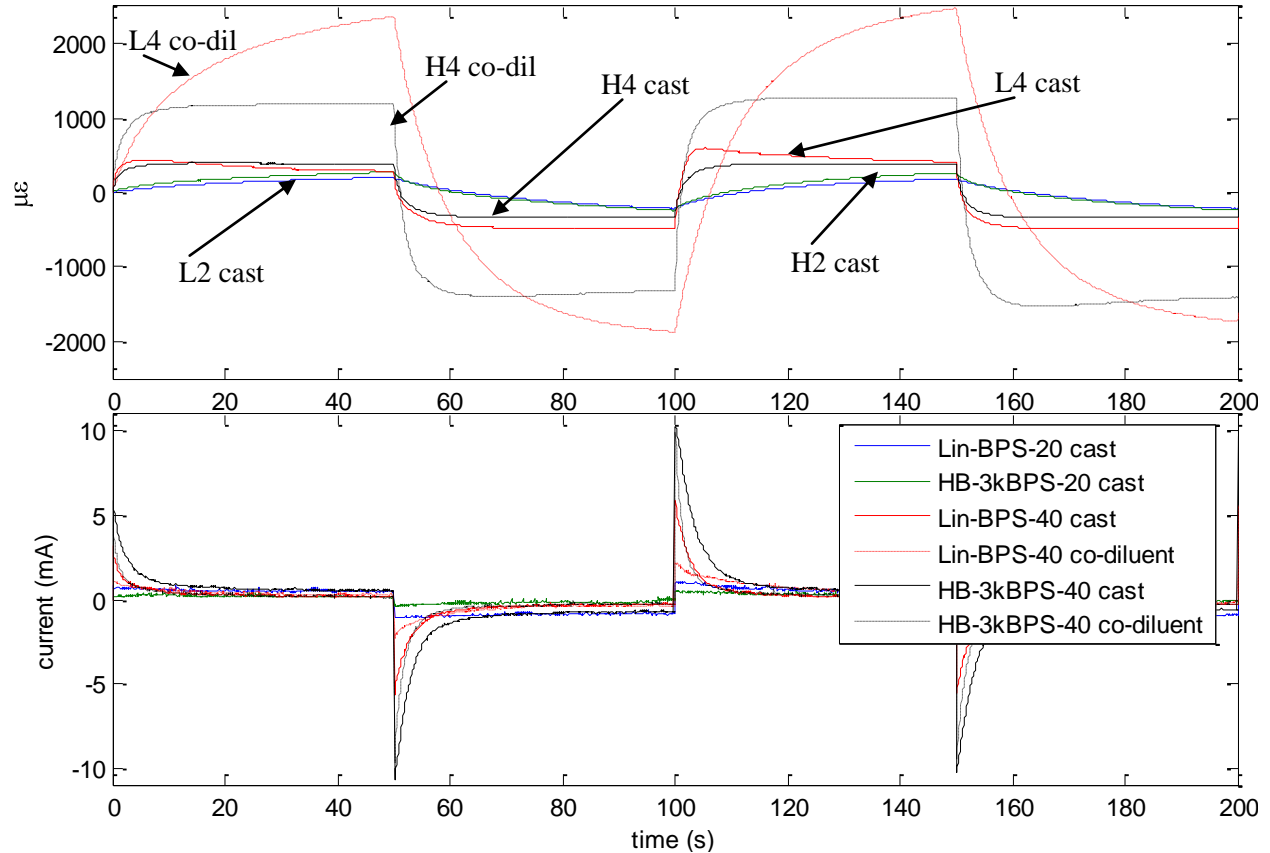


Figure 5.16: Bending actuation response of representative sBPS – IPTs subjected to a ± 2 V square wave input at 10 mHz

Although back relaxation was detected at long step voltage durations for the highly sulfonated IPTs, these results are primarily important for station-holding applications and long-term motion control. Regardless, many of the IPTs did demonstrate steady-state strains after some back relaxation. IPTs are also developed for dynamic applications in flapping flight and oscillatory swimming motions.[1, 28, 87] These applications concentrate more on the combination of actuation speed and peak strain to achieve the maximum deflection with the minimum time and voltage. Tests for this type of behavior are normally based on sine waves or square wave voltage inputs. The responses of the representative sBPS – IPTS to a 10 mHz, ± 2 V square wave are shown in Figure 5.16. The results are similar to those for the $+2$ V step responses, although with the 50 s half-period the peak strains are easier to observe. All transducer compositions demonstrate very repeatable actuation in both directions for the two periods observed. Again, the co-diluent swollen samples display larger strains than those created with the casting method, where Lin-BPS-40 achieves the maximum peak to peak strain (ϵ_{pp}) of

~0.45 %. Although the Lin-BPS-40 co-diluent IPT demonstrates the maximum strain it does not appear to demonstrate the largest strain rate. This situation creates a cross-over point in dynamic testing at short times where tests at higher frequencies would result in different trends based on composition.

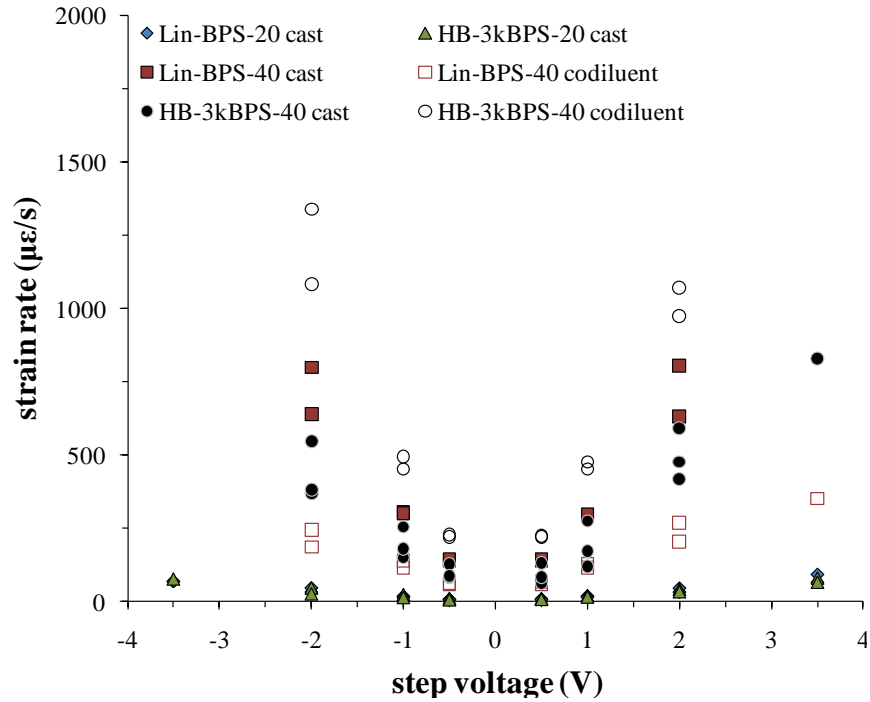


Figure 5.17: Initial strain rates for sBPS – IPTs versus the applied step voltage

The initial strain rate ($\mu\epsilon/s$) for each experiment was calculated for the first 100 ms following the applied step potential. Rise time to the peak strain differs within the sBPS – IPT series and averages over longer periods would demonstrate varying trends with composition and uptake technique. The initial strain rate is the focus here primarily for correlation with the charge transport capability of the IPT that manifests as a spike in the current for step responses. Since historically the majority of IPTs are water-based, the initial strain rate also provides a better comparison with those transducers that are typically much faster. The calculated initial strain rate versus the applied step voltage for the sBPS – IPT series is shown in Figure 5.17. Similar to the results for peak stain, the actuation speed correlates linearly with the magnitude of the applied step voltage. However, unlike the peak strain results the co-diluent swollen IPT for HB-3kBPS-40 demonstrates the greatest performance ($\sim 1000 \mu\epsilon/s$ at 2 V). As noted earlier, the primary

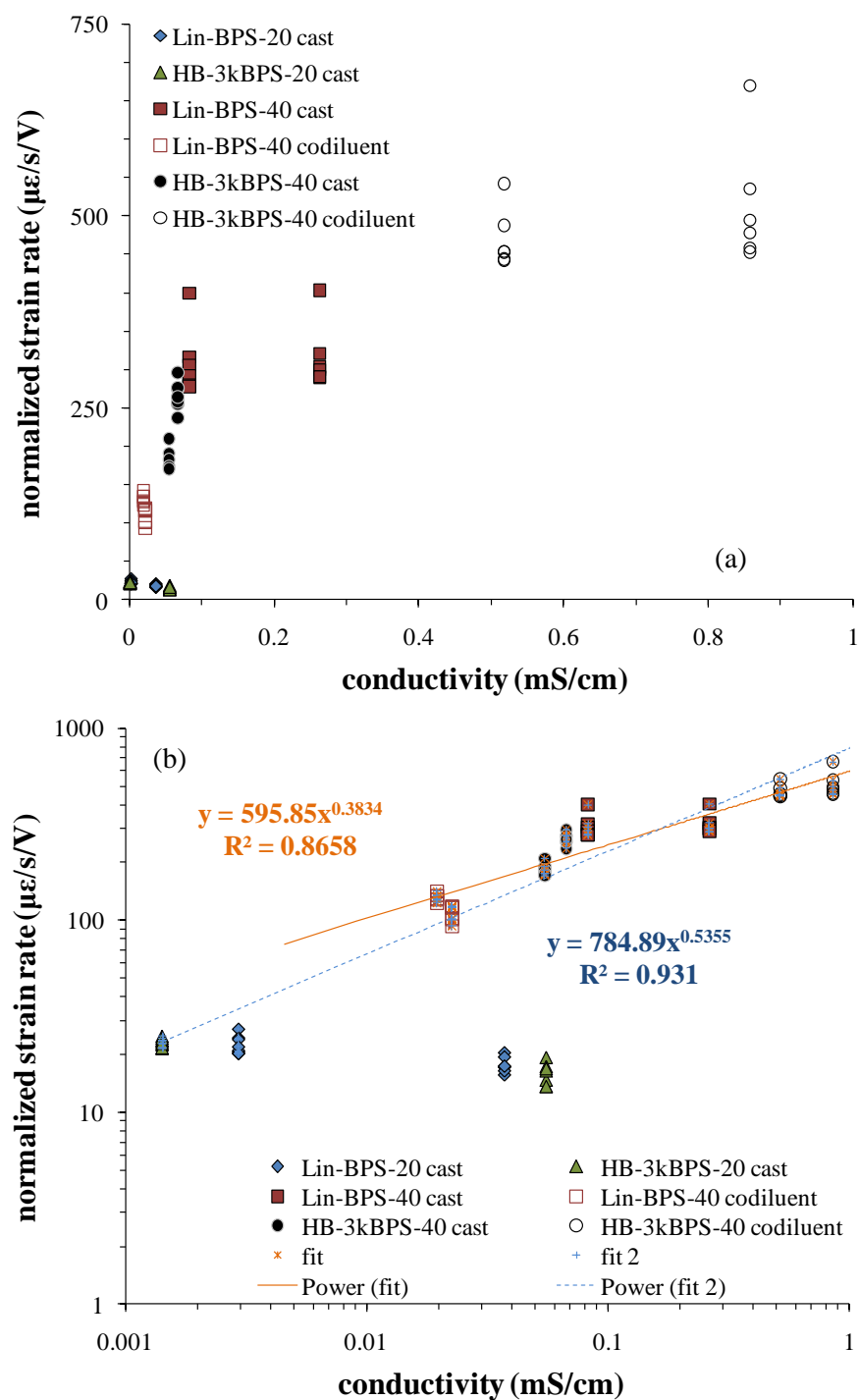


Figure 5.18: Initial strain rates (normalized to step voltage) versus the corresponding through thickness conductivity of the sBPS – IPT determined with EIS, plotted on a (a) linear scale (b) log-log scale

difference in the actuation responses is based on the degree of sulfonation of the IPT ionomer. Even for 3.5 V step voltages the 20 % sulfonated IPTs only achieve a maximum strain rate of 95 $\mu\epsilon/s$.

The seminal studies on ionic liquid swollen Nafion[®] – IPTs demonstrated a linear correlation between the initial strain rate and the conductivity of transducers fabricated with both hydrophilic and hydrophobic diluents.[61] Figure 5.18a provides the same comparison for the present series of EMI-Tf swollen sBPS – IPTs. Note that the conductivity values employed here are based on the through-thickness EIS analysis of the built transducer, already shown as a comparable technique with similar results to those obtained from the frequency responses. To construct the comparison, the strain rate data was normalized to the step voltage to give $\mu\epsilon/s/V$. This treatment was justified based on the linear relationship between the applied voltage and strain rate previously described. The overall trend shows increased strain rate for the series of sBPS – IPTs based on greater conductivity of the transducers. Although the overall shape of the plot resembles a logarithmic relationship, caution is taken before drawing immediate conclusions.

To verify the presence of any power law relationship, the results were plotted on a log-log scale in Figure 5.18b. For clarification, each group of data points at a single conductivity level represents data taken from the step responses for a single transducer. Two IPTs were tested for each of the six compositions, with one extra for the cast HB-3kBPS-40 set. The extra sample was necessary due to an electrical short in one of the tested IPTs, which led to artificially large conductivity and current responses. Data from that sample is excluded from this analysis. This series of IPTs displays large parametric variations in ionomer composition and uptake technique for the ionic liquid, although as reported previously, the effective double layer capacitance for the series is essentially constant. Due to the variations in the ionomer composition and uptake, two distinct regions emerge for the data in Figure 5.18b. The data for the less sulfonated IPTs displays expectedly lower strain rates ($\sim 20 \mu\epsilon/s/V$), although the discrepancy in the ionic conductivity between the two samples of each composition is somewhat unexpected. Based on the current responses to the step voltage, a percolated pathway through the thickness of the IPT appeared to increase its conductivity by allowing a path for the current to essentially circumvent the resistance of the central membrane. The second region displays higher strain rates, on the order of 100 – 600 $\mu\epsilon/s/V$. Best fits of a power law dependence to the data displays an

exponential dependence of strain rate on conductivity of approximately 0.38 when only the 40 % sulfonated samples are included. When all of the data, excluding the percolated samples, is fit the power law dependence increases to ~ 0.54 and displays a better quality of fit to the total data range.

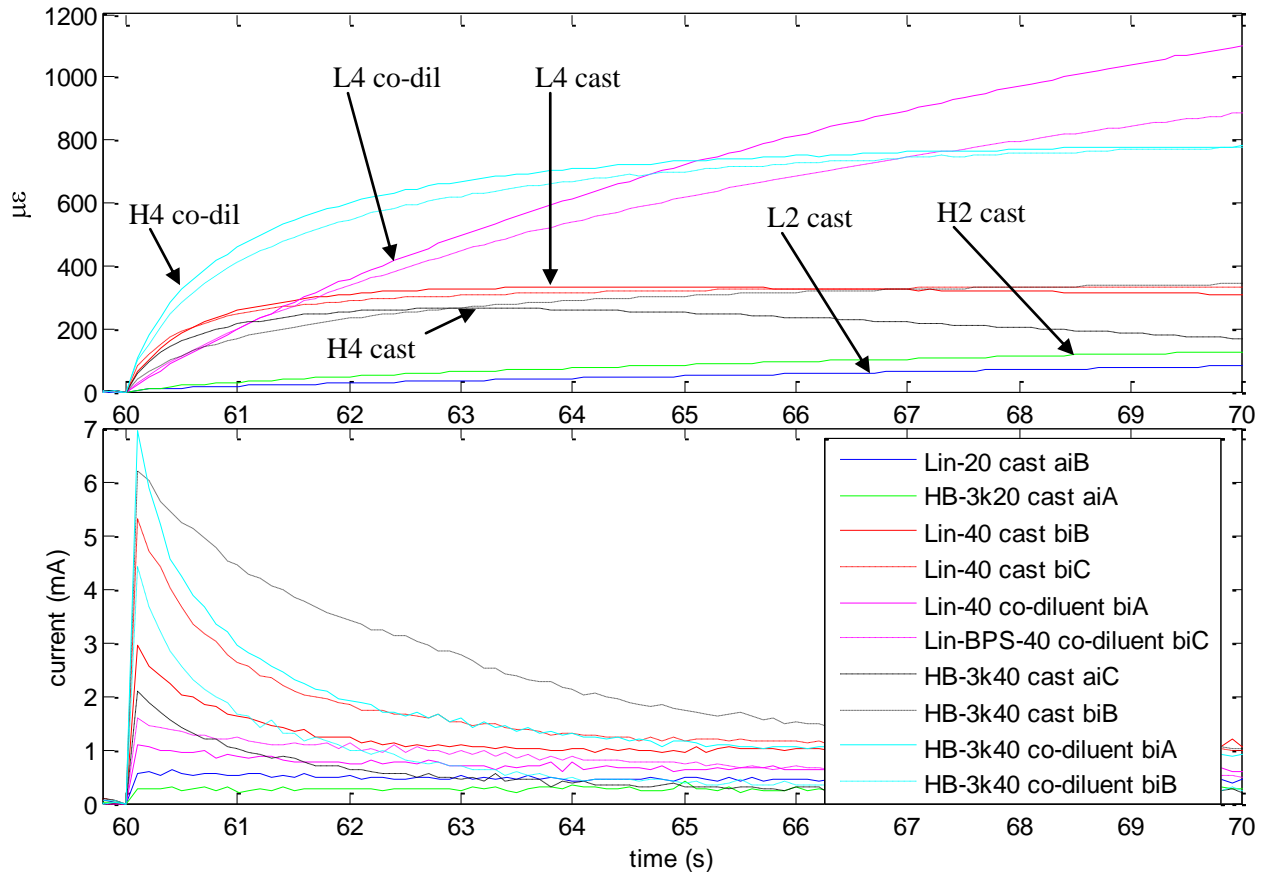


Figure 5.19: Initial 10 s of bending actuation response for sBPS – IPTs subjected to a +2 V step input (10 IPTs from full fit in Figure 5.18b)

The physical phenomenon associated with the trends seen in the log-log plot of strain rate versus conductivity appear to have correlation with the time constant for charging the electric double layer of the IPT electrodes. This time constant can essentially be observed from the real-time current responses to the step voltages, shown in Figure 5.19 for all 10 transducers fit with the power law dependence in Figure 5.18b. Data for both the current and strain response are provided for the first 10 s of actuation. The peak current associated with the initial spike following the step voltage input appears to correlate well with the trend in strain rate versus conductivity. Note that the data shown in Figure 5.19 is for a +2 V step but the small variance in

the overall normalized strain rate data per IPT allows for comparison with representative curves at one voltage. By definition, the current represents charge transported as a function of time. Many researchers have previously correlated the charge transport with time to IPT responses.[41] However, it is interesting here to see the differences in actuation correlate across a range of transducers that have very similar uptakes but use ionomers with very different ion contents. Also interesting is the fact that all of the 40 % sulfonated samples are fit well with the same power law dependence despite differences in uptake and the large difference in membrane formation based on the uptake technique.

The samples analyzed by Bennett *et al.* varied primarily on the basis of the matrix free cation, ionic liquid composition, and uptake level. In that study, actuation speed also displayed a linear correlation with the uptake of ionic liquid. Plots of the actuation rate versus both molar uptake and wt % uptake are provided in Figure 5.20a and b respectively. When compared to the uptake level, the actuation rates fall along a much more linear trend. Correspondingly, power law fits to the data display a larger exponential dependence of 1.12 and 1.40 for the normalized strain rate versus uptake in mol/mol and weight percent respectively. Spread in the data for each individual IPT composition is essentially imported from slight deviations from linearity in the relationship between strain rate and the applied voltage. The primary deviation from linearity overall is based on the degree of sulfonation for the ionomeric matrix. For both molar and weight-based uptake, transducers constructed with the 20 % sulfonated linear and branched ionomers show much lower actuation speeds per uptake than the comparable IPTs with higher degrees of sulfonation. The previous model for charge transport and electromechanical transduction in ionic liquid swollen IPTs concluded that the counterions of the ionomer were the primary charge carriers.[61] Actuation speed was shown to increase for diluent uptakes above a critical value associated with exchange of all the counterions on the backbone for those contained in the ionic liquid. In the neat state, sBPS-20 has an IEC that is nearly equal to the value for Nafion[®]. This property quantifies nearly the same number of charge carriers per gram of polymer for each IPT membrane. However, EIS characterization for cast samples of Lin-BPS-20 and HB-3kBPS-20 in Chapter 4 demonstrated that the conductivity of the central membranes was primarily dependent on the uptake level, regardless of topology or composition. Combination of these observations from characterization and performance of the IPTs highlights the effect of uptake technique and IPT fabrication on the charge transport pathway.

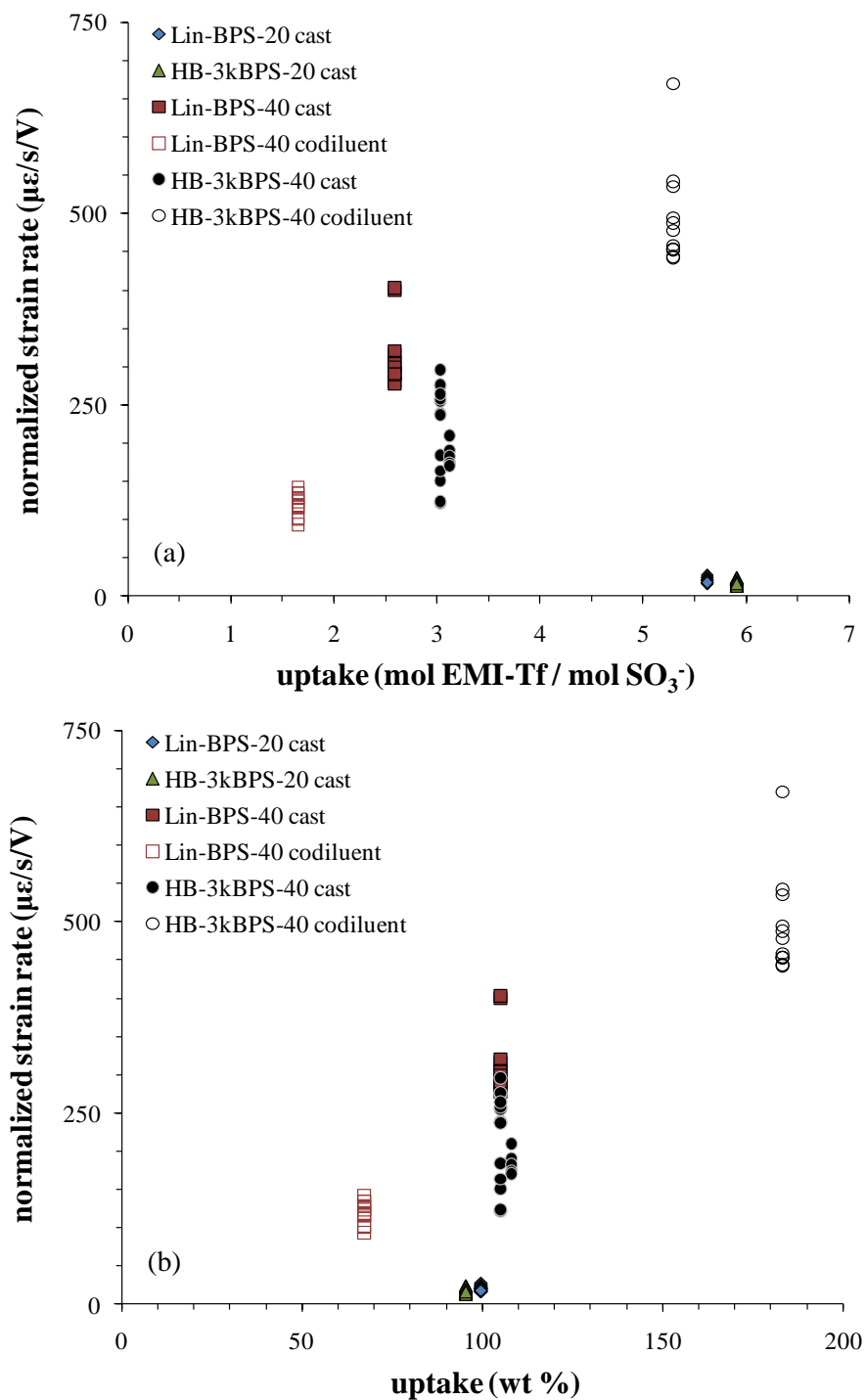


Figure 5.20: Initial strain rates (normalized to step voltage) versus experimental uptake in (a) mol EMI-Tf / mol SO₃⁻ (b) weight percent, of ionic liquid in the central membrane and electrodes

Capacitance of the six sBPS – IPT compositions was already shown to be similar and well controlled based on the constant volumetric loading of RuO₂ in the electrodes. Therefore, the contribution of capacitance to variations in the actuation performance is not significant. Step responses were dominated by the two compositions where the microphase separated morphology was formed at 0 % uptake and then swollen as a secondary step. Lower uptake for Lin-BPS-40 (co-diluent) resulted in comparably lower conductivity of the IPT but the largest peak strains. Very high molar and weight-based uptake for HB-3kBPS-40 (co-diluent) resulted in IPTs with the highest conductivity and fastest strain rates combined with the second highest peak strains. IPTs constructed from cast samples of these 40 % sulfonated ionomers contained the same population of free cations from the ionomer but very likely contained a much more tortuous charge transport pathway. If macrophase separation of the ionic liquid from the ionomer occurs during casting, then the effective number of charge carriers may be decreased within the primary channel for charge transport, thus decreasing actuation. This situation would be further accentuated for the 20 % sulfonated IPTs and could explain their very low actuation rates.

5.3.4.3 *Estimation of blocked force and energy densities*

In addition to free deflection, blocked force is the other primary actuation metric for evaluation of electromechanical transducers. In this case, the tip of the transducer is restricted to zero displacement in the cantilever configuration and typically a load cell measures the force developed per the input voltage. Experimental verification of blocked force resulting from this series of sBPS – IPTs was not yet available. However, estimations of blocked force are derived based on the relationships developed by Newbury and Leo [40, 277, 278] for the six representative IPTs discussed above in terms of their capacitance and step responses. Calculations were performed based on step responses to positive and negative input voltages of 0.5, 1, and 2 V. Newbury and Leo’s model allows for estimation of the maximum free deflection that results from step input voltages with the expression

$$\left(\frac{\delta}{v}\right)^f = \frac{-3dL_f^2}{T^2}, \quad (5.9)$$

where d is the electromechanical coupling coefficient (m/V) of the transducer. The coupling coefficient was determined from Equation 5.9 with the experimental applied voltage and peak

displacement for each transducer. Estimation of the blocked force (f) and normalized blocked force (F_n) is then performed according the relationships

$$\left(\frac{f}{v}\right)^\delta = \frac{3dwTY}{4L_f} \quad \text{and} \quad F_n = \left(\frac{f}{v}\right)^\delta \frac{4L_f}{3wT} = dY, \quad (5.10)$$

where Y is the experimentally determined bending modulus (N/m^2) of the transducer. Determination of values for both blocked force and free deflection further allows for estimation of the gravimetric (e_m) and volumetric (e_v) energy density based on

$$e_m = \frac{f_{bl}\delta_{fr}}{2\rho wTL_f} \quad \text{and} \quad e_v = \frac{f_{bl}\delta_{fr}}{2wTL_f}, \quad (5.11)$$

where ρ is the density (kg/m^3) of the transducer. Note that each energy density is based on the active mass or volume outside of the clamp, indicated by the use of the free length (L_f) instead of the transducer total length in the calculation. Calculation of energy densities allows for direct comparison of these sBPS – IPTs to previous iterations of IPTs as well as other electromechanical transducers.

Plots of the estimated blocked force versus experimental free deflection are shown in Figure 5.21 for all six primary compositions of sBPS – IPTs. The overall trend for each composition displays the expected increase in blocked force due to increased input voltage, with only small differences based on the direction of the applied voltage. Both the composition of the ionomer and the uptake method appear to significantly affect the final estimation of blocked force. As was mentioned earlier, all compositions of sBPS – IPTs that were cast in the presence of ionic liquid (100 wt % uptake) achieved similar performance in free deflection, up to nearly 1 mm for a 2 V input. The magnitude of the electromechanical coupling in the 20 mol % samples results in an estimated blocked force of approximately 1 mN for a 2 V input. The IPT constructed with the branched ionomer (HB-3kBPS-20) consistently produces a higher force output per volt than the linear composition. For the IPTs composed of the higher degree of sulfonation (40 mol %), the estimated blocked force decreases significantly to 0.4 mN (2 V), although the branched sample again results in higher blocked force than the linear composition for large input voltage.

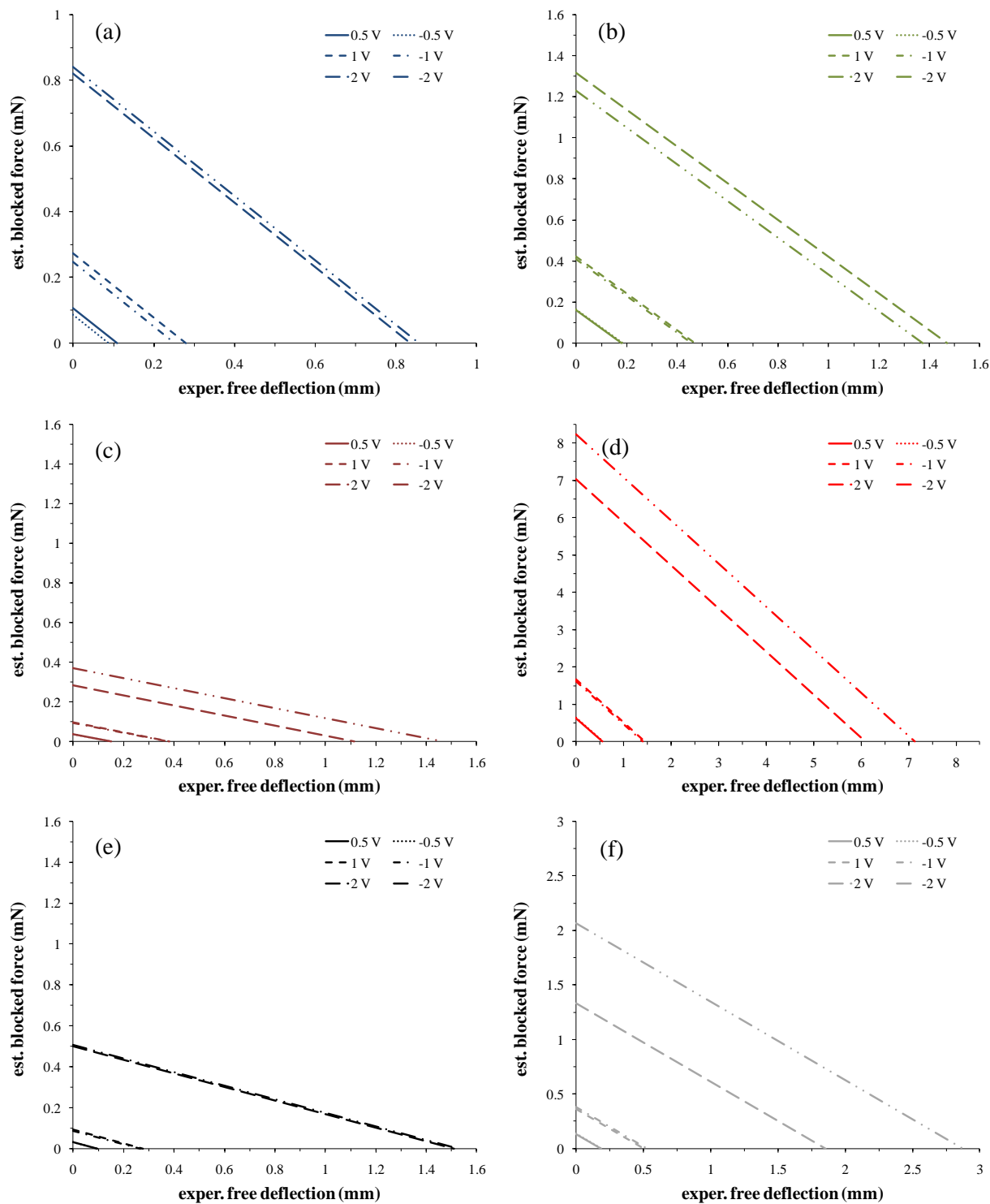


Figure 5.21: Estimated blocked force vs. experimentally measured free deflection at 0.5, 1, and 2 V for sBPS – IPTs constructed with (a) Lin-BPS-20 cast, (b) HB-3kBPS-20 cast, (c) Lin-BPS-40 cast, (d) Lin-BPS-40 co-diluent, (e) HB-3kBPS-40 cast, (f) HB-3kBPS-40 co-diluent

All values for free deflection, blocked force and energy density are provided in Table 5.3. The change in blocked force due to modification of the uptake technique produces the largest difference in the series of sBPS – IPTs. For the branched sample (HB-3kBPS-40), use of the co-diluent method results in nearly 180 wt % uptake while attaining an effective bending modulus of 1.51 GPa. The resultant blocked force is a minimum of three times larger per volt (~ 1.75 mN for 2 V) than the values estimated for the cast HB-3kBPS-40 – IPT with 100 wt % EMI-Tf. IPTs constructed with Lin-BPS-40 and the co-diluent method achieved a minimum of fifteen times larger blocked force per volt (~ 7.5 mN and 180 N/V·m for 2 V) than the analogously cast IPT. The much larger blocked force value originates both with a larger bending modulus (2.52 GPa) and the previously described increases in charge transport efficiency due to the co-diluent method's uptake of the ionic liquid. If the increased blocked force was solely based on larger modulus, then the HB-3kBPS-20 sample should have produced a much larger force per its 2.26 GPa modulus. The overall trends are further confirmed despite differences in transducer geometry and applied voltage through calculation of the normalized blocked force. The use of ionic liquids and the co-diluent method produces the Lin-BPS-40 – IPT capable of blocked force values greater than those of previous water-based sBPS – IPTs (2 mN for 2 V [54], 80 N/V·m [108]), Nafion – IPTs (1.73 mN for 2 V [40]), and with no detected back relaxation.

The combined actuation performance of the sBPS – IPTs can be quantified with the gravimetric and volumetric energy densities as the maximum mechanical work performed per mass or volume of the transducer. For the cast samples, branched IPTs demonstrate double the e_m and e_v of the IPTs built with linear ionomers, for both degrees of sulfonation. HB-3kBPS-20 displays the maximum energy densities for the cast series of 56 mJ/kg and 1×10^{-4} mJ/mm³ (2 V input). Due to a combination of the largest recorded blocked force and free deflection, the IPT constructed with Lin-BPS-40 through the co-diluent method displays the greatest overall energy densities of 1153 mJ/kg and 2×10^{-3} mJ/mm³ (2 V input). The elimination or significant reduction in back relaxation of the transducer response also allows for more practical realization of these energy densities (based on maximum values) in applications of the IPT. Other than the maximum values shown by the Lin-BPS-40 – IPT (co-diluent), the remaining sBPS – IPTs demonstrated energy densities similar to previously reported water-based Nafion[®] – IPTs (6.6 mJ/kg, 2.1×10^{-5} mJ/mm³ for 1 V).[40] Notably, the application of both sBPS and ionic liquids

to IPT design is still recent as of these studies, so energy densities for water-based sBPS – IPTs and ionic liquid-swollen Nafion[®] – IPTs are not presently available.

Table 5.3: Experimental free deflection and estimated blocked force and energy densities for sBPS – IPTs subjected to a positive step voltage

ionomer composition	uptake method	step voltage (V)	exper. free deflection (mm)	est. blocked force (mN)	norm. blocked force (N/V·m)	e_m	e_v
						(mJ/kg)	(mJ/mm ³)
Lin-BPS-20	cast	0.5	0.11	0.11	12.17	0.33	6.83E-07
		1	0.28	0.27	15.55	2.18	4.46E-06
		2	0.84	0.82	23.32	19.60	4.01E-05
HB-3kBPS-20	cast	0.5	0.18	0.16	17.39	0.84	1.58E-06
		1	0.47	0.42	22.67	5.68	1.08E-05
		2	1.47	1.32	35.45	55.58	1.05E-04
Lin-BPS-40	cast	0.5	0.15	0.04	6.49	0.20	4.97E-07
		1	0.38	0.10	8.20	1.30	3.18E-06
		2	1.11	0.28	11.98	11.11	2.71E-05
	co-diluent	0.5	0.55	0.63	65.03	9.33	1.80E-05
		1	1.44	1.66	85.56	64.59	1.25E-04
		2	6.09	7.02	180.75	1152.91	2.23E-03
HB-3kBPS-40	cast	0.5	0.09	0.03	4.68	0.09	2.25E-07
		1	0.28	0.09	6.83	0.78	1.92E-06
		2	1.51	0.50	18.69	23.39	5.74E-05
	co-diluent	0.5	0.18	0.13	14.56	0.69	1.36E-06
		1	0.50	0.36	19.79	5.12	1.01E-05
		2	1.85	1.33	36.57	70.00	1.38E-04

5.4 Summary

Ionic liquid swollen IPTs were successfully constructed with sBPS according to the design parameters set forth in Chapters 3 and 4 for a series that included four polymer compositions and two uptake methods. Very good control of the electrode composition was demonstrated with the casting version of the DAP method. The casting and co-diluent swelling methods also showed good repeatability for producing target uptakes of ionic liquid into sBPS. Furthermore, modifications to both processes mainly based on reduction of heat and increased time for membrane formation resulted in increased overall conductivity. EIS was employed to track the ionic conductivity of the IPT through the entire process of device fabrication. Notable decreases

in conductivity were observed for membranes with a lower degree of sulfonation, likely due to greater loss of the ionic liquid during the melt fabrication steps. Based on variations in conductivity with the fabrication process, charge transport should be further tuned as a design parameter to better predict and reflect the final state of the transducer. Impedance data for the built transducers was successfully modeled with the EC-2 equivalent circuit previously applied in Chapter 3. Excellent fits of the data were obtained that provided correlation between the model parameters and material/phenomenological processes within the IPT. Successful fits of the impedance data also enabled accurate estimations of the effective double layer capacitance. The capacitance of the DAP electrodes, similar to previous findings, was not found to be dependent on the ionomer composition or the technique employed for uptake of the diluent.

The full series of transducers was tested for actuation in free displacement for the cantilevered beam configuration. Frequency response functions provided information on the strain response of the transducers to a random input over a wide frequency range. Strain per volt responses were dominated by IPTs with higher degrees of sulfonation and a low frequency maximum of $91 \mu\epsilon/V$ was achieved for the co-diluent swollen HB-3kBPS-40 IPT. Normalization of the actuation response to electric displacement decreased the spread of actuation values, which was significant considering the large range of ionomer compositions and the different uptake levels due to two different techniques. Effective bending modulus of the transducers was derived from the frequency response functions and was an average of 2 GPa for the series, much higher than comparably swollen Nafion[®]. Step responses demonstrated linear relationships between peak strain, strain rate, and back relaxation to the applied voltage. The co-diluent swollen samples, both with 40 % sulfonation, dominated the step responses. Lin-BPS-40 consistently achieved the greatest peak strain, while HB-3kBPS-40 demonstrated the fastest actuation speed. IPTs fully constructed with the casting process demonstrated a distinct difference for actuation in the time domain based on the degree of sulfonation. The overall factor that appeared to differentiate performance was the state of the charge transport pathway in the IPT. This hypothesis requires further investigation with techniques that directly observe morphological structure.

However, the best actuation resulted from membranes whose charge transport pathway was formed prior to introduction of the ionic liquid diluent. For this case branching does appear to result in higher actuation, although specifically for strain rate. The morphology that resulted

from the branched nature of HB-3kBPS-40 allowed for greater uptake of ionic liquid at the same conditions applied to the Lin-BPS-40 membrane. The greater ionic liquid content led to increased strain rate of the resultant transducers. Not without precedent, this study concludes that all changes made to the charge transport pathway defined by the ionomer's microphase separated morphology have a direct effect on electromechanical transduction of the IPT, including polymer topology. These effects are exaggerated in comparisons of actuation for IPTs with very different populations of free counterions in the base ionomer. Based on estimates of blocked force, introduction of branching to the ionomer consistently increases the force production capability of the final transducer. Furthermore, the resultant energy densities of sBPS – IPTs fabricated with ionic liquids are comparable other IPT compositions described in the literature and greatly increased for Lin-BPS-40 fabricated with the co-diluent method. This study aligns well with the results and phenomena observed in previous studies of ionic liquid swollen Nafion[®] – IPTs. Through large improvement over the actuation shown in Chapter 3, the successful optimization of ionic liquid containing sBPS – IPTs contributes a new series of compositions to this division of electroactive polymer devices.

Chapter 6 CONCLUSIONS

6.1 Summary and conclusions

The overall goal of this research is to increase understanding of electromechanical transduction in ionic polymer transducers through the establishment of structure – property relationships between the ionomeric matrix and device actuation. More specifically, polymer topology was controlled in synthetic design of the ionomer to identify the effect of this fundamental polymer property on electromechanical coupling. The resultant comparison between linear and branched sulfonated polysulfones was kept constant throughout investigations of the neat ionomeric membranes, the interface with conducting RuO₂ particles in DAP electrodes, the interaction with imbibed ionic liquids, and characterization of actuator performance in fully fabricated IPTs.

Biphenol-based sulfonated polysulfones were chosen as the target ionomeric matrix for their combined overall stability, elastic modulus, and ionic conductivity. Optimization of these three membrane properties is critical to achieve maximum IPT performance. The oligomeric A₂ + B₃ step-growth reaction was successfully employed to provide direct control over the distance between branch points, the overall degree of branching, and the ion content present in the final ionomer. Prior to use in IPTs, polymer characterization revealed that these highly-branched ionomers display high molecular weight in the absence of gelation, thermal stability above 400 °C, glass transition temperatures greater than 200 °C, and hydrophilic/hydrophobic phase separation. Controlled degrees of branching decreased the overall tensile strain and narrowed the size distribution of microphase separated domains in comparison to the linear sBPS analogues. Ionic content significantly influenced the development of molecular weight (especially in branched samples), ionic conductivity, glass transition temperatures, and stress-strain behavior of the ionomer. These neat membrane properties confirmed the series of sulfonated polysulfones as good candidates for IPT membranes however; qualification for performance was also proven for interactions of the ionomer with other IPT components.

The first major interface studied in the IPT was between the electrode conductor and the novel ionomer. State-of-the-art IPT electrodes were constructed based on a casting version of the direct application process using RuO₂ nanoparticles dispersed in a matrix of the ionomer and hydrated with ionic liquid. A series of isolated electrodes and corresponding IPTs were constructed for a range of RuO₂ volume loadings and evaluated for ionic conductivity and bending actuation. A percolation threshold was identified for ionic conductivity of the isolated electrodes at ~18 vol % RuO₂ which was also correlated to increases in strain rate for the IPTs tested for free deflection. Modeling of the impedance results with an equivalent electrical circuit identified the source of electrode percolation as the interfacial resistance between the ionomer and the RuO₂ particles. Furthermore, this was the first demonstration of an IPT constructed with 100 % novel ionomers using both the direct application process and ionic liquids. A method was also developed based on the impedance of constant phase elements designated in the equivalent electrical circuit to provide a frequency independent estimation of effective double layer capacitance for the interface of the ionomer and conducting particles. Maximum capacitance values corresponded with optimum peak strain of the IPTs at 42 vol % for the RuO₂/sBPS electrodes.

The second and most significant interaction investigated was between the ionomer and the ionic liquid diluent. Ionic liquids are desirable as diluents for IPTs based on their high electrolytic limit, near-zero volatility, and increased viscosity that allow for greater actuation, longer lifetimes, and reduction of back-relaxation in comparison to water-based IPTs. A full study was undertaken for linear and branched ionomers to investigate the changes in electrical and mechanical properties of the membrane based on the method for uptake through either casting in the presence of ionic liquids or swelling with co-diluents. Significant uptake levels up to 100 % for the casting method and near 200 % for the co-diluent method were achieved for sBPS imbided with EMI-Tf. As predicted, overall ionic conductivity increased and modulus decreased (cast samples) for higher uptakes of ionic liquid. However, electrical impedance spectroscopy combined with data from SEM and SAXS suggested that the casting method created macroscopic heterogeneities in the membrane due to separation of the ionic liquid from the ionomer during fabrication, especially at high uptake levels. This result correlated with ionic conductivity results that demonstrated dominance of the impedance response by ionic liquid loading, regardless of ion content or topology of the polymer. Swelling preformed membranes

with ionic liquid – co-diluent solutions produced higher ionic conductivities than casting at equivalent uptakes, where the optimal solution concentration was 20 wt % MeOH in EMI-Tf. The swelling method also benefited from polymer topology where highly branched sBPS achieved greater ionic liquid uptake at both sulfonation levels than the linear analogues. However, the casting method was able to produce model central membranes with ionic liquid uptakes and corresponding ionic conductivities that were not achieved with the co-diluent method for sBPS at lower degrees of sulfonation. Hydrated modulus values were also retained above 1 GPa for sBPS membranes containing up to 100 wt % uptake of ionic liquid. Comparison of the conductivity per uptake that resulted from these two methods highlighted the benefit of forming stable charge transport pathways prior to introduction of ionic liquids.

Optimized levels of the two interfaces were enacted to create a series of transducers from varied compositions of sulfonated polysulfones with both increased capacitance and ionic conductivity. The series allowed for comparison of polymer topology, ion content of the ionomer, and the uptake method employed to imbibe the central membrane with ionic liquid. Systematic characterization with electrical impedance spectroscopy during the fabrication process identified a dependence of the final IPT conductivity on both the degree of sulfonation and the uptake method. However, the design criteria from the central membrane conductivity per uptake was met with all values above 1 $\mu\text{S}/\text{cm}$ for the series. The equivalent circuit model was shown to be robust when applied to impedance data for a wide range of IPT composition. Capacitance values for the series were greatly improved over the initial study and demonstrated relative independence of the ionomer composition and uptake level. Both the degree of sulfonation and the presence of branching were found to influence actuation in bending while the device modulus was increased significantly above previous Nafion[®]-IPTs. The primary effect of polymer topology was on the uptake of ionic liquid for the co-diluent samples. Branching allowed for greater uptake of the HB-3kBPS-40 sample which translated into the largest strain per volt frequency response (91 $\mu\epsilon/\text{V}$) and the maximum detected strain rates in step responses (1000 $\mu\epsilon/\text{s}$). Due to its interference with formation a well-defined microphase separated morphology, the casting method appears to have minimized the effect of branching in those IPTs despite its benefit of targeting otherwise unreachable conductivities for less sulfonated ionomers and application to the DAP method for electrode fabrication. Despite the variation of design parameters, the total sBPS series displayed a logarithmic relationship between strain rate and IPT

conductivity. Samples with central membranes fabricated with the co-diluent process demonstrated the greatest peak strains and strain rates of 0.45 % and 0.1 % / s respectively. Estimation of blocked force values also indicated that the co-diluent method resulted in greater values than the casting method, up to 180 N/V·m. Calculated energy densities were greater than or equal to values for water-based IPTs, and were augmented by the presence of branching in the ionomeric matrix. Overall, the series confirmed viable actuation performance is available with ionic-liquid swollen sBPS ionomers where the introduction of branching allows for further tuning of the IPT for increased performance.

The role of polymer topology in IPT design and performance was directly investigated in this dissertation. Through isolation of the component interfaces with the ionomeric matrix, both advantages and disadvantages associated with the use of branched ionomers were found. Specific findings based on linear versus branched ionomers were:

Advantages

- Increased mobility of charges on polymer branches appears to decrease the size distribution and distance between ionic aggregates (SAXS).
- Branching does not decrease thermal stability or significantly vary the thermal transitions of the ionic aggregates or the matrix.
- Solution viscosity appeared to decrease, improving the processability of the electrode dispersions for casting with implications for painting and spraying versions of the DAP. All filtering steps were also significantly less energy intensive with branched ionomers compared to linear.
- Branching allowed for increased swelling with the co-diluent method for both degrees of sulfonation. This trend resulted in faster IPTs due to a higher final uptake after processing.
- Slight increases in modulus/stiffness with the introduction of branching may be the source of increased blocked force and energy densities compared to the linear ionomers.

Disadvantages

- Synthetic methods for highly branched polymers are subject to gelation.
- Use of charged monomers appears to decrease the conversion of linear to dendritic units in the branching reaction, making high molecular weights more difficult to attain for branched, high IEC target compositions.
- Tensile strain before break is decreased for branched polymers. The more brittle character also resulted in increased fragility when swollen with ionic liquids. Resultant cracks may have been the source of electrical shorts through the thickness of IPTs at large strains during actuation testing.
- In the neat state and when swollen with ionic liquid diluents, central membranes of branched ionomers result in lower conductivity per uptake than the linear analogues.

6.2 Significant contributions

Through the research surrounding this investigation of the effects of polymer topology on electromechanical transduction, several primary contributions were made to the field of ionic polymer transducers and science as a whole. Those contributions are presented here.

- Synthesis and characterization of a novel series of sulfonated polysulfones was successfully demonstrated with the oligomeric $A_2 + B_3$ method. The series is systematically varied in terms of the degree of branching and the ion content for comparison with linear analogues. Characterization of the series' polymer properties will be useful for further development of sBPS as an IPT as well as in other applications.
- The casting method was presented as a viable technique to target uptake of ionic liquids into sBPS. Furthermore, the method was adapted to the DAP to produce well-defined electrodes.
- The co-diluent method was tuned to optimize charge transport for uptake of ionic liquid into sBPS membranes and correlated with increased actuation in sBPS – IPTs.
- An equivalent circuit was applied to model the impedance of IPTs and was found to be robust for changes in ionomer composition, uptake level and method, and electrode composition. Furthermore, estimation of frequency independent capacitance for the electric double layer was accomplished in relation to the contributing materials and interfaces within the IPT.

- Linear and branched sBPS were demonstrated and optimized as the first 100 % novel ionomer IPTs (central membrane and electrodes) to employ the DAP and/or ionic liquids as the diluent. Electromechanical characterization was performed and demonstrated significant improvement in actuation over the first generation sBPS – IPT.
- Polymer topology was linked to electromechanical transduction through its effect on the ionomer morphology and ionic liquid uptake of IPTs, thus influencing the charge transport essential to operation.

6.3 Recommendations for future work

In accordance with the breadth of this research and new insights based on the above contributions, several primary areas of interest arise for future work. These are listed below.

- Characterization of sBPS – IPTs as extensional actuators is a logical next step following the bending actuation demonstrated in this dissertation. Experimental verification of blocked force actuation in both bending and extensional modes is necessary to confirm the estimated blocked force and energy densities. These experiments will verify the significance of the trade-off between increased stiffness and decreased free deflection due to IPT design with sBPS. Comparison of IPT performance in bending and extension will also allow for observation of potential benefits from tailoring ionomer composition to a specific mode of actuation.

Ionomer

- The interface between the ionic liquid and sBPS ionomers was shown to be a delicate balance where polymer topology, uptake level and method, and IPT fabrication influenced charge transport through the ionomer’s microphase separated morphology. However, confirmation and interpretation of these trends in ionic conductivity would benefit significantly from a direct parametric study of the ionomer’s morphological structure (see Section 4.3.1.1), especially at the interface with the ionic liquid.
- This dissertation investigated a single type of polymer branching. Due to the observed advantages and disadvantages of highly branched versus linear ionomers, further studies to develop graft, star, long-chain branched, short-chain branched, fully hyperbranched,

dendrimer, or pom-pom / dumbbell architectures are warranted. The large breadth of available topologies should allow for further tailoring of the effects of branching on charge transport, morphological structure, uptake of the diluent, and processability as measured by minimal decreases in conductivity during IPT fabrication.

- Very few bound anions have been attempted outside of sulfonates for IPTs. Ionomer development should expand to other bound ions such as carboxylate and phosphonate salts for reduced back relaxation and increased conductivity respectively. Ionenes would also be directly applicable for IPTs based on bound cations and anion transport, a nearly untouched area for this class of transducers. The very regular distribution of charges along the backbone could have beneficial implications for charge transport if oriented in the direction of actuation. These studies should also include varied counterions, especially large ions which have been linked to faster actuation.
- As reviewed in Chapter 1, step-growth ionomers are relatively untouched in studies for IPT applications. Further iterations on polysulfones would simply vary the bisphenol composition to allow for increased flexibility and solubility (bis-A), increased matrix hydrophobicity (bis-F), and/or increased chain stiffness (terphenol). Polymers containing varied ratios of these monomers would allow for tuning of the desired physical and chemical properties of the ionomer. For sBPS – IPTs with EMI-Tf as a diluent, the use of bis-F should increase microphase separation and augment morphological stability during introduction of the ionic liquid. Increased hydrophobicity and flexibility of the non-charged monomer could also result from reactions with dimethyl siloxane containing monomers. Further resistance to dissolution, especially for uptake of ionic liquids, may be gained through synthesis of ionomeric polyimides. Synthesis of ionomers with crystallizable compositions would also allow for solvent/diluent resistance. Charged polyurethanes and polyureas would be very interesting based on increased hydrogen bonding competing with ionic associations. The elastomeric nature of some polyurethanes is also very attractive for large strain applications of IPTs.
- As in the development of fuel cell technology, IPTs are very likely to experience increased performance based on charged block copolymers that form long-range continuous domains for ion transport in the direction of actuation. An interesting variation would be to use a

mixture of highly charged and non-charged A_2 oligomers in an $A_2 + A_2' + B_n$ reaction, combining blocks with mediated levels of branching.

- Synthesis and application of sulfobetaines as IPT membranes is an extremely interesting possibility. The bound nature of both ions in these polymers allows for fundamental exploration of a potentially new mechanism for actuation in IPTs, especially when swollen with ionic liquids. In this case the population of free ions would solely originate with the diluent, while the polymer would provide the charge transport pathway.

Electrodes

- Production of a flexible, stable, highly conductive outer electrode that is compatible or at minimum adaptable to present state-of-the-art IPT technology is highly desirable. Tuning of polymer composition to increase adhesion with such an electrode is an important option and a breakthrough for this final component of the IPT would greatly extend the lifetime and viability of IPT technology, especially for high strain applications.
- Further development of the DAP method to increase consistency and improve its adaptability to a wide range of novel ionomers would be beneficial to the field and further fundamental investigations concerning polymer parameters. Specifically, methods to control deposition of the electrode dispersion that balance film stability of the central membrane with creation of a seamless transition to the electrode would eliminate at least one melt press step and likely increase total quality and performance of the IPT.

Diluent

- Investigation of sBPS – IPTs with other ionic liquids than EMI-Tf would also benefit from tuning of the chemical composition and viscosity to increase both stability of the interface with the ionomer and actuation. Experimentation with other ionic liquids and sBPS through the casting process could reveal tuned combinations that increase homogeneous dispersion of the ionic liquid and formation of better defined morphologies than achieved here.
- The co-diluent method demonstrated the greatest ionic conductivity per uptake of ionic liquid which led to the maximum detected actuation performance. Further tuning of the co-diluent ratio and the applied conditions could further increase both uptake and the bulk conductivity of the imbibed membrane. A corresponding stress-strain and/or dynamic mechanical analysis

study should compare the effects of ionic liquid uptake on the hydrated modulus of co-diluent swollen sBPS in comparison to the values reported for the casting method in this dissertation.

BIBLIOGRAPHY

- [1] Shahinpoor M and Kim K J 2005 Ionic polymer-metal composites: IV. Industrial and medical applications *Smart Materials and Structures* **14** 197-214
- [2] Bar-Cohen Y 2009 Worldwide Electroactive Polymer Actuators Webhub <http://ndea.jpl.nasa.gov/nasa-nde/lommas/eap/EAP-web.htm>
- [3] Farinholt K and Leo D J 2004 Modeling of electromechanical charge sensing in ionic polymer transducers *Mechanics of Materials* **36** 421-433
- [4] Farinholt K M and Leo D J 2008 Modeling the electrical impedance response of ionic polymer transducers *Journal of Applied Physics* **104**
- [5] Park J K, Page K A, Hussey D S, Jacobson D L, Arif M and Moore R B 2007 Neutron imaging of an electrically-stimulated water gradient in ionic polymer metal composite actuators *Polymer Preprints (American Chemical Society, Division of Polymer Chemistry)* **48** 503-504
- [6] Naji L, Chudek J A and Baker R T 2008 Magnetic resonance imaging study of a soft actuator element during operation *Soft Matter* **4** 1879-1886
- [7] Mauritz K A and Moore R B 2004 State of understanding of nafion *Chemical Reviews* **104** 4535-4585
- [8] Duncan A J, Leo D J and Long T E 2008 Beyond Nafion: Charged Macromolecules Tailored for Performance as Ionic Polymer Transducers *Macromolecules* **41** 7765-7775
- [9] Fukada E and Yasuda I 1957 On the piezoelectric effect of bone *Journal of the Physical Society of Japan* **12** 1158-1162
- [10] Jaffe B, Cook W R and Jaffe H 1989 *Piezoelectric Ceramics* (Falls Church, VA, USA: Techbooks)
- [11] Eberle G, Schmidt H and Eisenmenger W 1996 Piezoelectric polymer electrets *IEEE transactions on dielectrics and electrical insulation* **3** 624-646
- [12] Leo D J 2007 *Engineering Analysis of Smart Material Systems* (New York, NY: John Wiley & Sons, Inc.)
- [13] Ashley S 2003 Artificial muscles *Scientific American* **289** 52-59
- [14] Bar-Cohen Y ed. 2004 *Electroactive Polymer (EAP) Actuators as Artificial Muscles: Reality, Potential, and Challenges* (Bellingham, WA: SPIE Press)
- [15] Madden J D 2007 Mobile Robots: Motor Challenges and Materials Solutions *Science* **318** 1094-1097
- [16] Madden J D W, Vandesteeg N A, Anquetil P A, Madden P G A, Takshi A, Pytel R Z, Lafontaine S R, Wieringa P A and Hunter I W 2004 Artificial Muscle Technology: Physical Principles and Naval Prospects *IEEE Journal of Oceanic Engineering* **29** 706-728
- [17] Mirfakhrai T, Madden J D W and Baughman R H 2007 Polymer artificial muscles *Materials Today* **10** 30-38
- [18] Bar-Cohen Y and Zhang Q 2008 Electroactive polymer actuators and sensors *MRS Bulletin* **33** 173-181
- [19] Park I-S, Jung K, Kim D, Kim S-M and Kim K J 2008 Physical principles of ionic polymer-metal composites as electroactive actuators and sensors *MRS Bulletin* **33** 190-195
- [20] Akle B J, Bennett M D and Leo D J 2006 High-strain ionomeric-ionic liquid electroactive actuators *Sensors and Actuators, A: Physical* **126** 173-181

- [21] Vohnout S, Kim S-M, Park I-S, Banister M, Tiwari R and Kim K J 2007 IPMC-assisted miniature disposable infusion pumps with embedded computer control *Proceedings of SPIE-The International Society for Optical Engineering* **6524** 65241U/65241-65241U/65247
- [22] Oguro K, Fujiwara N, Asaka K, Onishi K and Sewa S 1999 Polymer electrolyte actuator with gold electrodes *Proceedings of SPIE-The International Society for Optical Engineering* **3669** 64-71
- [23] Fujiwara N, Asaka K, Nishimura Y, Oguro K and Torikai E 2000 Preparation of gold-solid polymer electrolyte composites as electric stimuli-responsive materials *Chemistry of Materials* **12** 1750-1754
- [24] Kim D and Kim K J 2007 Ionic polymer-metal composite actuators exhibiting self-oscillation *Sensors and Actuators, A: Physical* **A137** 129-133
- [25] Bonomo C, Brunetto P, Fortuna L, Giannone P, Graziani S and Strazzeri S 2008 A tactile sensor for biomedical applications based on IPMCs *IEEE Sensors Journal* **8** 1486-1493
- [26] Brufau-Penella J, Puig-Vidal M, Giannone P, Graziani S and Strazzeri S 2008 Characterization of the harvesting capabilities of an ionic polymer metal composite device *Smart Materials and Structures* **17** 015009/015001-015009/015015
- [27] Farinholt K M, Pedrazas N A, Schluneker D M, Burt D W and Farrar C R 2009 An Energy Harvesting Comparison of Piezoelectric and Ionically Conductive Polymers *Journal of Intelligent Material Systems and Structures* **20** 633-642
- [28] Yeom S W and Oh I K 2009 A biomimetic jellyfish robot based on ionic polymer metal composite actuators *Smart Materials and Structures* **18**
- [29] Yim W, Lee J and Kim Kwang J 2007 An artificial muscle actuator for biomimetic underwater propulsors *Bioinspiration and Biomimetics* **2** S31-41
- [30] Nisar A, Afzulpurkar N, Mahaisavariya B and Tuantranont A 2008 MEMS-based micropumps in drug delivery and biomedical applications *Sensors and Actuators, B: Chemical* **B130** 917-942
- [31] Williams A M, Griffiths D J and Vlachos P P 2009 Laminar mixing using oscillating cantilevered ionic polymer actuators *Sensors and Actuators, A: Physical* **153** 105-113
- [32] Gierke T D, Munn G E and Wilson F C 1981 The morphology in nafion perfluorinated membrane products, as determined by wide- and small-angle x-ray studies *Journal of Polymer Science, Part B: Polymer Physics* **19** 1687-1704
- [33] Schmidt-Rohr K and Chen Q 2008 Parallel cylindrical water nanochannels in Nafion fuel-cell membranes *Nature Materials* **7** 75-83
- [34] Leo D J, Farinholt K and Wallmersperger T 2005 Computational models of ionic transport and electromechanical transduction in ionomeric polymer transducers (Invited Paper) *Proceedings of SPIE-The International Society for Optical Engineering* **5759** 170-181
- [35] Nemat-Nasser S and Li J Y 2000 Electromechanical response of ionic polymer-metal composites *Journal of Applied Physics* **87** 3321-3331
- [36] Asaka K and Oguro K 2000 Bending of polyelectrolyte membrane platinum composites by electric stimuli: Part II. Response kinetics *Journal of Electroanalytical Chemistry* **480** 186-198
- [37] Lee S, Kim K J and Park I-S 2007 Modeling and experiment of a muscle-like linear actuator using an ionic polymer-metal composite and its actuation characteristics *Smart Materials and Structures* **16** 583-588

- [38] Weiland L M and Leo D J 2004 Electrostatic analysis of cluster response to electrical and mechanical loading in ionic polymers with cluster morphology *Smart Materials and Structures* **13** 323-336
- [39] Akle B J and Leo D J 2007 Characterization and modeling of extensional and bending actuation in ionomeric polymer transducers *Smart Materials and Structures* **16** 1348-1360
- [40] Newbury K M and Leo D J 2002 Electromechanical Modeling and Characterization of Ionic Polymer Benders *Journal of Intelligent Material Systems and Structures* **13** 51-60
- [41] Nemat-Nasser S and Wu Y 2003 Comparative experimental study of ionic polymer-metal composites with different backbone ionomers and in various cation forms *Journal of Applied Physics* **93** 5255-5267
- [42] Kim D and Kim K J 2007 Can we overcome the relaxation of ionic polymer-metal composites? *Proceedings of SPIE-The International Society for Optical Engineering* **6524** 65240A/65241-65240A/65211
- [43] Shahinpoor M and Kim K J 2001 Ionic polymer-metal composites: I. Fundamentals *Smart Materials and Structures* **10** 819-833
- [44] Kim K J and Shahinpoor M 2003 Ionic polymer-metal composites: II. Manufacturing techniques *Smart Materials and Structures* **12** 65-79
- [45] Eisenberg A, Hird B and Moore R B 1990 A new multiplet-cluster model for the morphology of random ionomers *Macromolecules (Washington, DC, United States)* **23** 4098-4107
- [46] Gebel G 2000 Structural evolution of water swollen perfluorosulfonated ionomers from dry membrane to solution *Polymer* **41** 5829-5838
- [47] Nemat-Nasser S 2002 Micromechanics of actuation of ionic polymer-metal composites *Journal of Applied Physics* **92** 2899-2915
- [48] Eisenberg A, Kim, J-S. 1998 *Introduction to Ionomers* (New York, NY: John Wiley & Sons, Inc.)
- [49] Tant M R, Mauritz K A and Wilkes G L eds. 1997 *Ionomers: Synthesis, Structure, Properties, and Applications* (New York, NY: Van Nostrand Reinhold Co. Inc.)
- [50] Akle B, Leo D, Bennett M, Wiles K and McGrath J E 2006 Direct assembly process for fabrication of ionomeric polymer devices (U.S. Patent 20060266642)
- [51] Kim K J and Shahinpoor M 2001 A novel method of manufacturing three-dimensional ionic polymer-metal composites (IPMCs) biomimetic sensors, actuators and artificial muscles *Polymer* **43** 797-802
- [52] Bennett M D and Leo D J 2003 Manufacture and characterization of ionic polymer transducers employing non-precious metal electrodes *Smart Materials and Structures* **12** 424-436
- [53] Asaka K, Oguro K, Nishimura Y, Mizuhata M and Takenaka H 1995 Bending of polyelectrolyte membrane-platinum composites by electric stimuli. I. Response characteristics to various waveforms *Polymer Journal* **27** 436-440
- [54] Akle B J, Leo D J, Hickner M A and McGrath J E 2005 Correlation of capacitance and actuation in ionomeric polymer transducers *Journal of Materials Science* **40** 3715-3724
- [55] Akle B, Nawshin S and Leo D 2007 Reliability of high strain ionomeric polymer transducers fabricated using the direct assembly process *Smart Materials and Structures* **16** S256-S261
- [56] Oguro K, Takenaka H and Kawami Y 1993 Actuator element (U.S. Patent 5268082)

- [57] Bennett M D and Leo D J 2004 Ionic liquids as stable solvents for ionic polymer transducers *Sensors and Actuators, A: Physical* **115** 79-90
- [58] Wang J, Xu C Y, Taya M and Kuga Y 2007 A FLEMION-based actuator with ionic liquid as solvent *Smart Materials and Structures* **16** S214-S219
- [59] Akle B J, Bennett M D and Leo D J 2005 Ionic electroactive hybrid transducers *Proceedings of SPIE-The International Society for Optical Engineering* **5759** 153-164
- [60] Akle B J, Bennett M D, Leo D J, Wiles K B and McGrath J E 2007 Direct assembly process: a novel fabrication technique for large strain ionic polymer transducers *Journal of Materials Science* **42** 7031-7041
- [61] Bennett M D, Leo D J, Wilkes G L, Beyer F L and Pechar T W 2006 A model of charge transport and electromechanical transduction in ionic liquid-swollen Nafion membranes *Polymer* **47** 6782-6796
- [62] Oguro K, Kawami Y and Takenaka H 1992 Bending of an ion-conducting polymer filmelectrode composite by an electric stimulus at low voltage *Journal of the Micromachine Society* **5** 27-30
- [63] Shahinpoor M 1992 Conceptual design, kinematics and dynamics of swimming robotic structures using ionic polymeric gel muscles *Smart Materials and Structures* **1** 91-94
- [64] Sadeghipour K, Salomon R and Neogi S 1992 Development of a novel electrochemically active membrane and 'smart' material based vibration sensor/damper *Smart Materials and Structures* **1** 172-179
- [65] Bar-Cohen Y 2007 Electroactive polymers as an enabling materials technology *Proceedings of the Institution of Mechanical Engineers, Part G: Journal of Aerospace Engineering* **221** 553-564
- [66] Wallmersperger T, Leo D J and Kothera C S 2007 Transport modeling in ionomeric polymer transducers and its relationship to electromechanical coupling *Journal of Applied Physics* **101** 024912/024911-024912/024919
- [67] Chen Z, Tan X, Will A and Ziel C 2007 A dynamic model for ionic polymer-metal composite sensors *Smart Materials and Structures* **16** 1477-1488
- [68] Buechler M A and Leo D J 2007 Characterization and variational modeling of ionic polymer transducers *Journal of Vibration and Acoustics-Transactions of the Asme* **129** 113-120
- [69] Kim S J, Kim S M, Kim K J and Kim Y H 2007 An electrode model for ionic polymer-metal composites *Smart Materials and Structures* **16** 2286-2295
- [70] Jo C H, Naguib H E and Kwon R H 2008 Modeling and optimization of the electromechanical behavior of an ionic polymer-metal composite *Smart Materials and Structures* **17**
- [71] Kothera C S, Leo D J and Lacy S L 2008 Characterization and modeling of the nonlinear response of ionic polymer actuators *Journal of Vibration and Control* **14** 1151-1173
- [72] Porfiri M 2008 Charge dynamics in ionic polymer metal composites *Journal of Applied Physics* **104**
- [73] Wallmersperger T, Akle B J, Leo D J and Kroeplin B 2008 Electrochemical response in ionic polymer transducers: An experimental and theoretical study *Composites Science and Technology* **68** 1173-1180
- [74] Di Pasquale G, Fortuna L, Graziani S, La Rosa M, Nicolosi D, Sicurella G and Umana E 2009 All-Organic Motion Sensors: Electromechanical Modeling *Ieee Transactions on Instrumentation and Measurement* **58** 3731-3738

- [75] Wallmersperger T, Horstmann A, Kroplin B and Leo D J 2009 Thermodynamical Modeling of the Electromechanical Behavior of Ionic Polymer Metal Composites *Journal of Intelligent Material Systems and Structures* **20** 741-750
- [76] Heitner-Wirguin C 1996 Recent advances in perfluorinated ionomer membranes: structure, properties and applications *Journal of Membrane Science* **120** 1-33
- [77] DuPont™ Nafion(R) PFSA Membranes: N-115, N-117, NE-1110. pp. 1-4 (DuPont Fuel Cells, 2006).
- [78] Yeager H L and Steck A 1981 Cation and Water Diffusion in Nafion Ion Exchange Membranes: Influence of Polymer Structure *Journal of the Electrochemical Society* **128** 1880-1884
- [79] Hsu W Y and Gierke T D 1983 Ion transport and clustering in nafion perfluorinated membranes *Journal of Membrane Science* **13** 307-326
- [80] Page K A, Cable K M and Moore R B 2005 Molecular Origins of the Thermal Transitions and Dynamic Mechanical Relaxations in Perfluorosulfonate Ionomers *Macromolecules* **38** 6472-6484
- [81] Asaka K, Fujiwara N, Oguro K, Onishi K and Sewa S 2001 State of water and ionic conductivity of solid polymer electrolyte membranes in relation to polymer actuators *Journal of Electroanalytical Chemistry* **505** 24-32
- [82] Yung C, Kim D and Bhat N 2007 Benefits and challenges of using ionic polymer metal composites in medical device applications *Proceedings of SPIE-The International Society for Optical Engineering* **6524** 652405/652401-652405/652410
- [83] Kottke E A, Partridge L D and Shahinpoor M 2007 Bio-potential Neural Activation of Artificial Muscles *Journal of Intelligent Material Systems and Structures* **18** 103-109
- [84] Onishi K, Sewa S, Asaka K, Fujiwara N and Oguro K 2000 Morphology of electrodes and bending response of the polymer electrolyte actuator *Electrochimica Acta* **46** 737-743
- [85] Park I-S, Kim S-M and Kim K J 2007 Mechanical and thermal behavior of ionic polymer-metal composites: effects of electroded metals *Smart Materials and Structures* **16** 1090-1097
- [86] Chung R-J, Chin T-S, Chen L-C and Hsieh M-F 2007 Preparation of gradually compositional metal electrode on solution-casted Nafion membrane *Biomolecular Engineering* **24** 434-437
- [87] Jeon J-H, Yeom S-W and Oh I-K 2008 Fabrication and actuation of ionic polymer metal composites patterned by combining electroplating with electroless plating *Composites, Part A: Applied Science and Manufacturing* **39A** 588-596
- [88] Akle B J and Leo D J 2008 Single-Walled Carbon Nanotubes -- Ionic Polymer Electroactive Hybrid Transducers *Journal of Intelligent Material Systems and Structures* **19** 905-915
- [89] Baughman R H, Cui C X, Zakhidov A A, Iqbal Z, Barisci J N, Spinks G M, Wallace G G, Mazzoldi A, De Rossi D, Rinzler A G, Jaschinski O, Roth S and Kertesz M 1999 Carbon nanotube actuators *Science* **284** 1340-1344
- [90] Landi B J, Raffaele R P, Heben M J, Alleman J L, VanDerveer W and Gennett T 2002 Single Wall Carbon Nanotube-Nafion Composite Actuators *Nano Letters* **2** 1329-1332
- [91] Levitsky I A, Kanelos P and Euler W B 2004 Electromechanical actuation of composite material from carbon nanotubes and ionomeric polymer *The Journal of Chemical Physics* **121** 1058-1065

- [92] Landi B J, Raffaella R P, Heben M J, Alleman J L, VanDerveer W and Gennett T 2005 Development and characterization of single wall carbon nanotube-Nafion composite actuators *Materials Science and Engineering B* **116** 359-362
- [93] Lee D Y, Park I-S, Lee M-H, Kim K J and Heo S 2007 Ionic polymer-metal composite bending actuator loaded with multi-walled carbon nanotubes *Sensors and Actuators, A: Physical* **A133** 117-127
- [94] Li C, Thostenson E T and Chou T-W 2008 Sensors and actuators based on carbon nanotubes and their composites: A review *Composites Science and Technology* **68** 1227-1249
- [95] Farinholt K M and Leo D J 2007 Counterion and diluent effects on the response of ionic polymer transducers *Journal of Intelligent Material Systems and Structures* **18** 677-692
- [96] Wang J, Xu C Y, Taya M and Kuga Y 2006 Mechanical stability optimization of FLEMION-based composite artificial muscles by use of proper solvent *Journal of Materials Research* **21** 2018-2022
- [97] Kim S J, Lee I T, Lee H-Y and Kim Y H 2006 Performance improvement of an ionic polymer-metal composite actuator by parylene thin film coating *Smart Materials and Structures* **15** 1540-1546
- [98] Barramba J, Silva J and Costa Branco P J 2007 Evaluation of dielectric gel coating for encapsulation of ionic polymer-metal composite (IPMC) actuators *Sensors and Actuators, A: Physical* **140** 232-238
- [99] Nemat-Nasser S, Zamani S and Tor Y 2006 Effect of solvents on the chemical and physical properties of ionic polymer-metal composites *Journal of Applied Physics* **99** 104902/104901-104902/104917
- [100] Park J K and Moore R B 2009 Influence of Ordered Morphology on the Anisotropic Actuation in Uniaxially Oriented Electroactive Polymer Systems *ACS Applied Materials & Interfaces* **1** 697-702
- [101] Bourne J R, Calhoun B H, Phillips A K and Moore Robert B 2006 Effect of Ionomer Processing Procedures on the Behavior of IPMC Morphology-Actuation Relationships in Processed PFSI Membranes *Polymer Preprints (American Chemical Society, Division of Polymer Chemistry)* **47** 580-581
- [102] Page K A, Landis F A, Phillips A K and Moore R B 2006 SAXS Analysis of the Thermal Relaxation of Anisotropic Morphologies in Oriented Nafion Membranes *Macromolecules* **39** 3939-3946
- [103] Bennett M D and Leo D J 2004 Hybrid actuation in coupled ionic/conducting polymer devices *Materials Research Society Symposium Proceedings* **785** 253-258
- [104] Chen Z, Shen Y, Xi N and Tan X 2007 Integrated sensing for ionic polymer-metal composite actuators using PVDF thin films *Smart Materials and Structures* **16** S262-S271
- [105] Hickner M A, Ghassemi H, Kim Y S, Einsla B R and McGrath J E 2004 Alternative Polymer Systems for Proton Exchange Membranes (PEMs) *Chemical Reviews* **104** 4587-4612
- [106] Kreuer K D 2001 On the development of proton conducting polymer membranes for hydrogen and methanol fuel cells *Journal of Membrane Science* **185** 29-39
- [107] Kreuer K D 1997 On the development of proton conducting materials for technological applications *Solid State Ionics* **97** 1-15

- [108] Wiles K B, Akle B J, Hickner M A, Bennett M, Leo D J and McGrath J E 2007 Directly Copolymerized Poly(arylene sulfide sulfone) and Poly(arylene ether sulfone) Disulfonated Copolymers for Use in Ionic Polymer Transducers *Journal of the Electrochemical Society* **154** P77-P85
- [109] Weinberg S A and El-Hibri J. Polyarylethersulfones (PAES). In Margolis, J M, ed. *Engineering plastics handbook*, pp. 289-325 (McGraw-Hill, New York, NY, 2006).
- [110] Wang S and McGrath J E. Synthesis of Poly(arylene ether)s. In Rogers, M E and Long, T E, eds. *Synthetic Methods in Step-Growth Polymers* (Wiley-Interscience, Hoboken, NJ, 2003).
- [111] Harrison W L, Hickner M A, Kim Y S and McGrath J E 2005 Poly(Arylene Ether Sulfone) Copolymers and Related Systems from Disulfonated Monomer Building Blocks: Synthesis, Characterization, and Performance - A Topical Review *Fuel Cells* **5** 201-212
- [112] Wiles K B, Wang F and McGrath J E 2005 Directly copolymerized poly(arylene sulfide sulfone) disulfonated copolymers for PEM-based fuel cell systems. I. Synthesis and characterization *Journal of Polymer Science, Part A: Polymer Chemistry* **43** 2964-2976
- [113] Harrison W L, Wang F, Mecham J B, Bhanu V A, Hill M, Kim Y S and McGrath J E 2003 Influence of the bisphenol structure on the direct synthesis of sulfonated poly(arylene ether) copolymers. I *Journal of Polymer Science, Part A: Polymer Chemistry* **41** 2264-2276
- [114] Supriya L and Claus R O 2004 Solution-based assembly of conductive gold film on flexible polymer substrates *Langmuir* **20** 8870-8876
- [115] Akle B J, Leo D J, Hickner M and McGrath J E 2003 Electroactive polymers based on novel ionomers *AD (American Society of Mechanical Engineers)* **68** 445-452
- [116] Akle B J, Wiles K B, Leo D J and McGrath J E 2004 Effects of electrode morphology on the performance of BPSH and PATS ionic polymer transducers *Proceedings of SPIE-The International Society for Optical Engineering* **5385** 413-424
- [117] Nemat-Nasser S and Wu Y 2006 Tailoring the actuation of ionic polymer-metal composites *Smart Materials and Structures* **15** 909-923
- [118] Duncan A J, Leo D J and Long T E 2006 Synthesis of Highly Branched Sulfonated Polysulfones for High Performance Electromechanical Transducers *Polymer Preprints (American Chemical Society, Division of Polymer Chemistry)* **48** 853-854
- [119] Lin Q, Unal S, Fornof A R, Yilgor I and Long T E 2006 Highly Branched Poly(arylene ether)s via Oligomeric A₂ + B₃ Strategies *Macromolecular Chemistry and Physics* **207** 576-586
- [120] Duncan A J, Sarles S A, Griffiths D, Leo D J, Cashion M P, Layman J M, Long T E, Beyer F L, Colby R H, Fragiadakis D and Runt J 2008 Influence of topology and morphology in sulfonated polysulfone transducers *Polymer Preprints (American Chemical Society, Division of Polymer Chemistry)* **49** 1022-1023
- [121] Duncan A J, Sarles S A, Leo D J, Long T E, Akle B J and Bennett M D 2008 Optimization of active electrodes for novel ionomer-based ionic polymer transducers *Proceedings of SPIE-The International Society for Optical Engineering* **6927** 69271Q/69271-69271Q/69212
- [122] Shahinpoor M and Kim K J 2002 Mass transfer induced hydraulic actuation in ionic polymer-metal composites *Journal of Intelligent Material Systems and Structures* **13** 369-376

- [123] Tamagawa H and Nogata F 2004 Bending response of dehydrated ion exchange polymer membranes to the applied voltage *Journal of Membrane Science* **243** 229-234
- [124] Tamagawa H, Nogata F and Popovic S 2005 Roles of Ag redox reaction and water absorption inducing the Selemion bending *Journal of Membrane Science* **251** 145-150
- [125] Tamagawa H, Goto S and Sugiyama T 2008 Bending direction of Ag-plated IPMC containing immobile anions and/or cations *Composites Science and Technology* **68** 3412-3417
- [126] Onouchi Y, Sasaki M and Tamagawa H 2009 Current-controlled Selemion bending in the controlled humidity environment *Sensors and Actuators, B: Chemical* **135** 465-471
- [127] Tamagawa H, Watanabe H and Sasaki M 2009 Bending direction change of IPMC by the electrode modification *Sensors and Actuators, B: Chemical* **140** 542-548
- [128] Katchalsky A 1949 Rapid Swelling and Deswelling of Reversible Gels of Polymeric Acids by Ionization *Experientia* **5** 319-320
- [129] Kuhn W, Hargitay B, Katchalsky A and Eisenberg H 1950 Reversible Dilation and Contraction by Changing the State of Ionization of High-Polymer Acid Networks *Nature* **165** 514-516
- [130] Steinberg I Z, Oplatka A and Katchalsky A 1966 Mechanochemical Engines *Nature* **210** 568-571
- [131] Hamlen R P, Kent C E and Shafer S N 1965 Electrolytically Activated Contractile Polymer *Nature* **206** 149-150
- [132] Yannas I V and Grodzinsky A J 1973 Electromechanical Energy Conversion with Collagen Fibers in an Aqueous Medium *Journal of Mechanochemistry and Cell Motility* **2** 113-125
- [133] Grodzinsky A J and Melcher J R 1974 Electromechanics of Deformable Charged Polyelectrolyte Membranes *Proceedings of the 27th Annual Conference on Engineering in Medicine and Biology* **16** 485
- [134] Grodzinsky A J and Melcher J R 1976 Electromechanical Transduction with Charged Polyelectrolyte Membranes *IEEE Transactions in Biomedical Engineering* **23** 421-433
- [135] Asaka K and Fujiwara N 2003 Electric deformation response of anion-exchange membrane/gold composites *Electrochimica Acta* **48** 3465-3471
- [136] Kim D S, Park H B, Rhim J W and Lee Y M 2005 Proton conductivity and methanol transport behavior of cross-linked PVA/PAA/silica hybrid membranes *Solid State Ionics* **176** 117-126
- [137] Wang X-L, Oh I-K, Lu J, Ju J and Lee S 2007 Biomimetic electro-active polymer based on sulfonated poly (styrene-b-ethylene-co-butylene-b-styrene) *Materials Letters* **61** 5117-5120
- [138] Wang X L, Oh I K and Kim J B 2009 Enhanced electromechanical performance of carbon nano-fiber reinforced sulfonated poly(styrene-b-[ethylene/butylene]-b-styrene) actuator *Composites Science and Technology* **69** 2098-2101
- [139] Du F P, Tang C Y, Xie X L, Zhou X P and Tan L 2009 Carbon Nanotube Enhanced Gripping in Polymer-Based Actuators *Journal of Physical Chemistry C* **113** 7223-7226
- [140] Dai C A, Hsiao C C, Weng S C, Kao A C, Liu C P, Tsai W B, Chen W S, Liu W M, Shih W P and Ma C C 2009 A membrane actuator based on an ionic polymer network and carbon nanotubes: the synergy of ionic transport and mechanical properties *Smart Materials and Structures* **18**

- [141] Sangeetha D 2005 Conductivity and solvent uptake of proton exchange membrane based on polystyrene(ethylene-butylene)polystyrene triblock polymer *European Polymer Journal* **41** 2644-2652
- [142] Phillips A K and Moore R B 2005 Ionic actuators based on novel sulfonated ethylene vinyl alcohol copolymer membranes *Polymer* **46** 7788-7802
- [143] Gong G, Li L and Zhang Y 2007 Actuator based on sulfonated comb copolymer of poly (ethylene-co-vinyl alcohol) grafted by poly (ethylene glycol) *Proceedings of SPIE-The International Society for Optical Engineering* **6423** 64234B/64231-64234B/64236
- [144] Dai L, Li L and Zhang Y 2007 Microstructure effects on proton conductivity in EVOH based ionic polymer-metal composites actuator *Proceedings of SPIE-The International Society for Optical Engineering* **6423** 64230X/64231-64230X/64237
- [145] Jeong H Y and Kim B K 2006 Electrochemical behavior of a new type of perfluorinated carboxylate membrane/platinum composite *Journal of Applied Polymer Science* **99** 2687-2693
- [146] Jeong H M, Woo S M, Kim H S, Kim B K, Bang J H, Lee S and Mun M S 2004 Preparation and characterization of electroactive acrylic polymer-platinum composites *Macromolecular Research* **12** 593-597
- [147] Jeong H M, Woo S M, Lee S, Cha G-C and Mun M S 2005 Effect of molecular structure on performance of electroactive ionic acrylic copolymer-platinum composites *Journal of Applied Polymer Science* **99** 1732-1739
- [148] Jeong H M, Kim H S, Lee S, Jung S H and Mun M S 2005 Characteristics of ionic polymer-metal composites prepared with fluorinated acrylic copolymer containing sulfonate anion *Journal of Macromolecular Science, Part B: Physics* **B44** 225-235
- [149] Jeong H M, Kim H S and La Y S 2006 The Effect of Cross-Linking on the Actuation of an Electroactive IPMC Prepared with a Fluorinated Acrylic Copolymer *Journal of Macromolecular Science, Part B: Physics* **45** 119-130
- [150] Jeong H M, Jo A Y, Choi M Y, Han M J and Jho J Y 2006 Preparation and characterization of electroactive anion-exchange acrylic polymer-gold composites *Journal of Macromolecular Science, Part B: Physics* **45** 789-799
- [151] Lu J, Kim S G, Lee S and Oh I K 2008 Fabrication and actuation of electro-active polymer actuator based on PSMI-incorporated PVDF *Smart Materials and Structures* **17**
- [152] Lu J, Kim S G, Lee S and Oh I K 2008 A biomimetic actuator based on an ionic networking membrane of poly(styrene-alt-maleimide)-incorporated poly(vinylidene fluoride) *Advanced Functional Materials* **18** 1290-1298
- [153] Chen J-L, Liu W-L and Cheng L-C 2004 Ionic electroactive graft copolymer with a fluorine-containing backbone and a carbazole-containing side chain, blend thereof and actuator (U.S. Patent 20040127986)
- [154] Han M J, Park J H, Lee J Y and Jho J Y 2006 Ionic polymer-metal composite actuators employing radiation-grafted fluoropolymers as ion-exchange membranes *Macromolecular Rapid Communications* **27** 219-222
- [155] Rao S S, Ojha P K, Rath S K, Palla K B and Patri M 2008 Ionic polymer-metal composites made from radiation grafted FEP-g-styrene-SO₃H membranes *Journal of Applied Polymer Science* **110** 2041-2046
- [156] Yao L and Krause S 2003 Electromechanical Responses of Strong Acid Polymer Gels in DC Electric Fields *Macromolecules* **36** 2055-2065

- [157] Adolf D B, Shahinpoor M, Segalman D J and Witkowski W R 1993 Electrically controlled polymeric gel actuators (U.S. Patent 5250167)
- [158] Shahinpoor M 1994 Continuum electromechanics of ionic polymeric gels as artificial muscles for robotic applications *Smart Materials and Structures* **3** 367-372
- [159] Shahinpoor M 1995 Micro-electro-mechanics of ionic polymeric gels as electrically controllable artificial muscles *Journal of Intelligent Material Systems and Structures* **6** 307-314
- [160] Shahinpoor M 1996 Ionic polymeric gels as artificial muscles for robotic and medical applications *Iranian Journal of Science and Technology* **20** 89-136
- [161] Shahinpoor M 1996 Ionic flexoelectric effect in polymeric gels *Proceedings of SPIE-The International Society for Optical Engineering* **2779** 1006-1011
- [162] De Gennes P G, Okumura K, Shahinpoor M and Kim K J 2000 Mechanoelectric effects in ionic gels *Europhysics Letters* **50** 513-518
- [163] Liu Z S and Calvert P 2000 Multilayer hydrogels as muscle-like actuators *Advanced Materials* **12** 288-291
- [164] Jung J-Y and Oh I-K 2007 Novel nanocomposite actuator based on sulfonated poly(styrene-*b*-ethylene-co-butylene-*b*-styrene) polymer *Journal of Nanoscience and Nanotechnology* **7** 3740-3743
- [165] Jho J Y, Han M J, Park J H, Lee J Y and Wang H S 2005 The effect of ionic membrane properties on the performance of ionic polymer-metal composite (IPMC) actuator *Proceedings of SPIE-The International Society for Optical Engineering* **5759** 497-505
- [166] Wang Q-M, Du X-H, Xu B and Cross L E 1999 Electromechanical Coupling and Output Efficiency of Piezoelectric Bending Actuators *IEEE TRANSACTIONS ON ULTRASONICS, FERROELECTRICS, AND FREQUENCY CONTROL* **46** 638-646
- [167] Moskalik A J and Brei D 1999 Force-deflection behavior of piezoelectric C-block actuator arrays *Smart Materials and Structures* **8** 531-543
- [168] Tsuda T and Hussey C L 2007 Electrochemical Applications of Room-Temperature Ionic Liquids *Electrochemical Society Interface* **16** 42-49
- [169] Duncan A J, Layman J M, Cashion M P, Leo D J and Long T E 2010 Oligomeric A₂ + B₃ synthesis of highly branched polysulfone ionomers: novel candidates for ionic polymer transducers *Polymer International* **59** in press
- [170] Fréchet J M J 2003 Dendrimers and other dendritic macromolecules: From building blocks to functional assemblies in nanoscience and nanotechnology *Journal of Polymer Science, Part A: Polymer Chemistry* **41** 3713-3725
- [171] McKee M G, Unal S, Wilkes G L and Long T E 2005 Branched polyesters: recent advances in synthesis and performance *Progress in Polymer Science* **30** 507-539
- [172] Voit B 2005 Hyperbranched polymers - All problems solved after 15 years of research? *Journal of Polymer Science, Part A: Polymer Chemistry* **43** 2679-2699
- [173] Fossum E and Tan L-S 2005 Geometrical influence of AB_n monomer structure on the thermal properties of linear-hyperbranched ether-ketone copolymers prepared via an AB+AB_n route *Polymer* **46** 9686-9693
- [174] Jikei M and Kakimoto M-a 2001 Hyperbranched polymers: a promising new class of materials *Progress in Polymer Science* **26** 1233-1285
- [175] Odian G 2004 *Principles of Polymerization* (Hoboken, NJ: John Wiley & Sons, Inc.)
- [176] Massa D J, Shriner K A, Turner S R and Voit B I 1995 Novel Blends of Hyperbranched Polyesters and Linear Polymers *Macromolecules* **28** 3214-3220

- [177] Markoski L J, Moore J S, Sendijarevic I and McHugh A J 2001 Effect of Linear Sequence Length on the Properties of Branched Aromatic Etherimide Copolymers *Macromolecules* **34** 2695-2701
- [178] Jikei M, Fujii K and Kakimoto M-a 2003 Synthesis and characterization of hyperbranched aromatic polyamide copolymers prepared from AB₂ and AB monomers *Macromolecular Symposia* **199** 223-232
- [179] Doerpinghaus P J and Baird D G 2003 Separating the effects of sparse long-chain branching on rheology from those due to molecular weight in polyethylenes *Journal of Rheology* **47** 717-736
- [180] Orlicki J A, Viernes N O L, Moore J S, Sendijarevic I and McHugh A J 2002 Roles of Molecular Architecture and End-Group Functionality on the Surface Properties of Branched Polymers *Langmuir* **18** 9990-9995
- [181] Peleshanko S and Tsukruk V V 2008 The architectures and surface behavior of highly branched molecules *Progress in Polymer Science* **33** 523-580
- [182] Radke W, Litvinenko G and Muller A H E 1998 Effect of Core-Forming Molecules on Molecular Weight Distribution and Degree of Branching in the Synthesis of Hyperbranched Polymers *Macromolecules* **31** 239-248
- [183] Czupik M and Fossum E 2003 Manipulation of the molecular weight and branching structure of hyperbranched poly(arylene ether phosphine oxide)s prepared via an A₂ + B₃ approach *Journal of Polymer Science, Part A: Polymer Chemistry* **41** 3871-3881
- [184] Oguz C, Gallivan M A, Cakir S, Yilgor E and Yilgor I 2008 Influence of polymerization procedure on polymer topology and other structural properties in highly branched polymers obtained by A₂ + B₃ approach *Polymer* **49** 1414-1424
- [185] Flory P J 1952 Molecular Size Distribution in Three Dimensional Polymers. VI. Branched Polymers Containing A--R--B_f-1 Type Units *Journal of the American Chemical Society* **74** 2718-2723
- [186] Jikei M, Chon S-H, Kakimoto M-a, Kawauchi S, Imase T and Watanebe J 1999 Synthesis of Hyperbranched Aromatic Polyamide from Aromatic Diamines and Trimesic Acid *Macromolecules* **32** 2061-2064
- [187] Unal S, Yilgor I, Yilgor E, Sheth J P, Wilkes G L and Long T E 2004 A New Generation of Highly Branched Polymers: Hyperbranched, Segmented Poly(urethane urea) Elastomers *Macromolecules* **37** 7081-7084
- [188] Unal S, Lin Q, Mourey T H and Long T E 2005 Tailoring the degree of branching: Preparation of poly(ether ester)s via copolymerization of polyethylene glycol oligomers (A₂) and 1,3,5-benzenetricarbonyl trichloride (B₃) *Macromolecules* **38** 3246-3254
- [189] Unal S and Long T E 2006 Highly Branched Poly(ether ester)s via Cyclization-Free Melt Condensation of A₂ Oligomers and B₃ Monomers *Macromolecules* **39** 2788-2793
- [190] Fornof A R, Glass T E and Long T E 2006 Degree of branching of highly branched polyurethanes synthesized via the *oligomeric* A₂ plus B₃ methodology *Macromolecular Chemistry and Physics* **207** 1197-1206
- [191] Oguz C, Unal S, Long T E and Gallivan M A 2007 Interpretation of molecular structure and kinetics in melt condensation of A₂ oligomers, B₃ monomers, and monofunctional reagents *Macromolecules* **40** 6529-6534
- [192] Unal S, Oguz C, Yilgor E, Gallivan M, Long T E and Yilgor I 2005 Understanding the structure development in hyperbranched polymers prepared by oligomeric A₂+B₃ approach: comparison of experimental results and simulations *Polymer* **46** 4533-4543

- [193] Sheth J P, Unal S, Yilgor E, Yilgor I, Beyer F L, Long T E and Wilkes G L 2005 A comparative study of the structure-property behavior of highly branched segmented poly(urethane urea) copolymers and their linear analogs *Polymer* **46** 10180-10190
- [194] McKee M G, Park T, Unal S, Yilgor I and Long T E 2005 Electrospinning of linear and highly branched segmented poly(urethane urea)s *Polymer* **46** 2011-2015
- [195] Benetatos N M, Chan C D and Winey K I 2007 Quantitative Morphology Study of Cu-Neutralized Poly(styrene-ran-methacrylic acid) Ionomers: STEM Imaging, X-ray Scattering, and Real-Space Structural Modeling *Macromolecules* **40** 1081-1088
- [196] Roy A, Hickner M A, Yu X, Li Y, Glass T E and McGrath J E 2006 Influence of chemical composition and sequence length on the transport properties of proton exchange membranes *Journal of Polymer Science, Part B: Polymer Physics* **44** 2226-2239
- [197] Osborn S J, Hassan M K, Divoux G M, Rhoades D W, Mauritz K A and Moore R B 2007 Glass transition temperature of perfluorosulfonic acid ionomers *Macromolecules* **40** 3886-3890
- [198] Atorngitjawat P and Runt J 2007 Dynamics of Sulfonated Polystyrene Ionomers Using Broadband Dielectric Spectroscopy *Macromolecules* **40** 991-996
- [199] Kim S M and Kim K J 2008 Palladium buffer-layered high performance ionic polymer-metal composites *Smart Materials and Structures* **17** 035011
- [200] Asano N, Aoki M, Suzuki S, Miyatake K, Uchida H and Watanabe M 2006 Aliphatic/Aromatic Polyimide Ionomers as a Proton Conductive Membrane for Fuel Cell Applications *Journal of the American Chemical Society* **128** 1762-1769
- [201] Pang J H, Zhang H B, Li X F and Jiang Z H 2007 Novel wholly aromatic sulfonated poly(arylene ether) copolymers containing sulfonic acid groups on the pendants for proton exchange membrane materials *Macromolecules* **40** 9435-9442
- [202] Saito T, Mather B D, Costanzo P J, Beyer F L and Long T E 2008 Influence of Site-Specific Sulfonation on Acrylic Graft Copolymer Morphology *Macromolecules* **41** 3503-3512
- [203] Sankir M, Bhanu V A, Harrison W L, Ghassemi H, Wiles K B, Glass T E, Brink A E, Brink M H and McGrath J E 2006 Synthesis and characterization of 3,3'-disulfonated-4,4'-dichlorodiphenyl sulfone (SDCDPS) monomer for proton exchange membranes (PEM) in fuel cell applications *Journal of Applied Polymer Science* **100** 4595-4602
- [204] Li Y, VanHouten R A, Brink A E and McGrath J E 2008 Purity characterization of 3,3'-disulfonated-4,4'-dichlorodiphenyl sulfone (SDCDPS) monomer by UV-vis spectroscopy *Polymer* **49** 3014-3019
- [205] Bernal D P, Bedrossian L, Collins K and Fossum E 2003 Effect of Core Reactivity on the Molecular Weight, Polydispersity, and Degree of Branching of Hyperbranched Poly(arylene ether phosphine oxide)s *Macromolecules* **36** 333-338
- [206] Viswanathan R, Johnson B C and McGrath J E 1984 Synthesis, kinetic observations and characteristics of polyarylene ether sulphones prepared via a potassium carbonate DMAC process *Polymer* **25** 1827-1836
- [207] Li Y, Wang F, Yang J, Liu D, Roy A, Case S, Lesko J and McGrath J E 2006 Synthesis and characterization of controlled molecular weight disulfonated poly(arylene ether sulfone) copolymers and their applications to proton exchange membranes *Polymer* **47** 4210-4217

- [208] Iojoiu C, Maréchal M, Chabert F and Sanchez J-Y 2005 Mastering Sulfonation of Aromatic Polysulfones: Crucial for Membranes for Fuel Cell Application *Fuel Cells* **5** 344-354
- [209] Himmelberg P and Fossum E 2005 Development of an efficient route to hyperbranched poly(arylene ether sulfone)s *Journal of Polymer Science, Part A: Polymer Chemistry* **43** 3178-3187
- [210] Grunzinger S J, Hayakawa T and Kakimoto M A 2008 Synthesis of multiblock hyperbranched-linear poly(ether sulfone) copolymers *Journal of Polymer Science, Part A: Polymer Chemistry* **46** 4785-4793
- [211] Martínez C A and Hay A S 1997 Synthesis of poly(aryl ether) dendrimers using an aryl carbonate and mixtures of metal carbonates and metal hydroxides *Journal of Polymer Science, Part A: Polymer Chemistry* **35** 1781-1798
- [212] Chikashige Y, Chikyu Y, Miyatake K and Watanabe M 2006 Branched and Cross-Linked Proton Conductive Poly(arylene ether sulfone) Ionomers: Synthesis and Properties *Macromolecular Chemistry and Physics* **207** 1334-1343
- [213] Wang Y and Morawetz H 1990 Reaction rates in ionomer solutions. 2. Search for the kinetic excluded volume effect *Macromolecules* **23** 1753-1760
- [214] Roovers J, Toporowski P M and Ethier R 1990 Viscoelastic properties of melts of Radel R polysulfone fractions *High Performance Polymers* **2** 165-179
- [215] Fetters L J, Lohse D J, Richter D, Witten T A and Zirkel A 1994 Connection between Polymer Molecular Weight, Density, Chain Dimensions, and Melt Viscoelastic Properties *Macromolecules* **27** 4639-4647
- [216] Hawker C J, Lee R and Frechet J M J 1991 One-step synthesis of hyperbranched dendritic polyesters *Journal of the American Chemical Society* **113** 4583-4588
- [217] Hölter D, Burgath A and Frey H 1997 Degree of branching in hyperbranched polymers *Acta Polymer* **48** 30-35
- [218] Kricheldorf H R, Vakhtangishvili L and Fritsch D 2002 Synthesis and functionalization of poly(ether sulfone)s based on 1,1,1-tris(4-hydroxyphenyl)ethane *Journal of Polymer Science, Part A: Polymer Chemistry* **40** 2967-2978
- [219] Dobrynin A V, Colby R H and Rubinstein M 1995 Scaling Theory of Polyelectrolyte Solutions *Macromolecules* **28** 1859-1871
- [220] Layman J M, Borgerding E M, Williams S R, Heath W H and Long T E 2008 Synthesis and Characterization of Aliphatic Ammonium Ionenenes: Aqueous Size Exclusion Chromatography for Absolute Molecular Weight Characterization *Macromolecules* **41** 4635-4641
- [221] Hara M ed. 1993 *Polyelectrolytes: Science and Technology* (New York, NY: Marcel Dekker, Inc.)
- [222] Bordi F, Cametti C, Tan J S, Boris D C, Krause W E, Plucktaveesak N and Colby R H 2002 Determination of Polyelectrolyte Charge and Interaction with Water Using Dielectric Spectroscopy *Macromolecules* **35** 7031-7038
- [223] Rubinstein M and Colby R H 2003 *Polymer Physics* (New York, NY: Oxford University Press)
- [224] Liu D, Kyriakides S, Case S W, Lesko J J, Li Y and McGrath J E 2006 Tensile behavior of Nafion and sulfonated poly(arylene ether sulfone) copolymer membranes and its morphological correlations *Journal of Polymer Science, Part B: Polymer Physics* **44** 1453-1465

- [225] Nguyen D, Kim, J-S., Guiver, M. D., Eisenberg, A. 1999 Clustering in carboxylated polysulfone ionomers: A characterization by dynamic mechanical and small-angle X-ray scattering methods *Journal of Polymer Science, Part B: Polymer Physics* **37** 3226-3232
- [226] Drzewinski M and MacKnight W J 1985 Structure and properties of sulfonated polysulfone ionomers *Journal of Applied Polymer Science* **30** 4753-4770
- [227] Yarusso D J and Cooper S L 1983 Microstructure of ionomers: interpretation of small-angle x-ray scattering data *Macromolecules (Washington, DC, United States)* **16** 1871-1880
- [228] Hird B and Eisenberg A 1992 Sizes and stabilities of multiplets and clusters in carboxylated and sulfonated styrene ionomers *Macromolecules* **25** 6466-6474
- [229] Kirkmeyer B P, Taubert A, Kim J-S and Winey K I 2002 Vesicular Ionic Aggregates in Poly(styrene-ran-methacrylic acid) Ionomers Neutralized with Cs *Macromolecules* **35** 2648-2653
- [230] Tsang E M W, Zhang Z, Shi Z, Soboleva T and Holdcroft S 2007 Considerations of Macromolecular Structure in the Design of Proton Conducting Polymer Membranes: Graft versus Diblock Polyelectrolytes *Journal of the American Chemical Society* **129** 15106-15107
- [231] Duncan A J, Long T E and Leo D J 2009 Design for optimized electromechanical transduction in ionic polymer transducers fabricated with architecturally controlled ionomers *Proceedings of ASME: Conference on Smart Materials, Adaptive Structures and Intelligent Systems* **2** 1-9
- [232] Shahinpoor M and Kim K J 2004 Ionic polymer-metal composites: III. modeling and simulation as biomimetic sensors, actuators, transducers, and artificial muscles *Smart Materials and Structures* **13** 1362-1388
- [233] Barsoukov E and Macdonald J R eds. 2005 *Impedance Spectroscopy: Theory, Experiment, and Applications* (Hoboken, NJ: John Wiley & Sons, Inc.)
- [234] Boukamp B A 1986 A package for impedance/admittance data analysis *Solid State Ionics* **18-19** 136-140
- [235] Miller J M and Dunn B 1999 Morphology and Electrochemistry of Ruthenium/Carbon Aerogel Nanostructures *Langmuir* **15** 799-806
- [236] Brug G J, van den Eeden A L G, Sluyters-Rehbach M and Sluyters J H 1984 The analysis of electrode impedances complicated by the presence of a constant phase element *Journal of Electroanalytical Chemistry* **176** 275-295
- [237] Pajkossy T 1994 Impedance of rough capacitive electrodes *Journal of Electroanalytical Chemistry* **364** 111-125
- [238] Hsu C H and Mansfeld F 2001 Concerning the conversion of the constant phase element parameter Y_0 into a capacitance *Corrosion* **57** 747-748
- [239] Jovic V D 2009 Capacitance value from CPE, R_{parallel} : A Calculator <http://www.consultsr.com/resources/eis/cpecalc.htm>
- [240] Shervedani R K and Mozaffari S A 2006 Impedimetric sensing of uranyl ion based on phosphate functionalized cysteamine self-assembled monolayers *Analytica Chimica Acta* **562** 223-228
- [241] Duncan A J, Akle B J, Long T E and Leo D J 2009 Ionomer design for augmented charge transport in novel ionic polymer transducers *Smart Materials and Structures* **18** 104005
- [242] Duncan A J, Leo D J, Long T E, Akle B J, Park J K and Moore R B 2009 Electromechanical performance and membrane stability of novel ionic polymer

- transducers constructed in the presence of ionic liquids *Proceedings of SPIE-The International Society for Optical Engineering* **7287** 728711
- [243] Ueki T and Watanabe M 2008 Macromolecules in Ionic Liquids: Progress, Challenges, and Opportunities *Macromolecules* **41** 3739-3749
- [244] Saab A P, Garzon F H and Zawodzinski T A 2002 Determination of ionic and electronic resistivities in carbon/polyelectrolyte fuel-cell composite electrodes *Journal of the Electrochemical Society* **149** A1541-A1546
- [245] Soboleva T, Xie Z, Shi Z, Tsang E, Navessin T and Holdcroft S 2008 Investigation of the through-plane impedance technique for evaluation of anisotropy of proton conducting polymer membranes *Journal of Electroanalytical Chemistry* **622** 145-152
- [246] Cooper E I and O'Sullivan E J 1992 New, stable, ambient-temperature molten salts. *Proceedings of the Eighth International Symposium on Molten Salts* **PV 92-16** 386-396
- [247] Chen H and Elabd Y A 2009 Polymerized Ionic Liquids: Solution Properties and Electrospinning *Macromolecules* **42** 3368-3373
- [248] Cho E, Park J-S, Sekhon S S, Park G-G, Yang T-H, Lee W-Y, Kim C-S and Park S-B 2009 A study on proton conductivity of composite membranes with various ionic liquids for high-temperature anhydrous fuel cells *Journal of the Electrochemical Society* **156** B197-B202
- [249] Sekhon S S, Park J-S, Cho E, Yoon Y-G, Kim C-S and Lee W-Y 2009 Morphology Studies of High Temperature Proton Conducting Membranes Containing Hydrophilic/Hydrophobic Ionic Liquids *Macromolecules* **42** 2054-2062
- [250] Schlick S ed. 1996 *Ionomers: Characterization, Theory, and Applications* (Boca Raton, FL: CRC Press)
- [251] Williams C E, Russell T P, Jerome R and Horron J 1986 Ionic aggregation in model ionomers *Macromolecules* **19** 2877-2884
- [252] Ding Y S, Hubbard S R, Hodgson K O, Register R A and Cooper S L 1988 Anomalous small-angle x-ray scattering from a sulfonated polystyrene ionomer *Macromolecules* **21** 1698-1703
- [253] Register R A and Cooper S L 1990 Anomalous small-angle x-ray scattering from nickel-neutralized ionomers. 1. Amorphous polymer matrixes *Macromolecules* **23** 310-317
- [254] Wu D Q, Chu B, Lundberg R D and MacKnight W J 1993 Small-angle x-ray scattering (SAXS) studies of sulfonated polystyrene ionomers. 2. Correlation function analysis *Macromolecules* **26** 1000-1007
- [255] Wang Z-G, Phillips R A and Hsiao B S 2000 Morphology development during isothermal crystallization. I. Isotactic and atactic polypropylene blends *Journal of Polymer Science Part B: Polymer Physics* **38** 2580-2590
- [256] Moore R B, Gauthier M, Williams C E and Eisenberg A 1992 Heterogeneities in Random Ionomers - A Small-Angle X-Ray-Scattering Investigation of Alkylated Polystyrene-Based Materials *Macromolecules* **25** 5769-5773
- [257] Li Y, Peiffer D G and Chu B 1993 Long-range inhomogeneities in sulfonated polystyrene ionomers *Macromolecules* **26** 4006-4012
- [258] Benetatos N M, Heiney P A and Winey K I 2006 Reconciling STEM and X-ray Scattering Data from a Poly(styrene-*ran*-methacrylic acid) Ionomer: Ionic Aggregate Size *Macromolecules* **39** 5174-5176

- [259] McLean R S, Doyle M and Sauer B B 2000 High-Resolution Imaging of Ionic Domains and Crystal Morphology in Ionomers Using AFM Techniques *Macromolecules* **33** 6541-6550
- [260] Sauer B B and McLean R S 2000 AFM and X-ray Studies of Crystal and Ionic Domain Morphology in Poly(ethylene-co-methacrylic acid) Ionomers *Macromolecules* **33** 7939-7949
- [261] Li J, Wilmsmeyer K G, Hou J B and Madsen L A 2009 The role of water in transport of ionic liquids in polymeric artificial muscle actuators *Soft Matter* **5** 2596-2602
- [262] Li J, Wilmsmeyer K G and Madsen L A 2009 Anisotropic Diffusion and Morphology in Perfluorosulfonate Ionomers Investigated by NMR *Macromolecules* **42** 255-262
- [263] Shaw M T and MacKnight W J 2005 *Introduction to Polymer Viscoelasticity* (Hoboken, NJ: John Wiley & Sons, Inc.)
- [264] Kim J-S, Jackman R J and Eisenberg A 1994 Filler and Percolation Behavior of Ionic Aggregates in Styrene-Sodium Methacrylate Ionomers *Macromolecules* **27** 2789-2803
- [265] Kim J-S, Yoshikawa K and Eisenberg A 1994 Molecular Weight Dependence of the Viscoelastic Properties of Polystyrene-Based Ionomers *Macromolecules* **27** 6347-6357
- [266] Nishida M and Eisenberg A 1996 Dynamic Mechanical Study of Sodium Sulfonated Random Ionomers Based on Hydrogenated Styrene-Butadiene Copolymer *Macromolecules* **29** 1507-1515
- [267] Kim Y S, Hickner M A, Dong L, Pivovar B S and McGrath J E 2004 Sulfonated poly(arylene ether sulfone) copolymer proton exchange membranes: composition and morphology effects on the methanol permeability *Journal of Membrane Science* **243** 317-326
- [268] Nemat-Nasser S and Zamani S 2006 Modeling of electrochemomechanical response of ionic polymer-metal composites with various solvents *Journal of Applied Physics* **100** 064310/064311-064310/064318
- [269] Subianto S, Mistry M K, Choudhury N R, Dutta N K and Knott R 2009 Composite Polymer Electrolyte Containing Ionic Liquid and Functionalized Polyhedral Oligomeric Silsesquioxanes for Anhydrous PEM Applications *ACS Applied Materials & Interfaces* **1** 1173-1182
- [270] Mistry M K, Subianto S, Choudhury N R and Dutta N K 2009 Interfacial Interactions in Aprotic Ionic Liquid Based Protonic Membrane and Its Correlation with High Temperature Conductivity and Thermal Properties *Langmuir* **25** 9240-9251
- [271] Inman D J 2008 *Engineering Vibration* (Upper Saddle River, N.J.: Pearson Prentice Hall)
- [272] Ewins D J 2000 *Modal Testing: Theory, Practice, and Application* (Philadelphia, P.A.: Research Studies Press)
- [273] Ma S, Siroma Z and Tanaka H 2006 Anisotropic Conductivity Over In-Plane and Thickness Directions in Nafion-117 *Journal of the Electrochemical Society* **153** A2274-A2281
- [274] Blachot J F, Diat O, Putaux J-L, Rollet A-L, Rubatat L, Vallois C, Muller M and Gebel G 2003 Anisotropy of structure and transport properties in sulfonated polyimide membranes *Journal of Membrane Science* **214** 31-42
- [275] Essafi W, Gebel G and Mercier R 2004 Sulfonated Polyimide Ionomers: A Structural Study *Macromolecules* **37** 1431-1440
- [276] Rollet A-L, Diat O and Gebel G 2004 Transport Anisotropy of Ions in Sulfonated Polyimide Ionomer Membranes *The Journal of Physical Chemistry B* **108** 1130-1136

- [277] Newbury K M and Leo D J 2003 Linear electromechanical model of ionic polymer transducers - Part I: Model development *Journal of Intelligent Material Systems and Structures* **14** 333-342
- [278] Newbury K M and Leo D J 2003 Linear electromechanical model of ionic polymer transducers - Part II: Experimental validation *Journal of Intelligent Material Systems and Structures* **14** 343-357
- [279] Angell C A 1986 Recent developments in fast ion transport in glassy and amorphous materials *Solid State Ionics* **18-19** 72-88
- [280] Angell C A, Liu C and Sanchez E 1993 Rubbery solid electrolytes with dominant cationic transport and high ambient conductivity *Nature* **362** 137-139
- [281] Snyder J F, Carter R H and Wetzel E D 2007 Electrochemical and Mechanical Behavior in Mechanically Robust Solid Polymer Electrolytes for Use in Multifunctional Structural Batteries *Chemistry of Materials* **19** 3793-3801
- [282] Forsyth M, Jiazeng S and MacFarlane D R 2000 Novel high salt content polymer electrolytes based on high T_g polymers *Electrochimica Acta* **45** 1249-1254
- [283] Imrie C T and Ingram M D 2001 Decoupled ion transport in mesomorphic polymer electrolyte glasses *Electrochimica Acta* **46** 1413-1417
- [284] Wei X and Shriver D F 1998 Highly Conductive Polymer Electrolytes Containing Rigid Polymers *Chemistry of Materials* **10** 2307-2308
- [285] Berthier C, Gorecki W, Minier M, Armand M B, Chabagno J M and Rigaud P 1983 Microscopic investigation of ionic conductivity in alkali metal salts-poly(ethylene oxide) adducts *Solid State Ionics* **11** 91-95
- [286] Yilgor I, Mather B D, Unal S, Yilgor E and Long T E 2004 Preparation of segmented, high molecular weight, aliphatic poly(ether-urea) copolymers in isopropanol. In-situ FTIR studies and polymer synthesis *Polymer* **45** 5829-5836
- [287] Muggli M W, Ward T C, Tchatchoua C, Ji Q and Mcgrath J E 2003 End-group effect on physical aging and polymer properties for poly(ether sulfones) *Journal of Polymer Science, Part B: Polymer Physics* **41** 2850-2860
- [288] Suga T, Wi S and Long T E 2009 Synthesis of Diazocine-Containing Poly(arylene ether sulfone)s for Tailored Mechanical and Electrochemical Performance *Macromolecules* **42** 1526-1532
- [289] Saxena P, Gaur M S, Shukla P and Khare P K 2008 Relaxation investigations in polysulfone: Thermally stimulated discharge current and dielectric spectroscopy *Journal of Electrostatics* **66** 584-588

APPENDIX A: SYNTHESIS OF LONG-CHAIN BRANCHED POLYSULFONES FOR MULTIFUNCTIONAL TRANSPORT MEMBRANES

Motivation

Increasing numbers of technologies are based on the idea of harnessing charge transport for useful processes such as energy harvesting, actuation, sensing, and permselectivity.[107] Although much progress exists based on perfluorosulfonated platforms (Nafion[®], $\sigma \approx 10^{-1} - 10^{-2}$ S/cm),[7] new and more complicated parameters arise as applications require multifunctionality in engineering materials. For instance, in addition to using lightweight, durable, stable, high conductivity proton-exchange membranes in a fuel cell it may be desirable to have the energy source bear load and operate as a structural installment. The most prevalent class of materials potentially capable of such a tradeoff are rubbery “salt-in-polymer” electrolytes that employ polymer segmental motion for transport of free ions from co-dissolved salts.[279, 280] Recently, Snyder *et al.* synthesized a series of “salt-in-polymer” electrolytes from various vinyl-ester resins, poly(ethylene glycol)s (PEO), and lithium trifluoromethanesulfonate (Li-Tf).[281] Various polymer topologies and other parameters were investigated, although none significantly varied the inverse relationship between mechanical stiffness and ionic conductivity. Another promising material class is conductive ionic glasses that demonstrate a high dielectric constant such that ion hopping through lattice defects provides sufficient conductivity in the glassy state.[282] Imrie and Ingram did not investigate branching, but did show that liquid crystalline polyether sidegroups prevented packing of PEO sections of the main chain and resulted in increased conductivity in the glassy state.[283] The multifunctional requirement starkly reflects the difficulty of using materials that display low ambient temperature modulus (especially when hydrated), including PEO and Nafion[®], or consideration of the significant decrease in ionic conductivity with the removal of the hydrating diluent/electrolyte. An overall approach to

achieve both goals is to decouple ion transport from the segmental motion of the polymer through macromolecules designed to incorporate polar, bulky, irregular, rigid monomers into the backbone.[284]

An $A_2 + B_2 + B_3$ polycondensation route is chosen to build upon existing methods and understanding of polymer branching.[171] As reviewed, very few investigations exist concerning the effect of branching on decoupled ion transport in glassy, low humidity single-ion conductors. The chosen matrix of materials includes linear and long-chain branched polysulfone phosphine oxides. The use of polar B_2 and B_3 monomers will aid in the complexation of mobile ions from the imbibed salt within the matrix for charge stabilization and a decrease in the activation energy for ion-hopping. The investigation of decoupled ion transport in such materials is also interesting for reasons of its implications in the electromechanical transducer field. Increases in ion transport without diluents or charges bound to the backbone are likely to augment ionic polymer transducer performance through additive increases in ionic conductivity when introduced into ionomer composition and construction of the IPT composite. IPTs also do not require the same modulus levels as multifunctional batteries and fuel cells, thus providing a potential application for high conductivity composites that fall short of the structural target.

Previous systems demonstrated with PEO that 3-4 etheric oxygens serve to complex a single monovalent cation.[285] Inclusion of branching into the system anticipates the difficult balance between establishing rigidity in the material while increasing intermolecular and intramolecular free volume for the purpose of complexation. To further extend the free volume effect all chosen monomers are bulky in addition to their rigid nature, placing at least four aromatic rings in the backbone of each repeat unit. The monomers were recrystallized for purity before examining their characteristic spectra in comparison to the final polymers with FTIR. The final polymers are characterized with NMR, SEC, TGA, DSC, and DMA. Films cast in the presence of Li-Tf and lithium bis(trifluoromethane)sulfonimide (Li-Bim) were also characterized for their ionic conductivity with electrical impedance spectroscopy (EIS).

Experimental materials and methods

4,4'-dihydroxydiphenylsulfone (DHDPS, Alfa Aesar, 99.9 %) was purified by dissolving in 5% NaHCO_3 solution and precipitation through adjustment of the pH to a value of 5 with concentrated HCl. The crystals were redissolved in aqueous methanol (50%) for a final

precipitation before drying *in vacuo* at 100 °C for 24 h.[206] DHDPS was otherwise used as received from monomer grade material. Bis(4-fluorophenyl)phenylphosphine oxide (BFP3O, Aldrich, 97%) was purified by recrystallization from toluene in triplicate. Anhydrous K₂CO₃ was purchased from Fluka and dried *in vacuo* at 120 °C for 24 h. 1-bromo-4-fluorobenzene (99 %), Mg, and PCl₃ (99.9+ %) were purchased from Aldrich and used as received without further purification to synthesize the B₃ monomer, tris(4-fluorophenyl) phosphine oxide (TFPPO), according to previously reported procedures. [205] Further supply of TFPPO was synthesized through oxidation of tris(4-fluorophenyl) phosphine (Aldrich, purum, >98.0 %) with hydrogen peroxide (30 wt %). Dimethylacetamide (DMAc, Aldrich, anhydrous, 99.8%) was stored over molecular sieves under a nitrogen atmosphere until use. Toluene (Aldrich, 98 %) was dried using a fully contained solvent purification system and stored over molecular sieves under a nitrogen atmosphere until use.

DHDPS, BFP3O, TFPPO, K₂CO₃, DMAc, and toluene (2:1 v/v DMAc to toluene) were charged in a 100 ml three-neck, round-bottom flask at approximately 20 wt % solids in DMAc. The reaction setup was equipped with an overhead mechanical stirrer, a dry nitrogen inlet (w/condenser), and a Dean-Stark trap attached to a reflux condenser. The system was purged with nitrogen for 30 minutes before immersion in a constant temperature bath at 145 °C for 4 h, allowing reflux to remove the water/toluene azeotrope from the reaction mixture. Dropwise removal of water/toluene was performed during the temperature ramp to 165 °C. The reaction at 165 °C was allowed to proceed for approximately 110 h. The reaction solution was allowed to cool to ambient conditions without stirring while remaining under an N₂ atmosphere. The reaction mixture was directly vacuum filtered with filter paper to remove the salt residue condensed by the reaction. The resulting polymer was precipitated into stirring deionized water. The polymers were collected by vacuum filtration and dried *in vacuo* at 250 °C for 1h followed by a slow cooling under reduced pressure to room temperature. The polymers resulting from this synthesis are classified as LIN (linear) and LCB-X (long-chain branched) where X is the mol percent of TFPPO incorporated into the polymer to enable branching.

The reaction solution and solutions of the final polymers were analyzed for disappearance of the aromatic carbon fluorine bond on BFP3O and TFPPO with an ASI ReactIR 4000 *in-situ* FTIR Spectrometer. ¹H NMR and ¹³C NMR analysis of the long-chain branched polysulfones were performed on a Bruker 600 MHz spectrometer at ambient temperature in DMSO-d₆.

Absolute molecular weights and polydispersity indices (PDI) were determined by size exclusion chromatography (SEC) in a Waters system having three in-line Polymer Laboratories PLgel 5 μm MIXED-C columns with an autosampler. Detection is performed through a Waters 2414 Refractive Index detector, a Viscotek 270 Dual Detector viscometer, and a Wyatt Technologies miniDAWN multiangle laser light scattering (MALLS) detector in N-methyl pyrrolidone (NMP) at 50 °C. Thermogravimetric analysis was performed with a TA HighRes-2950 instrument at 10 °C/min under a nitrogen flow. Sub-ambient and high temperature thermal transitions were detected and analyzed with a TA Q1000 differential scanning calorimeter at 10 °C/min under a nitrogen flow. Transitions were determined from the second heat cycle. Membranes were cast from 10 wt % solutions in DMAc on level glass substrates. Casting was performed at ~40 °C under a heat lamp for 24 h. Sub-ambient and high temperature dynamic mechanical analysis was performed with a TA Q800 instrument at 10 °C/min under a nitrogen flow. Electrical properties of the PSF-PO membranes were evaluated through EIS with an Autolab PGSTAT12 Potentiostat/Galvanostat and FRA2 Impedance Module over a frequency range of 1 MHz – 0.1 Hz (procedure same as in Section 4.2.2).

Results and discussion

Following their respective purification steps the DHDPS (A_2), BFP3O (B_2), and TFPPPO (B_3) were confirmed to be of suitable monomer grade purity for step-growth reactions by both thin layer chromatography and elemental analysis . The monomers were combined, as shown in Figure A.1, using 0, 0.2, 0.4, and 0.6 mol percent of TFPPPO to facilitate the polymerization of long-chain branches from the backbone. Long reaction times were employed initially due to the expected decrease in reactivity of DHDPS compared to other bisphenols that have been demonstrated for polysulfones. Indicators for molecular weight development were mainly changes in viscosity of the reaction solution during the first screenings of the reaction.

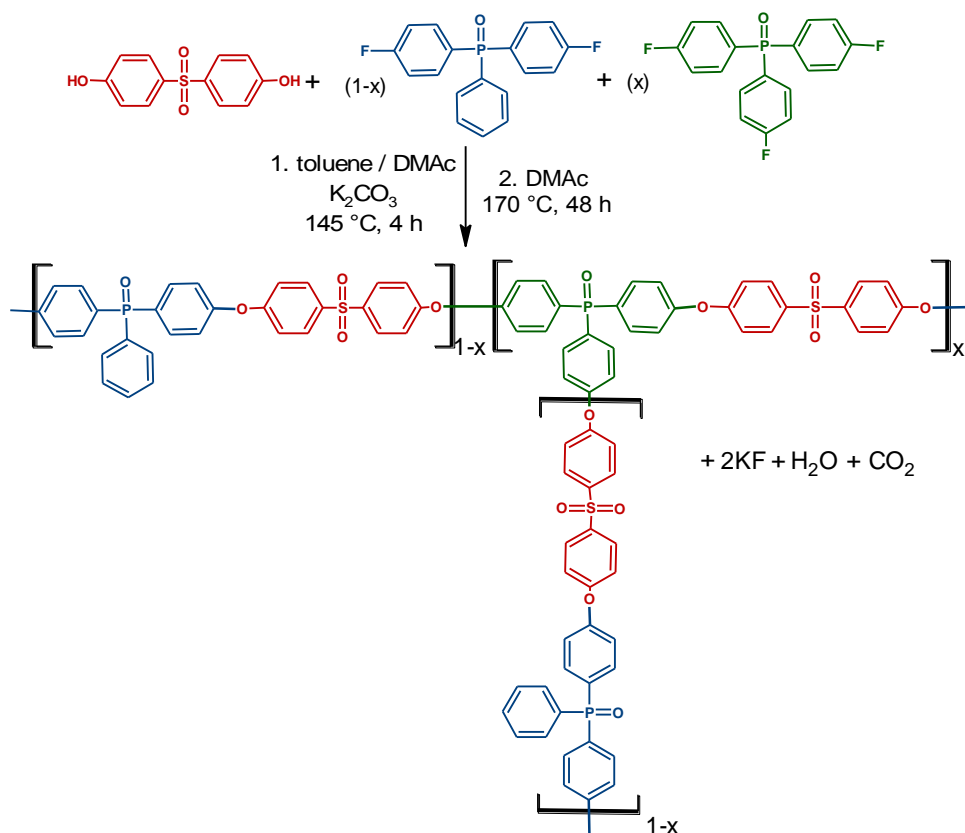


Figure A.1: $A_2 + B_2 + B_3$ synthesis of long-chain branched PSF-PO

In-situ FTIR[286] trials were planned to monitor molecular weight development in the backbone and branches due to condensation of the carbon-fluorine functionality on the aryl ring [C-F bond at $\sim 664\text{ cm}^{-1}$] of BFP3O and TFPPO to the ester bond on reaction with DHDPS. Not only does this technique allow for estimation of sufficient time to reach near 100 % conversion, but it also provides for observation of the limitations of converting the linear branch unit on the PSF-PO backbone to a dendritic one, namely the genus of a long-chain branch. However, the study only reached initial observations of the reaction solution, including all monomers, solvent, and reactants. Use of the FTIR also allowed for analysis solution spectra for Lin-PSF-PO and LCB-0.4-PSF-PO polymers which are shown in Figure A.2[i.] and [ii.] respectively. Comparison between those spectra of monomers and polymers in DMAc confirmed that the C-F bond decreased significantly in the polymer and is a viable candidate to track with realtime *in-situ* FTIR.

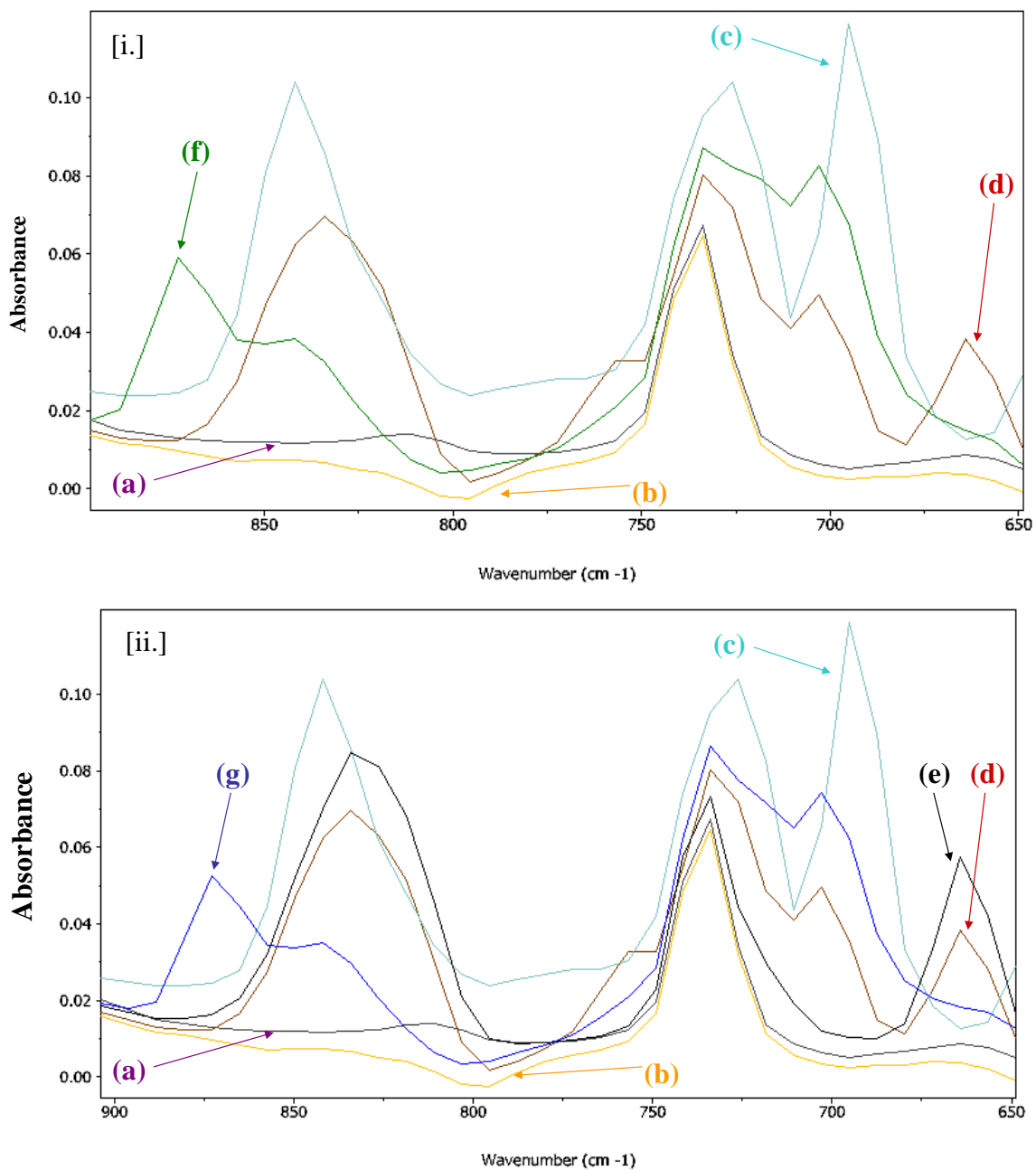


Figure A.2: [i.] LIN-PSF-PO and [ii.] LCB-0.4-PSF-PO analyzed with 2-D FTIR in (a) DMAc solution with (b) K_2CO_3 and (c) DHDPS for disappearance of the aromatic C-F bond [664 cm^{-1}] from the monomers (d) BFP3O and (e) TFPPPO reacting to form the polymers (f) LIN-PSF-PO and (g) LCB-0.4-PSF-PO (alphanumeric characters indicate each individual curve)

The structure of the resulting long-chain branched polymers (and linear analogue) was confirmed with shift assignment and integration of the corresponding peaks in 1H NMR and ^{13}C NMR. A spectral comparison of the linear and branched polymers is provided in Figure A.3. The

protons on the aromatic rings immediately adjacent to the sulfone display a shift at 8 ppm. Similarly located protons on the aromatic rings bonded to the phosphine oxide display a peak at 7.65 ppm. All aromatic protons adjacent to the etheric oxygen show a peak shift of 7.23 ppm. The small peak at 7.55 ppm is associated with the two opposing aromatic protons furthest from the backbone in BFP3O. ^{19}F NMR was planned to observe residual endgroups in the linear polymers as well as the linear and terminal units from partially reacted TFPPPO in the long-chain branched polymers. The full distribution of branching efficiency, conversion to dendritic units, would also be visible in ^{31}P -NMR with increasing inclusion of the B_3 unit and molecular weight. These characterizations were not available at the time of analysis and are yet to be completed.

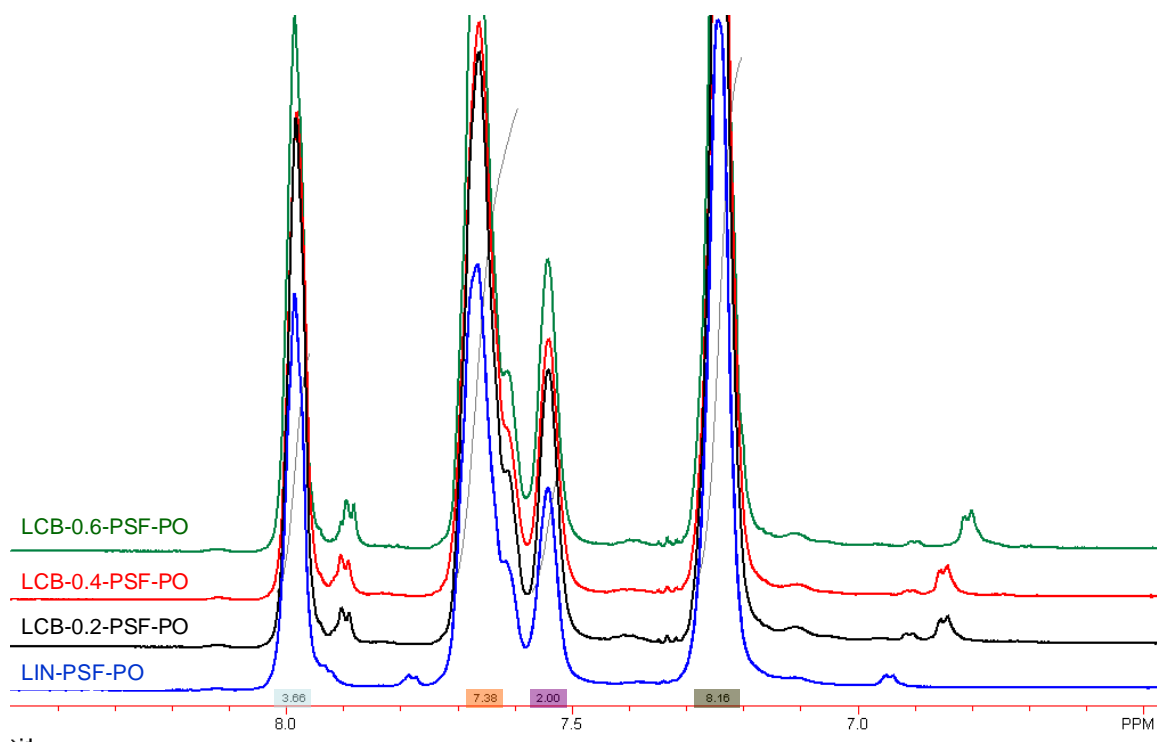


Figure A.3: ^1H NMR spectra overlaid for the series of linear and branched PSF-PO

Absolute molecular weights resulting from the $\text{A}_2 + \text{B}_2 + \text{B}_3$ reaction, as determined from the MALLS traces given by SEC analysis, are shown in Figure A.4. The curves are color coded to the molecular weight data. Curves not identified were other synthetic iterations that do not contribute to the discussion here. Development of molecular weight in the linear system is more easily achieved, almost by two times the molecular weight of the branched polysulfones. To qualify as long-chain branches, each branch must have an individual molecular weight greater

than that of the entanglement molecular weight for the linear polymer. Although the degree of branching is not yet confirmed from NMR, the multi-modal peaks in SEC are typical of branched polymer elution. Due to the low level of total branching associated with long-chain branches, the polydispersity index is approximately equal to the linear sample and does not show the high values normally observed for hyperbranched systems.[183] Overall, the final polymer molecular weights from reactions with identical conditions may indicate that the development of molecular weight from the TFPPPO (B_3) monomers is hindered as compared to reaction with the chemically similar BFP3O (B_2) monomer.

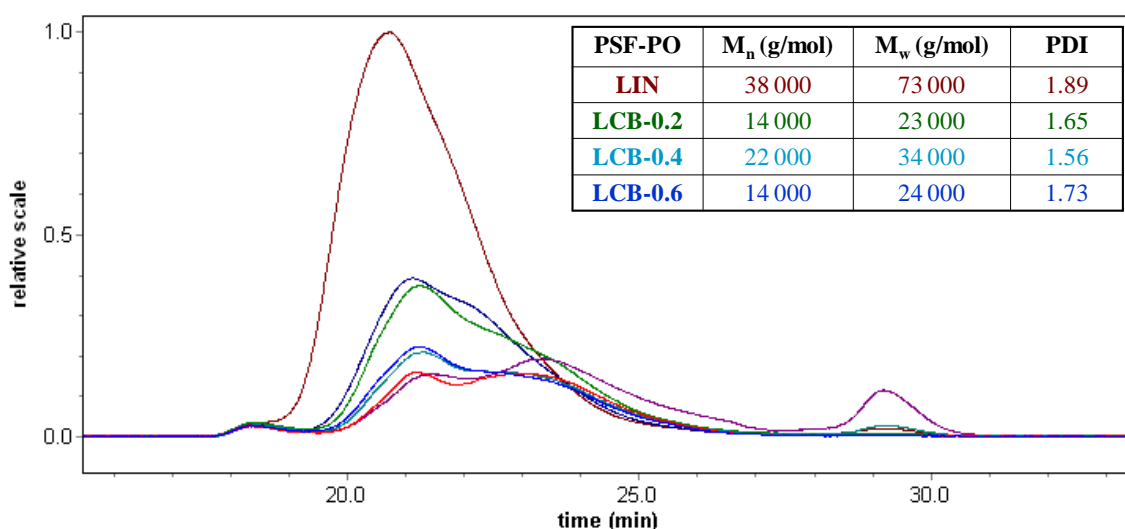


Figure A.4: SEC traces and molecular weight results for LIN-PSF-PO (maroon) and LCB PSF-PO (mol % TFPPPO: 0.2 = green, 0.4 = light blue, 0.6 = dark blue)

The thermal stability of the polymer series was investigated with TGA. Very little difference in degradation temperatures (5 % wt loss, $T_{d5\%}$) is observed between the linear and branched samples or due to the level of branching. The average $T_{d5\%}$ is approximately 460 °C and proceeds quickly through two steps to a significant char yield (~20 %) at 800 °C. The TGA test also reveals that even after drying these materials are very hygroscopic, likely due to the high concentration of polar groups in the backbone. The thermal transitions were initially observed with DSC. As expected, the effect of introducing low levels of long-chain branching has very little effect on the glass transition temperature (T_g) in comparison to the linear material. Based upon second heat measurements these fully amorphous polymers display a T_g between 231 – 236 °C for the linear and branched samples (Figure A.5). However, of greater interest is the

comparison between the glass transition regions of the first and second heats. Although the speed of the cooling ramp associated with drying/annealing was not measured, the cool was not forced and is assumed to be much slower than the 10 °C cooling cycle programmed for DSC. Whereas the first heating cycle does not display any physical aging post- T_g , the second heat does display a maximum post- T_g , indicative of free volume isolated within the polymer during the cooling cycle.[287] This characteristic is likely due to the use of rigid, bulky monomers that restrict the polymer from achieving its thermodynamic equilibrium during transition from the rubbery to the glassy state.

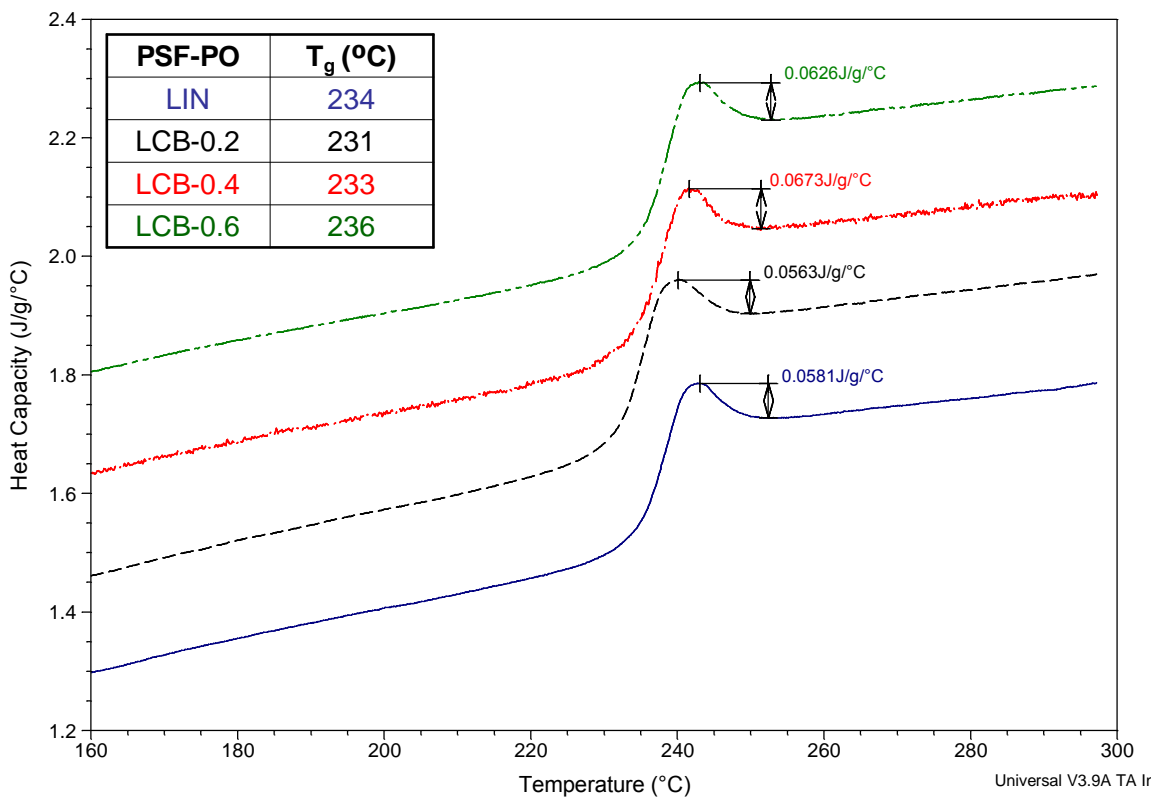


Figure A.5: DSC heat capacity traces and T_g for LIN-PSF-PO (blue) and LCB PSF-PO (mol % TFPPPO: 0.2 = black, 0.4 = red, 0.6 = green)

The dynamic mechanical performance of these linear and long-chain branched polysulfone phosphine oxides was determined with DMA across a wide range of temperature (Figure A.6). It should be noted that casting films of the long-chain branched polymers was severely limited, likely due to insufficient development of molecular weight. Tough films were characteristic for LIN-PSF-PO while the LCB series was very brittle. The linear film displayed a storage modulus

of ~1 GPa in the glassy state across a wide range of temperature, which may be useful for structural applications. The appearance of the glass transition agrees with the range observed in DSC. Furthermore, at subambient temperature peaks are observed in the tan delta signal. The peak at 10 °C is likely the detection of free water melting in the hygroscopic polymer matrix. The lower beta transition at -100 °C is attributed to the aromatic rings of the backbone (and BFP3O sidegroup) flipping and twisting, which is typically observed in bisphenol-A polycarbonates or polysulfones of similar structure.[288] These subambient motions are often attributed to toughening mechanisms in engineering thermoplastics.

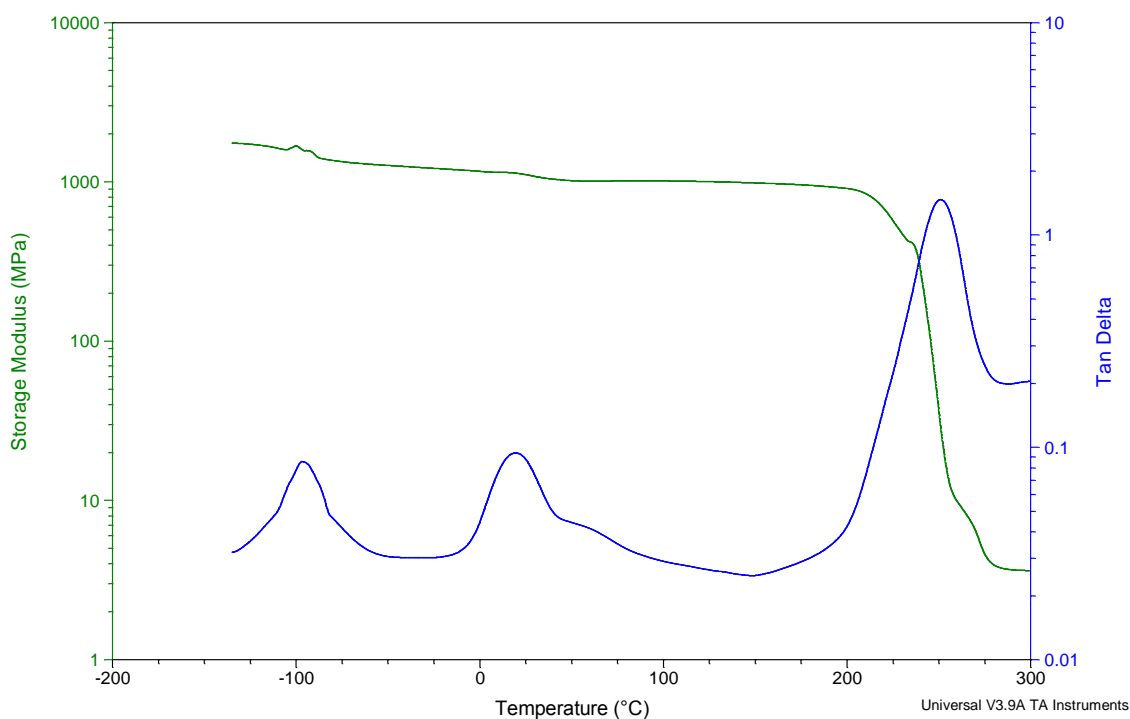


Figure A.6: DMA storage modulus and tan delta signals versus temperature showing T_g and sub- T_g transitions for LIN PSF-PO

As an initial test of the PSF-PO matrix as a host for conductive salts, membranes were cast from solution to contain 1:40 M:O of either $\text{Li}^+ \text{Tf}^-$ or $\text{Li}^+ \text{Bim}^-$. A neat sample was also cast for comparison. In-plane electrical impedance measurements were carried out as shown in the Bode plot in Figure A.7. The impedance response of the membranes is also plotted against the baseline for the empty cell. The measurements were carried out at RT (~22 °C) and a controlled RH of ~40 % in a humidity chamber. Although there is some deviation from the baseline that begins

around 10 Hz, all three membranes demonstrate the same trend. Although no direct estimate of the bulk resistance could be made based on the Nyquist plot, the value is likely to be above 10 GΩ. Also, it is possible that either changes in annealing of the membranes or changes in the salt ratio could further affect the resistance. Regardless, the PSF-PO matrix is has a very high resistance that may not allow for sufficient resolution of the effects of minor levels of branching.

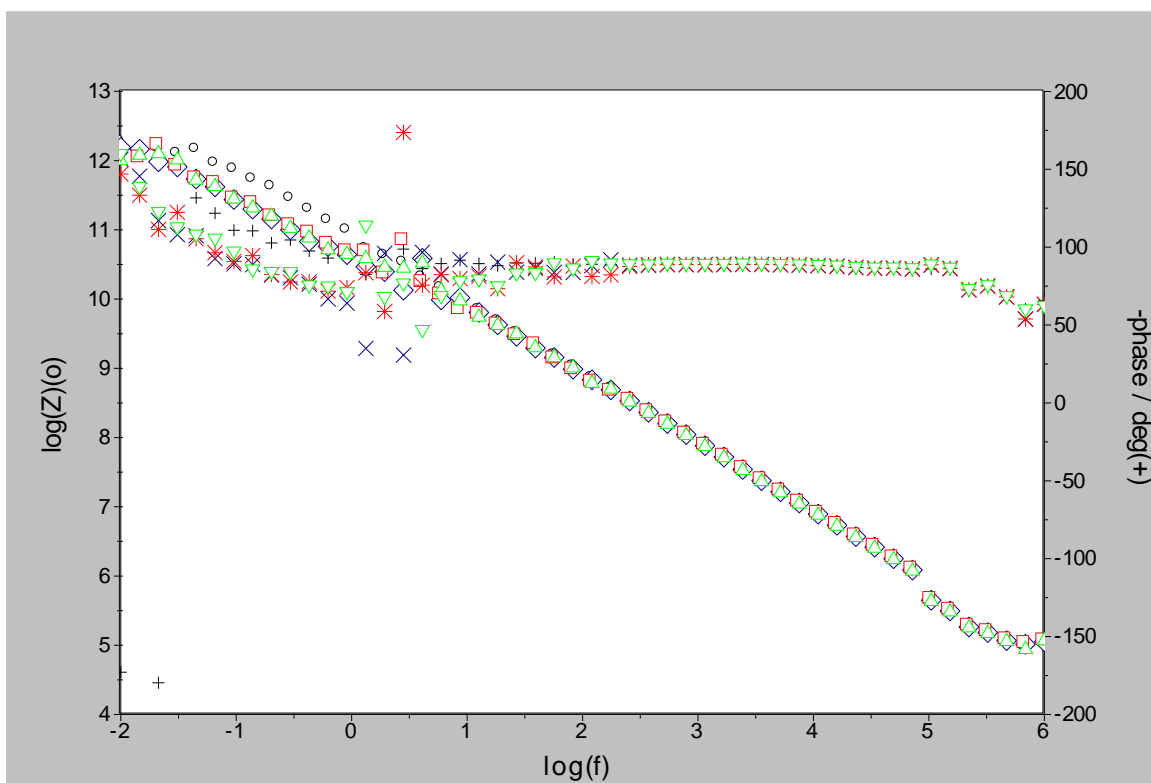


Figure A.7: Combined Bode plot ($|Z|$, phase) for LIN PSF-PO cast (blue: diamond, X) in the presence of Li^+ Tf (red: square, asterisk) or Li^+ Bim $^-$ (green, up triangle, down triangle) against an empty background (black: circle, cross)

Summary

Linear and long-chain branched poly(arylene ether sulfone phosphine oxide)s were synthesized by an $A_2 + B_2 + B_3$ method without gelation. The structure and molecular weight were verified by NMR and SEC. The thermal transitions were observed through TGA, DSC, and DMA across a wide temperature range. Thermal analysis suggests that these polymers retain significant modulus while displaying higher than expected levels of hydrophilicity. The detection of physical aging due to enhanced bulkiness of the chosen monomers suggests an increase in free

volume around the chain which could be explored for complexation of ions during transport. However, the initial tests for membrane electrical properties demonstrated very high resistances potentially on the order of $10\text{ G}\Omega$, even when cast in the presence of conductive lithium salts. Further experiments are necessary to conclude if this result is due to overloading of the salt or truly the high bulk resistance of the membrane. Also, through-thickness measurements should be carried out to provide an estimate of charge transport in the primary direction of interest.

APPENDIX B: INITIAL INVESTIGATIONS OF SBPS MEMBRANES WITH SAXS PERFORMED AT THE U.S. ARMY RESEARCH LABORATORY

Following completion of the synthesis of the sBPS series there was interest in confirmation of a phase-separated morphology within the membranes based on the differences in polarity between the sulfonate and nonsulfonated parts of the polymer backbone. Initial investigation of sBPS morphology was carried out at the U.S. Army Research Laboratory with the aid of Dr. Frederick L. Beyer of the Multifunctional Materials Branch. The laboratory scale equipment consisted of a Rigaku Cu drum-type anode X-ray generator and a pinhole collimated system kept under vacuum. Two sample chambers were available for analysis of different scattering angles and provision of a large range of q for analysis. SAXS was performed at the U.S. Army Research Laboratory using a pinhole-collimated system and X-rays of 1.542 Å wavelength produced from a Cu rotating drum anode. The scattering experiments were run for 120 min due to high transmission numbers for these ionomers. The detector patterns were averaged azimuthally, corrected for film thickness, background scatter, and detector noise, and calibrated versus the scattering of glassy carbon to produce data for the radial scattering vector, q , versus absolute scattering intensity. $q = 2\pi/d$ where d is the lattice constant characteristic of Bragg diffraction in an ordered system.

All of the linear and highly branched polysulfones capable of film forming were examined with SAXS for all levels of sulfonation. The obtained data is provided here for those membranes both in the Na⁺ form and post-acidification in the H⁺ form. Note that the nonsulfonated samples may have trace amounts of KCl remaining in the polymer despite isolation techniques. The most significant trend in the data is the detection of an ionomer peak at $q = 0.05 - 0.1 \text{ \AA}^{-1}$ in the sulfonated materials. According to Bragg's Law and the assumption of ionomer multiplet/cluster morphology this indicates an intercluster (center-to-center) periodicity on the 1 – 10 nm scale. Furthermore, the increase in degree of sulfonation causes a significant increase in scattering

intensity, although not much shift in the location of the ionomer peak. Both ionomers display a large range of q associated with the ionomer peak, indicating that the size distribution of multiplets/clusters is broad and possibly not well defined. Comparison of similar ionic contents with changing distance between branch points suggests possible correlation with shifts of the ionomer peak distribution.

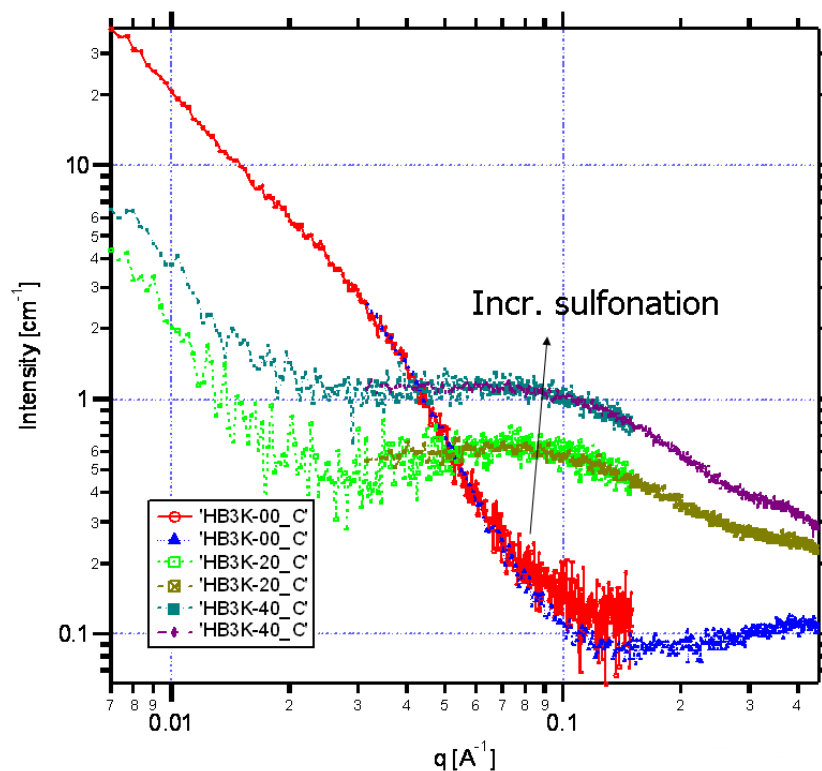


Figure B.1: SAXS spectrum of highly branched sulfonated polysulfones synthesized with a 3 000 g/mol oligomeric spacer between branch points (Na^+ form)

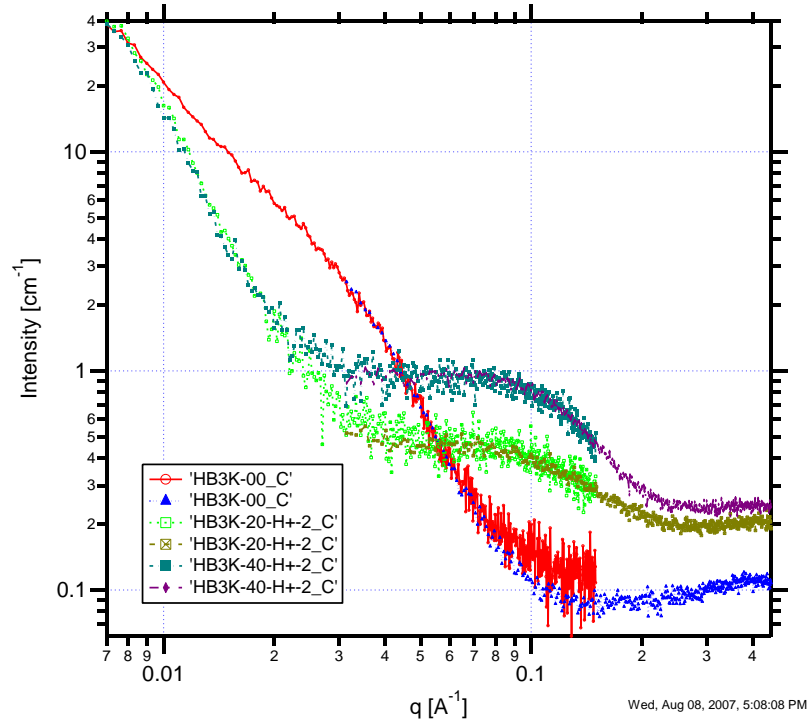


Figure B.2: SAXS spectrum of highly branched sulfonated polysulfones synthesized with a 3 000 g/mol oligomeric spacer between branch points (H⁺ form)

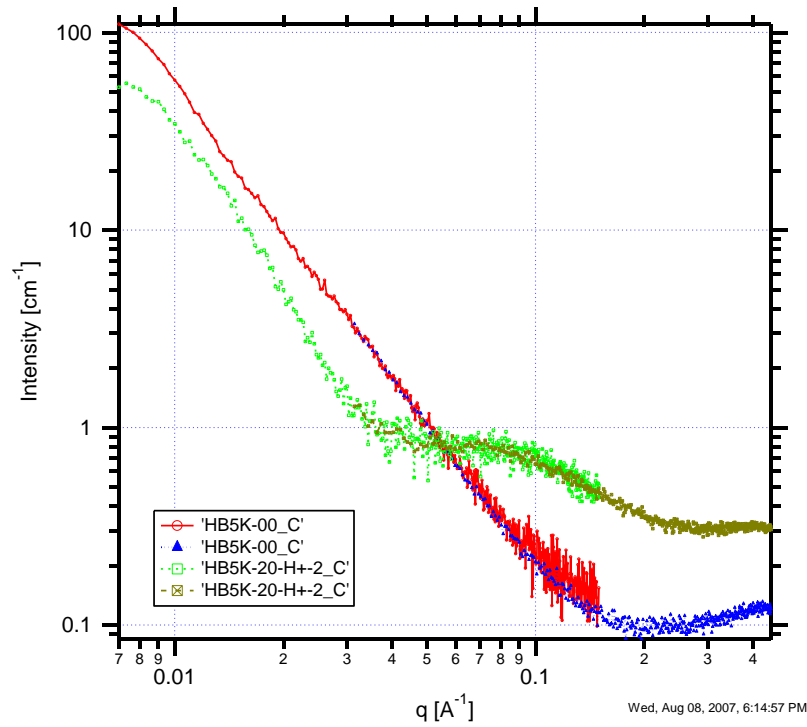


Figure B.3: SAXS spectrum of highly branched sulfonated polysulfones synthesized with a 5 000 g/mol oligomeric spacer between branch points (H⁺ form)

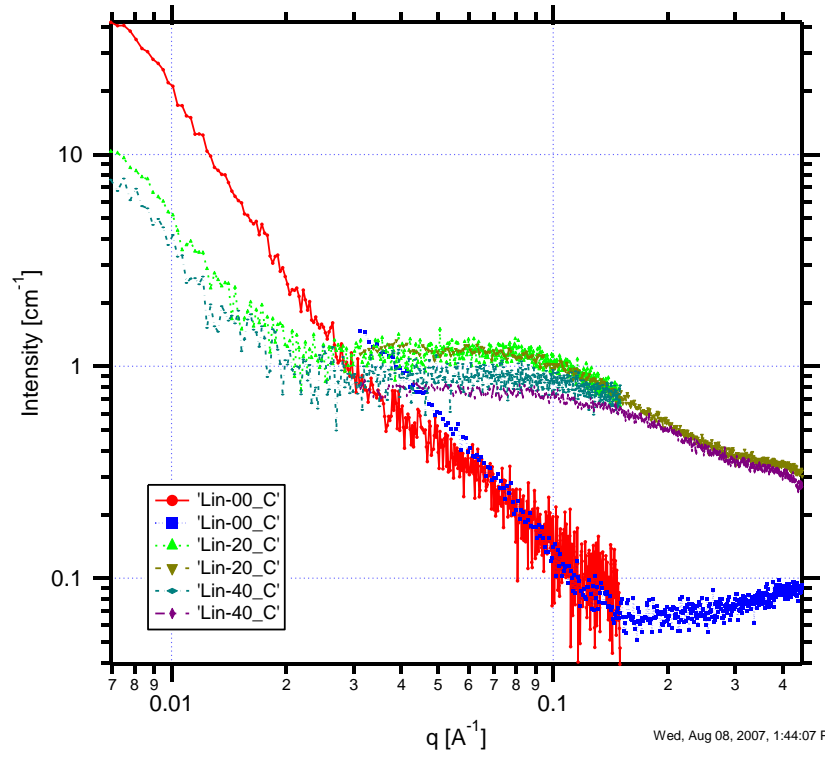


Figure B.4: SAXS spectrum of linear polysulfones with varied degrees of sulfonation (Na⁺ form)

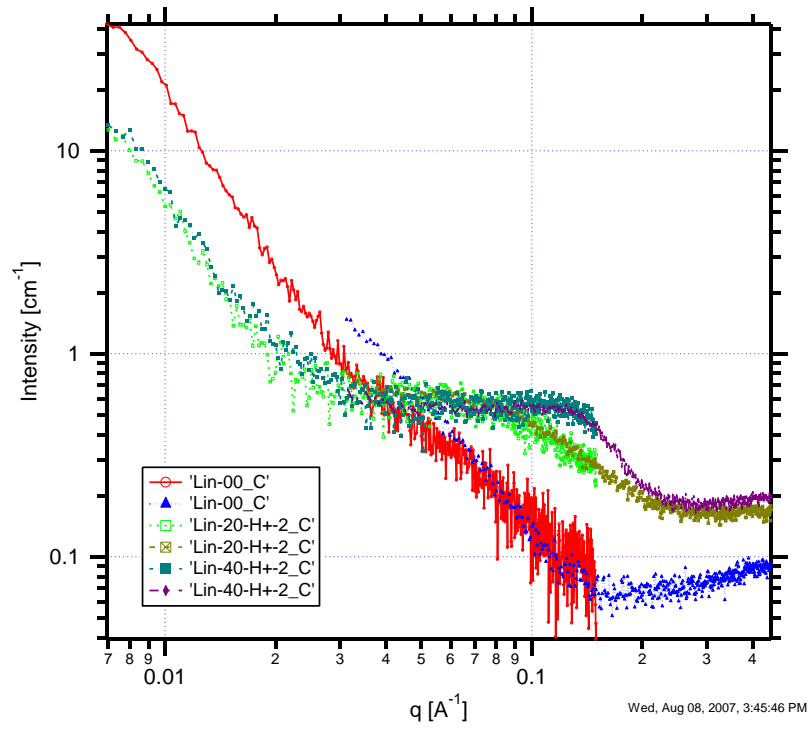


Figure B.5: SAXS spectrum of linear polysulfones with varied degrees of sulfonation (H⁺ form)

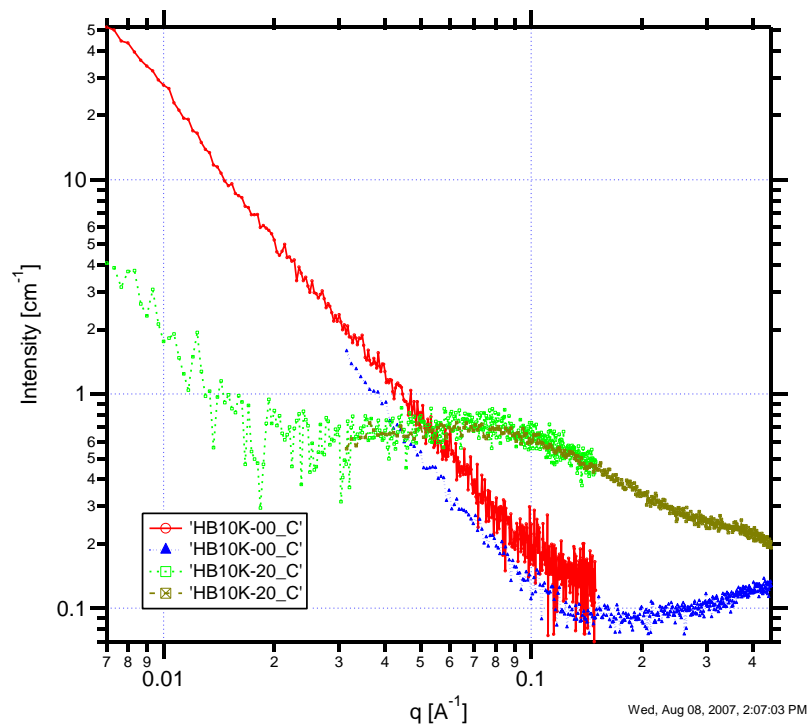


Figure B.6: SAXS spectrum of highly branched sulfonated polysulfones synthesized with a 10 000 g/mol oligomeric spacer between branch points (Na⁺ form)

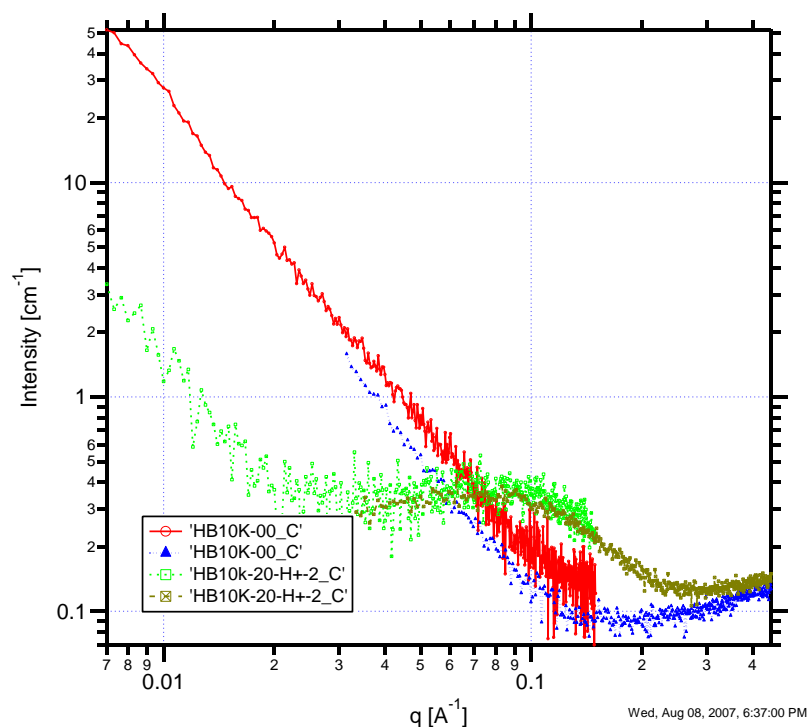


Figure B.7: SAXS spectrum of highly branched sulfonated polysulfones synthesized with a 10 000 g/mol oligomeric spacer between branch points (Na⁺ form)

APPENDIX C: DIELECTRIC RELAXATION SPECTROSCOPY OF SBPS MEMBRANES PERFORMED AT THE PENNSYLVANIA STATE UNIVERSITY

The work described below was performed in collaboration primarily with Dr. Ralph Colby and Daniel Fragiadakis (J. Runt Group) in the Materials Science and Engineering Department at the Pennsylvania State University. Broadband dielectric relaxation spectroscopy (DRS) was performed on a Novocontrol GmbH Concept 40 spectrometer allowing for examination of the changing dielectric environment within the sBPS ionomers based on frequency (0.1 Hz – 10 MHz) of an applied potential and varying temperature (-140 – 350 °C). Temperature stability was controlled within 0.2 °C during each frequency sweep. Films were melt pressed at $T_g + 5$ °C for 1 min at 2 MPa (~300 psi) between a 15 mm and a 20 mm brass electrode. The films were dried in vacuo at 170 °C for 2 h before a slow cool to room temperature under reduced pressure.

Due to the design of these highly branched ionomers specifically for application in electromechanical devices it is interesting to investigate the dynamic response of their dielectric properties through DRS. Morphological changes with temperature in a system that is mainly phase separated based on inclusion of charge into the backbone are detectable with this technique.[198] DMA analysis demonstrated overlapping thermal transitions in the sBPS ionomers based upon the high $T_{g,m}$ of the non-sulfonated polysulfone in relation to the typical range of ionic dissociation for sulfonate salts (~200 – 300 °C).[48] Ionic association normally leads to thermal transitions greater than the $T_{g,m}$ of the base, non-charged polymer, although the difference between the matrix and cluster T_g is greater than seen with the present polysulfones. A frequency sweep of each sample was performed isothermally at 10 °C steps from -140 – 350 °C. DRS curves for highly branched polysulfones (HB-3kBPS) with varied degrees of sulfonation are provided in Figure C.1 for the temperature range 120 – 180 °C. The most prominent feature in this temperature range is the shoulder in ϵ' shown by HB3K-40 at approximately 150 °C and 1Hz. A similar sub- T_g shoulder is present, although small and difficult to distinguish, at 150 °C

in ϵ' for HB3K-20. No such transition is detected for HB-3kBPS-00, indicating origin with the sulfonate salts on the backbone of the ionomers which may be the loss of tightly bound water as was seen in DMA. The α -transition temperatures detected with DRS (320, 280, and 240 °C respectively) as well as the ionic transitions match well with data from DMA. The magnitude of the dielectric constant in these materials is also comparable to typical values for similar polysulfones.[289] However, the low dielectric constant for HB-3kBPS-20 is likely due to delamination of the electrode from the membrane, which effectively lowered the value and disrupted the trend based on degree of sulfonation. More runs were needed to correct this value and provide repeatability for further confirmation of the DMA assignments.

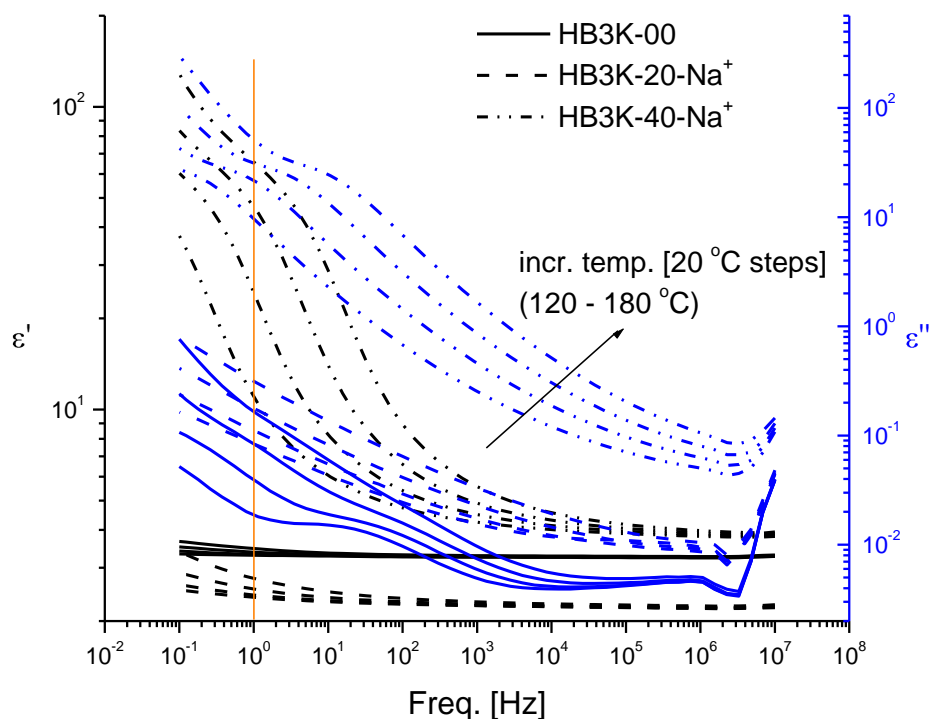


Figure C.1: DRS spectrum of dielectric constant (black) and dielectric loss (blue) for highly branched polysulfones with varied ionic content from 120 – 180 °C

APPENDIX D: COPYRIGHT PERMISSIONS

Chapters 1 – 4 have a foundation in previously published manuscripts and conference papers as indicated. All other cited figures are presently referenced per the provided permissions from the respective publishers.